Quantitative Analysis of Intra-Operative Magnetic Resonance Images and Tissue Survival for Laserthermia of 9L Gliosarcoma

by
Stephen Gerard Hushek

B.S., Massachusetts Institute of Technology, 1986

Submitted to the Department of Nuclear Engineering
in partial fulfillment of the requirements for the degree of

Doctor of Philosophy in Nuclear Engineering

at the

Massachusetts Institute of Technology

May 1994

Author.....
Department of Nuclear Engineering
May 12, 1994

Certified by.....
Jacquelyn Yanch
Associate Professor of Nuclear Engineering, MIT
Thesis Committee Chairperson

Certified by.....
Ferenc Jolesz
Associate Professor of Radiology, Harvard Medical School
Thesis Supervisor

Certified by.....
Bruce Rosen
Visiting Associate Professor of Nuclear Engineering, MIT
Thesis Supervisor

Certified by.....
Beverly Teicher
Associate Professor of Medicine and Radiation Therapy,
Harvard Medical School
Thesis Supervisor

Accepted by.....
Allan F. Henry
Chairman, Departmental Committee on Graduate Students

Quantitative Analysis of Intra-Operative Magnetic Resonance Images and Tissue Survival for Laserthermia of 9L Gliosarcoma

by

Stephen Gerard Hushek

Submitted to the Department of Nuclear Engineering
on May 12, 1994, in partial fulfillment of the
requirements for the degree of
Doctor of Philosophy

Abstract

This thesis explores the use of magnetic resonance imaging (MRI) as a control system for laser thermal therapy treatments. The objective of thermal therapy is the delivery of a lethal thermal dose to the target tissue without damaging the surrounding tissue. A variety of energy delivery methods including RF heating, microwaves, focussed ultrasound and lasers have the ability to rapidly deposit large amounts of energy in a limited volume of tissue but require a system to guide or control the spatial and temporal extent of the energy deposition. This thesis explores the relationship between images acquired during a laser thermal therapy treatment and the biological results of the treatment as measured with a colony growth assay. The images are processed to produce an image-derived surviving fraction which is compared to the measured surviving fraction.

Phantom experiments are also conducted to evaluate the temperature sensitivity and accuracy of several pulse sequences and the criteria for evaluation of different techniques was discussed. The potential of polyacrylamide gel to simulate the optical and MR properties of tissue was examined. The ability of MRI to determine thermal distributions in homogeneous media was also tested.

Female Fischer 344 rats that have the 9L-50 gliosarcoma implanted subcutaneously on both flanks are treated by 1064nm Nd:YAG infra-red laser irradiation (LaserScope Inc., San Jose, CA) with a diffusing tip optical fiber (Dornier Medical Systems, Kennesaw, GA). The imaging is

performed with a standard clinical imager (GE Medical Systems., Waukesha, WI) and consists of: a pre-treatment tissue characterization series to determine the T1 and T2 of the tumor tissue; a dynamic, T1-weighted fast spin echo series acquired during each laser treatment; and a repeat of the tissue characterization imaging. The temperatures at 4 locations in the tumor are recorded between images with copper-constantin thermocouples (Omega Inc., Stamford, CN). The tumors are irradiated for 10 minutes.

The tumors are excised approximately 2-3 hours after treatment and sectioned into regions. In one set of experiments the entire tumor was processed. In another set of experiments a single slice of tissue, which approximately matched the imaging slice, was used for the colony growth assay and tissue immediately adjacent to the excised slice was processed for histological evaluation.

Regions of interest (ROIs) on the images were designed to match the tumor excision regions in the experiments. An estimate of the surviving fraction for the piece of tissue represented by each pixel was derived from the signal intensity changes in the intra-operative images. These individual, image-derived surviving fractions were then averaged to yield the image-derived surviving fraction for the complete region, which was then compared to the surviving fraction of the equivalent region of tissue as measured by the colony growth assay.

Different equations were tested to investigate the relationship between the images and the measured cell survival. The Marquardt-Levenberg, non-linear, least-squares fitting algorithm was used to determine the values of the coefficients for each equation that yield the best fit between the image-derived surviving fraction values and the measured values.

This thesis contains the first report of measured surviving fraction values for an in vivo thermal therapy treatment with MRI control. This thesis also contains the first attempt to correlate intra-operative MR images with a quantifiable measure of the treatment on a pixel-by-pixel basis. The thermal treatments induced levels of cell kill in the tumor ranging from 60% to ~100%. The image-derived surviving fractions were able to match measured surviving fractions of 10% or greater to within ±6% in the single slice excision experiments but were not successful in predicting greater levels of cell kill. The histology results indicated little or no thermally specific damage and indicate that acute histology is not an accurate assessment of thermal treatments.

This thesis demonstrates that polyacrylamide-based gel phantoms can be doped with optical and MR materials to independently control the optical and MR parameters of the material. The combination of agar and

polyacrylamide appears to produce a gel with temperature-sensitive phase changes that could mimic similar behavior in tissue. Good temperature sensitivity and temperature accuracy can be achieved with fast spin echo sequences with acquisition times of 15 seconds or less.

Thesis Supervisor: Ferenc Jolesz
Title: Associate Professor of Radiology, Harvard Medical School

Thesis Supervisor: Jacquelyn Yanch
Title: Associate Professor of Nuclear Engineering, MIT

Thesis Supervisor: Beverly Teicher
Title: Associate Professor of Medicine and Radiation Therapy, Harvard Medical School

Thesis Supervisor: Bruce Rosen
Title: Visiting Associate Professor of Nuclear Engineering, MIT

ACKNOWLEDGEMENTS

I would like to express my appreciation to my thesis advisors: Dr. Ferenc Jolesz, Dr. Beverly Teicher, Dr. Jacquelyn Yanch and Dr. Bruce Rosen. I owe the opportunity to do this research to Dr. Jolesz and his willingness to support my interests and ideas. I owe him a great deal, not only for his sponsorship but for his constant encouragement of all aspects of my career. I am also deeply indebted to Dr. Beverly Teicher, who, together with the staff in her lab, taught this engineer more than he ever wanted to know about biology and biological lab techniques and made the unique data in this thesis possible. I would also like to thank Dr. Yanch and Dr. Rosen who were not directly involved in the experiments but were always ready with encouragement and advice.

I would also like thank everyone at the Brigham and Women's Hospital MR Division: clinical staff, staff researchers, students and also everyone in the Surgical Planning Lab. The cameraderie I have enjoyed with everyone has made my time there enjoyable and has made my graduate years truly fly by. I would especially like to thank Jean Valk for all the admnistrative hassles she has gone through on my behalf, Mary Maloney for her constant help and smiles, and Mark Anderson and Adam Shostack for their many hours of help with the computers. I also owe a great deal to Dr. Larry Panych for being a great intellectual sparring partner and an even better friend. I would also like to thank Gilberto Kernahan, who was the extra set of hands at most of my experiments. I would especially like to thank Paul Morrison for so many things but mostly for being such a great person to work with. In addition to everyone at the Brigham, I would like to thank Jim Mitchell at GE Medical Systems who helped me with the FSE pulse sequence work and Dr. Randall Margolis who reviewed the histology slides.

There have been so many people who have helped me in one way or another in all my years here, I cannot possibly mention them all. Thanks!

Finally, I would like to thank my entire family for all the support that they have provided throughout my academic career. I couldn't have done it without them. I would like to dedicate this thesis to my parents, Allan and Lucille Hushek, who taught me everything I needed to know before, during and after kindergarden and to my wife Laurie, who has made it all worthwhile.

TABLE OF CONTENTS

List of Figures

List of Tables

Chapter 1 Thermal Therapy

1.1 Introduction

This thesis describes an integrated MR imaging/laser/temperature measurement system designed and built for laser thermal therapy with MR control. Initial data acquired with the system from phantom and animal experiments is reviewed and discussed. The reader is introduced to the biological and physical concepts relevant to MR-guided laser thermal therapy with discussions of the MR imaging, optical, biological, and thermodynamic processes involved. The concept of an Image-to-Actual-Function is presented and the improvements in the concept incorporated in this thesis are discussed. The quantum and classical physics of MR parameter temperature sensitivity and temperature sensitive imaging contrast are reviewed. The phantom experiments are described and the issues relating to temperature sensitivity, temperature accuracy and thermal distribution mapping with MR imaging are illuminated with a review of the data from the phantom experiments.

The animal experiments are described, with the details of the integrated thermal therapy system discussed in the context of data acquisition for an in vivo thermal therapy treatment of a 9L-50 gliosarcoma implanted subcutaneously in a rat. The two types of tissue analysis and the motivation for their use are described. The methodology for fitting the image derived estimates of the surviving fraction values is presented. The surviving fraction data obtained from the animal experiment are reviewed and the results of the computer fitting process are presented and discussed.

The significance of the the results presented in the thesis is discussed and opportunities for further investigations in the area are postulated.

1.2 Background

The use of intense, localized changes in temperature is slowly emerging as a viable therapeutic technique for tissue destruction.[1, 2,3,4,5,6] The destructive thermal energy can be deposited with laser light, microwaves, RF-induced heating, focussed ultrasound or by freezing with specially designed cryo-probes. Such techniques have come to be known as thermal techniques or thermal surgeries to distinguish them from hyperthermia techniques that seek to generate a uniform temperature distribution of approximately 43°C throughout a target region.

Initial attempts to use laser energy to generate lesions in tissue sought to establish a relationship between the amount of energy delivered and the lesion size. Studies varied laser power, wavelength, optical source geometry and energy and examined the relative significance of these variables in a variety of tissues.[7,8,9,10,11,12] Variability of the optical and thermal tissue parameters from tissue to tissue and from sample to sample within the same tissue type, combined with the dynamic behavior of these parameters, prevented reliable predictions of lesion size for a given treatment. The lesion size variations, combined with patient safety concerns, precluded the use of these techniques without a reliable control system that could monitor the effects intra-operatively.[1,13,14,15]

The use of lasers flourished in specialties in which the treatment effects could be observed visually: dermatology and opthalmology. In these specialties the surgeon can observe the changes at the surface of the treated area and adjust the laser parameters to optimize the treatment. Treatment

of interstitial tissue volumes was not attempted because of the inability to determine the effects of the treatment in real time. Several techniques were proposed to overcome this difficulty and provide the information necessary to effectively control the therapy.[1,2,3,14,16,17,18]

1.2.1 Control Systems

1.2.1.1 Invasive Thermometry

The thermal distribution within the tissue cannot be analytically determined so techniques for direct measurement of the thermal distribution during the treatment have been developed. The ability of any system to provide the necessary feedback for control of thermal therapy treatments is dependent on its spatial resolution, temporal resolution, temperature sensitivity and temperature accuracy. Many studies have attempted to use multi-point thermometry to infer the temperature distribution throughout the treatment volume. These studies have had limited success because the number of thermometers required to adquately characterize the temperature throughout a treatment volume on the order of several cubic centimeters can become impractical for some clinical procedures. They also suffer from spatial irregularities such as large blood vessels, fascia planes, organ boundaries and bones that can distort the temperature distribution over very short distances. Furthermore, the presence of the temperature sensing devices can modify the thermal distribution in the tissue because their thermal conductivity is often very different from that of tissue. Thus, the temperature distribution is modified

by the attempt to measure it and the uniform temperature distribution the treatment is trying to create is disturbed.

1.2.1.2 Radiologic Control Systems

1.2.1.2.1 CT

Radiologic modalities have an advantage over invasive thermometry because they are non-invasive and have very good spatial resolution, while they tend to be at a disadvantage in terms of temporal resolution and temperature accuracy. CT, ultrasound, and MRI were all proposed as potential imaging modalities that could be used for control of interstial laser therapy.[1,2,3,4,5,6,13,14,15,16,17,18] CT was determined to be inappropriate because of the lack of temperature sensitivity.[17] CT contrast depends on variation in electron density, which is not a strong function of temperature. In addition, the high radiation dose associated with the exposure of a long treatment could render the technique inappropriate.

1.2.1.2.2 Ultrasound

The real-time and 3D properties of ultrasound suggested its potential as a thermal therapy control modality. Ultrasound is able to detect the presence of discontinuites in acoustic impedance, which is the product of the speed of sound and the material's density, so tissue boundaries can be seen clearly. The two components of acoustic impedance are both temperature sensitive, but not strongly enough to clearly see the temperature increases.[19] However, some of the effects of the treatment,

such as vapor pockets, microbubbles or coagulation necrosis, can be seen relatively clearly in real time with ultrasound.[19,20]

1.2.1.2.3 Magnetic Resonance

The temperature sensitivity of magnetic resonance imaging has been studied by several investigators.[21,22, 23,24] Early studies concluded that the temperature accuracy of T1-, T2- or proton density-weighted MRI was insufficient for its use as a control system for hyperthermia.[22,25] However, recent technological developments yielding shorter scan times and improved signal-to-noise ratios have enhanced MRI's ability to detect temperature changes in tissue.[26] Gradient echo and spin echo imaging have both been tested, exploiting the temperature sensitivity of the T1 relaxation parameter.[26] Diffusion weighted imaging, which is sensitive to changes in the molecular diffusion coefficient of water, has also been tested for temperature sensitivity.[27,28] Starting with the initial proposal to use MRI to monitor interstitial laser thermal therapy[1] the field has progressed from animal studies.[4,29,30,31,32] to trials in humans.[3,6,33,34,35,36] A detailed discussion of the theoretical basis for temperature sensitivity in MRI, along with a review of the relevant literature, will be included in Chapter 2.

1.3 Control System Motivation: Complexity and Interactions

The need for an adquate control system for laser-based thermal therapy techniques is clearly demonstrated by a review of the underlying physical processes involved in the treatment. The first process involved is

the irradiation of the tissue with the laser system. The optical distribution in the tissue is a function of the laser source geometry and the optical properties of the tissue at the wavelength used. The optical properties of the tissue are spatially heterogeneous, temperature sensitive, chemically sensitive and dynamic. The optical distribution combines with the spatial distribution of the optical absorbers in the tissue to determine the thermal source.

The thermal source is one term in a complex equation that determines the spatial distribution of heat in the tissue. Other terms in the equation include the conduction of heat through the bulk tissue, the convection of heat by flowing blood and the generation of heat by metabolic processes. The metabolic term is often insignificant relative to the other terms in the equation. These parameters combine to produce a dynamic, heterogeneous temperature distribution.

The temperature distribution, combined with knowledge of the thermal sensitivity of the tissue, would yield a map of the treatment's effects. However, the thermal sensitivity of the tissue can also be heterogeneous, is difficult to quantify and depends on many factors, with the exact damage mechanisms and their relative significance not well understood at this time. In addition, the temperature distribution changes with time and the relationship between time, temperature and cell survival in vivo is not clear.

The interaction of several sets of spatially heterogeneous, dynamic distributions that cannot be measured non-invasively suggests two possible

approaches. In one approach we develop models of increasing complexity that deal with the interactions. Such a model could take the form of a computer simulation with 3 components: an optical source component, a thermodynamics component and a MR temperature sensitivity component, each interacting with the other. The model could produce synthetic images that could be compared to actual images, with updates to the model attempting to account for the differences.

The potential of this approach is limited because of the multiple interacting processes involved in the model. It would be difficult to determine which model parameters to adjust to match the MR image to the simulated image. A change in the spatial distribution of an optical parameter could yield simulated images that would be equivalent to images produced with a modified thermal parameter distribution. The inability to simultaneously measure both the intermediate optical distribution and the intermediate thermal distribution along with the final MR image prohibits determination of the uniquely correct parameter adjustment.

This thesis takes a different approach. It attempts to determine if there is a direct correlation between the images and the cell survival, without trying to determine the optical distribution or the exact temperature map. The correlation is investigated retrospectively, but if the relationship between images and cell survival could be determined it could be applied proactively during clinical treatments. The information gathered within this paradigm would not be appropriate for immediate clinical application because it is specific to the tumor type, imaging

technique and treatment technique in the experimental protocol. However, it can serve as a basis for further studies that more closely relate to actual clinical treatments. It may also yield information as to the nature of the MR-detectable changes that occur in the tissue that could be used as universal indicators of treatment efficacy.

In this investigation, the significance of the changes seen in the images during the treatment must be considered in the context of the biological response of the tissue to a temperature increase. The tissue response to a temperature increase at both the macroscopic and microscopic level is an entire field of hyperthermia biology research, but the MR-specific contrast mechanisms associated with the different aspects of the tissue response have not been characterized. There may be other factors beyond the explicit temperature sensitivity of the MR relaxation parameters that could produce changes in image signal intensity. Physiologic and metabolic responses to the temperature increase could modify the tissue's MR parameters, but the nature of these modifications, their magnitude and their relationship to the explicit temperature-induced changes are not known.

One example of a physiologic change in response to temperature whose MR characteristics are beginning to be studied is the change from hemoglobin to methemoglobin when blood reaches a temperature of 60°C. A preliminary report of this phenomenon and the associated shortening of the T1 relaxation parameter was produced by Lufkin et al[37]. No quantitative data on the magnitude of the change was reported.

1.3.1 Treatment Spatial Heterogeneity

The magnitude of the temperature increase, its duration and the rate of temperature increase must all be considered when discussing the tissue response. The laser thermal therapy technique employed in this investigation creates a radial distribution of temperatures and a radial distribution of treatment effects. The geometry of the affected volumes is rarely, if ever, symmetric or uniform, but this discussion will assume so for simplicity. We will define the Zone immediately adjacent to the optical fiber, which can experience temperatures in excess of 60 °C, as Zone I. The tissue response to the extreme temperature increase in this Zone usually consists of immediate coagulation necrosis, coagulation of vessels and macroscopic destruction of the tissue.[5,7,14,16,29,31] Thus, the tissue in this Zone is killed regardless of its pH, oxygenation or perfusion state. The tissue in this Zone will be substantially altered by the treatment and any tissue characterization performed prior to the treatment cannot be applied to this tissue.

The outer treatment Zone that experiences mild temperature increases with no permanent effects will be labelled Zone III. By definition, the tissue in this Zone does not undergo significant changes from its pre-treatment status, the changes it experiences are reversible and the tissue retains its original MR properties after the return to physiologic temperature. Thus, this tissue is effectively untreated. The temperature increases in this Zone could theoretically approach the classical

hyperthermia range of 43-45°C without permanently affecting the tissue if the exposure duration was short enough. The tissue response to the 43-45°C hyperthermia temperature range has been most extensively studied and is reviewed in Section 1.4.3. All the factors that will be discussed regarding the modifiers of tissue sensitivity such as pH, oxygenation and perfusion will apply to this Zone. This Zone will most likely experience a temporary increase in perfusion with minimal or no change in cell structure.

The area between these will be labelled Zone II, and it is of most interest in clinical procedures because it contains the boundary between reversible and irreversible tissue changes. The tissue sensitivity modifiers discussed later will significantly impact the size and shape of this Zone. This Zone will contain the shift from perfusion increases to coagulation and the transition from structurally intact cells to dead cells. The cell survival probability and probably the mechanisms of cell killing are a function of location in this Zone because it contains a wide variety of temperature-duration combinations.

Clinical treatments in an organ with expendable normal tissue, such as the liver or kidney, will attempt to cover the tumor with Zone I to maximize the cell kill in the tumor. The fraction of healthy tissue in Zone II that is killed could be sacrificed in the interest of complete coverage of the tumor. Treatment of organs such as the brain, where preservation of the surrounding healthy tissue is of paramount importance, could shift the balance between the probability of killing a significant fraction of tumor

cells and sparing as much healthy tissue as possible. Knowledge of the exact distribution of the cell kill in Zone II is critically important in these cases.

The size of the different Zones is a function of the therapy modality employed, the energy deposition rate, the duration of exposure and the tissue properties. The size of the central Zone can range from fractions of a cubic centimeter for opthalmic laser treatments to 10 cubic centimeters for interstitial laser treatments of the liver.[19] In general, the larger the treated volume the less severe the level of treatment applied and the less distinct the border between the zones. This is dictated by thermodynamics. A high energy deposition rate required for severe treatments is usually limited to small treatment volumes. The treatment can continue for an extended period, but eventually the treated volume will expand to the point that energy loss through its surface equals the energy deposition rate. Thus, many thermal therapy treatments can be self-limiting.[29]

This investigation will attempt to determine the MR signal intensity history that is characteristic of the different damage Zones.[29,26] Previous investigations have relied on histology as a means of grading the effects of the treatment.[11,30,31] However, histological evaluation is subjective and difficult to quantify, the differentiation of the different Zones could be problematic and modifications in metabolism or structure that might not be visible with histological evaluation could impact the survival of the cell. These considerations suggested the use of cell survival as a means for evaluation of the treatment. A discussion of the biological response to a

temperature increase will demonstrate the significance of this approach.

The temperatures generated in the treatments in this thesis are higher and exist for shorter periods of time than those employed in hyperthermia studies, which are the source of the majority of information in this area. The tissue response to the type of thermal stimulus employed in this thesis is not well characterized. The majority of the cellular level biological effects discussed in the following sections apply only to temperatures increases in the range of 37 - 45°C which are typically applied for a minimum of 15-30 minutes. Extrapolation of the mechanisms and effects beyond that temperature range has not been shown to be valid but a brief survey of results from the field is included here for illustrative purposes.

1.4 Lesion Development

1.4.1 Introduction

An understanding of the evolution and characteristics of the different damage Zones requires information on the physical, biological and physiologic processed involved in a thermal therapy procedure. The following sections review the optical and thermodynamic properties of tissue and discuss the interactions between the relevant tissue parameters. The analysis of the thermal distribution in the tissue leads to a review of the effects of heat on tissue. The entire discussion attempts to illustrate the relationship between the energy deposition and the different levels of effect that characterize the different treatment Zones.

1.4.2 Biophysical Processes

1.4.2.1 Optical Considerations

The damage Zone configuration is determined by a complex sequence of processes. In the first step the optical energy (fluence) distribution within the tissue combines with the spatial distribution of absorbing centers to determine the spatial distribution of the thermal source term.

The optical absorber distribution can be both spatially heterogeneous and temperature sensitive, as well as dynamic as a result of the temperature sensitivity. The behavior of blood during a thermal therapy treatment demonstrates these properties. Blood can have a vastly different absorption coefficient than bulk tissue, particularly in the brain, so the spatial distribution of the vessels would affect the absorption distribution. In addition, environmental factors such as oxygenation can also modify blood's optical absorption properties. The contrast between the deoxygenated, blue blood seen in one's veins and the red oxygenated blood exposed to air is a simple example of this.

Char development at the tip of the optical fiber is one example of how the temperature sensitivity of the tissue can produce a dynamic absorber distribution. Char development is an obviously temperature sensitive process, and the char would act as a strong absorber. The high local absorption would prevent a significant portion of the laser energy from penetrating into the tissue, yielding a thermal source term that more closely approximates a point source than the distributed thermal source

produced with the current generation of diffusing tip fibers. The high local absorption could also cause the optical fiber to melt, changing the optical source term in addition to the absorber distribution.

1.4.2.2 Thermodynamics

The next complex process that determines lesion size is the flow of heat within the tissue, which is determined by the thermodynamic properties of the tissue. The conduction and convection of heat in treated tissue has been extensively studied, with contradictory or inconclusive results. There are conflicting reports as to the significance of blood flow, which determines the convective term, relative to the diffusion of heat through the bulk tissue. Gullino et al suggest that conduction dominates in tumors[38] while Dave et al have determined that convection dominates.[39] Other studies indicate that theoretical modelling of the problem is difficult even for simple cases. In a study by Lyons, energy absorption could be well characterized by analytic expressions but cooling terms were very difficult to determine.[40]

The spatial heterogeneity of the thermal properties is also of significance. Vascular tree patterns, fascia planes or other tissue boundaries can have significant effects on the spatial temperature distribution. The inability to determine the thermodynamic properties of the tissue, combined with the dynamic response of tissue components that dictate the thermal parameters, indicates that an accurate characterization of the thermal distribution within the tissue over the

course of a treatment session would be very difficult.

1.4.3 Biological and Physiologic Processes

The optical and thermal properties of the tissue determine the dynamic temperature distribution in the tissue. The next step in the problem involves the spatial distribution of the temperature sensitivity of the tissue and the map of the treatment's effectiveness. Irregularities in the sensitivity of the tissue as a function of its local blood supply would have a significant impact on the treatment strategy. Pre-treatment analysis of the tumor, such as MR spectroscopic imaging, MR perfusion imaging, PET, SPECT or other radiologic evaluation of the vascular distribution, could yield information that would be used in treatment planning.

1.4.3.1 Mechanisms

Thermal treatments are cytotoxic in both a time-temperature and cell cycle dependent manner. The different damage mechanisms at hyperthermia temperature levels of 37-45°C are poorly understood at this time. The primary cellular target appears to be the cell membrane. The range of heat-induced cell membrane modifications includes protein conformation changes yielding phospholipid bilayer instability[41] and cation permeability changes[42,43] as well as changes in the number and distribution of membrane surface receptors for hormones and growth factors.[44] Cytoskeleton disaggregation affects the membrane and other intracellular membrane structures.[44] Heat also affects other cellular

structures and processes. DNA replication as well as RNA and protein synthesis can be disrupted.[44] Cellular metabolic processes can also be inhibited, with the Kreb's cycle apparently more sensitive than the glycolytic pathway.[45] All these mechanisms appear to act both in vitro and in vivo.

1.4.3.2 Microenvironment

The microenvironment surrounding the cell also plays a major role in the efficiency of the treatment. Tumor cells tend to be acidic, hypoxic or even anoxic, and either nutrient or energy deprived, or both.[46,47] This hostile environment is caused by the inadequate and heterogeneously distributed nutritive blood supply in a solid tumor.[48,49] The microenvironment tends to make tumor cells preferentially sensitive to hyperthermia compared to normal tissues with an adequate blood supply.[50] Specific features of the microenvironment can affect different aspects of a cell's thermal sensitivity. For instance, the acidity of tumor cells appears to impede the development of thermotolerance.[51,52,53]

1.4.3.3 Perfusion

Perfusion plays a significant role in the effectiveness of many cancer therapy modalities because it impacts the physiochemical environment of the cells. The perfusion determines the oxygenation of the tumor cells, which has a significant impact on the effectiveness of radiation treatments. It also determines the ability to deliver chemotherapeutic agents to the

neoplastic cells. Perfusion is doubly significant in thermal therapies because it affects both the chemical environment of the cells and the thermal distribution within the target region. Identical treatment parameters will produce different lesion sizes in vivo and in freshly sacrificed animals, where the experiments were performed before any significant tissue changes could occur.[29] Other experiments determined that the ability of blood flow to remove heat from the treated volume has a significant impact on the maximum lesion size.[53]

1.4.3.3.1 Dynamic Perfusion Response

The complexity of perfusion's role in thermal treatments is compounded because it changes as a function of the severity of the treatment. Tumor perfusion will increase slightly in response to a moderate thermal dose. If a moderate temperature is continued for an extended period of time or if the temperature continues to increase, the perfusion can decrease significantly, even to the point of coagulation and stasis if the thermal dose is large enough.

1.4.3.3.2 Experimental Results

There have been numerous animal studies of quantification of blood flow in response to hyperthermia but data on human tumors are rare. Tables 1.1-1.3 are reproduced from Vaupel and Kallinowski and summarizes many of the studies that have been done.[44] There are several important factors that must be considered when reviewing the data. There

is obviously a wide variation in responses among species, tumors and treatments. An important factor to consider is the time course of the flow changes. Flow reduction that occurs during treatment will have repercussions different from flow that only changes after the treatment. The duration of the flow change is also significant. Permanent coagulation would have more dramatic impact on long-term tumor survival compared to a flow decrease that recovers over several hours or days.

Table 1.1. Response of tumor blood flow (TBF) to localized hyperthermia in mice.

Hyperthermia level (°C)	Exposure time (min)	Tumor	Flow Response
42-45	35	S_2 sarcoma	Temperature- and time-dependent flow stoppage[54]
41	-	Mammary carcinomas	TBF increase up to 41°C, a decline thereafter[55]
Continuous increase up to 45°C	-		TBF increase at T≤ 41° C, flow collapse above 41°C[44]
42/44	30		No significant flow changes during heating, flow decrease after heating[56]
41.5/44	ca.60		Immediate TBF increase after heating for 3 min, at longer exposure times TBF decreases[57]
43.5	30		No significant changes during heating, TBF decrease after heating[58]
42.5	60	SA FA fibrosarcoma	Transient TBF increase and return to pre-treatment level during heating, TBF decrease after heating[59]
40-45	15-75	Glioma	TBF increase at low thermal doses, flow decline at high thermal doses[60]
42/45	40	S-180 tumor	42°C: TBF decline; flow restored 16 h after heating
43.5	60	RIF-1 tumor	45°C: marked decrease in TBF[61] Initial TBF increase, flow decrease after heating[62]

Table 1.2. Response of TBF to localized hyperthermia in rats.

Hyper-thermia level (°C)	Exposure time (min)	Tumor	Flow response
39.5/42	30	DS carcino-sarcoma	39.5°C:TBF increases[63] 42.0°C:TBF decreases [64]
39.5-44	30		TBF increase at 39.5°C,[65] TBF decreases above 42°C
43	100		Significant flow drop with heat alone in only a few cases[66]
41.3	60	BA 1112 rhabdo-myosarcoma	Significant flow reduction[67]
41-44	30-60		TBF reduction dependent on temperature and exposure time[68]
42/42.5	160/226		Flow stoppage in 50% of the tumors[69]
43	180		Red blood cell velocity increases slightly within the first 30 min of treatment, followed by a decrease and eventually a complete stop[70]
42-43.5	180		Stoppage of microcirculation dependent on temperature and exposure time[71]
40.3-43	30-60	Walker 256 tumor	No significant flow change[72,73]
42-45	30-60		43°C:TBF remains unchanged 45°C:TBF increases slightly in very small tumors; TBF in large tumors decreased after heating[74,75,76,77]
42	60-180	Yoshida sarcoma	TBF reduction dependent on exposure time[78]
40-46	20-60		TBF reduction dependent on exposure time and temperature[79,80]
43.5	60	Mammary adeno-carcinomas 13762A	TBF decreases after heating[81]
39/42/44	3-60	SMT-2A	39°C: no change 42°C: TBF decreases after heating for 10 min, then returns to control level 44°C: TBF decreases after heating for 3 min, then returns to initial level[82]
Continuous increase up to 45°C		R3230	Vascular statsis at 42.5°C[83]
41-45	120	Hepatoma AH 100 B	41°C:TBF increase during heating 43°C: initial TBF increase, gradual decrease thereafter 45°C: continuous TBF decrease[84]

Table 1.3. Response of TBF to localized hyperthermia in various species (other than mice and rats)

Hyper-thermia level (°C)	Exposure time (min)	Tumor (host)	Flow response
40	>10	TV tumor (dog)	TBF increase[85]
44	40	Mast cell tumor (dog)	No TBF change on first treatment[86]
42.5	10/60	Melanoma A-MEL-3 (hamster)	Fifty percent reduction in TBF after 15 min heating[87]
40-52	60	VX2 carcinoma (rabbit)	Rise in red blood cell velocity at temperatures <41°C, at higher temperatures vascular stasis can occur[88,89]
40-42	30/60	Different tumors (human)	TBF increased in 7/9 tumors during heating and decreased in 8/12 patients after heating[90]
41-44	40	Different tumors (human)	TBF increased during heating[91]
41.5-42	240	Melanoma, colon carcinoma (human)	Melanoma: initial flow increase, TBF decline thereafter Colon carcinoma: flow decrease[84]

1.4.3.3.3 Spatial Distribution

The spatial distribution of flow changes within a tumor and the surrounding normal tissue is also significant. Rappaport and Song reported that blood flow in the skin and muscle adjacent to a tumor is roughly twice that in normal skin, possibly due to inflammatory reactions at the expanding edge of the tumor.[81] Karino et al have noted that flow changes are different in central and peripheral areas of a tumor, which could be determined by the proportion of normal and neovascular vessels in different parts of a tumor.[84] The perfusion increase is a locally regulated phenomenon in which the smooth muscle in the vessel wall relaxes to encourage flow and dissipate the increased thermal load.[92] Neovascular

vessels present in malignant tumors do not contain the same auto-regulatory capability as normal vessels because they do not have a contractile smooth muscle component.[80,93] There is also evidence to suggest that a "steal phenomenon" occurs in which the normal vessels around the tumor expand and divert flow from the tumor.[64]

1.4.3.3.4 Coagulation Mechanisms

The heat induced flow reduction is caused by a complex combination of processes that modify blood components, vessel walls and the hydrodynamics of the system. Increased temperature and acidity cause red blood cells (RBC) to stiffen and promote formation of RBC-platelet aggregates, while acidosis alone encourages formation of intravascular fibrinogin gels.[64,94] However, transit times of RBC's and erythrocytes are difficult to quantify, so the extent of these factors' contributions is difficult to assess.

The vessel lining damage reduces flow through a process that modifies the hydrodynamic properties of the various tissue compartments. Plasma leakage or hemorrhage into the interstitial space increases the pressue there, "squeezing" the venules and increasing venous resistance.[74] This combines with any of the blood modifications mentioned above to reduce flow velocity, decrease the arterio-venous pressure gradient and push more fluid into the interstitial space.[87] Tumors have no lymphatic drainage system to remove the edematous fluid, so the effects can spiral to one of two conditions: reduced flow or complete stasis and coagulation.[44]

The flow would stabilize at a significantly reduced level when the pressure in the interstitial compartment equalled the pressure in the venules, the diameter of the venules stabilized and fluid exchange between the intra- and extra-vascular compartments reached an equilibrium. Complete stasis would occur if the feedback loop was extended slightly. The flow reduction promotes the processes that lead to flow reduction: formation of RBC-platelet aggregates, formation of fibrinogin gels and leukocyte adhesion to venule walls.[95]

This series of positive feedback mechanisms could compete with the tissue's inherent mechanisms for flow maintenance to produce the pattern of flow changes typical in hyperthermia. The initial flow increase would be explained by an attempt to dissipate the increased thermal load. Flow reduction would represent increasing dominance of the heat-induced mechanisms that reduce flow with complete stasis representing complete dominance by these mechanisms. The wide variety of thermal doses required to achieve these states could represent the different acidity levels and vascular damage thresholds among tumors and even in different parts of the same tumor. The magnitude of these effects varies but the uniformity of histopathological findings across animal and human tumors suggests that the same set of mechanisms is acting in all cases.[96]

This also suggests that images of tissue perfusion could be relevant to an evaluation of the treatment. There have been several attempts to image perfusion with flow sensitive pulse sequences or diffusion sensitive pulse sequences that try to treat perfusion as macro-diffusion.[97] These have the

potential to reveal dynamic changes in the tissue during a thermal treatment that cannot be seen with standard fast spin echo sequences and are an obvious choice for the pulse sequences employed in subsequent investigations. A paper by Hill et al indicates that perfusion could be a better indicator of treatment effectiveness than knowledge of the temperature history.[98] This also suggests that imaging of perfusion in tumors could provide critical information on a treatment's effectiveness.

1.5 Thermal Therapy Studies

1.5.1 Introduction

The majority of the hyperthermia studies employ modalities designed to create a uniformly heated tissue volume and elevate the tumor temperature to between 39 °C and 45 °C for periods ranging from 10 minutes to 4 hours.[60,82,84,87] Studies employing more focal treatment modalities have fostered development of a separate approach within the hyperthermia community. This approach employs high energy, short duration focussed ultrasound or lasers to treat deep seated tumors with temperatures in excess of 50-60°C. The therapy strategy differs from the traditional hyperthermia approach because of the inherent spatial inhomogeniety of the treatment severity. The focussed ultrasound approach uses a stearable transducer to cover the entire tumor volume with multiple focal lesions.[99] Theoretically, there is no restriction on the size of the tumor that could be treated. The laser-based approach will frequently over-treat the center of the tumor to insure that peripheral regions receive

the minimum required thermal dose. This would equate to expanding the severe treatment Zone I discussed in Section 1.3.1 to cover the entire tumor. Experiments have been performed to determine the maximum lesion size that can be generated[29] and in vivo lesions as large as 24.0 x 15.5mm have been created in rabbit liver.

1.5.2 Laserthermia Studies

The ability of optical fibers to conduct laser light to relatively inaccessible locations prompted attempts to use this technology in interstitial laserthermia applications. The optical fibers are small enough to fit in standard size needles and are capable of conducting large amounts of optical energy. Clinicians are willing and able to put a needle tip nearly anywhere in the body to perform a biopsy, so optical fibers are also able to be positioned nearly anywhere in the body. The access problem being solved, the clinicians then needed to be confident that the laser treatment would reliably produce a predictable lesion.

A large number of studies have examined the relationship between dose and lesion size for different lasers with different irradiation profiles. The laser properties that can be varied include wavelength, pulse mode vs continuous wave, pulse duration, total amount of energy delivered and the geometry of the optical source. Elias et al studied the effects of various wavelengths including 454, 514.5, 700, 750 and 1060 nm from both bare fibers and diffusing tip fibers in normal rat brains.[7] Temperatures were measured at distances of 1, 3 and 5 mm from the fiber tip 4 minutes after

the laser was turned on. A bare fiber increased the temperature 1mm away roughly twice as much as the diffusing tip fiber and created a coagulum of tissue immediately surrounding the probe. The results strongly suggest the use of diffusing tips to prevent local temperature increases that would damage the fiber and limit the lesion size. No lesion size measurements were made.

Sato et al used an optical fiber probe with a built-in thermocouple to study laser hyperthermia in cat brains.[8] Laser exposures of 2.5 W for 30 minutes were followed by MRI scans, then the animals were sacrificed and the tissue analyzed by histological examination. The temperature measured 5mm from the fiber tip was maintained at 42.5-43.5 °C during irradiation while the temperature at the fiber tip reached 61°C. The 43°C contour was a roughly elliptical area 10X13 mm. The treatment produced a central coagulation necrosis surrounded by a thin layer of edema. Electron microscopy showed enfolding vacuoles and swelling of the endothelium and astrocytic foot processes. The post-treatment MRI scans revealed a hypointense ring around the coagulation necrosis on the T1-weighted scan which enhanced with contrast injection and matched the 43°C contour.

A partially calcified, 18X18X16mm astrocytoma located in the right thalamus of a 15 year old girl was treated with the same system. Laser irradiation of 2.0-2.3W for 30 minutes elevated the temperature at the probe to 45-48°C while 5mm away from the fiber tip the temperature was maintained at 42.5-43.5°C. Two separate irradiations were used. No char formation was observed. Post-operative CT and MRI scans revealed no

hemorrhage and an insignificant amount of edema. No long term follow-up was documented.

A study by Dowlatshahi et al studied dosimetry of Nd:YAG irradiation in Sprague-Dawley rat mammary carcinomas.[9] Their interstitial device employed a 600 micron core fiber with its cladding removed, inside a 19G catheter with a 1cc/min saline flow down the catheter lumen to prevent fiber damage and a thermocouple at the catheter tip. The laser power was set at 5W and the total energy delivered ranged from 500-2000J with 2cm diameter tumors receiving 500-1000J and 3cm tumors receiving 1000-2000J. A gradual fiber movement technique that maintained fiber tip temperatures in the 42-45°C range was employed. Tumors were excised 48 hours after treatment and the coagulation necrosis volume determined histologically.

The investigators were able to establish a roughly linear relationship between the total energy delivered and the volume of necrosis. A two minute exposure created roughly 1cc of necrosis with little or no damage to the optical fiber. Several tumors were liquified and could not be processed histologically. The tumor type was characterized as very cellular and moderately vascular. The authors were pleased with the system performance and rated it favorably compared to more complex, computer controlled, multi-fiber, multi-thermocouple systems.

A series of studies by collaborators at the Univ. Coll. Hosp. and St. James Hosp. in London have produced valuable results.[10,11] One study in normal rat liver employed an Nd:YAG laser with powers of 0.5-2.0W,

exposures of 50-2400 sec and pulses of 100 usec with a 40 Hz repetition rate. Seven animals were treated with 1W for 1000 sec to determine lesion size variability. In another set of animals a fixture positioned 5 thermocouples spaced 2mm apart along a line perpendicular to the optical fiber. Duplicate experiments were done to evaluate reproducibility of the temperature profiles. The dynamic properties of the tissue were tested by positioning an optical fiber 4mm from and opposite to the treatment fiber and measuring the intensity of the incoming light. The vascular impact of the treatment was studied by filling the vasculature with a radiopaque polymer after treatment and x-raying the area.

The results yielded consistent lesion sizes with a mean diameter of 12.6mm and a standard deviation of 1.0mm. Increasing energy doses yielded increasing lesion sizes which plateau'd after 1000J or slightly earlier for the high power exposures. Occasionally, a wedge-shaped necrotic area was observed spreading out from the lesion to the lobe periphery. This probably represents occlusion of a major vessel. Thermocouple measurements revealed that a steady state temperature distribution was established within approximately 200 secs. Higher power treatments produced steeper distributions with fiber tip temperatures reaching 100°C for a 300 sec exposure at 2W.

The evolution of the lesions was studied also. Animals sacrificed 1 hour after a 1W 1000 sec treatment had a small, central charred and cavitated area surrounded by a region of degeneration. Some tissue preservation in the area of a large vessel indicated that it acted as a heat

sink. There was a sharp boundary between intact liver cells and the degenerate area, unlike liver lesions produced with systemic or localized RF current hyperthermia[100, 101, 102]. The nuclei in the degenerate area were preserved but shrunken and densely staining. The degenerate zone became necrotic and acquired a peripheral inflammatory infiltrate over the course of 2-3 days. Day 4 produced granulation tissue at the edge of the lesion with occasional groups of giant cells, proliferating bile ductules and isolated hepatocytes. The necrotic area reached its maximum diameter at day 7. The lesion eventually matured into a fibrous scar.

The optical properties of the tissue changed significantly for exposures above 1W. Delivery of 600J reduced the light intensity at the sensing fiber by 30% for a 1W exposure, 66% for 1.5W and 73% for 2W. The vasculature was also affected. Small vessels in the necrotic region were totally obliterated with significant lumen reductions or even occlusion of vessels up to 1.5mm diameter.

1.5.3 MR Imaging Studies

The laser therapy literature demonstrated that fairly reproducible lesions could be generated in specific cases but the variability of all the parameters discussed in Sections 1.4 and the concern for patient safety prompted the investigation of radiologic techniques for control of the procedures. A number of MR studies were conducted to examine the immediate post-operative appearance of the lesions on MR images and the relationship between the images and the actual lesion.[1,31,103] As the

technology advanced and imaging times became shorter the emphasis shifted to intra-operative imaging.[30,26,104] The ability to image the treated volume during the treatment with sufficient temporal resolution suggested that MR scanners could be used as a true control system for thermal therapy procedures. MR's ability to image thermally-induced tissue changes is summarized in Table 1.4, reproduced from Jolesz et al.[1] Several studies are reviewed which exploited these capabilities to characterize the MR appearance of thermally-induced lesions in a variety of tissues.

Table 1.4

Laser Effects on Tissue Detectable with MR Imaging

Temperature (°C)	Effects on Tissue	Effects on MR images
<45	Reversible tissue heating	Reversible increase in T1 [106], [107] and reversible decrease in M_0 [24]
45-60	Changes in cell metabolism and cellular water distribution.	Reversible and irreversible changes in T1[106, 108]
~60-100	Coagulation[105]	Irreversible changes in T1 and T2[108]
~70-100	Shrinkage of collagen matrix[105]	Geometric changes in images
>100	Carbonization, vaporization and ablation.	Large decreases in M_0 and volume displacement

1.5.3.1 Animal Studies

1.5.3.1.1 MR Imaging Studies

The first report of MR imaging of laser irradiation of tissue samples was presented by Jolesz et al.[1] They used a 1064nm wavelength Nd:YAG

laser with a 600 um core optical fiber to irradiate in vitro samples of rabbit brain and ex vivo samples of an RIF-1 tumor that had been implanted subcutaneously on a mouse. The imaging time was longer than the laser exposure so the laser exposure was coordinated with the image data acquisition to maximize the laser-induced image contrast. The T1-, intermediate- and T2-weighted images all showed both reversible and irreversible signal decrease near the fiber tip.

The study also examined the relationship between temperature and signal intensity with a non-imaging experiment. A 1 mL sample of minced rabbit brain was irradiated and the MR signal was collected. The results revealed significant hysteresis in the signal intensity vs temperature curves. This suggests that the temperatures reached caused changes in the tissue that were not reversible during the duration of the experiment.

Investigators began to report results of MR imaging of thermal procedures. Higuchi et al examined the relationship between both intra- and post-operative images with histologic lesions.[30] Imaging of rat liver after in vivo irradiation with a 1064 nm wavelength Nd:YAG laser and liver resection was performed for both a constant power series and a constant energy series. The constant power series used a power of 9W and varied the energy between 45 and 360J. The constant energy series used powers ranging from 2 to 18W and deposited 180J of energy in the tissue. The post-operative imaging demonstrated 3 characteristic rings that represented 3 specific zones in the lesion. The innermost ring was hyperintense on T1-weighted images and represented the bulk of the lesion. The middle ring

was hypointense on both T1- and T2-weighted images and the outer ring was hyperintense on T2-weighted images. The outer 2 rings corresponded to an area of sinusoidal dilatation with a rim of congested erythrocytes and apparently normal hepatocytes.

In vivo irradiation of rabbit brain, muscle and liver was also performed with post-operative imaging. T2-weighted images clearly demonstrated the extent of the laser induced lesions in all three tissues. T1-weighted images were not able to detect the lesions in muscle. The T1-weighted scans in the rabbit liver showed a pattern similar to that found in rat liver, while the brain images revealed the central cavitation as a signal void with a hyperintense ring that corresponded to an area of fragmented neurophils with pyknotic nuclei.

In vivo irradiation with intra-operative imaging was also tested. The imaging sequence used was as long as or longer than the irradiation exposure, so the exposure was timed to occur during the middle of the image acquisition to maximize the laser-induced image contrast. The image acquired during the laser irradiation showed a noticable signal decrease in the heated area and the post-operative images were again able to detect the extent of the laser induced lesions.

Matsumoto et al studied laser ablation of in vivo and ex vivo rabbit liver and attempted to develop a laser delivery protocol that maximized the size of the laser-induced lesion.[29] In the in vivo portion of the study, laser powers of 2 and 3W delivered with a bare tip optical fiber were used to create 3 or 4 lesions for each energy dose between 120 and 900J. A 3 minute

exposure followed by a 2 minute exposure was used in 6 additional cases in an attempt to enlarge the lesion size. In 3 of the 6 cases the fiber was advanced 3mm for the 2W exposures and 5mm for the 3W exposures. The animals were sacrificed 10 minutes after laser treatment, the lesion diameters were measured macroscopically in planes parallel to and perpendicular to the fiber and the samples were stained with hemotoxylin and eosin for histological evaluation.

The second half of the study compared in vivo treatments to ex vivo treatments. The animal was sacrificed with an overdose of anesthetic and lesions were created immediately so that the temperature and optical and thermal properties would be as similar as possible to the in vivo case. Lesions were created with 4 exposures of 2W for 3 and 5 minutes, as well as 4 treatments with the exposure-advancement-exposure protocol that had been used for the in vivo experiments. In some cases MR imaging was performed during the irradiation. A single image was aquired every 30 seconds with a T1-weighted fast spin echo sequence with parameters TR=300 msec, TE=18 msec, 5mm slice thickness, 12cm FOV and 256X192 matrix. The lesions were measured macroscopically and fixed in formalin for comparison with the in vivo lesions.

The lesions were symmetric, unless they were located near a blood vessel or biliary tract. The lesions were characterized by three distinct areas: an inner area of acellular tissue, surrounded by a area of coagulated tissue with enucleated hepatocytes and some vacuolation, with the outermost area consisting of nucleated hepatocytes and some vacuolation.

Hyperemic changes were also seen in some otherwise normal tissue around the lesion. There was no correlation between power or energy and either hemorrhage or the extent of vacuolation.

There was significant variation between the lesion sizes, with standard deviations for identical treatments reaching as much as 25% of the average value. The lesions created with the repeat irradiation protocol were smaller than those created with continuous irradiation, but fiber advancement with repetition yielded larger transverse diameters than repetition alone. MR images of the ex vivo irradiation showed an expanding low signal area that regressed after the laser was turned off. The transverse diameter of the dark area increased with the fiber advancement technique, suggesting a relationship between the dark area and the lesion size. An examination of the size of the dark area revealed that it did not represent an area of cavitation but that it showed a region of increased temperature.

A comparison of the lesions sizes in vivo and ex vivo revealed that in vivo lesions were larger for low energy doses but smaller for higher energy doses. This could be explained by the presence of perfusion. In the low energy cases, the perfusion will distribute the thermal load more evenly and deliver a heat dose to a larger amount of tissue. In the high energy cases, the perfusion is able to remove the thermal energy from the regions far from the fiber faster than it can be inserted. This is supported by the intersection of the in vivo and ex vivo lesion size curves at exposures that match the time required for development of a thermal steady state.

Anzai et al studied the effects of laser irradiation of ex vivo bovine liver with MRI.[31] They used an Nd:YAG laser with a special conical, sapphire tip optical fiber with an outer diameter of 2.2 mm and exposed the liver to 15W power for 5, 10 and 20 seconds. Each experiment was repeated 3 times. T1-weighted images were taken 30 minutes after laser exposure, by which time the temperature had returned to baseline. The images showed a central dark region representing cavitation and with a bright ring. The histological appearance of the lesion demonstrated the central cavitation with charring and carbonized debris, a layer of microvaporization and a peripheral area of tissue necrosis and edema. The authors reported a linear correlation between energy density, thermal changes, MRI density changes and histological damage.

1.5.3.1.2 MR Spectroscopy Studies

Some investigators sought to exploit the capabilities of MR spectroscopy to detect thermally-induced changes in the tissue. Jolesz et al acquired spectra of in vivo canine muscle and kidney, as well as in vitro mouse liver.[32] The canine muscle samples were irradiated with 1500, 3200 and 6520J of 1064nm Nd:YAG laser energy and changes in the phosphocreatine (P_{Cr}), inorganic phosphate (P_i), phosphate monoester(P_m) and ATP-related peaks were observed. Significant drops in the P_{Cr}/β-ATP and P_{Cr}/P_i ratios were observed but were not proportional to the amount of energy deposited. Similar effects were seen in the irradiated kidney.

The in vitro mouse liver was perfused with Krebs-Henseleit solution

via the portal vein. The temperature of the perfusate was raised from 37°C to 47°C and spectra were recorded at 5 or 10 minute intervals. All the ATP, P_m, P_i and mobile phosphodiester peaks diminished over the course of the 4 hour exposure compared to a non-treated control. The spectra at the end of the treatment only consisted of "a small phosphodiester line superimposed on a broad asymmetric resonance which is attributed to membrane phospholipids." The authors went on to comment on the limitations of spectroscopy's ability to control hyperthermia imposed by the spatial and temporal resolution restrictions.

Sijens et al also used ^{31}P spectroscopy to try and evaluate tumor response to hyperthermia.[109] They treated the NU-82 mammary carcinoma, which had been implanted subcutaneously in female DBA-2 mice, with a computer-controlled microwave hyperthermia system. The tumors were treated with 41, 43, 44 and 45°C for 15, 30 and 60 minutes. Spectra of the entire tumor were taken periodically after the treatment and revealed that the acute, reversible changes are resolved by approximately 18 hours after the treatment. The data also indicates that the ratio of the major high energy phosphate ATP peak to the inorganic phosphate peak could be related to the thermal dose.

However, the study did not correlate the changes in the ATP/P_i ratio with cell survival or histology. Thus, this experiment re-affirmed that a relationship exists between hyperthermia treatments and spectroscopicly-detectable changes in the tissue, but the poor temporal resolution and spatial resolution of current spectroscopic techniques does not allow their

use intra-operatively.

1.5.3.2 Human Studies

Introduction of the concept of image-guided laser surgery had an immediate impact on clinical application of interstitial laser thermal therapy. MRI has been used in humans to monitor the intraoperative tissue alterations and to evaluate permanent effects during the postoperative period. Ascher and associates have reported stereotactic placement of Nd:YAG laser fibers in eight patients with intracranial tumors.[110] The delay in MR imaging with respect to tissue temperature changes and the obviously empiric nature of the dosimetry remains a shortcoming. Despite these limitations, the feasibility of the technique is apparent from these preliminary studies.

Bettag et al delivered laser energy interstitially to treat brain gliomas.[33] Imaging was performed pre- and postoperatively, but no measure of effect was available during the procedure. Castro et al reported treatment of a patient with recurrent metastatic squamous cell carcinoma to the neck from a laryngeal primary.[34] The patient underwent two procedures of Nd:YAG laser ILT using multiple fibers, microthermocouple measurement of temperature changes and MRI. The lack of appropriate dosimetry was noted by the authors. Gewiese et al applied ILT to treat liver tumors under MRI control.[35]

Various fast imaging paradigms have been tested by several investigators for observing thermally induced changes within tissues.[27,28]

The fundamental concept of MRI monitoring and controlling of ILT procedures[6, 36, 111] can be extended to other thermally induced, minimally invasive procedures such as cryosurgery and focused ultrasound heating[26, 112] and preliminary experiments in these areas have already been performed.[113, 114]

The current MRI techniques employed to study thermal procedures include gradient echo, spin echo (SE) and echo planar (EPI) sequences with diffusion- and T1-weighting.[32,110,112,] The EPI techniques employ specialized hardware to acquire image data within a few hundred msec and can acquire approximately one image per second. However, these images have relatively poor resolution and signal-to-noise ratio (SNR). Gradient echo images can be acquired every 2-10 sec and their resolution is good while their SNR is only slightly better than EPI. Standard SE images take from 10 sec to minutes to acquire but they have very good SNR and resolution. Recent developments in pulse sequence design have yielded SE sequences known as fast SE or RARE sequences that can acquire an image every 5-20 seconds at only a slight cost in SNR.[26,115]

1.6 Thermal Surgery Control Systems

1.6.1 Image-to-Actual Function Definition

The ability to acquire images of the treated volume during the procedure is obviously critical to the development of a control system for thermal surgeries, but interpretation of the images is equally important.

The conceptual framework of image interpretation was discussed by Wyman et al when they introduced the term Image-to-Actual-Function (IAF), which incorporates knowledge of the appearance of the treatment images with information on the chronic behavior of the lesions to relate the intra-operative images taken during the treatment to the ultimate resolution of the lesion.[116] They state that for an IAF to be successful "acute lesion images must either predict reliably or correspond exactly with the resulting chronic lesions." The development of an IAF for a specific treatment, imaging scheme and post-treatment benchmark combination is the central goal of this thesis.

1.6.2 Geometric Approach

Wyman et al's approach to the development of an IAF is based on geometric considerations of the outward expansion of the treatment boundaries. They develop a theoretical framework for discussion of this concept but do not provide any data demonstrating its capabilities. The concept of a contrast boundary is introduced to represent the spatial extent of the changes in the image that are above some threshold. The criteria used to determine the contrast boundary would most likely be specific to the imaging parameters selected. The treatment boundary would be determined empirically with histological evaluation of experimental treatments. The relationship between the contrast boundary and the estimated treatment boundary would then be applied proactively during subsequent treatments.

A potential strength in this approach is its allowance for the possibility that the changes in the tissue may not be detectable on the images. Effects may extend beyond the contrast boundary because the imaging technique is not sensitive enough or because the effects can be delayed and will not be detected during the treatment. The geometric approach compensates for these possibilities.

One weakness in this approach is in its geometry-based transformation between the image contrast boundary and the treatment boundary. The location of the treatment source is considered the center of the transform space and the relationship between the contrast radius and the treatment radius is determined empirically. The inhomogeneity of the tissue's thermal properties will cause inconsistencies in the thermal map, yielding a variety of temperature gradients. The temperature gradients near a blood vessel that acts as a heat sink will be much steeper than in a homogeneous region of tissue. Thus, the estimation of the effected tissue volume could differ significantly in the presence of blood vessels or fascia planes.

The properties of the optical source and the geometric relationship between the thermal source and the imaging plane would also effect the relationship between the contrast boundary and the treatment boundary. If the thermal source can be considered a point source and the imaged plane contains the thermal source, the transform between the contrast boundary and the treatment boundary can be a simple extrapolation along the ray originating at the thermal source. However, if the optical source is not

spherically symmetric the relationship between the contrast boundary and the treatment boundary may depend on position.

The geometric relationship between the imaging plane and the thermal source can affect the contrast-treatment boundary relationship even if the thermal source is symmetric. One advantage of MR imaging is that in most cases multiple, parallel image planes can be acquired in the same amount of time it takes to image a single plane. This gives us the opportunity to acquire additional data at no cost in temporal resolution and observe the treatment in a larger fraction of the tumor volume. Figure 1.1 demonstrates how the contrast-treatment boundary relationship for an image taken in the plane of the optical fiber would compare to an image taken parallel to it. Since the ray originating at the thermal source crosses the imaging plane at an angle, the contrast-treatment boundary relationship must be scaled by the cosine of the angle between the imaged plane and the ray. The same concept applies if the imaging planes are perpendicular to the axis of the fiber, also shown in Figure 1.1.

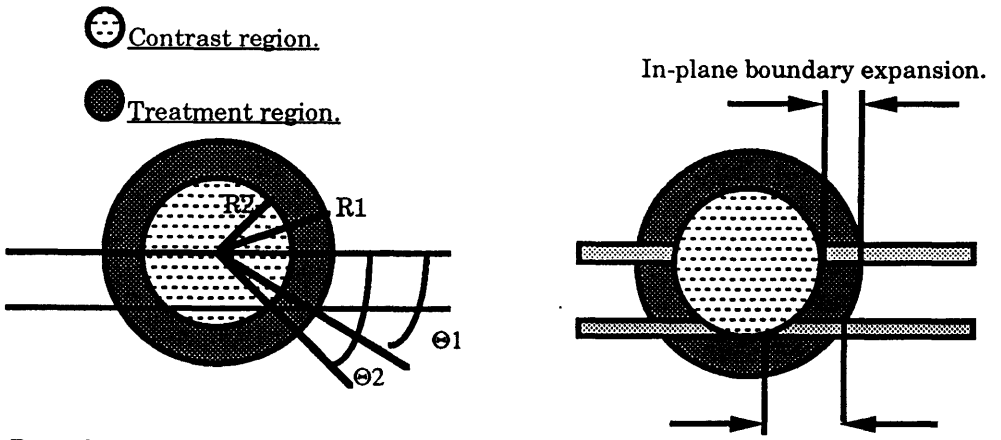

R1 is the radius of the treatment region.
R2 is the radius of the contrast region.

R1-R2 is the difference between the contrast boundary and the treatment boundary in the plane containing the thermal source. The expansion in the parallel plane is R1*cos(Θ1) - R2*cos(Θ2). If the thickness of the slices is taken into account the relationship is more complex.

The same relationship holds for imaging planes perpendicular to the axis of the fiber because of spherical symmetry.

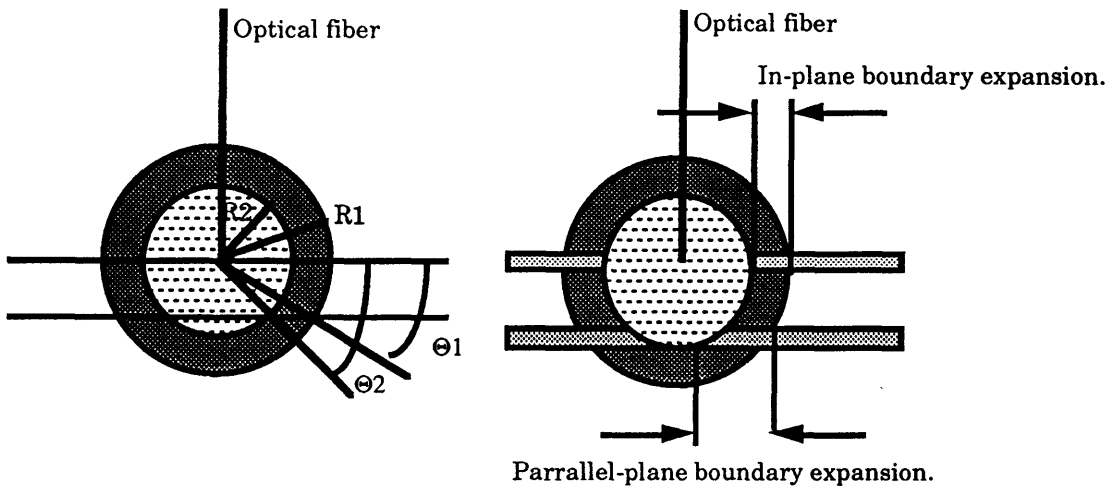

Figure 1 Image-to-Actual-Function Geometric Complications. The contrast<–>treatment boundary relationship is a function of imaging slice location for imaging planes parallel or perpendicular to the optical fiber axis.

1.6.3 Pixel-by-Pixel Approach

This investigation takes a different approach to the development of image to actual functions. Instead of geometric considerations relating

contrast boundaries to treatment boundaries, this thesis attempts to relate the survival probability of a voxel of tissue to its signal intensity history over the duration of the treatment. This approach is more complex because it requires a pixel-by-pixel determination of survival probabilities, but it has the potential to be more accurate because it makes no geometric assumptions about the treatment boundary, the contrast boundary, the properties of the optical source or the relationship between the thermal source and the imaged plane. Thus, it is able to deal with several of the weaknesses of the geometric approach.

However, it does have a potential weakness in that if there are changes in the tissue during the treatment that are not detectable with MRI it has no ability to account for them. We do not believe this is a significant limitation because the temperature sensitivity of the MR pulse sequences used in this investigation was found to be at least 1% signal intensity change per °C in gels, which allows us to detect temperature changes of 5°C even in poor signal to noise conditions. The sensitivity of the pulse sequence in tissue is unknown but should be of the same order of magnitude. Since the treatment durations employed are short and the temperature in the majority of the tumor is relatively high, small temperature increases that would not be detected on the images would probably have a relatively minor effect on the tissue in comparison to the large, detectable temperature increases.

The other weakness of the pixel-by-pixel approach is that it does not base the survival probability on an inherent property of the tissue but on

signal intensity. The relationship between signal intensity and survival may differ for different temperatures, exposure durations, rates of temperature change and pulse sequences. This prevents application of the empirically-derived signal intensity-survival relation to other tissues and pulse sequences. Measurement of physiologic or inherent MR properties of the tissue could allow extrapolation of the results to other tissues and pulse sequences, but these types of measurements cannot be performed with sufficient temporal resolution with currently available technology.

This thesis proposes to investigate the relationship between the intra-operative images and the effect on the tissue by postulating a possible mathematical relation between the percentage signal intensity change of a pixel and the fraction of surviving cells in the volume element it represents. This is done by imaging the tumors during treatment and then excising the tumors after the treatment. The excised tumor is divided into regions and the average surviving fraction of cells in that region is determined with a colony growth assay. The images are divided into regions of interest (ROI) that approximately match or represent the different sections of the excised tumor. The basic form of the mathematical relationship between the percentage signal change on the images and the cell survival is fed into a computer program with an initial estimate of the coefficients of the equation. The program computes the cell survival on a pixel-by-pixel basis and averages the results for all the pixels in a region. The average image-derived cell survival is compared to the measured value for that region and the procedure is repeated for every region. The program then begins an

iterative process to adjust the coefficients of the equation to optimize the match between the image-derived and measured values.

The equation that is produced with this process represents the best fit between the image-derived cell survival and the measured cell survival, but only for the form of the equation tested and the imaging sequence employed. Other mathematical formulas must be tested in the same way to evaluate which form best represents the relationship between the images and the cell survival. The number of equations that could be tested is infinite, but forms derived from hyperthermia relationships, cell culture studies and also mathematically simple forms were tested.

The control of thermal therapy is a very complex problem incorporating multiple biophysical processes and a variety of academic and engineering disciplines. The theoretical framework of each step in the process has been reviewed and its significance discussed. We now briefly review the exact nature of the temperature sensitivity of MR images with a summary of the quantum and classical treatments of the sources of MR image contrast.

REFERENCES

1. Jolesz FA, Bleier AR, Jakab P, Ruenzel PW, Huttl K, Jako GJ. NMR imaging of laser tissue interactions. *Radiology*. 168:249-253, 1988.

2. Castro DJ, Saxton RE, Layfield LJ, Fetterman HR, Tartell PB, Robinson JD, To SYD, Nishimura E, Lufkin RB, Ward PH. Interstitial laser phototherapy assisted by magnetic resonance imaging: A new technique for monitoring of laser-tissue interactions. *Lasers Surg Med.*, Suppl 1, p3, 1990.

3. Schrottner O, Ascher PW, Ebner F. Interstitial laser thermotherapy on brain tumours under MRI control. *Fifth Int Congress of the European Laser Assoc*, Graz, Austria 1990, C-24.

4. Bleier AR, Higuchi N, Panych LP, Jakab PD, Colucci VM, Hrovat MI, Loughlin KR, Moore M, Jolesz FA. Magnetic resonance imaging of interstitial Nd:YAG laser effects on tissue. *Lasers Surg Med.*, suppl.2, p.4(abstr.), 1990.

5. Masters A, Steger AC, Lees WR, Walmsley KM, Bown SG, Boulos PB. Interstitial laser hyperthermia for liver cancer. *Lasers Surg Med*, Suppl 3, p29 (abstr), 1991.

6. Tracz RA, Wyman DR, Little PB, Towner RA, Stewart WA, Schatz SW, Wilson BC. Magnetic resonance imaging of interstitial laser photocoagulation in brain. *Lasers Surg. Med.*. 12:165-173, 1992.

7. Elias Z, Powers S, Atstupenas E, Brown T. Hyperthermia from interstitial laser irradiation in normal rat brain. *Lasers in Surg and Med.* 7:370-375, 1987.

8. Sato H, Sakai T, Fujishima I, Sugiyama K, Sekiguchi Y, Senzaki F, Hiraga T, Daikuzono. Laserthermia for deep seated brain tumors using a hybrid laserthermia probe. *SPIE Optical Fibers in Medicine V.* 1201:637-641, 1990.

9. Dowlatshahi K, Babich D, Bangert J, Kluiber R. Histologic evaluation of rat mammary tumor necrosis by interstitial Nd:YAG laser hyperthermia. *Lasers in Surg and Med.*, 12:159-164, 1992.

10. Matthewson K, Coleridge-Smith P, O'Sullivan JP, Northfield TC, Bown SG. Biological effects of intrahepatic neodymium: yttrium-aluminum-garnet laser photocoagulation in rats.

Gastroenterology, 93:550-557, 1987.

11. Matthewson K, Coleridge-Smith P, Northfield TC, Bown SG. Comparison of continuous-wave and pulsed excitation for interstitial neodymium-YAG laser-induced hyperthermia. *Lasers in Medical Science*, 1:197-201, 1986.

12. Halldorsson T, Rother W, Langerhold J, Frank F. Theoretical and experimental investigations prove Nd:YAG laser treatment to be safe. *Lasers in Surg and Medicine*, 1:253-262, 1981.

13. Lees WR, Walmsley K, Maser A, Steger AC, Bown SG. Image-guided fine needle tumor destruction with the Nd:YAG laser: New radiologic technique. *Radiology* , 17(P), p252, 1990.

14. Dachman AH, McGehee JA, Beam TE, Burris JA, Powell DE. U.S. guided percutaneous laser ablation of liver tissue in a chronic pig model. *Radiology* , 176:129-133, 1990.

15. Bleier AR, Jolesz FA, Cohen MS, Weisskoff RM, Dalcanton JJ, Higuchi N, Feinberg DA, McKinstry RC, Hushek SG. Real-time magnetic resonance imaging of laser-tissue interactions. *Magnetic Resonance in Medicine*, 21:132-137, 1991.

16. Malone DE, Wyman DR, Moote DJ, MoriH, Lewis R, DeNardi F, Swift CL, Wilson BC. Ultrasound-controlled laser photocoagulation in pig liver. *Lasers Surg Med*, Suppl 3, p28, 1991.

17. Robinson JD, Tartell PB, Nishimura E, To SYD, Layfield LJ, Grant EG, Lufkin RB, Saxton RE, Ward PH, Castro DJ. MR imaging of interstitial laser therapy in comparison to CT and ultrasound. *Lasers Surg. Med.*. suppl. 2, p.4, 1990.

18. Steger AC, Lees WR, Walmsley K, Bown SG. Interstitial laser hyperthermia: A new approach to local destruction of tumours. *Brit Med J.*, 299:362-365, 1989.

19. Amin Z, Donald J, Masters A, Kant R, Steger A, Bown S, Lees W. Hepatic metastases: interstitial laser photocoagulation with real-time US monitoring and dynamic CT evaluation of treatment. *Radiology*, 187(2):339-347, 1993.

20. Godlewski G, Bourgeois JM, Sambuc P, Gouze C, Ould-Said H, Eledjam JJ, Rouy S, Pignodel C. Ultrasonic and histopathological correlations of deep focal hepatic lesions induced by stereotaxic Nd-YAG laser applications. *Ultrasound in Med. & Biol.*, 14(4):287-

291, 1988.

21. Parker D, Smith V, Sheldon P, Crooks L, Fussell L. Temperature distribution measurements in two dimensional MR imaging. *Med. Phys.*, 10(3):321-325, 1982.

22. Parker D. Applications of NMR imaging in hyperthermia: an evaluation of the potential for localized tissue heating and noninvasive temperature monitoring. *IEEE Transactions on Biomedical Engineering*, BME(1):Jan 1984.

23. Dickinson RJ, Hall AS, Hind AJ, Young IR. Measurement of changes in tissue temperature using MR imaging. *Journal of Computer Assisted Tomograhy*, 10(3):468-472, 1986.

24. Lewa CJ, Majewska Z. Temperature relationships of proton spin-lattice relaxation time T1 in biological tissues. *Bull Cancer* (Paris) ,67:525-530, 1980.

25. Cetas TC. Will thermometric tomography become practical for hyperthermia treatment monitoring? *Cancer Res*, 44:4805-4808, 1984.

26. Matsumoto R, Oshio K, Jolesz FA. T1-weighted MR monitoring for interstitial laser- and freezing-induced ablation in the liver. *JMRI,* 2:555-562, 1992.

27. Bleier AR, Higuchi N, Panych LP, Jakab PD, Hrovat, Jolesz. Magnetic resonance imaging of interstitial laser photocoagulation. *Proc SPIE*, 1202:188-195, 1990.

28. LeBihan D, Delannoy J, Levin RL. Temperature mapping with MR imaging of molecular diffusion: application to hyperthermia. *Radiology*, 171:853-857, 1989.

29. Matsumoto R, Selig A, Colucci M, Jolesz F. Interstitial Nd:YAG laser ablation in normal rabbit liver: trial to maximize the size of laser-induced lesions. *Lasers in Surg and Med.* 12(6):650-658, 1992.

30. Higuchi N, Bleier AR, Jolesz Fa, Colucci VM, Morris JH. Magnetic resonance imaging of the accute effects of interstitial neodymium:YAG laser irradiation on tissues. *Investigative Radiology*: 27(10):814-821, 1992.

31. Anzai Y, Lufkin RB, Saxton RE, Fetterman H, Farahani K, Layfield LJ, Jolesz FA, Hanafee WH, Castro DJ. Nd:YAG

interstitial laser phototherapy guided by magnetic resonance imaging in an ex vivo model: Dosimetry of laser-MR-tissue interaction. *Laryngoscope* 101:755-760, 1991.

32. Jolesz FA, Moore GJ, Mulkern RV, Bleier AR, Gonzales RG, Bowers JL, Metz KR, Higuchi N, Colucci VM. Response to and control of destructive energy by magnetic resonance. *Invest Rad*, 24(12):1024-1027, 1989.

33. Bettag M, Ulrich F, Kahn T, Seitz R. Local interstitial hyperthermia in malignant brain tumors using a low power Nd:YAG laser. *Proc SPIE*. 1525:409-411, 1991.

34. Castro DJ, Lufkin RB, Saxton RE, Nyerges A, Soudant J, Layfield LJ, Jabour BA, Ward PH, Kangarloo H. Metastatic head and neck malignancy treated using MRI guided interstitial laser phototherapy: an initial case report. *Laryngoscope*, 102:26-32, 1992.

35. Gewiese B, Beuthan J, Fobbe F, Stiller D, Muller G, Boese-Landgraf J, Wolf K, Deimling M. MRI-controlled laser-induced interstitial thermo-therapy of the liver. submitted to *Radiology*.

36. Ebner F, Fan M, Stollberger R, Ascher PW, Kleiner R, German RH. MRI for mapping the ND:YAG laser heat distribution in brain specimen. *11th SMRM Abstract* 1, 864 1992

37. Lufkin RB, Saxton RE, Kirlew K, Sinha S, Anzai Y, DeSalles AAF, Black KL. MR imaging of thermally coagulated blood: Applications in image-monitored thermal ablations. *Journal of Magnetic Resonance Imaging (Suppl.)* 4(P):S41, 1994.

38. Gullino PM, Jain RK, Grantham FH. Temperature gradients and local perfusion in a mammary carcinoma. *Journal of the National Cancer Institute.* 68:519-533, 1982.

39. Dave S, Vaupel P, Mueller-Klieser W, Blendstrup K. Temperature distribution in peripheral s.c. tumors in rats. In: Overgaard J (ed) *Hyperthermic Oncology*. Taylor and Francis, London. pp503-506, 1984.

40. Lyons BE, Samulski TV, Cox RS, Fessenden P. Heat loss and blood flow during hyperthermia in normal canine brain. I: Empirical study and analysis. *Int. J. Hyperthermia*, 5(2):225-247, 1989.

41. Arancia G, Malorni W, Mariutti G, Trovalusci P. Effect of

hyperthermia on the plasma membrane structure of Chinese hamster V79 fibroblasts: a quantitative freeze-fracture study. *Radiat. Res.*, 106:47-55, 1986.

42. Anghileri LJ, Marcha C, Crone-Escanye MC, Robert J. Effects of extracellular calcium on calcium transport during hyperthermia of tumor cells. *Eur J Cancer Clin Oncol.* 21:981-984, 1985.

43. Ruifrock ACC, Kanon B, Konings AWT. Correlation between cellular survival and potassium loss in mouse fibroblasts after hyperthermia alone and after a combined treatment with X rays. *Radiat Res*, 101:326-331, 1985.

44. Vaupel P, Kallinowski F. Physiological effects of hyperthermia. *Recent Results in Cancer Research.* 104:71-109, 1987.

45. Streffer C. Mechanism of heat injury. In: Overgaard J (ed) *Hyperthermic Oncology*. Talor and Francis, London, 2:213-222, 1984.

46. Mueller-Klieser W, Vaupel P. Tumor oxygenation under normobaric and hyperbaric conditions. *Br J Radiol*, 56:559-564, 1983.

47. Vaupel P, Frinak S, Bicher HI. Heterogeneous oxygen partial pressure and pH distribution in C3H mouse mammary adenocarcinoma. *Cancer Res*, 41:2008-2013, 1981.

48. Peterson HI. Tumor blood circulation: angiogenesis, vascular morphology and blood flow of experimental and human tumors. *CRC, Boca Raton*, 1979.

49. Vaupel P, Hammersen F. Midrozirkulation in malignen Tumoren. *Karger, Basel* , 1983.

50. Gerweck LE, Richards B. Influence of pH on the thermal sensitivity of cultured human glioblastoma cells. *Cancer Res*, 41:845-849, 1981.

51. Dikomey E, Eickhoff J, Jung H. The effect of extracellular pH on heat-sensitivity and thermotolerance of CHO and R1H cells. *Strahlentherapie*, 157:617, 1981.

52. Goldin EM, Leeper DB. The effect of reduced pH on the induction of thermotolerance. *Radiology* , 141:505-508, 1981.

53. Nielsen OS, Overgaard J. Effect of extracellular pH on

thermotolerance and recovery of hyperthermic damage in vitro. *Cancer Res* 39:2772-2778, 1979.

54. Scheid P. Funktionale besonderheiten der mikrozirkulation im karzinom. Bibl Anat 1:327-335, 1961.

55. Johnson RJR. Radiation and hyperthermia. In: Streffer C, vanBeuningen D, Dietzel F, Röttinger E, Robinson JE, Scherer E, Seeber S, Trott KR (eds) Cancer hyperthermia and radiation. Urban aund Schwarzenberg, Baltimore, pp 89-95, 1978.

56. Robinson JE, McCulloch D, McCready WA. Blood perfusion of murine tumores at normal and hyperthermal temperatures. *Natl Cancer Inst Monogr.* 61:211-215, 1982.

57. Peck JW, Gibbs FA. Capillary blood flow in murine tumors, feet and intestines during localized hyperthermia. *Radiat Res.* 96:65-81, 1983.

58. Song CW, Kang MS, Rhee JG, Levitt SH. The effect of hyperthermia on vascular function, pH and cell survival. *Radiology.* 137:795-803, 1980.

59. Stewart F, Begg A. Blood flow changes in transplanted mouse tumors and skin after mild hyperthermia. *Br J Radiology.* 56:477-482, 1983.

60. Sutton CH. Discussion. *Ann NY Acad Sci* 335:35-47, 1980.

61. Tanka Y, Hasegawa T, Murata T. Effect of irradiation and hyperthermia on vascular function in normal and tumor tissue. In: Overgaard J (ed) *Hyperthermic Oncology 1984*, Taylor and Francis, London. pp 145-148, 1984.

62. Song CW, Pattan MS, Rhee JG, Schuman VL, Levitt SH. Role of blood flow in the response of RIF-1 tumors to combined treatment of hyperthermia and radiotherapy. In: Overgaard J (ed) *Hyperthermic Oncology 1984*, Taylor and Francis, London. pp.293-296, 1984.

63. Vaupel P, Ostheimer K, Thomé H. Blood flow, vascular resistance, and oxygen consumption of malignant tumors during normothermia and hyperthermia. Ann Meeting Gesellschaft für Mikrozirkulation, Aachen, FRG (*Microvasc Res* 13:272, 1977)., 1976

64. Vaupel P, Ostheimer K, Mueller-Klieser W. Circulatory and

metabolic responses of malignant tumors during localized hyperthermia. *J Cancer Res Clin Oncol.* 98:15-29, 1980.

65. Vaupel P. Einfluß einer lokalisierten Mikrowellenhyperthermie auf die pH-Verteilung in bösartigen Tumoren. *Strahlentherapie.* 158:168-173, 1982.

66. vonArdenne M, Reitnauer PG. Die manipulierte selektive Hemmung der Midrozirkulation im Krebsgewebe. *J Cancer Res Clin Oncol.* 103:269-279, 1982.

67. Endrich B, Zweifach BW, Reinhold HS, Intaglietta M. Quantitative studies of microcirculatory function in malignant tissue: influence of temperature on microvascular hemodynamics during the early growth of the BA 1112 rat sarcoma. *Int J Radiat Oncol Biol Phys.* 5:2021-2030, 1979.

68. Emami B, Nussbaum GH, Ten Haken RK, Hughes WL. Physiological effects of hyperthermia: response of capillary blood flow and structure to local tumor heating. *Radiology.* 137:805-809, 1980.

69. Reinhold HS, van den Berg-Blok A. Enhancement of thermal damage to the microcirculation of "sandwich" tumors by additional treatment. *Eur J Cancer Clin Oncol.* 17:781-795, 1981.

70. Reinhold HS, van den Berg-Blok AE. Hyperthermia-induced alteration in erythrocyte velocity in tumors. *Int J Microcirc Clin Exp.* 2:285-295, 1983.

71. van den Berg-Blok AE, Reinhold HS. Time-temperature relationship for hyperthermia induced stoppage of the microcirculation in tumors. *Int J Radiat Oncol Biol Phys.* 10:737-740, 1984.

72. Gullino PM. Influence of blood supply on thermal properties and metabolism of mammary carcinomas. *Ann NY Acad Sci,* 335:1-21, 1980.

73. Gullino PM, Yi PN, Grantham FH. Relationship between temperature and blood supply or consumption of oxygen and glucose by rat mammary carcinomas. *J Natl Cancer Inst.* 60:835-847, 1978.

74. Song CW. Effect of local hyperthermia on blood flow and microenvironment. *Cancer Res* (Suppl) 44:4721s-4730s, 1984.

75. Song CW, Rhee JG, Levitt SH. Blood flow in normal tissues and tumors during hyperthermia. *J Natl Cancer Inst.* 64:119-124, 1980.

76. Song CW, Kang MS, Rhee JG, Levitt SH. The effect of hyperthermia on vascular function, pH, and cell survival. *Radiology.* 137:795-803, 1980.

77. Song CW, Kang MS, Rhee JG, Levitt SH. Vascular damage and delayed cell death in tumors after hyperthermia. *Br J Cancer.* 41:309-312, 1980.

78. Dickson JA, Calderwood SK. Temperature range and selective sensitivity of tumors to hyperthermia: a critical review. *Ann NY Acad Sci.* 335:180-205, 1980.

79. Kallinowski F, Vaupel P, Schaefer C, Benzing H, Mueller-Schauenburg W, Fortmeyer HP. Hyperthermia-induced blood flow changes in human mammary carcinomas transplanted into nude (*rnu/rnu*) rats. In:*Overgaard J (ed) Hyperthermic Oncology.* Taylor and Francis, London. pp 133-136, 1984.

80. Vaupel P, Mueller-Klieser W, Otte J, Manz R, Kallinowski F. Blood flow, tissue oxygenation, and pH-distribution in malignant tumors upon localized hyperthermia. *Strahlentherapie.* 159:73-81, 1983.

81. Rappaport DS, Song CW. Blood flow and intravascular volume of mammary adenocarcinoma 13726A and normal tissues of rat during and following hyperthermia. *Int J Radiat Oncol Biol Phys.* 9:539-547, 1983.

82. Shrivastav S, Kaelin WG, Joines WT, Jirtle RL. Microwave hyperthermia and its effect on tumor blood flow in rats. *Cancer Res.* 43:4665-4669, 1983.

83. Dewhirst M, Sim DA, Gross JF, Kundrat MA. Effect of heating rate on tumor and normal tissue microcirculatory function. In: *Overgaard J (ed) Hyperthermic oncology.* Taylor and Francis, London. pp177-180, 1984.

84. Karino T, Koga S, Maeta M, Hamazoe R, Yamane T, Oda M. Experimental and clinical studies on effects of hyperthermia on tumor blood flow. In: *Overgaard J (ed) Hyperthermic oncology.* Taylor and Francis, London. pp 173-176, 1984.

85. Voorhees WD, Babbs CF. Hydralazine-enhanced selective heating

of transmissible venereal tumor implants in dogs. *Eur J Cancer Clin Oncol.* 18:1027-1033, 1982.

86. Milligan AJ, Panjehpour M. Canine normal and tumor tissue blood flow during fractionated hyperthermia. In: Broerse JJ, Barendsen GW, Kal HB, van der Kogel AJ (eds) *Proc. 7th ICRR.* Martinus Nijhoff Publ., Boston, The Hague, Nr D6-035, 1983.

87. Endrich B, Voges J, Lehmann A. The microcirculation of the amelanotic melanoma A-Mel-3 during hyperthermia. In: Overgaard J (ed) *Hyperthermic oncology.* Taylor and Francis, London. pp137-140, 1984.

88. Dudar TE. Flow modifications in normal and neoplastic tissues during growth and hyperthermia. *Ph.D. thesis,* Faculty of Carnegie Institute of Technology, Carnegie - Mellon University, Pittsburgh, PA. 1982.

89. Dudar TE, Jain RK. Differential response of normal and tumor microcirculation to hyperthermia. *Cancer Res.* 44:605-612, 1984.

90. Olch AJ, Kaiser LR, Silberman AW, Storm FK, Graham LS, Morton DL. Blood flow in human tumors during hyperthermia therapy: demonstration of vasoregulation and an applicable physiological model. *J Surg Oncol* 23:125-132, 1983.

91. Waterman FM, Fazekas J, Nerlinger RE, Leeper DB. Blood flow rates in human tumors during hyperthermia treatments as indicated by thermal washout. Proc 2nd Ann meeting *North American Hyperthermia Group,* Salt Lake City, pE-6, 1982.

92. Emami B, Song CW. Physiological mechanisms in hyperthermia: a review. *Int J Radiat Oncol Biol Phys*, 10:289-295, 1984.

93. Vaupel P, Gabbert H. Evidence for and against a tumor type-specific vascularity. *Strahlentherapie Onkol.*, 162:633-638, 1986.

94. von Ardenne M, Reitnauer PG. Selective occlusion of cancer tissue capillaries as the central mechanism of the cancer multistep therapy. *Jpn J Clin Oncol.*, 10:31-48, 1980.

95. Copley AL, King RG. A survey of surface hemorrheological experiments on the inhibition of fibrinogenin formation employing surface layers of fibrinogen systems with heparins and other substances. A contribution on antithrombogenic action. *Thrombosis Res*, 35:237-256, 1984.

96. Overgaard J. Histopathologic effects of hyperthermia. In: Storm FD (ed) *Hyperthermia in cancer therapy*. Hall Medical, Boston, pp 163-185, 1983.

97. LeBihan D, Brenton E, Lallemand D, Aubin ML, Vignaud J, Laval-Jeantet M. Separation of diffusion and perfusion in intravoxel incoherent motion MR imaging. *Radiology* 168:497-505, 1988.

98. Hill SA, Smith KA and Denekamp J. Reduced thermal sensitivity of the vasculature in a slowly growing tumour. *Int. J. Hyperthermia*, 5(3):359-370, 1989.

99. Hynynen K, Darkazanli A, Unger E, Schenk J. MRI-guided noninvasive ultrasound surgery. *Med. Phys.*, 20(1):107-115, 1993.

100. Gore I, Isaacson NH. The pathology of hyperpyrexia. Observations at autopsy in 17 cases of fever therapy. *American Journal of Pathology*. 25:1029-1060, 1948.

101. Willis EJ, Findlay JM, McManus JPA. Effects of hyperthermia therapy on the liver. II. Morphological observations. *Journal of Clinical Pathology*. 29:1-10, 1976.

102. Fajardo LF. Pathological effects of hyperthermia in normal tissues. *Cancer Research (Suppl.)* 44:4826-4835, 1984.

103. Anzai Y, Lufkin R, Castro D, Farahani K, Jabour B, Layfield L, Udkoff R, Hanafee W. MR imaging-guided interstitial Nd:YAG laser phototherapy: dosimetry study of acute tissue damage in an in vivo model. *JMRI*, 1:553-559, 1991.

104. El-Ouahabi A, Guttman C, Hushek S, Bleier A, Dashner K, Dikkes P, Black P, Jolesz F. MRI guided interstial laser therapy in a rat malignant glioma model. *Lasers in Surg and Med.* 13:503-510, 1993.

105. Hawkes RC, Patz SA. Rapid Fourier imaging using steady-state free precession. *Magn Reson Med* ., 4:9-23, 1987.

106. Svaasand LO, Boerslic T, Oeveraasen M. Thermal and optical properties of living tissue: Application to laser -induced hyperthermia. *Laser Surg Med,* 5:589-602, 1985.

107. Waldow SM Henderson BW, Dougherty TJ. Enhanced tumor control following sequential treatment of photodynamic therapy

(PDT) and localized microwave hyperthermia in vivo. *Laser Surg Med* , 4:79-85, 1984.

108. Morrison PRM. *The Nd:YAG laser in the hyperthermal treatment of cancer: Response in an animal tumor model to continuous IR surface irradiation*. Master's thesis. Illinois Institute of Technology, Chicago, 1987.

109. Sijens PE, Bovee WMM, Koole P, Schipper J. *Int. J. of Hyperthermia*, 5(3):351-357, 1989.

110. Ascher PW, Justich E, Schröttner O. Interstitial thermotherapy of central brain tumors with the Nd:YAG laser under real time monitoring by MRI. *Journal of Clinical Laser Medicine, Surgery.* 9(1):79-83, 1992.

111. Higuchi N, Bleier AR, Jolesz FA, Colucci VM, Morris JH. MRI of the acute effects of interstitial Nd:YAG laser irradiation on tissues. *Invest Radiol*, 27:814-821, 1992.

112. Cline HE, Schenck JF, Hynynen K, Watkins RD, Souza SP, Jolesz FA. Magnetic resonance guided focused ultrasound surgery. submitted to *Radiology*.

113. Matsumoto R, Selig AM, Colucci VM, Jolesz FA. Real-time MR monitoring of cryotherapy in the liver: predictability of the histological outcome. *Journal of Magnetic Resonance Imaging*, 2(5): 555-562, 1992.

114. Cline HE, Schenck JF, Watkins RD, Hynyen K, Jolesz FA. Magnetic resonance guided thermal surgery. submitted to *Magn Res in Med.*

115. Mulkern RV, Melki PS, Jakab P, Higuchi N, Jolesz FA. Phase encode order and its effect on contrast and artifact in single shot RARE sequences. Medical Physics. 18(5):1032-1037, 1991.

116. Wyman DR, Wilson BC, Malone DE. Medical Imaging Systems for Feedback Control of Interstitial Laser Photocoagulation. *Proc IEEE*, 80:890-902, 1992.

Chapter 2. Theoretical Analysis of Nuclear Magnetic Resonance Phenomena

2.1 Introduction

The quantum theory of NMR deals with spins in energy states defined by the Hamiltonian of a magnetic moment in a field, $H = -\gamma\hbar\hat{I}\cdot\vec{H}$. Initial theoretical treatments of the problem produced a result that the spin system would be unable to continually absorb power, which contradicted reality. However, the analysis looked at the spin system in isolation. In any physically realizable system the spin system interacts with the lattice of the material. The lattice can either be a literal crystal lattice in a solid or it can be the "lattice" environment for spins in a liquid solution. Theoretical analyses usually assume that a thermal equilibrium exists between the spin system and the lattice. The quantum analysis employing quantized angular momentum and discrete energy states yields results equivalent to the classical or semi-classical treatment employing the interaction between a magnetic moment and a magnetic field. The results of either treatment are put in the form of the phenomenological Bloch equations, which give the equations of motion for individual spins. A thorough analysis is contained in Abragam[1], McConnell[2] or Slichter.[3] This summary of their analyses seeks to illustrate the microscopic source of the temperature sensitivity of the MR parameters.

2.2 Net Magnetism Temperature Sensitivity

2.2.1 Analysis

Since the Bloch equations are linear, the macroscopic magnetism is treated as the sum of all the magnetic moments in the sample, which then allows application of the equations to the ensemble average of the spins. For a system of spin=1/2 protons in thermal equilibrium, the occupation number is proportional to exp(-E/KT), where E is the energy for the particular state, T is temperature and K is the Boltzman constant. The ratio of the populations parallel and anti-parallel to the field is

$$\frac{n\uparrow}{n\downarrow} = \exp\left(\frac{-\Delta E}{KT}\right) \qquad 2.1$$

where ΔE is the energy spacing between the levels, $\Delta E = h\omega_0 = h\gamma H_0$. The energy spacing is much smaller than KT, so the Taylor expansion is used and the higher order terms are dropped. Then the equation for the net magnetization is used to determine that the net magnetization is proportional to 1/T and $\frac{\Delta M}{M} \approx \frac{-\Delta T}{T}$.

2.2.2 Implications

The implications of this result are noteworthy. The first consideration is that application of typical physiological values to the relationship between temperature and magnetization only produces a 0.3% change in signal for a 1°C temperature change. This indicates that contrast-to-noise values of MR pulse sequences sensitive to the net magnetization and approximately insensitive to the relaxation parameters would be inadequate for any non-invasive temperature monitoring application.

The net magnetization temperature dependence has another implication which is relevant to this thesis. It is significant to note that a temperature increase produces a signal decrease. If an attempt is made to develop an MR imaging pulse sequence that is sensitive to temperature via some other parameter, the temperature response of the system could improve if it could induce signal decreases with temperature increases. In this way the two processes could act synergistically.

2.3 T1 Temperature Dependence

2.3.1 Interactions: Types and Relative Significance

The net magnetization contrast is insufficient for any physiological application so the temperature dependence of the relaxation parameters T_1 and T_2, the other main sources of contrast in NMR images, is examined. T_1 is known as the spin-lattice relaxation time and T_2 is known as the spin-spin relaxation time. The spins interact with each other and with the spins in the lattice via their fields. In a liquid at room temperature, the molecules of the lattice can move past the spins at any range and at nearly any speed. The fields felt by the spin will cover a wide range of magnitudes and also a wide range of rise and fall times. The Fourier transform of the time course of these interactions would produce a wide band, continuous frequency spectrum. Another way of saying this is that the lattice has so many degrees of freedom that the energy levels with which the spins can interact approach a continuum. The spins will interact most strongly with

the frequency component at the Larmor frequency. Brownian motions and some rotational and torsional motions of the lattice molecules will contribute frequency components in the interaction range. Electronic motions and molecular vibrations will contribute mostly to the higher frequency components, so their interaction with the spin system will be negligible.

There are a number of specific interaction processes which are further classified as intramolecular or intermolecular interactions. The intramolecular processes will tend to dominate for a combination of two reasons. The interaction between two dipoles is

$$W_{12} = \frac{\mu_1 \cdot \mu_2 - 3(n \cdot \mu_1)(n \cdot \mu_2)}{|x_1 - x_2|^3} \qquad 2.2$$

Since atoms in the same molecule will tend to be closer to each other than atoms on different molecules the $1/r^3$ term indicates that the closer atom will dominate. In addition, atoms on the same molecule are held close to each other for a long period of time so the interaction is stronger. Atoms on different molecules can approach very close to each other when the molecules collide, but the duration of their interaction is very short, so the intramolecular interaction tends to dominate. The dipole-dipole interaction is very strong for spin=1/2 species such as protons and is both an intra- and inter-molecular process.

Other interactions that can contribute to NMR relaxation are

anisotropic chemical shift, spin rotational interactions and scalar interactions. The anisotropic chemical shift interaction involves the change in the field that the nucleus sees because an external field has modified the flow of the atomic electrons. Spin rotational interactions are caused by the motion of atomic electrons around the nucleus when an entire molecule rotates. Scalar interactions between nuclei on the same molecule that have anti-parallel spins is a second order intramolecular interaction. The electric quadrapolar interaction is an example of this type of interaction and it tends to dominate for spins greater than 1/2, but it is not relevant for protons so we will not dicuss it here. The relative significance of the different interactions will vary for spin-lattice and spin-spin relaxation.

2.3.2 Interaction Formalism

The interaction of a spin with a field can be represented by the Hamiltonian $H = -\gamma\hbar\hat{I}\cdot\vec{H}$. The field of interest for NMR phenomena is the static field H_0 and the interaction field. In physiological systems the species of interest is the spin=1/2 proton. The dominant interaction is the dipole-dipole interaction between the 2 protons on the water molecule. The flux density at one proton due to the other is (SI units)

$$B = \frac{\mu_0\mu_p}{4\pi r^3} = \frac{4\pi\times10^{-7}\ \mathrm{H\ m^{-1}} \times 1.521\times10^{-26}\ \mathrm{J\ T^{-1}}}{4\pi \times (1.5\times10^{-10}\mathrm{m})^3} = 0.451\times10^{-3}\ \mathrm{T}$$

2.3

Since typical NMR imagers operate near 1T, the interaction field is much smaller than the static field and the Hamiltonian can be separated into a large static component H_0 and a small time dependent component H_1. This allows use of the powerful interaction formalism in the quantum mechanical analysis of the temperature dependent relaxation parameters.

2.3.3. Separation of Interaction and Position Terms

Molecules in solution tend to move more violently at higher temperatures so the frequency spectrum of the interactions associated with the molecular motion will have more high frequency components at higher temperatures. However, the nature of the interactions between the spins do not depend on temperature. Thus, to simplify analysis, the time dependent position component of the Hamiltonian is separated from the interaction component. The position component is related to the frequency spectrum and the temperature dependence of the relaxation parameter is expressed in that way. To accomplish this the Hamiltonian is expressed as

$$H_1 = \sum_q F^{(q)} A^{(q)}$$

2.4

where $F^{(q)}$ is a random function of the relative position of the two spins and $A^{(q)}$ are operators acting on the spin variables. The form of $F^{(q)}$ will depend on the model of molecular motion that is used. The form will in some way represent random motion to represent molecules in a liquid near room temperature.

2.3.4 Analysis of the Spectral Density Function

The convention

$$A^{(q)} = A^{(-q)\uparrow} \text{ and } F^{(q)} = F^{(-q)*}. \tag{2.5}$$

is used. The temperature dependent spectral density is related to the position function via the correlation function $G^{(q)}(\tau)$, where

$$\overline{F^{(q)}(t) \cdot F^{(q')*}(t+\tau)} = \delta_{qq'} \cdot G^{(q)}(\tau) \tag{2.6}$$

and

$$J^{(q)}(\omega) = \int_{-\infty}^{\infty} G^{(q)}(\tau)\, e^{-i\omega\tau}\, d\tau \tag{2.7}$$

where J is the spectral density function. The overbar in the definition of G represents an ensemble average over the probability distribution of the random function. The definition applies for isotropic random motion of the orientation of the vector between the 2 spins. The quantum mechanical equivalent of the correlation function is

$$G(\tau) = TR_{fl}[F(t)\, P(F)\, F(t+\tau)] \tag{2.8}$$

where

$$P(F) = \frac{e^{\frac{-hF}{KT}}}{TR\left[e^{\frac{-hF}{KT}}\right]} \tag{2.9}$$

The two interacting spins are labelled I and S. The quantity of

interest is the expectation value of the spins <I> and <S> and, since the spins are identical, the observed quantity is <I>+<S>. The equation of motion for the spins is used with the reduced density matrix to derive an equation of motion for the observed quantity that can be related to the phenomenological Bloch equations. This produces an equation that expresses T_1 as a function of the gyromagnetic ratio, the spin number and the spectral densities,

$$\frac{1}{T1} = \frac{3}{2}\gamma^4 h^2 I(I+1)\{ J^1(\omega) + J^2(2\omega) \} \qquad 2.10$$

Next, the nature of the spectral densities must be determined for the intramolecular dipole-dipole interaction.

2.3.5 Intramolecular Dipole-Dipole Interaction

For this interaction the dipole-dipole distance is fixed, but rotation of the molecule will change the orientation of the spin-spin axis. The molecule is treated as a rigid sphere of diameter a in a medium of viscosity n. θ and ϕ are polar angles, Ω is the spin-spin axis vector, and the probability that the spin-spin axis is lying along these angles at time t is

$$\psi(\theta,\phi,t) = \psi(\Omega,t) \qquad 2.11$$

The equation of motion for the spin-spin axis is

$$\frac{\partial \psi}{\partial t} = \frac{D_s}{a^2}\nabla^2\psi \qquad 2.12$$

Where

$$D_s = \frac{KT}{8\pi a\eta} \qquad 2.13$$

from the Stoke's formula. Expanding Ψ in spherical harmonics yields

$$\psi(\Omega,t) = \sum c_l^m Y_l^m(\Omega) \qquad 2.14$$

Since

$$\nabla^2 Y_l^m(\Omega) = -l(l+1)\, Y_l^m(\Omega) \qquad 2.15$$

and the spherical harmonics are orthogonal, this yields

$$c_l^m(t) = c_l^m(0)e^{\frac{-t}{\tau_l}} \qquad 2.16$$

where

$$\frac{1}{\tau_l} = \frac{D_s}{a^2}l(l+1) \qquad 2.17$$

$\psi(\Omega,t)$ is built from $P(\Omega,\Omega_0,t)$, the conditional probability that the spin-spin axis lies along Ω at time t given that it started along Ω_0 at t=0. The initial condition is mathematically represented by

$$\psi(\Omega,0) = \delta(\Omega-\Omega_0) \qquad 2.18$$

The expansion of the delta function into

$$\delta(\Omega-\Omega_0) = \sum_{lm} Y_l^{m*}(\Omega_0)\, Y_l^m(\Omega) \qquad 2.19$$

combined with

$$c_l^m(0) = Y_l^{m*}(0) \qquad 2.20$$

yields

$$P(\Omega,\Omega_0,t) = \sum Y_l^{m*}(\Omega_0)\, Y_l^m(\Omega)\, e^{\frac{-t}{\tau_1}}. \qquad 2.21$$

This produces the correlation function

$$G(t) = \frac{1}{4\pi}\int\int F^*(\Omega_0)\, F(\Omega) \sum_{lm} Y_l^{m*}(\Omega_0)\, Y_l^m(\Omega)\, e^{\frac{-t}{\tau_1}}\, d\Omega d\Omega_0 \qquad 2.22$$

Abragam shows that

$$F^{(1)}(\Omega) = \frac{1}{r^3}\sqrt{\frac{8\pi}{15}}\, Y_2^1(\Omega) \quad \text{and} \quad F^{(2)}(\Omega) = \frac{1}{r^3}\sqrt{\frac{32\pi}{15}}\, Y_2^2(\Omega) \qquad 2.23$$

The correlation function then reduces to

$$G^{(1)}(t) = \frac{1}{r^6}\frac{2}{15} e^{\frac{-|t|}{\tau_2}} \quad \text{and} \quad G^{(2)}(t) = \frac{1}{r^6}\frac{8}{15} e^{\frac{-|t|}{\tau_2}} \qquad 2.24$$

This gives us solutions for the spectral densities,

$$J^{(1)}(\omega) = \frac{1}{r^6}\frac{4}{15}\frac{\tau_2}{(1+\omega^2\tau_2^2)} \quad \text{and} \quad J^{(2)}(\omega) = \frac{1}{r^6}\frac{16}{15}\frac{\tau_2}{(1+\omega^2\tau_2^2)} \tag{2.25}$$

The solution for T_1 then reduces to

$$\frac{1}{T1} = \frac{2\gamma^4h^2}{5\,r^6} I(I+1)\left\{\frac{\tau_2}{(1+\omega^2\tau_2^2)} + \frac{4\tau_2}{(1+4\omega^2\tau_2^2)}\right\} \tag{2.26}$$

The equation for T_1 can be reduced further by examining the relative magnitudes of the Larmor period and the correlation time. The correlation time

$$\tau_2 = \frac{4\pi\eta a^3}{3KT} = \frac{4\pi\,(.85\,\frac{g}{m\,sec})(1.5\times10^{-10}m)^3}{3(1.381\times10^{-16}\frac{erg}{°K})(300°K)} = 2.9\times10^{-12}\,sec \tag{2.27}$$

is much smaller than the Larmor period = $2.3X10^{-8}$ sec. This is the narrow line limit, which allows simplification of the T_1 equation for spin=1/2 protons to

$$\frac{1}{T1} = 2\pi\frac{\gamma^4h^2}{r^6}\frac{a^3\eta}{KT} \tag{2.28}$$

Thus, T_1 is directly proportional to temperature, and an increase in temperature would cause T_1 to increase. To maximize the temperature contrast in an image, the NMR pulse sequence could be designed for signal decrease with T_1 increase. In this way the signal changes from T_1

temperature effects will add to the signal changes from M_0 effects and sensitivity to temperature will be maximized.

2.3.6 Intermolecular Interactions

The previous analysis dealt only with the intramolecular dipole-dipole interaction associated with rotation of the molecule. To describe the spin-spin interactions of spins on different molecules, the spins of entire molecules can be summed and the effect of net spins on net spins can be analyzed or the effect of each spin on every other spin can be examined. For water the methods are equivalent.

The movement of one spin past another is studied by again using a diffusion equation

$$\frac{\partial \psi(r,t)}{\partial t} = D \nabla^2 \psi \qquad 2.29$$

with the inital conditions $\psi(r,0) = \delta(r-r_0)$. If r is treated as the molecular separation, this yields

$$P(r,r_0,t) = (8\pi Dt)^{-3/2} \exp\left(\frac{(r-r_0)^2}{8Dt}\right) \qquad 2.30$$

The correlation function then becomes (for m=0,1,2)

$$G^{(m)}(t) = \alpha^{(m)} N (8\pi Dt)^{-3/2} \int\int \frac{Y_2^{m*}(\Omega_0)}{r_0^3} \frac{Y_2^m(\Omega)}{r^3} \exp\left(\frac{-|r-r_0|^2}{8Dt}\right) d^3r \; d^3r_0 \qquad 2.31$$

where

$$\alpha^0 = \frac{48\pi}{15}, \quad \alpha^1 = \frac{8\pi}{15}, \quad \alpha^2 = \frac{32\pi}{15} \tag{2.32}$$

The Fourier expansion of

$$\exp\left(\frac{|\,r-r_0\,|^2}{8Dt}\right) \tag{2.33}$$

is used and the expansion terms are expressed in the form of spherical harmonics and Bessel functions. The distance of closest approach is determined by the diameter of the molecules, d. The Stokes formula is used for the translational diffusion coefficient

$$D = \frac{KT}{6\pi a\eta} \tag{2.34}$$

which is valid for a rigid sphere. This produces a solution for T_1 as a function of the spectral densities

$$\frac{1}{T1} = \frac{3}{2}\gamma^4 h^2 I(I+1)\,(J^{(1)} + J^{(2)}) \tag{2.35}$$

where

$$J = \frac{2\pi}{5}\frac{N\eta}{KT}, \quad J^{(1)} = \frac{8\pi}{15}J, \quad J^{(2)} = \frac{32\pi}{15}J \tag{2.36}$$

Which, for protons, yields,

$$\frac{1}{T1} = \frac{6\pi^2}{5}\gamma^4 h^2 \frac{N\eta}{KT} \tag{2.37}$$

Thus, the translation contribution to T_1 is also linearly proportional to

temperature and a pulse sequence that produces a signal decrease with increasing T_1 will optimize the temperature-induced contrast.

2.4 T2 Temperature Dependence

The spin-spin relaxation parameter T_2 is also temperature dependent. The derivation is equivalent to the T_1 temperature dependence derivation in many ways. It is again assumed that motions of the spins are uncorrelated and dipole-dipole interactions again dominate. The equation for the precession of the transverse magnetization around the z axis is used, with the initial magnetization position along the x axis at t=0. At time t the amplitude of the transverse magnetization is

$$I_x\cos(\omega t) + I_y\sin(\omega t) = e^{-iH_0t}\hat{I}_x e^{iH_0t} \qquad 2.38$$

and its expectation value

$$TR\left(e^{-iH_0t}\hat{I}_x e^{iH_0t}\right) = TR\left[I_x\sigma^*\right] = \langle I_x\rangle^* \qquad 2.39$$

The equation of motion for the transverse magnetization is

$$\frac{\partial\langle I_x + I_x'\rangle^*}{\partial t} = -TR(A_x\sigma^*) = -\langle A_x\rangle^* \qquad 2.40$$

A_x is again a function of the spectral density, I_x and I_x' and the interaction terms of the Hamiltonian $A^{(q)}$. The result of the derivation is again put in the form of the phenomenological Bloch equation

$$\frac{\partial\langle I_x + I_x'\rangle^*}{\partial t} = \frac{-1}{T2}\langle I_x + I_x'\rangle^* \qquad 2.41$$

and produces a solution for T_2

$$\frac{1}{T2} = \gamma^4 h^2 I(I+1)\left\{\frac{3}{8}J^2(2\omega) + \frac{15}{4}J^1(\omega) + \frac{3}{8}J^0(0)\right\} \qquad 2.42$$

If the correlation time of the randomly changing $H_1(t)$ is very short compared to the Larmor period the narrow line approximation used for T_1 can be used again. The spectral densities are approximately constant over the frequencies of interest and are proportional to the DC value. The relative magnitudes of the different spectral densities can be determined and the equation for T_2 reduces to

$$\frac{1}{T2} = \frac{3}{2}\gamma^4 h^2 I(I+1)\left\{J^1 + J^2\right\} \qquad 2.43$$

Thus we see that T_1=T_2.

2.5 Results from the Literature

The results of the theoretical analysis are immediately suspect because they suggest T_1=T_2 and they suggest an equivalent temperature dependence of T_1 and T_2. Experiment does not agree with this result. The temperature dependence of T_1 has been studied in a variety of physiological materials and the results collated by Bottomley et al.[4] Papers by Parker et

al and Dickinson et al demonstrated results in blood, muscle, doped water and agar.[5,6,7] Parker's data covered the 0-50°C range and Dickinson's data covered the 10-60°C range. Within these temperature ranges they achieved good agreement with the linear relationship between T_1 and temperature postulated by the theoretical analysis. The studies employed both *in vitro* and *in vivo* samples. The T_1's were measured with spectrometers and calculated from image data. The *in vivo* data is suspect because the invasive thermometry sampled the temperatures at a small number of discrete locations while the T_1 was calculated from a region of tissue.

Other experimental work suggests that the simplifying assumptions in the model may not be entirely accurate. One clue to an oversimplification lies in the T_1 dispersion data acquired by multiple groups. This suggests that a uniform correlation time cannot apply to all the spins because of the variety of bound states that occur in a physiological system. The model usually postulated to account for this situation is several layers of water molecules bound to macromolecules such as proteins. The most strongly bound inner layer would have the longest correlation time. This concept is usually dealt with by postulating a bound fraction **b** and calculating a relaxation time based on appropriate weighting of the bound T_1 and the free T_1. This model also incorporates the rapid exhange between the bound and free states.

An enhanced model that postulates a log-Gaussian distribution of

correlation times can explain the experimental T_1 dispersion times but requires that $\omega\tau_2 \geq 1$, which contradicts the narrow line assumption that was used in the theoretical analysis. The log-Gaussian distribution for the intramolecular correlation times can be expressed as

$$g(\tau) = \frac{\alpha}{\tau\sqrt{\pi}}\exp\left(-\left(\alpha\ln\left(\frac{\tau}{\tau_0}\right)\right)^2\right) \qquad 2.44$$

The temperature dependence of the correlation time is built into the parameters $\alpha = \alpha_0\sqrt{T}$ and $\tau_0 = \tau_{0\infty}e^{\frac{E_a}{KT}}$. Fung et al got good agreement with this model when they fit T_1 dispersion data over a 4.5-60 MHz frequency range and a temperature range of -70°C<T<+40°C.[8,9]

Other data from these studies that $\partial T_1/\partial T$ increases with increasing frequency also questions the validity of the narrow line assumption. The frequency dependence of T_1 can be extracted from the model, yielding an approximate relationship $T_1 \approx A\upsilon^B$. The temperature dependent correlation times are coefficients of the frequency terms and are implicit in the frequency. This yields an approximate dependence $\partial T_1/\partial T \approx \upsilon^B$ with B=1/3. This is roughly in agreement with the increase in $\partial T_1/\partial T$ between 7.5 MHz and 60 MHz seen by Fung et al and that seen by Koenig et al between 1 and 20 MHz.[10] The frequency dependence of the $\partial T_1/\partial T$ slope is consistent with the distributed correlation time model. The agreement of the enhanced model with the $\partial T_1/\partial T$ temperature dependence and dispersion values

suggests that Parker and Dickinson may have been able to demonstrate agreement between experiment and theory because they only covered a small temperature range and T_1 range.

2.6 Pulse Sequence Contrast Control

2.6.1 Basic Signal Equation

A mathematical analysis of the signal intensity dependence in MR images begins with the central equation describing the dependence of the signal intensity on the following parameters: M_0, the proton density; T2, the transverse magnetization decay parameter; T1, the longitudinal magnetization recovery parameter and D, the molecular water self-diffusion coefficient.

$$S_0 = M_0\left(1 - e^{\frac{-TR}{T1}}\right)\left(e^{\frac{-TE}{T2}}\right)\left(e^{-bD}\right) \qquad 2.45$$

The sensitivity of the signal intensity to each of these parameters is determined by taking the partial derivative with respect to each,

$$\begin{aligned}\partial S = {} & M_0\left(1 - e^{\frac{-TR}{T1}}\right)\left(e^{\frac{-TE}{T2}}\right)\left(e^{-bD}\right)(-b\partial D) \\ & + M_0\left(1 - e^{\frac{-TR}{T1}}\right)\left(e^{\frac{-TE}{T2}}\right)\left(e^{-bD}\right)\left(\frac{TE}{T2^2}\right)\partial T2 \\ & + M_0\left(e^{\frac{-TE}{T2}}\right)\left(e^{-bD}\right)\left(-e^{\frac{-TR}{T1}}\right)\left(\frac{TR}{T1^2}\right)\partial T1\end{aligned} \qquad 2.46$$

where the derivative with respect to M_0 is neglected because it is insignificant compared to the other terms unless tissue is vaporized. Simplifying the equation and expressing the signal change as a function of the original signal intensity produces

$$\partial S = S_0(-b\partial D) + S_0\left(\frac{TE}{T2^2}\right)\partial T2 + S_0\frac{\left(-e^{\frac{-TR}{T1}}\right)}{\left(1-e^{\frac{-TR}{T1}}\right)}\left(\frac{TR}{T1^2}\right)\partial T1 \qquad 2.47$$

2.6.2 T1-Weighted Contrast

The maximum contrast attainable with T1-weighted imaging can be determined by taking the derivative of the T1 contrast equation with respect to TR and setting the result equal to zero.

$$\frac{\partial\partial S}{\partial TR} = \frac{\partial}{\partial TR}\left(S_0\frac{\left(-e^{\frac{-TR}{T1}}\right)}{\left(1-e^{\frac{-TR}{T1}}\right)}\left(\frac{TR}{T1^2}\right)\partial T1 \right) = 0 \qquad 2.48$$

This yields a result that the TR should equal the T1 of the material of interest. A different value that may be of interest is the percentage change in signal intensity. The percentage signal intensity change can be determined by dividing the contrast by the original signal value

$$\frac{\partial S}{S_0} = \left(\frac{\left(-e^{\frac{-TR}{T1}}\right)}{\left(1-e^{\frac{-TR}{T1}}\right)}\left(\frac{TR}{T1^2}\right)\partial T1 \right) \qquad 2.49$$

Maximizing this value involves taking the derivative with respect to TR and again setting it equal to zero.

$$\frac{\partial\frac{\partial S}{S_0}}{\partial TR} = (-\partial T1)\left(\left(e^{\frac{TR}{T1}}-1\right)^{-2}\left(\frac{TR}{T1^2}\right)(-1)\left(e^{\frac{TR}{T1}}\right)\left(\frac{1}{T1}\right) + \left(e^{\frac{TR}{T1}}-1\right)^{-1}\left(\frac{1}{T1^2}\right)\right) = 0 \qquad 2.50$$

The equation has only one solution: TR=0. This is obviously not a practical

solution, but it does give us an insight into the behavior of the contrast as a function of TR.

2.6.2.1 Contrast-to-Noise Ratio

The analysis of the percentage signal change value indicates that the physical properties of the system must be accounted for. One factor that is very significant in these analyses is noise. If the contrast is below the noise level it will not be detected. Thus, optimization of the contrast to noise ratio is the goal. The first step in this analysis is determination of the relationship between the contrast equation used up to this point and the noise value. The standard method used to account for noise is to recognize that signal is proportional to TR, since 2 acquisitions will generate twice as much signal, while noise is proportional to $\sqrt{TR}$. Thus, converting a signal or contrast equation to a signal-to-noise or contrast-to-noise equation simply requires dividing by $\sqrt{TR}$. This produces a contrast-to-noise equation

$$\frac{\partial S}{\sqrt{TR}} = M_0\left(e^{\frac{-TE}{T2}}\right)\left(e^{-bD}\right)\left(-e^{\frac{-TR}{T1}}\right)\left(\frac{\sqrt{TR}}{T1^2}\right)\partial T1 \qquad 2.51$$

This value is optimized by again taking its derivative with respect to TR and setting the result equal to zero.

$$\frac{\partial \frac{\partial S}{\sqrt{TR}}}{\partial TR} = \frac{\partial}{\partial TR}\left(M_0\left(e^{\frac{-TE}{T2}}\right)\left(e^{-bD}\right)\left(-e^{\frac{-TR}{T1}}\right)\left(\frac{\sqrt{TR}}{T1^2}\right)\partial T1\right) = 0 \qquad 2.52$$

This yields the result TR = 1/2·T1. This is fortunate because shorter scan times improve the temporal resolution of our control system.

2.6.2.2 Contrast-to-Noise Per Unit Time

The concept of noise has been included in the determination of the optimum selection of pulse parameters, but now factors relevant to thermal therapy must also be included. The optimum control system for thermal therapy would have excellent temporal resolution to observe the changes in the treated tissue as soon as they occur. Thus, the time required to obtain the image should be included as a factor in the equation. Consideration of the contrast per unit time involves dividing the T1 contrast equation by TR. The noise factor is accounted for by dividing by √TR.

$$\frac{\partial S}{TR^{1.5}} = M_0\left(e^{\frac{-TE}{T2}}\right)\left(e^{-bD}\right)\left(-e^{\frac{-TR}{T1}}\right)\left(\frac{1}{T1^2\sqrt{TR}}\right)\partial T1 \qquad 2.53$$

This quantity is optimized by taking its derivative with respect to TR and setting it equal to zero.

$$\frac{\partial \frac{\partial S}{TR^{1.5}}}{\partial TR} = \frac{\partial}{\partial TR}\left(-M_0\left(e^{\frac{-TE}{T2}}\right)\left(e^{-bD}\right)\left(e^{\frac{-TR}{T1}}\right)\left(\frac{1}{T1^2\sqrt{TR}}\right)\partial T1\right) = 0 \qquad 2.54$$

This has a solution at TR = ∞, which is obviously not a practical value. It is also counterintuitive, since the contrast to noise ratio was maximum at TR=0. The contrast to noise per unit time would be expected to be maximum at TR=0 as well, and in reality it is. Use of the derivative to find the maximum is inappropriate for this curve because of the singularity in the curve at TR=0.

2.6.3 T2-Weighted Contrast

The temperature dependence of T2 is slightly more complicated than that of T1 in physiologic systems because the T2 frequently has multiple components arising from the presence of protons in free and bound states. The fractions of water in the various bound and free states change with temperature while the characteristic T2 for each state also changes. This complicates the extraction of temperature data from T2 data. The data of Belton et al[11] demonstrates that over a certain temperature range the compartment fraction changes cause T2 to increase while the inherent temperature dependence would cause it to decrease. T2 weighted imaging would also be inappropriate for thermal treatment control applications because it tends to be slower than T1 weighted imaging and the loss of temporal resolution could be significant. However, Fast Spin Echo or RARE images can acquire T2-weighted images relatively rapidly compared to standard sequences and recent developments suggest that these techniques could eventually have sufficient temporal resolution where they

could be applied in this application.

2.6.4 Diffusion Weighted Contrast

The theoretical analysis earlier in this chapter centered on the inherent temperature dependence of the NMR contrast parameters. The discussion has considered the translational motion of molecules relative to each other. This concept is expanded to consider the effect of this motion, taking into account the finite duration of RF and gradient pulses in an NMR pulse sequence. Normally, molecular diffusion is considered a nuisance, but now pulse sequences have been designed to be sensitive to diffusion. The signal intensities of the images can be analyzed to yield the diffusion coefficient on a pixel-by-pixel basis. The known relationship between temperature and the diffusion coefficient can then be used to create a high resolution temperature map of the image.

2.6.4.1 Analysis

The diffusion weighted contrast would be maximized by taking the derivative of the diffusion term in the original contrast equation (Eqn. #45) with respect to b and setting it equal to zero.

$$\frac{\partial(-bS_0)}{\partial b} = \frac{\partial}{\partial b}\left(-bM_0\left(1 - e^{\frac{-TR}{T1}}\right)\left(e^{\frac{-TE}{T2}}\right)\left(e^{-bD}\right)\right) = 0 \qquad 2.55$$

$$= S_0(1 - bD) = 0 \qquad 2.56$$

So the maximum diffusion contrast is achieved when b=1/D. The value of b

that maximizes the contrast sets the signal intensity to e^{-1} times its maximum possible value, dictating that the maximum contrast occurs when the signal intensity is only at 39% of the maximum.

A diffusion sensitive pulse sequence decreases the signal of moving spins by dephasing them with large gradient pulse placed symmetrically around the 180° rephasing pulse. Normally the 180° pulse in the center of the sequence restores the phase coherency of the spins that is lost due to the static inhomogeneities of the B_0 field. A spin that moves along the direction of the applied gradient during the scan encounters a dynamic inhomogeneity which is not refocussed so its phase coherence is lost. The moving spins do not contribute their full value to the macroscopic signal so their pixel of origin is darker than it would be without the gradient pulses. The motion of the spins must be along the direction of the gradient to experience this signal loss. The signal attenuation is given by A=exp(-bD), where D is the diffusion coefficient and b is a function of the gradient strength and its duration.

The diffusion coefficient is determined by acquiring 2 images, each with a differently sized gradient pulse. The attenuation equation can be used to solve for the diffusion coefficient on a pixel-by-pixel basis,

$$D_{x,y} = \frac{\ln\left(\frac{S_{1\,x,y}}{S_{0\,x,y}}\right)}{(b_0 - b_1)} \qquad 2.57$$

where $S_{x,y}$ is the signal from a particular pixel and the only difference between the images is the size of gradient pulse used. The diffusion

coefficients are then used to extract temperature information via the relation $D \approx \exp(-E_a/KT)$ where E_a is the activation energy for translational diffusion, which is assumed to be independent of temperature. A temperature change map can then be determined with the relationship

$$T-T_0 = \frac{KT_0^2(D-D_0)}{E_a \quad D_0} \qquad 2.58$$

which assumes that the temperature change is small relative to the absolute temperature (a good assumption).

2.6.4.2 Literature Results

Bleier et al were the first to study the temperature sensitvity of diffusion in vivo with echo planar MR imaging[12]. Diffusion-sensitive MR images were acquired during laser irradiation of gel phantoms and rabbit brains in vivo. The laser exposures were 3W and 9W for 20 seconds in both the gelatin phantoms and the rabbit brains. The authors reported maximum contrast-to-noise ratios of 54 in the phantom images and 20 in the rabbit images. No temperature measurements were made.

LeBihan et al also conducted a study examining NMR imaging of diffusion and its relation to temperature.[13] Experiments were conducted by creating a temperature gradient across 10cm of gel of approximately 1°C/cm. The temperature determined by image analysis was compared to that measured with thermocouples and the temperature accuracy, as derived from the water self-diffusion coefficient accuracy, was determined

to be 0.5 °C. Experiments were also conducted with a clinical microwave hyperthermia device. A numerical value was not provided in the article, but the graph of measured and image derived temperatures indicated a maximum temperature error of approximately 1.2°C. These experiments suggest that diffusion sensitive imaging may provide the resolution and sensitivity required for non-invasive thermometry. However, a number of practical constraints may limit the use of diffusion-sensitive imaging in this application.

2.6.4.3 Practical Constraints

There are significant differences between diffusion in a gel and diffusion in tissue. One consideration is that diffusion in tissues is often restricted diffusion because the motion of the water molecules is constrained by the various membranes that separate the biological compartments. In this case there is an upper limit on the diffusion coefficient that can be measured with NMR. This appears as a false plateau in the diffusion-temperature relationship. This would lead to lower-than-actual calculated temperatures for regions that were at the highest temperatures. This is particularly dangerous for the thermal therapy control applications motivating this discussion. In addition, restricted diffusion may be strongly anisotropic. In striated muscle the molecular motion along the striations may not be limited, a similar situation could apply for diffusion along a nerve axon. In these cases the temperature-diffusion relationship would depend on the direction of the applied

gradient. If diffusion-sensitizing gradients were applied along the axis of the axon the temperature plateau would be reached at a much higher temperature than if it were applied perpendicular to the axis.

A different consideration is the presence of capillary and macroscopic flow in tissues. Capillary flow has been theorized to be similar to molecular diffusion and has been called macrodiffusion because it is effectively isotropic over the distances of interest. When present, it can produce very large effective diffusion coefficients which depend on capillary geometry and blood flow volume. However, there is a significant difference between the measured intra-voxel incoherent motion and "perfusion", arising from the classical definition of perfusion in terminal deposition or washout studies[14]. Macroscopic flow is different from diffusion because it is not random. Voxels with a variety of moving and non-moving spins will have decreased signal because of the phase incoherency of the moving spins. Flow in vessels can also cause artifacts which characteristically appear along the phase direction in the image. The thermal sensitivity of perfusion discussed in Section 1.4.3.3 also indicates that analysis of temperature changes by imaging the changes in flow would be problematic because of the complex relationship between temperature and flow.

REFERENCES

1 Abragam, A. *The principles of Nuclear Magnetism.* Oxford University Press, Oxford, U.K. 1961.

2 McConnell, J. *The Theory of Nuclear Magnetic Relaxation in Liquids.* Cambridge University Press, NY, NY. 1987

3 Schlichter CP, *Principles of Magnetic Resonance.* Springer-Verlag, NY, NY. 1980.

4 Bottomley PA, Foster TH, Argersinger RE, Pfeifer LM, A review of normal tissue hydrogen NMR relaxation times and relaxation mechanisms from 1-100 MHz: Dependence on tissue type, NMR frequency, temperature, species, excision, and age. *Med. Phys.* 11(4):425, July/August, 1984.

5 Parker DL, Applications of NMR imaging in hyperthermia: An evaluation of the potential for localized tissue heating and noninvasive temperature monitoring. *IEEE Trans. on Biomed. Eng.* BME-31(1):161, Jan 1984.

6 Parker DL, Smith V, Sheldon P, Crooks L, Fussell L, Temperature distribution measurements in two dimensional MR imaging. *Med. Phys.* 10(3):321, May/June 1983.

7 Dickinson RJ, Hall AS, Hind AJ, Young IR, Measurement of changes in tissue temperature using MR imaging. *J. of Comp. Asst. Tom.* 10(3):468, May/June 1986.

8 Fung BM, McGaughy TW. State of water in muscle as studied by pulsed NMR. *Biochim. Biophys. Acta.* 343(3):663-673, 1974.

9 Fung BM, Durham DL, Wassill DA. State of water in biological systems as studied by proton and deuterium relaxation. *Biochim. Biophys. Acta.* 399(1):191-202, 1975.

10 Koenig SH, Brown III RD, Adams D, Emerson D, Harrison CG, *I.B.M. Research Report* RC10116(No.44807), 1983.

11 Belton PS, Jackson RR, Packer KJ. Pulsed NMR studies of water in striated muscle. I. Transverse nuclear spin relaxation times and freezing effects. *Biochim. Biophys. Acta.* 286:16, 1972.

12 Bleier AR, Jolesz FA, Cohen MS, Weisskoff RM, Dalcanton JJ, Higuchi N, Feinberg DA, Rosen BR, McKinstry RC, Hushek SG. Real-time magnetic resonance imaging of laser heat deposition in tissue. *Magnetic Resonance in Medicine*, 21:132-137, 1991.

13 Le Bihan D, Delannoy J, Levin RL, Temperature mapping with MR imaging of molecular diffusion: Application to hyperthermia. *Radiology*, 171:853, 1989.

14 Henkelmen RM. Does IVIM measure classical perfusion? *Magnetic Resonance in Medicine.* 16:470-475, 1990.

Chapter 3 Phantom Experiments

3.1 Introduction

There is a clear need for a phantom material that can be used for quantitative studies of the physical processes involved in MR-guided laser thermal therapy procedures [1, 2]. Polyacrylamide gelatin is a phantom material whose optical and MR properties can be controlled independently by adding different dopants to the base gel[3]. This chapter describes the gels, delineates the temperature dependance of their MR properties, investigates the most effective imaging strategies for measuring temperature variations within this material and demonstrates how imaging can be used to determine thermal contours within a laser-irradiated gel.

3.2 Applications of Phantoms

3.2.1 Optical Phantoms

The use of gel phantoms for optical experiments is well established. Gelatin phantoms with photoactivable fluorophores have been used in the study of fluence distribution in turbid media[4]. The optical properties of the phantom were controlled by varying the concentrations of India ink (Faber-Castell Inc; Newark, NJ) and latex microspheres (Duke Scientific; Palo Alto, CA). The ink acts as an absorber while the difference between the optical density of the microspheres and the medium they are in, combined with the shape of the spheres, causes scattering of the laser light. Madsen et al have shown that India ink acts as a scatterer as well as an absorber[5], but its effect is relatively small compared to the effect of the microspheres and

is usually neglected.

3.2.2 MR Phantoms

Gelatin phantoms have also been used extensively in MRI to study both equipment performance and fundamental physical interactions. Agar gels have been used extensively because of their simplicity and cost advantages but polyacrylamide gels and other hydrogels have also been used because of their tissue-like water binding properties [6,7]. The two relevant MRI parameters, T1 and T2, are usually varied by adjusting the concentration of a paramagnetic dopant and the gel solid concentration. The paramagnetic dopants that are frequently used include $NiCl_2$, $MnCl_2$ and $CuCl_2$. Agar gel solutions are heated to approximately 40°C to dissolve the agar, which then polymerizes with cooling, while polyacrylamide gels use catalysts to promote the polymerization process. Polyacrylamide gels are frequently used in DNA electrophoresis studies, part of which involves drying the gel at approximately 80-90 °C. The high temperature can modify the behavior and content of the water within the gel but it does not cause the gel matrix to break apart. Thus, polyacrylamide gels are superior to agar for high temperature studies because they do not melt at temperatures less than 60 °C.

The behavior of the water molecules in the polyacrylamide gel as a function of temperature is unknown, so a comprehensive comparison between agar and polyacrylamide gels cannot be made at this time. Initial investigations of thermally sensitive MR imaging of

polyacrylamide gels have already been conducted[8]. The study demonstrated that modification of the acrylamide content to adjust the T2 of the material cannot be done without adversely affecting the transparency of the gel.

3.2.3 Thermal Therapy Phantoms

Other thermal therapy modalities have used polyacrylamide gel phantoms as well. An electromagnetic hyperthermia study controlled the material's electrical properties by the addition of salts [9,10]. Focussed ultrasound studies have used the gel as a target and controlled the acoustic impedance [11]. An MRI study of a gel phantom heated with focussed ultrasound clearly demonstrated the energy deposition pattern [12]. This thesis demonstrates that the MR and optical properties of the polyacrylamide gel can be adjusted indpendently and that the presence of the optical dopants does not degrade the thermal sensitivity or accuracy of the gel.

3.3 Methods

3.3.1 Gel Sample Preparation.

The polyacrylamide/agar combination was tested to determine if the high melting point property of the polyacrylamide could be synergistically combined with the T2 adjustment properties of the agar. A base gel solution (10% solid acrylamide by weight, an acrylamide:bisacrylamide ratio of 40:1 and an agar concentration of 3.75% by weight dissolved in distilled water) was heated until the agar solution became clear. The base solution of acrylamide and agar was

diluted with either an equivalent acrylamide solution, distilled water, and/or solutions of the dopants to achieve the intended range of optical and MR dopants concentrations. The final gel sample volume was 10 mL.

The agar solid component in the final gel samples varied from 0% to 3% by weight and the $CuCl_2$ concentration varied from 0 to 4 millimolar. Polyacrylamide gels normally require the catalysts ammonium persulfate (concentration 0.7%) and TEMED (concentration $3.5X10^{-2}$%) for polymerization. Preliminary tests showed that if the catalysts are added to the warm gel solution containing agar the polymerization proceeds at a rapid pace and generates a large amount of heat. The heat generates multiple small bubbles that are trapped in the gel by the rapid polymerization. The bubbles cause susceptibility artifacts throughout the gel because of the multiple water/air interfaces and also reduce the proton density in the gel, reducing the available MR signal. Thus, the samples cannot be used for the experiment.

3.3.2 MRI Experiments

The temperature dependence of the MR properties was determined by imaging the gels with a Signa 1.5T clinical MR imaging system (GE Medical Systems, Waukesha WI) while they were in a warm water bath. The gels were submerged in 60°C water, encased in an insulating styrofoam box and imaged while the system slowly cooled to approximately 30°C. Copper-constantin thermocouples were placed in a gel sample in the center of the cluster, a gel sample in the outer row of

gels and in the water to insure that the entire group of samples was at a uniform temperature. Temperature differences between these thermocouples never exceeded 0.6°C and the average temperature of all three was used as the measured temperature.

A 48 echo Carr-Purcell-Meiboom-Gill (CPMG) sequence with echo spacing of 18 msec was used to measure T2. An inversion-recovery (IR) sequence with 8 different inversion times was used to measure T1. In addition, several different types of Fast Spin Echo (FSE) pulse sequences that would be appropriate for thermal monitoring were tested to determine the explicit relationship between signal intensity and temperature for these sequences.

Average signal intensities from circular, homogeneous regions of interest (ROI's) were sampled with the ANALYZE software package (Mayo Foundation, Rochester MN). The CPMG signal intensities were fit to a mono-exponential decay curve with a constant term and the inversion recovery signal intensities were fit to a recovering exponential. The T1 and T2 of each gel sample were plotted as a function of temperature. The signal intensity as a function of temperature for the FSE sequences was also plotted and fit to a linear curve. The slope of the line was expressed as signal intensity change per °C (ΔSI/°C) to compare the temperature sensitivity of the different pulse sequences. An alternative parameter which can be used to compare the pulse sequences is the slope of the line divided by the magnitude of the signal at the lowest temperature, which is the percentage signal intensity change per °C (%ΔSI/°C). The accuracy, or "temperature uncertainty", of the different pulse sequences was evaluated by dividing the standard

deviation of the signal intensity from a region of interest by the ΔSI/°C to produce a temperature standard deviation ±°C [2]. All curve fitting was done with the CPLOT program (Certified Scientific Software Inc., Cambridge MA).

3.3.3 Thermal Contour Experiment

Bulk volume samples (approximately 120 mL) of two different gels were prepared to examine the ability of MRI to visualize thermal distributions in homogeneous media. The first sample had concentrations of 2.5% agar, 4 mmol $CuCl_2$ and 0.5% ink (a fairly high percentage of absorber). This is labelled the "absorber only" gel. The second sample had concentrations of 1.5% agar, 2 mmol $CuCl_2$, 0.5% ink and 1.5% scattering spheres (a fairly high percentage of scattering centers) and was labelled the "scatterer + absorber" gel. The bulk gels were each irradiated with a 1064nm Nd:YAG laser (Laserscope, San Jose CA) at 1.7W for 6 minutes with both a diffusing tip fiber (Dornier Med. Systems, Kennesaw GA) and a 600 micron core, bare tip fiber.

The gels were imaged with a T1-weighted FSE sequence with TR=300msec, TE=18msec, echo train length of 4 and total image acquisition time of 10 seconds with a 1 second delay between images. The sequence acquires an image of the same plane repeatedly, rendering a "dynamic" image of the plane of interest. A computer program communicated with the imager and synchronized the temperature measurement from the 3 thermocouple array to occur

between images. Signal intensities from a circular ROI at a position symmetric to each thermocouple were sampled, normalized to the signal intensity prior to the irradiation and divided by the %ΔSI/°C linear coefficient determined in the MRI experiment to produce image derived temperature changes. It was assumed that the entire gel volume was at a uniform temperature at the beginning of the experiment. The temperatures at the thermocouple locations were plotted as a function of time and were compared to the image-derived temperatures to evaluate the accuracy of the image-derived temperature changes.

3.4 Results

3.4.1 Pulse Sequence Experiment

The parameters of the five different fast spin echo (FSE) pulse sequences tested are listed in Table 3.1. Table 3.2 summarizes the temperature sensitivity and accuracy of the FSE pulse sequences for the twenty-five different gel samples tested. Again, the sensitivity of the pulse sequences was evaluated by measuring ΔSI/°C which was converted to %ΔSI/°C by dividing by the signal magnitude at 33°C. The %ΔSI/°C for 20°C was computed by extrapolating along the ΔSI/°C curve and dividing the ΔSI/°C by the projected signal magnitude at 20 °C.

Table 3.3 displays the temperature accuracy of the different pulse sequences with the data in chart form to facilitate comparison of pulse sequences and dopant concentration. Table 3.4 displays the projected temperature sensitivity of the different pulse sequences at 20 °C with the data in chart form to facilitate comparison of pulse sequences and

dopant concentration. Table 3.5 compares the temperature sensitivity and accuracy of samples with and without optical dopants. The values for the samples with optical dopants are listed below the values for the samples without optical dopants. The slopes of the T1 and T2 vs temperature curves for all the samples are listed in Tables 3.6 and 3.7, according to $CuCl_2$ concentration and agar concentration. The values for gel samples with both MR and optical dopants are in parentheses next to the equivalent gels that do not contain optical dopants.

Table 3.1 Pulse sequence parameters of various pulse sequences.

Pulse Sequence	TR	TE	ETL	T_{tot}
FSE1	100	18	4	3
FSE2	300	18	4	10
FSE3	300	18	8	5
FSE4	500	18	4	16
FSE5	500	18	8	8

TR is the repetition time. TE is the effective echo time. T_{tot} is the total time required to acquire an image, in seconds. ETL is echo train length, the number of data acquisitions per 90° pulse.

Table 3.2. Thermal sensitivity and accuracy of MR imaging of gel phantoms. Sample size was 10 mL. Column 1 is the agar concentration (% by weight). Column 2 is the $CuCl_2$ concentration (mmol). Column 3 is the number of the FSE pulse sequence used (See Table 3.1 for imaging parameters.) Column 4 is the temperature sensitivity of the pulse sequence measured in absolute signal intensity units, i.e. the slope of the signal intensity-temperature curve as determined by the fitting program. Column 5 is the temperature accuracy (°C) determined by dividing the signal intensity -temperature slope by the standard deviation of the signal intensity. Column 6 is the temperature sensitivity of the pulse sequence measured in percentage signal intensity units, i.e. the slope of the signal intensity-temperature curve as determined by the fitting program divided by the signal magnitude at 33°C. Column 7 is the projected temperature sensitivity of the pulse sequence measured in percentage signal intensity units, i.e. the slope of the signal intensity - temperature curve as determined by the fitting program divided by the projected signal magnitude at 20°C.

[agar]	[$CuCl_2$]	FSE#	ΔSI/°C	°C(+/-)	%ΔSI/°C@20°C	%ΔSI/°C@33°C
1	0	1	-0.23	-79.3	-0.56%	-0.60%
1	0	2	-3.53	-5.7	-1.56%	-1.95%
1	0	3	-2.54	-7.6	-1.65%	-2.11%
1	0	4	-6.05	-3.4	-1.54%	-1.93%
1	0	5	-5	-3.2	-1.57%	-1.97%
1	1	1	-1.28	-13.0	-1.21%	-1.44%
1	1	2	-9.49	-2.9	-1.49%	-1.85%
1	1	3	-6.6	-3.2	-1.53%	-1.91%
1	1	4	-15.1	-2.5	-1.47%	-1.82%
1	1	5	-12.9	-2.2	-1.50%	-1.86%
1	2	1	-2.65	-8.4	-1.42%	-1.75%
1	2	2	-13.86	-2.7	-1.44%	-1.77%
1	2	3	-9.15	-2.0	-1.40%	-1.71%
1	2	4	-18.69	-2.1	-1.32%	-1.59%
1	2	5	-17.05	-2.0	-1.37%	-1.67%
1	3	1	-3.2	-5.6	-1.46%	-1.80%
1	3	2	-15.52	-1.9	-1.38%	-1.68%
1	3	3	-11.16	-2.5	-1.40%	-1.71%
1	3	4	-19.55	-2.0	-1.23%	-1.47%
1	3	5	-17.68	-1.8	-1.26%	-1.51%
1	4	1	-3.38	-6.5	-1.33%	-1.61%
1	4	2	-16.27	-2.3	-1.30%	-1.57%
1	4	3	-12.73	-2.0	-1.38%	-1.69%
1	4	4	-18.75	-2.4	-1.12%	-1.31%
1	4	5	-17.55	-1.9	-1.17%	-1.38%
1.5	0	1	-0.54	-30.9	-1.19%	-1.41%
1.5	0	2	-3.48	-5.9	-1.59%	-2.00%
1.5	0	3	-2.74	-6.5	-1.75%	-2.26%
1.5	0	4	-5.91	-2.9	-1.53%	-1.91%
1.5	0	5	-5	-3.1	-1.59%	-2.01%
1.5	1	1	-0.99	-16.0	-1.06%	-1.23%
1.5	1	2	-8.98	-2.5	-1.46%	-1.80%
1.5	1	3	-6.07	-3.5	-1.47%	-1.82%
1.5	1	4	-13.78	-2.1	-1.39%	-1.70%
1.5	1	5	-12.04	-2.2	-1.44%	-1.77%
1.5	2	1	-1.99	-12.7	-1.23%	-1.47%
1.5	2	2	-12.71	-2.4	-1.38%	-1.68%
1.5	2	3	-8.51	-2.7	-1.35%	-1.64%
1.5	2	4	-16.77	-2.3	-1.24%	-1.47%
1.5	2	5	-15.42	-2.7	-1.29%	-1.55%
1.5	3	1	-2.38	-10.3	-1.25%	-1.49%
1.5	3	2	-14.56	-2.2	-1.35%	-1.64%
1.5	3	3	-10.26	-2.3	-1.35%	-1.64%
1.5	3	4	-17.58	-2.0	-1.17%	-1.37%
1.5	3	5	-16.01	-2.0	-1.20%	-1.42%
1.5	4	1	-3.21	-5.3	-1.36%	-1.65%
1.5	4	2	-14.95	-2.7	-1.25%	-1.49%
1.5	4	3	-11.41	-2.6	-1.29%	-1.55%

1.5	4	4	-16.03	-2.9	-1.01%	-1.17%
1.5	4	5	-15.35	-3.4	-1.07%	-1.25%
2	0	1	-1.12	-19.2	-1.79%	-2.33%
2	0	2	-3.32	-7.2	-1.51%	-1.88%
2	0	3	-1.21	-21.2	-1.07%	-1.25%
2	0	4	-5.1	-4.1	-1.39%	-1.69%
2	0	5	-3.68	-5.5	-1.34%	-1.63%
2	1	1	-1.15	-20.3	-1.22%	-1.45%
2	1	2	-8.23	-3.7	-1.43%	-1.76%
2	1	3	-5.59	-4.9	-1.43%	-1.75%
2	1	4	-12.46	-2.4	-1.35%	-1.64%
2	1	5	-10.74	-2.8	-1.38%	-1.68%
2	2	1	-2.71	-12.8	-1.58%	-1.98%
2	2	2	-11.7	-3.5	-1.35%	-1.64%
2	2	3	-8.98	-4.0	-1.42%	-1.73%
2	2	4	-15.58	-2.8	-1.21%	-1.44%
2	2	5	-14.29	-3.1	-1.26%	-1.51%
2	3	1	-3.71	-7.8	-1.58%	-1.99%
2	3	2	-13.35	-2.7	-1.25%	-1.49%
2	3	3	-10.52	-3.3	-1.32%	-1.59%
2	3	4	-15.1	-2.4	-1.03%	-1.19%
2	3	5	-14.92	-2.2	-1.12%	-1.31%
2	4	1	-3.49	-8.7	-1.37%	-1.67%
2	4	2	-13.96	-2.1	-1.17%	-1.38%
2	4	3	-11.24	-3.2	-1.23%	-1.46%
2	4	4	-14.02	-2.4	-0.91%	-1.04%
2	4	5	-13.77	-3.3	-0.98%	-1.12%
2.5	0	1	-0.8	-21.5	-1.70%	-2.19%
2.5	0	2	-2.78	-8.2	-1.34%	-1.62%
2.5	0	3	-1.48	-15.4	-1.22%	-1.45%
2.5	0	4	-4.8	-5.1	-1.33%	-1.61%
2.5	0	5	-3.99	-4.7	-1.38%	-1.68%
2.5	1	1	-1.11	-14.9	-1.43%	-1.75%
2.5	1	2	-7.7	-2.9	-1.51%	-1.87%
2.5	1	3	-4.19	-5.2	-1.36%	-1.64%
2.5	1	4	-11.47	-2.6	-1.40%	-1.71%
2.5	1	5	-9.62	-2.6	-1.42%	-1.74%
2.5	2	1	-1.95	-15.9	-1.50%	-1.86%
2.5	2	2	-11.52	-3.0	-1.50%	-1.87%
2.5	2	3	-7.99	-3.2	-1.51%	-1.88%
2.5	2	4	-15.25	-2.2	-1.33%	-1.61%
2.5	2	5	-14	-2.3	-1.40%	-1.72%
2.5	3	1	-2.57	-11.3	-1.42%	-1.73%
2.5	3	2	-13.22	-2.6	-1.33%	-1.61%
2.5	3	3	-9.39	-5.3	-1.35%	-1.64%
2.5	3	4	-14.83	-2.7	-1.09%	-1.27%
2.5	3	5	-14.25	-3.1	-1.17%	-1.38%
2.5	4	1	-2.96	-10.0	-1.37%	-1.67%
2.5	4	2	-13.88	-3.0	-1.26%	-1.51%
2.5	4	3	-11.4	-4.8	-1.38%	-1.68%
2.5	4	4	-14.41	-3.4	-1.00%	-1.15%

2.5	4	5	-14.28	-3.5	-1.09%	-1.27%
3	0	1	-0.36	-62.0	-0.96%	-1.09%
3	0	2	-2.87	-7.0	-1.33%	-1.61%
3	0	3	-2.22	-12.1	-1.51%	-1.87%
3	0	4	-5.02	-4.1	-1.34%	-1.62%
3	0	5	-4.12	-5.7	-1.40%	-1.71%
3	1	1	-0.89	-16.3	-1.30%	-1.56%
3	1	2	-6.92	-3.4	-1.53%	-1.90%
3	1	3	-4.22	-6.2	-1.56%	-1.96%
3	1	4	-11.11	-2.9	-1.49%	-1.84%
3	1	5	-9.33	-2.4	-1.54%	-1.93%
3	2	1	-1.76	-13.8	-1.52%	-1.90%
3	2	2	-11.64	-2.5	-1.69%	-2.17%
3	2	3	-7.61	-2.9	-1.71%	-2.20%
3	2	4	-16.48	-2.1	-1.56%	-1.96%
3	2	5	-14.69	-2.1	-1.63%	-2.06%
3	3	1	-2.83	-9.8	-1.84%	-2.43%
3	3	2	-12.83	-2.3	-1.57%	-1.98%
3	3	3	-9.15	-3.3	-1.65%	-2.11%
3	3	4	-17.03	-2.0	-1.42%	-1.73%
3	3	5	-15.53	-3.1	-1.48%	-1.84%
3	4	1	-2.77	-6.7	-1.28%	-1.53%
3	4	2	-13.55	-2.6	-1.21%	-1.43%
3	4	3	-10.2	-2.8	-1.26%	-1.51%
3	4	4	-13.45	-2.7	-0.93%	-1.06%
3	4	5	-13.04	-2.5	-1.00%	-1.15%

Table 3.3 Thermal accuracy of MR imaging of gel samples. Sample size was 10 mL. Column 1 is the $CuCl_2$ concentration (mmol). Column 2 is the number of the FSE pulse sequence used (See Table 3.1 for imaging parameters.) Row 1 is the agar concentration (% by weight) for columns 3-7.

[$CuCl_2$]	FSE#	[agar]				
		1	1.5	2	2.5	3
0	1	-79.3	-30.9	-19.2	-21.5	-62.0
0	2	-5.7	-5.9	-7.2	-8.2	-7.0
0	3	-7.6	-6.5	-21.2	-15.4	-12.1
0	4	-3.4	-2.9	-4.1	-5.1	-4.1
0	5	-3.2	-3.1	-5.5	-4.7	-5.7
1	1	-13.0	-16.0	-20.3	-14.9	-16.3
1	2	-2.9	-2.5	-3.7	-2.9	-3.4
1	3	-3.2	-3.5	-4.9	-5.2	-6.2
1	4	-2.5	-2.1	-2.4	-2.6	-2.9
1	5	-2.2	-2.2	-2.8	-2.6	-2.4
2	1	-8.4	-12.7	-12.8	-15.9	-13.8
2	2	-2.7	-2.4	-3.5	-3.0	-2.5
2	3	-2.0	-2.7	-4.0	-3.2	-2.9
2	4	-2.1	-2.3	-2.8	-2.2	-2.1
2	5	-2.0	-2.7	-3.1	-2.3	-2.1

3	1	-5.6	-10.3	-7.8	-11.3	-9.8
3	2	-1.9	-2.2	-2.7	-2.6	-2.3
3	3	-2.5	-2.3	-3.3	-5.3	-3.3
3	4	-2.0	-2.0	-2.4	-2.7	-2.0
3	5	-1.8	-2.0	-2.2	-3.1	-3.1
4	1	-6.5	-5.3	-8.7	-10.0	-6.7
4	2	-2.3	-2.7	-2.1	-3.0	-2.6
4	3	-2.0	-2.6	-3.2	-4.8	-2.8
4	4	-2.4	-2.9	-2.4	-3.4	-2.7
4	5	-1.9	-3.4	-3.3	-3.5	-2.5

Table 3.4 Thermal sensitivity of MR imaging of gel samples as measured by percentage change in signal intensity per degree Celsius projected to the value at 20 °C. Sample size was 10 mL. Column 1 is the $CuCl_2$ concentration (mmol). Column 2 is the number of the FSE pulse sequence used (See Table 3.1 for imaging parameters.) Row 1 is the agar concentration (% by weight) for columns 3-7.

$CuCl_2$	PSD#	[agar]				
		1	1.5	2	2.5	3
0	1	-0.56%	-1.19%	-1.79%	-1.70%	-0.96%
0	2	-1.56%	-1.59%	-1.51%	-1.34%	-1.33%
0	3	-1.65%	-1.75%	-1.07%	-1.22%	-1.51%
0	4	-1.54%	-1.53%	-1.39%	-1.33%	-1.34%
0	5	-1.57%	-1.59%	-1.34%	-1.38%	-1.40%
1	1	-1.21%	-1.06%	-1.22%	-1.43%	-1.30%
1	2	-1.49%	-1.46%	-1.43%	-1.51%	-1.53%
1	3	-1.53%	-1.47%	-1.43%	-1.36%	-1.56%
1	4	-1.47%	-1.39%	-1.35%	-1.40%	-1.49%
1	5	-1.50%	-1.44%	-1.38%	-1.42%	-1.54%
2	1	-1.42%	-1.23%	-1.58%	-1.50%	-1.52%
2	2	-1.44%	-1.38%	-1.35%	-1.50%	-1.69%
2	3	-1.40%	-1.35%	-1.42%	-1.51%	-1.71%
2	4	-1.32%	-1.24%	-1.21%	-1.33%	-1.56%
2	5	-1.37%	-1.29%	-1.26%	-1.40%	-1.63%
3	1	-1.46%	-1.25%	-1.58%	-1.42%	-1.84%
3	2	-1.38%	-1.35%	-1.25%	-1.33%	-1.57%
3	3	-1.40%	-1.35%	-1.32%	-1.35%	-1.65%
3	4	-1.23%	-1.17%	-1.03%	-1.09%	-1.42%
3	5	-1.26%	-1.20%	-1.12%	-1.17%	-1.48%
4	1	-1.33%	-1.36%	-1.37%	-1.37%	-1.28%
4	2	-1.30%	-1.25%	-1.17%	-1.26%	-1.21%
4	3	-1.38%	-1.29%	-1.23%	-1.38%	-1.26%
4	4	-1.12%	-1.01%	-0.91%	-1.00%	-0.93%
4	5	-1.17%	-1.07%	-0.98%	-1.09%	-1.00%

Table 3.5. Thermal sensitivity and accuracy of MR imaging of gel phantoms with and without optical dopants. Sample size was 10 mL. Data for gels without optical dopants is above data for optically-doped samples. Column 1 is the agar concentration (% by weight). Column 2

is the CuCl concentration (mmol). Column 3 is the number of the FSE pulse sequence used (See Table 3.1 for imaging parameters.) Column 4 is the temperature sensitivity of the pulse sequence measured in absolute signal intensity units, the slope of the signal intensity - temperature curve as determined by the fitting program. Column 5 is the temperature accuracy (°C) determined by dividing the signal intensity-temperature slope by the standard deviation of the signal intensity. Column 6 is the temperature sensitivity of the pulse sequence measured in percentage signal intensity units, the slope of the signal intensity-temperature curve as determined by the fitting program divided by the signal magnitude at 33°C. Column 7 is the temperature sensitivity of the pulse sequence measured in percentage signal intensity units, the slope of the signal intensity-temperature curve as determined by the fitting program divided by the projected signal magnitude at 20°C.

[agar]	[$CuCl_2$]	FSE#	ΔSI/°C	°C(+/-)	%ΔSI/°C@20	%ΔSI/°C@33
Optical dopant concentration in doped sample: 0.3% ink, 0.75% scatterers						
1	1	1	-1.28	-13	-0.0121	-0.0144
1	1	1	-1.14	-10.5	-0.0107	-0.0125
1	1	2	-9.49	-2.9	-0.0149	-0.0185
1	1	2	-9.58	-3.4	-0.0157	-0.0198
1	1	3	-6.6	-3.2	-0.0153	-0.0191
1	1	3	-5.36	-3.5	-0.0142	-0.0175
1	1	4	-15.1	-2.5	-0.0147	-0.0182
1	1	4	-14.62	-3.2	-0.0153	-0.0191
1	1	5	-12.9	-2.2	-0.015	-0.0186
1	1	5	-11.96	-2.7	-0.0153	-0.0191
Optical dopant concentration in doped sample: 0.5% ink, 1.5% scatterers						
1.5	2	1	-1.99	-12.7	-0.0123	-0.0147
1.5	2	1	-2.05	-8.8	-0.0134	-0.0162
1.5	2	2	-12.71	-2.4	-0.0138	-0.0168
1.5	2	2	-12.86	-3.2	-0.0153	-0.0191
1.5	2	3	-8.51	-2.7	-0.0135	-0.0164
1.5	2	3	-7.92	-4.8	-0.0144	-0.0177
1.5	2	4	-16.77	-2.3	-0.0124	-0.0147
1.5	2	4	-17.14	-2.3	-0.0142	-0.0173
1.5	2	5	-15.42	-2.7	-0.0129	-0.0155
1.5	2	5	-14.34	-2.9	-0.0141	-0.0172

Optical dopant concentration in doped sample: 0.5% ink, 0% scatterers

2.5	4	1	-2.96	-10	-0.0137	-0.0167
2.5	4	1	-3.14	-5.9	-0.0127	-0.0152
2.5	4	2	-13.88	-3	-0.0126	-0.0151
2.5	4	2	-15.14	-2	-0.0125	-0.0149
2.5	4	3	-11.4	-4.8	-0.0138	-0.0168
2.5	4	3	-10.83	-2.8	-0.0125	-0.0149
2.5	4	4	-14.41	-3.4	-0.01	-0.0115
2.5	4	4	-15.31	-2.3	-0.01	-0.0115
2.5	4	5	-14.28	-3.5	-0.0109	-0.0127
2.5	4	5	-14.35	-2.9	-0.0104	-0.0121

Optical dopant concentration in doped sample: 0.1% ink, 0.25% scatterers

2	3	1	-3.71	-7.8	-0.0158	-0.0199
2	3	1	-3.2	-5.6	-0.0145	-0.0178
2	3	2	-13.35	-2.7	-0.0125	-0.0149
2	3	2	-15.08	-2.7	-0.0136	-0.0165
2	3	3	-10.52	-3.3	-0.0132	-0.0159
2	3	3	-10.13	-3.1	-0.0132	-0.0159
2	3	4	-15.1	-2.4	-0.0103	-0.0119
2	3	4	-17.13	-3.2	-0.0115	-0.0135
2	3	5	-14.92	-2.2	-0.0112	-0.0131
2	3	5	-15.8	-2.8	-0.0119	-0.0141

Optical dopant concentration in doped sample: 0.4% ink, 1.0% scatterers

3	4	1	-2.77	-6.7	-0.0128	-0.0153
3	4	1	-3.39	-7.1	-0.0136	-0.0165
3	4	2	-13.55	-2.6	-0.0121	-0.0143
3	4	2	-14.54	-2.9	-0.0123	-0.0147
3	4	3	-10.2	-2.8	-0.0126	-0.0151
3	4	3	-11.22	-3.1	-0.0129	-0.0155
3	4	4	-13.45	-2.7	-0.0093	-0.0106
3	4	4	-13.6	-3.3	-0.0094	-0.0108
3	4	5	-13.04	-2.5	-0.01	-0.0115
3	4	5	-13.19	-4	-0.0101	-0.0116

Table 3.6. Thermal sensitivity of T1 and percentage change of T1 per °C as a function of agar concentration and $CuCl_2$ concentration. Agar concentration ranges from 1% to 3% by weight. $CuCl_2$ concentration ranges from 0 to 4 mmol. Sample size was 10 mL. T1 evaluated with an inversion-recovery imaging sequence with 8 different TI values. Signal intensities fit to a recovering exponential SI = A - B*exp(-TI/T1). Curve fitting done with the CPLOT software package. The ERR code indicates that the T1 curve fitting was not successful for these samples.

Table 3.6A. Magnitude of T1 change per °C (milliseconds).

	[$CuCl_2$]				
	0	1	2	3	4
1	ERR	34.6 (37.4)	15.0	10.5	7.6

	1.5	ERR	29.3	14.4 (12.3)	10.9	7.9 (7.3)
[Agar]	2	0.0300	31.7	14.7	9.2 (9.3)	7.2
	2.5	-150.0	31.2 (48)	19.0	11.0	8.5 (7.2)
	3	104.0	40.6	42.5	21.1	7.7 (6.2)

Table 3.6B. Percentage change in T1 per °C, referenced to the T1 value measured at 31 °C at the end of the experiment.

		[$CuCl_2$]				
		0	1	2	3	4
	1	ERR	3.9 (4.7)	3.2	3.0	2.7
	1.5	ERR	3.4	3.1 (2.8)	3.1	2.9
[Agar]	2	0.7	3.8	3.3	3.0 (2.8)	2.9
	2.5	-4.1	3.4 (6.3)	3.8	3.3	3.2 (3.2)
	3	3.0	3.7	7.0	4.6	3.1 (3.1)

Table 3.7. Thermal sensitivity of T2 and percentage change of T2 per °C as a function of agar concentration and $CuCl_2$ concentration. Agar concentration ranges from 1% to 3% by weight. $CuCl_2$ concentration ranges from 0 to 4 mmol. Sample size was 10 mL. T2 evaluated with a 48 echo CPMG imaging sequence with 18msec echo spacing and first four echoes removed. Signal intensities fit to a mono-exponential: SI = A *exp(-TE/T2) + C. Curve fitting done with the CPLOT software package.

Table 3.7A. Magnitude of T2 change per °C (milliseconds).

		[$CuCl_2$]				
		0	1	2	3	4
	1	-2.2	4.9 (4.7)	3.8	3.2	2.8
	1.5	-0.7	4.4	3.5 (4.0)	2.9	2.5 (2.6)
[Agar]	2	0.0	3.7	3.3	2.4 (2.7)	1.7
	2.5	0.4	3.3 (2.9)	2.8	2.5	2.1 (2.3)
	3	0.6	3.2	2.9	2.8	1.9 (2.0)

Table 3.7B. Percentage change in T2 per °C, referenced to the T2 value measured at 31 °C at the end of the experiment.

		[$CuCl_2$]				
		0	1	2	3	4
	1	-0.9	2.6 (2.3)	2.4	2.4	2.7
	1.5	-0.4	2.9	2.8 (2.9)	2.7	2.5 (2.6)
[Agar]	2	-0.1	2.9	3.0	2.5 (2.7)	2.0
	2.5	0.3	3.1 (2.6)	3.0	3.0	2.4 (2.7)
	3	0.6	3.2	3.2	3.2	2.6 (2.5)

3.4.2 Thermal Contour Experiment

Imaging of the laser irradiation of the bulk gel samples produced temperature contours that graphically demonstrate the optical properties of the sample, the output pattern of the irradiating device and the thermal behavior of the material. The gel samples containing scatterers had broader, more diffuse temperature zones indicating significant optical scattering and widely distributed absorption. The gels without scatterers had distinct, sharp-edged, closely-spaced temperature zones that closely matched the output pattern of the fiber and indicated uniform thermal gradients. In the case of the diffusing tip fiber the iso-effect zone was peaked farther forward for the scatterer+absorber gel than for the absorber-only gel. In the case of the bare tip fiber, the heated zone was more spherical for the scatterer+absorber gel than for the absorber-only gel.

Figures 3.1, 3.3, 3.8 and 3.10 compare the measured and image-derived temperatures from the thermal contour experiment. For the experiment in which a bare tip fiber irradiated a gel containing only absorbers, the image derived temperatures match measured temperatures within 4.2 °C if the large errors due to the hysteresis in the heating portion of the proximal thermocouple are neglected (maximum error = 9.2°C including hysteresis). The image derived temperatures are higher than the measured temperatures in the bare tip fiber irradiation of the gel with absorbers and scatterers as well as in the diffusing tip fiber irradiation of both the gel with absorbers only and the gel with absorbers and scatterers. In all cases the shapes of the measured and image derived curves are very similar. The magnitude of

the temperature measurement error and the variability of the error depend on the gel and the type of optical fiber used.

The signal intensity as a function of temperature for all four thermal contour experiments is presented in Figures 3.2, 3.4-3.7, 3.9 and 3.11. In the case of the bare tip fiber irradiation of the gel containing scatterers and absorbers, the error bars were removed from the graph in Figure 3.4 to facilitate display of the very densely packed data. The individual thermocouple data with the error bars was graphed separately in Figures 3.5-3.7.

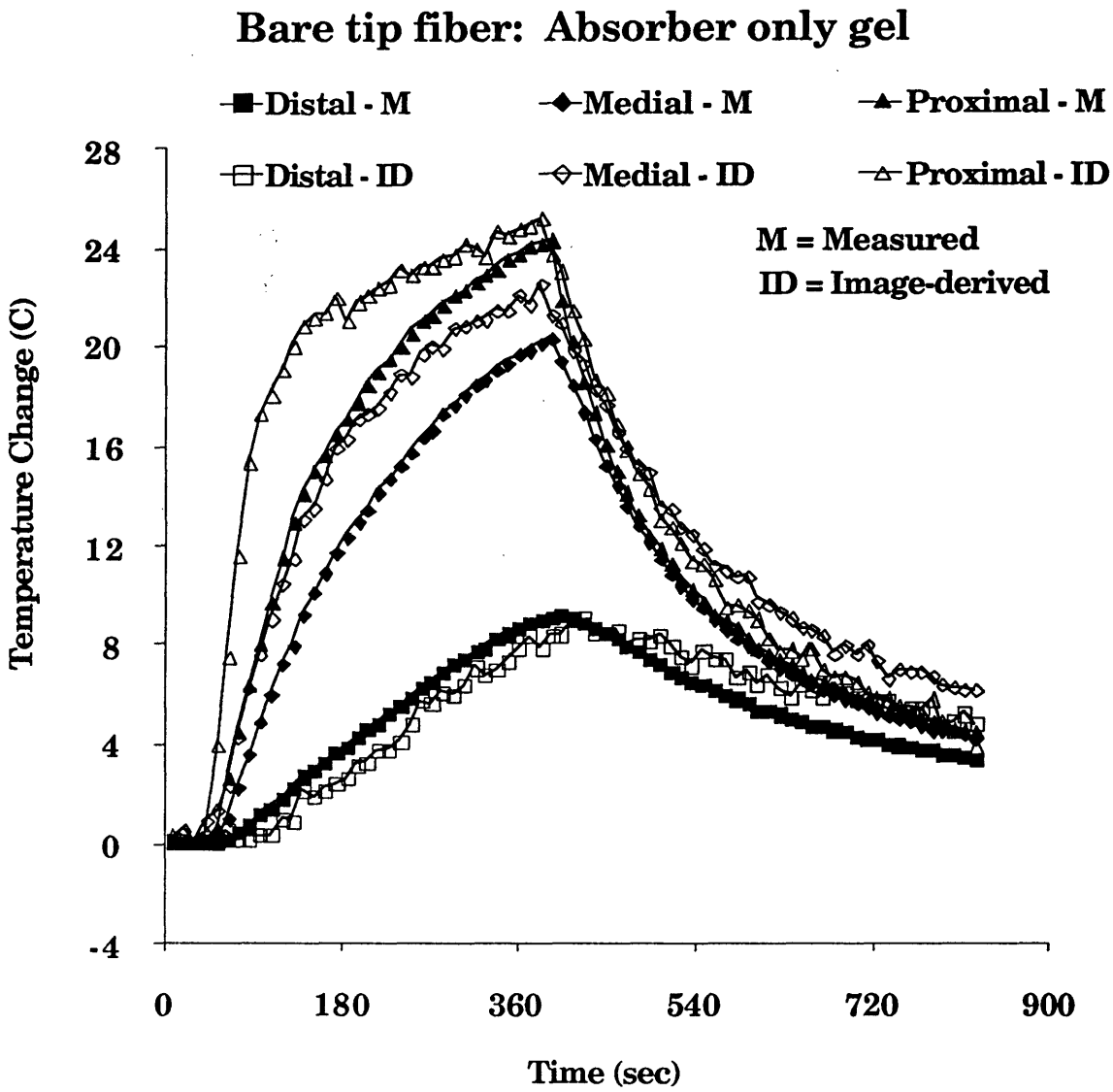

Figure 3.1 Plot of measured and image-derived temperatures at three locations for bare tip fiber laser irradiation of a gel containing absorbers only. Notice good agreement between measured and image-derived temperatures.

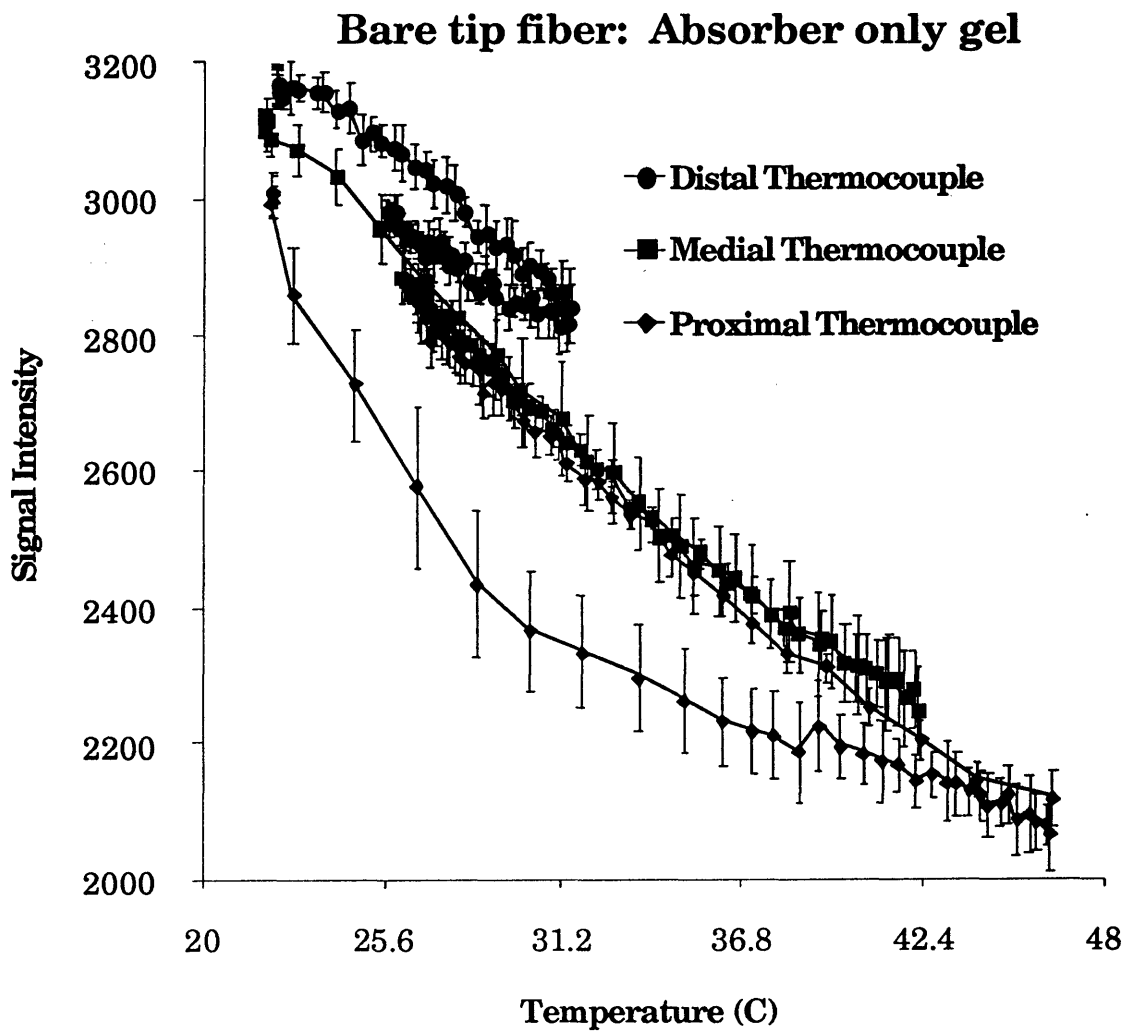

Figure 3.2 Plot of signal intensity versus temperature for bare tip fiber laser irradiation of gel containing absorbers only. Noticable hysteresis in proximal and distal thermocouple data. Cooling portion of proximal curve matches very well with medial curve. Slope of medial curve is 1.31 %ΔSI/°C.

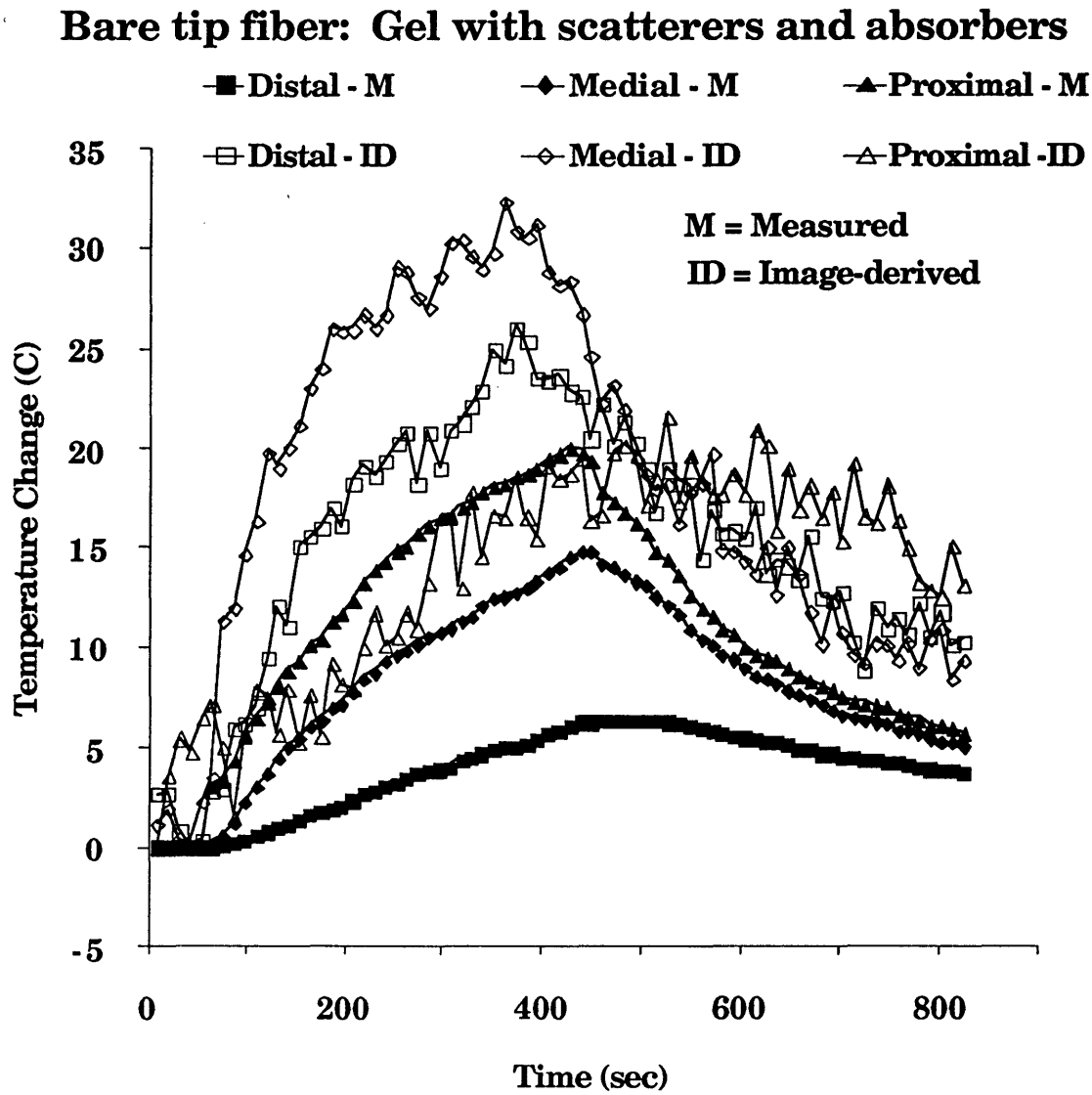

Figure 3.3 Plot of measured and image-derived temperatures at three locations for bare tip fiber laser irradiation of a gel containing scatterers and absorbers. Notice significant variations in image-derived temperature due to image noise and consistent over-estimation of temperature.

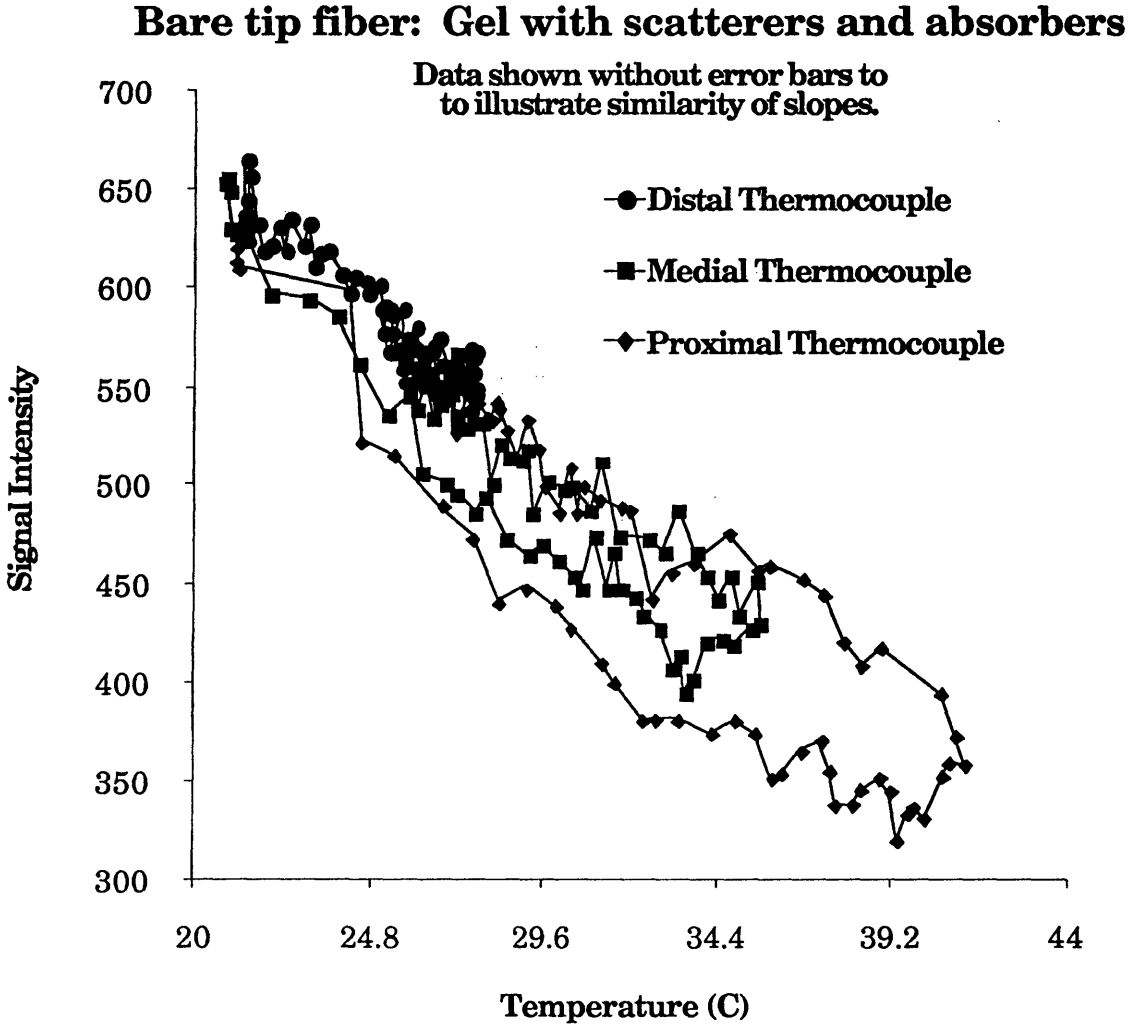

Figure 3.4 Plot of signal intensity versus temperature at three locations for bare tip fiber laser irradiation of gel containing absorbers and scatterers. Some hysteresis in proximal and medial thermocouple data. Average slope of all three thermocouples is 2.25 %ΔSI/°C.

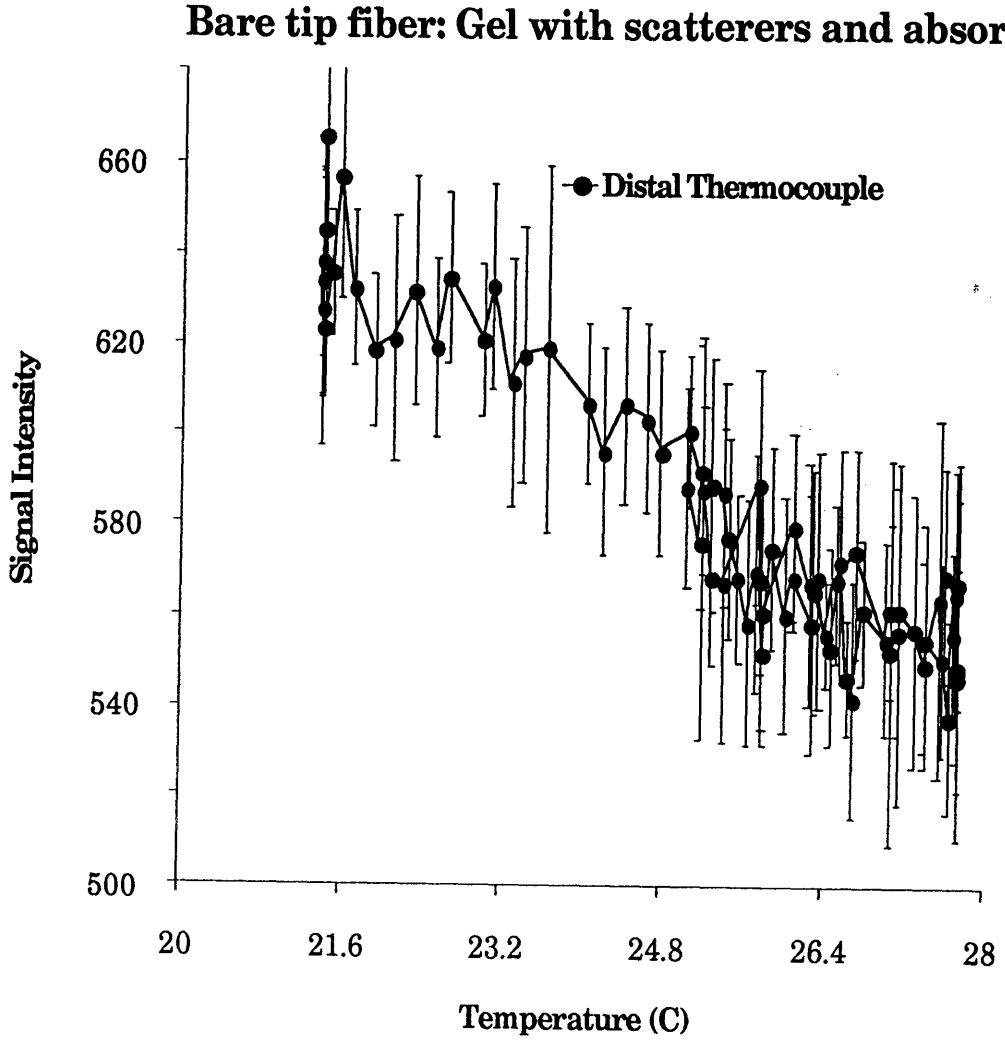

Figure 3.5 Plot of signal intensity versus temperature, distal location, for bare tip fiber laser irradiation of gel containing absorbers and scatterers, shown with error bars. Cooling data demonstrates that temperature sampling ended before sample returned to pre-irradiation temperature.

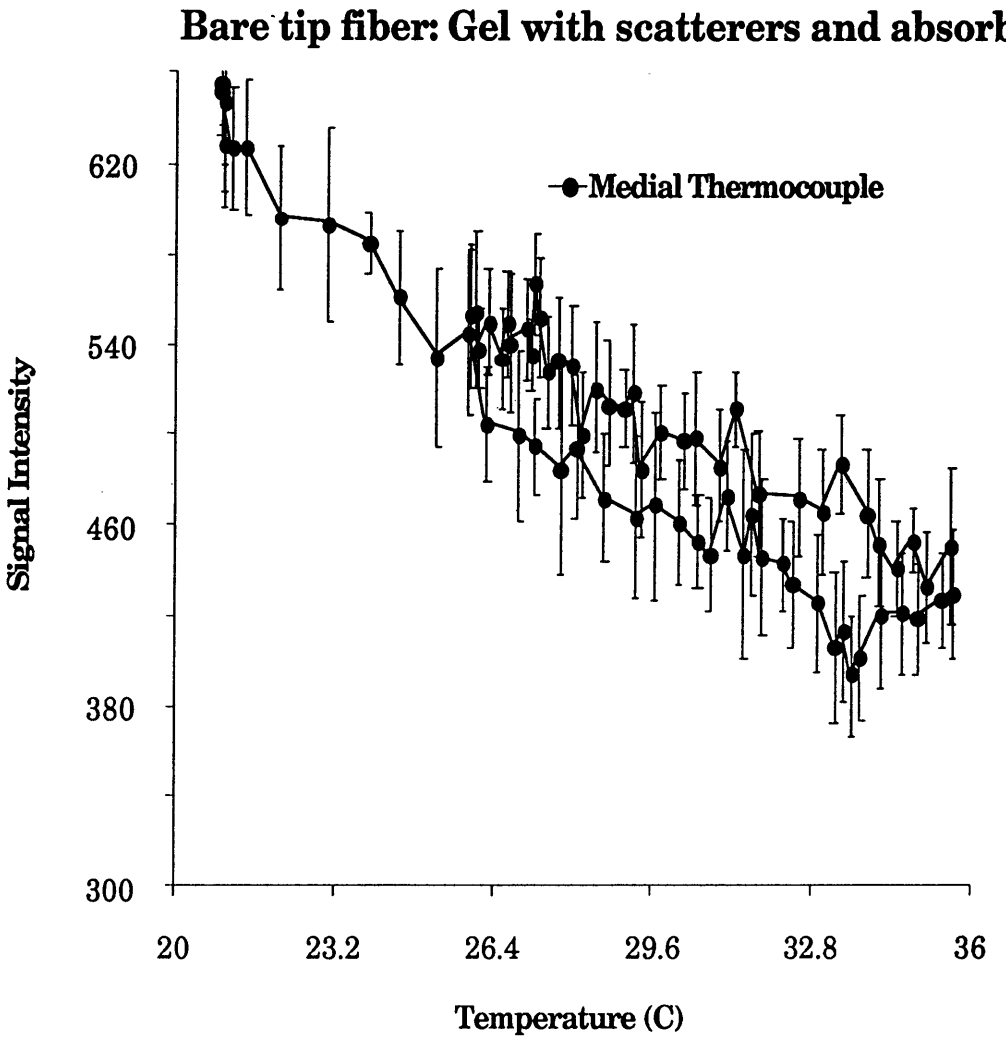

Figure 3.6 Plot of signal intensity versus temperature, medial location, for bare tip fiber laser irradiation of gel containing absorbers and scatterers, shown with error bars. Heating portion of curve is below cooling portion. Greater sample density at end of cooling curve demonstrates rate of temperature change.

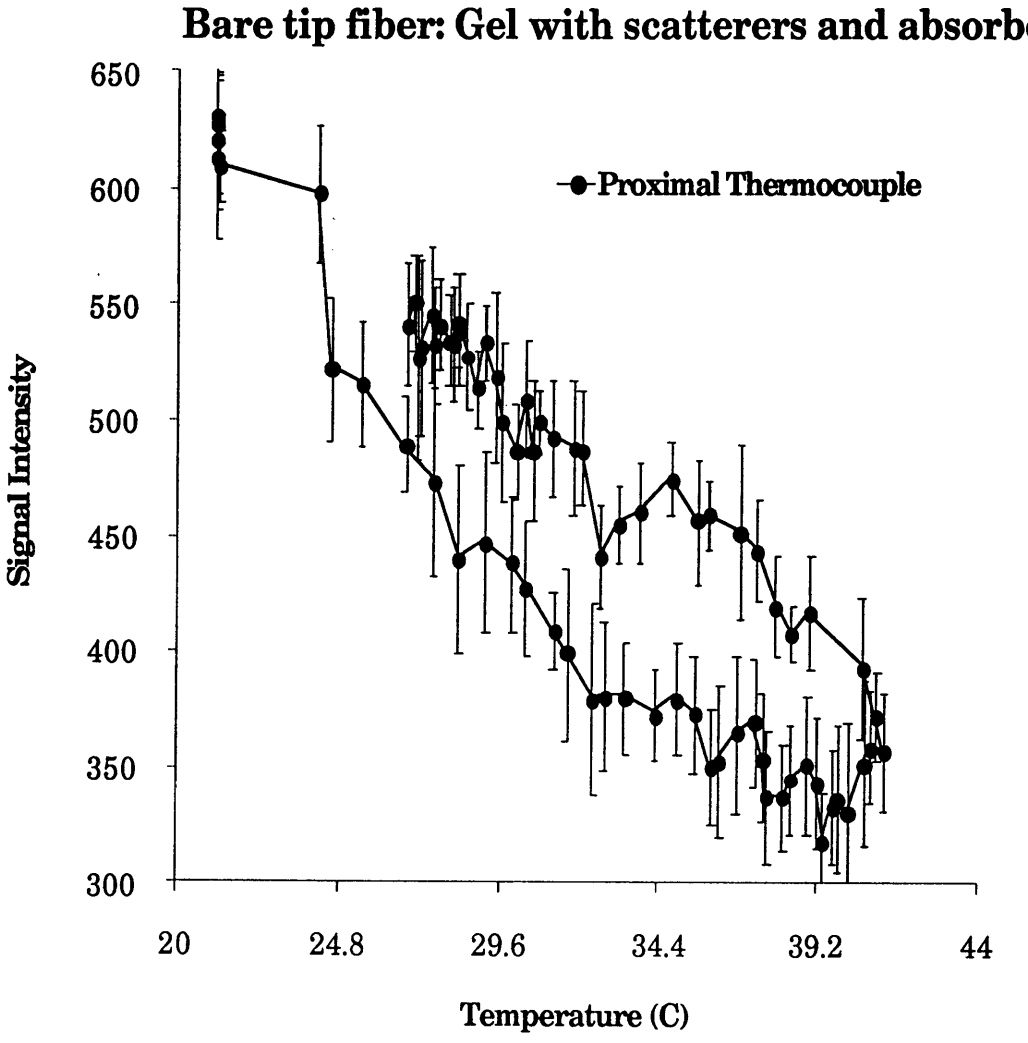

Figure 3.7 Plot of signal intensity versus temperature, proximal location, for bare tip fiber laser irradiation of gel containing absorbers and scatterers, shown with error bars..

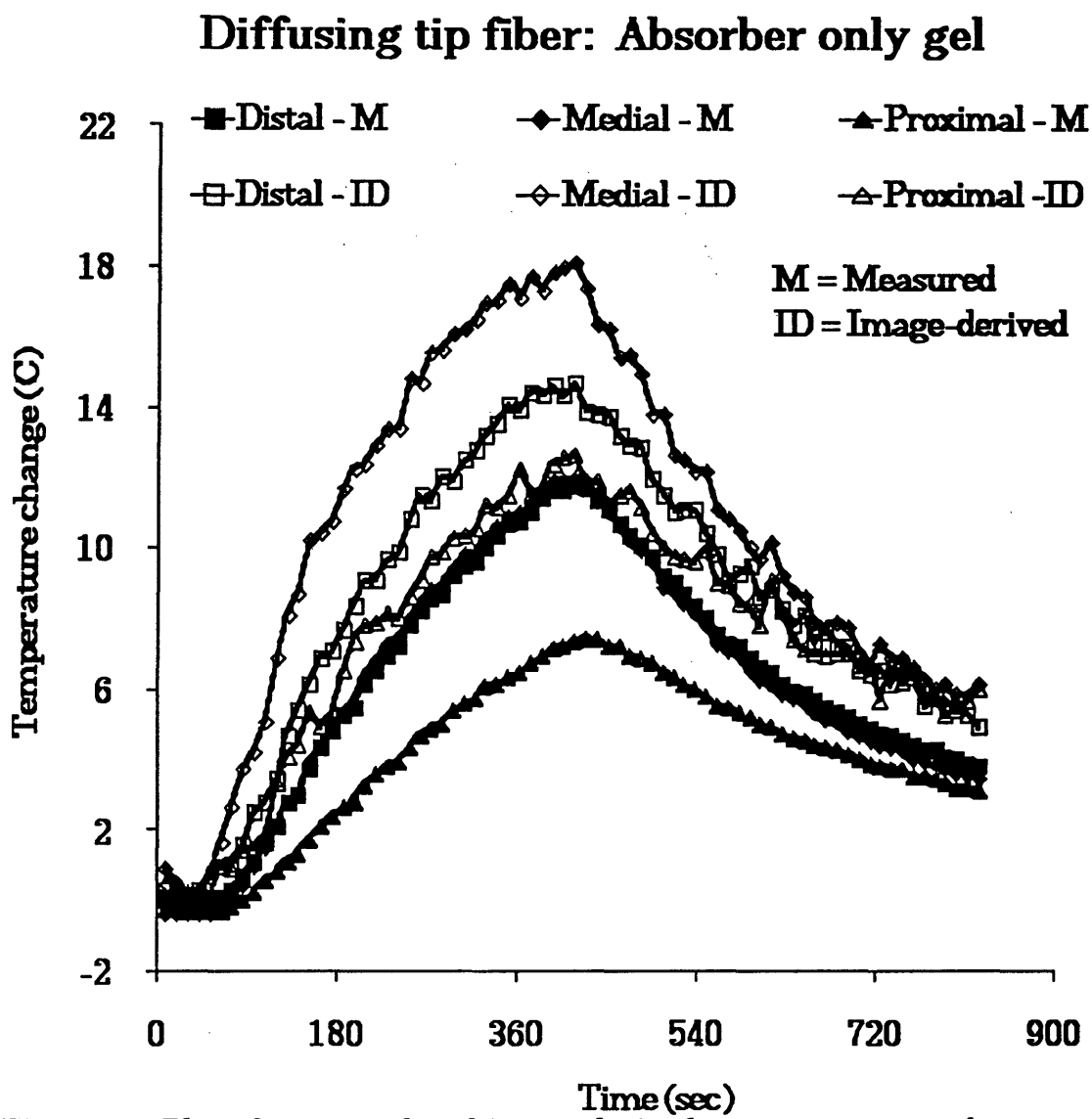

Figure 3.8 Plot of measured and image-derived temperatures at three locations for diffusing tip fiber laser irradiation of a gel containing absorbers only. Notice fair agreement between measured and image-derived temperatures with consistent agreement between shape of curves.

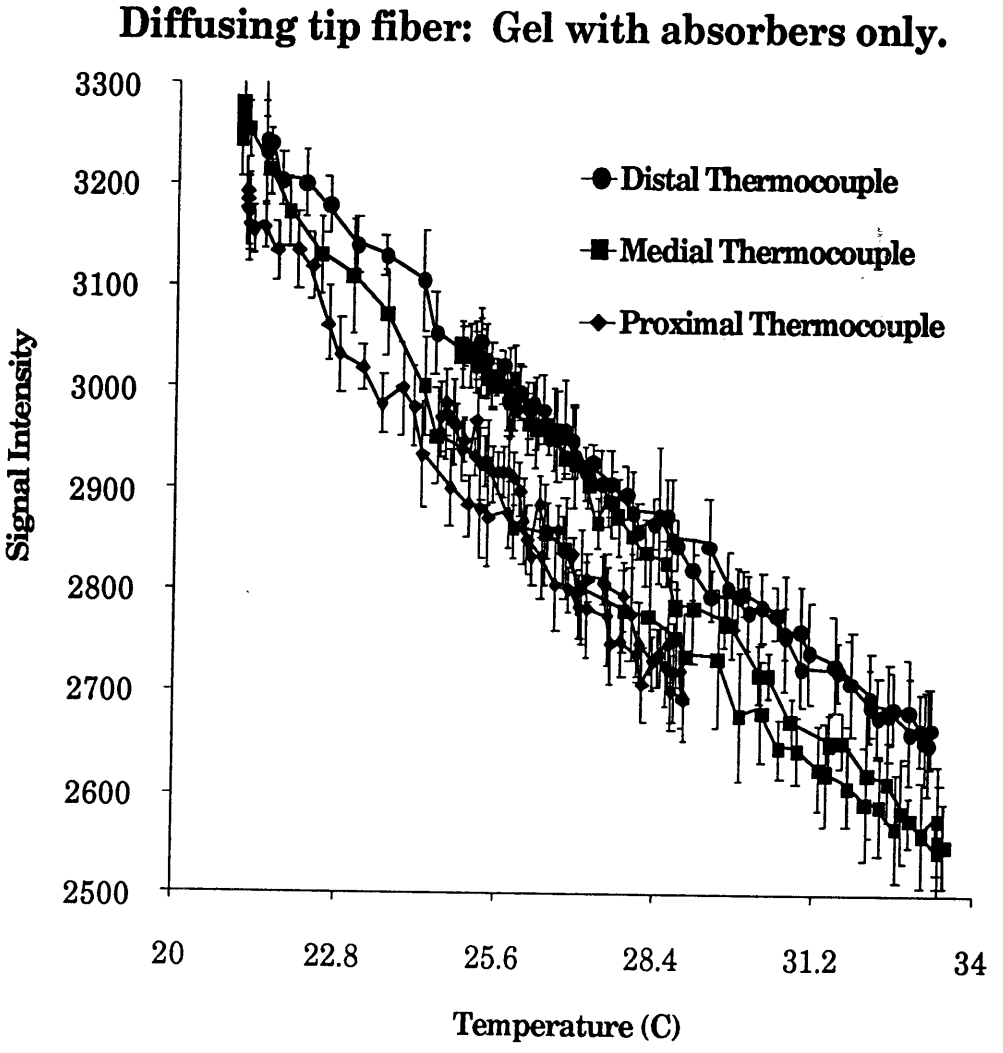

Figure 3.9 Signal intensity vs temperature for three thermocouples in gel irradiated with a diffusing tip fiber, containing absorbers only, shown with error bars. All three thermocouple locations display very linear response. Average slope is 1.7 %ΔSI/°C.

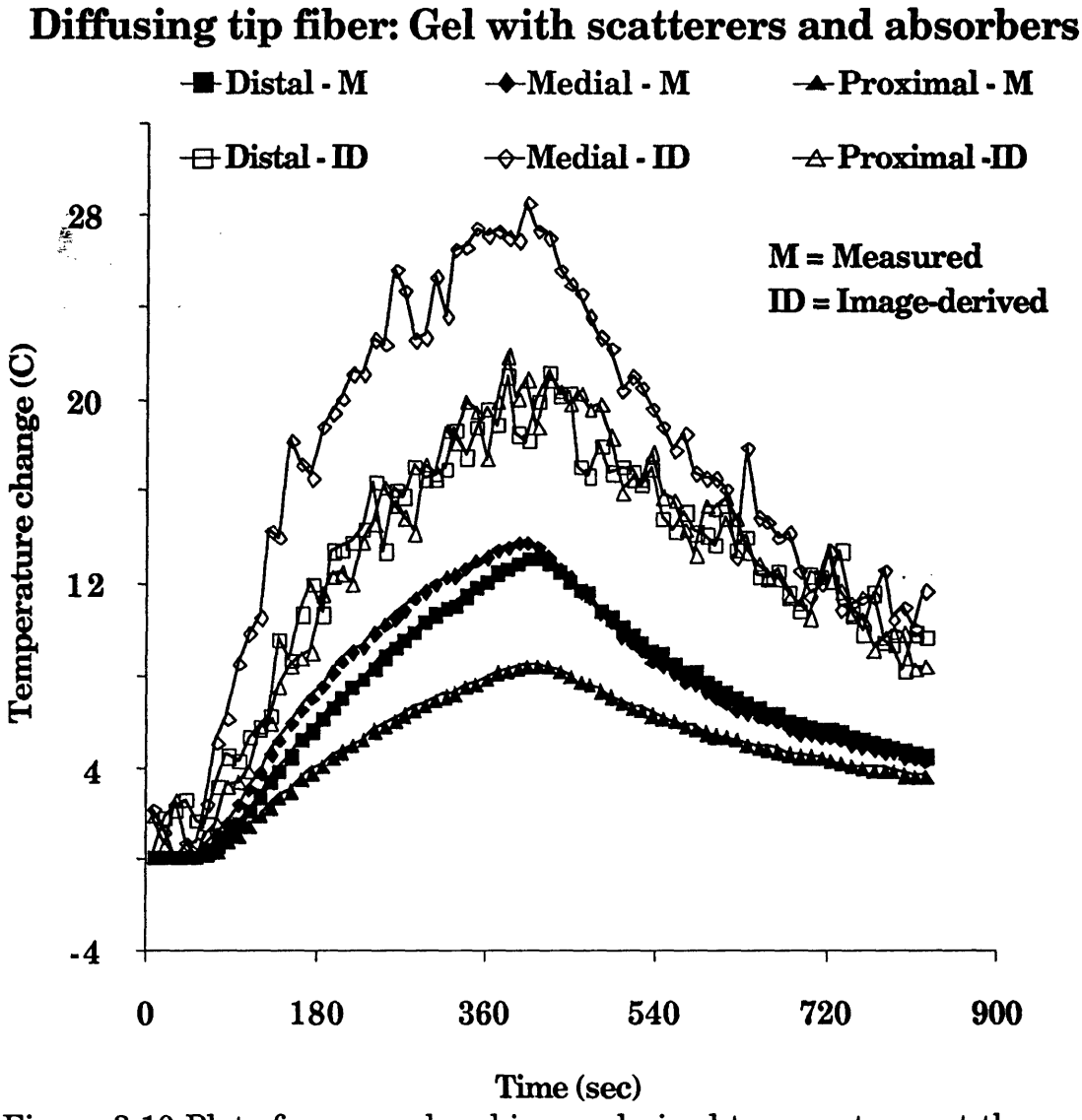

Figure 3.10 Plot of measured and image-derived temperatures at three locations for diffusing tip fiber laser irradiation of a gel containing scatterers and absorbers. Notice consistent agreement between shape of curves with significant over-estimation of temperature.

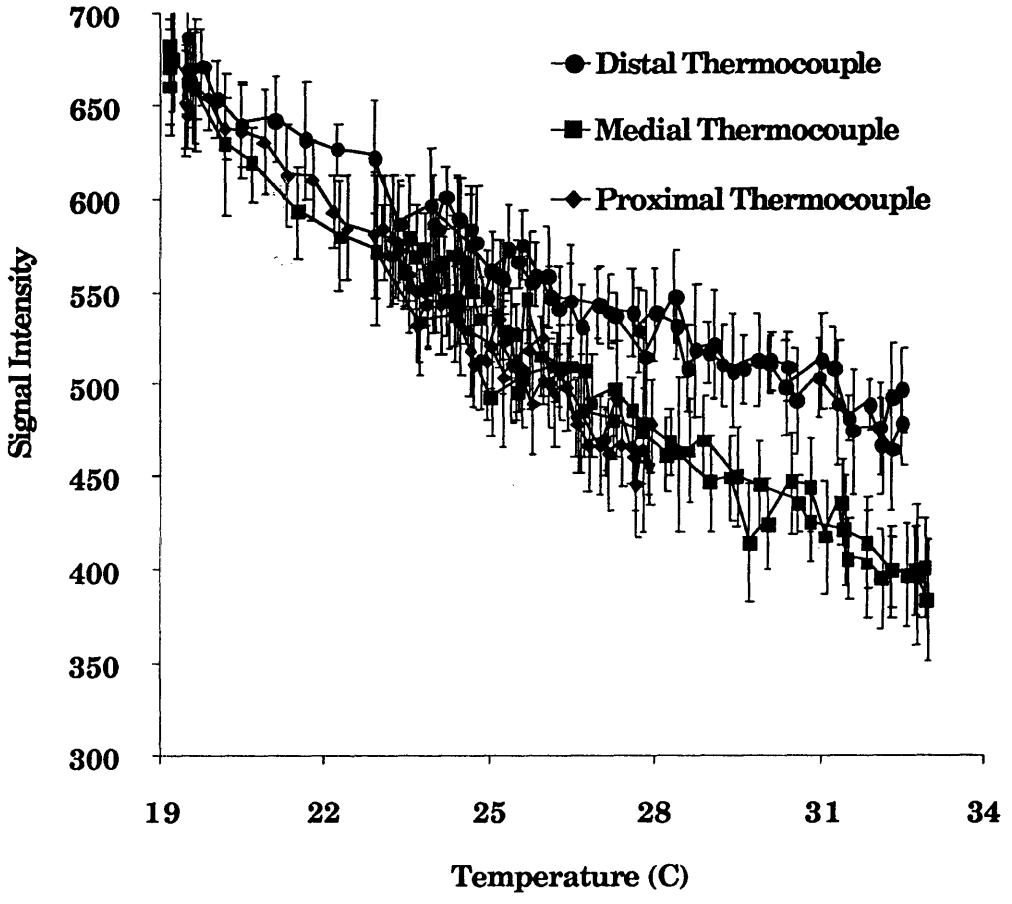

Figure 3.11 Signal intensity vs temperature for three thermocouples in gel irradiated with a diffusing tip fiber, containing scatterers and absorbers, shown with error bars. All three thermocouple locations display fairly linear response.

3.5 Discussion

3.5.1 Pulse Sequence Experiment

3.5.1.1 Temperature Sensitivity

An evaluation of the relative advantages and disadvantages of the sensitivity of the various FSE pulse sequences can be based on several different parameters. The magnitude of the signal intensity (SI) change per degree Celsius (ΔSI/°C) could be used to compare the pulse sequences, but the magnitude of the signal intensity and the noise in the image both have significant impacts on how accurately this parameter measures the thermal sensitivity of a pulse sequence. The magnitude of the signal must be considered because a signal change of 50SI/°C would obviously be more significant if the tissue's signal intensity was 500SI than if it was 5000SI. The noise in the image also plays a significant role because if the noise can modify the signal intensity by ±100SI and the signal change is 10SI/°C the temperature induced signal change would not be separable from random noise.

The percentage signal intensity change per degree Celsius (%ΔSI/°C) compensates for the effect of the magnitude of the signal and is often reported in the literature[2]. However, the temperature at which the percentage is computed must be cited since the "100% signal intensity" that is used to compute the percentage is a function of temperature. The differences in Table 3.2 columns 6 and 7 display the importance of this concept by displaying the percentage signal intensity change per degree Celsius at 20 and 33°C.

The %ΔSI/°C parameter has an advantage over the ΔSI/°C parameter in that it is insensitive to scaling that occurs in the image

reconstruction. This is significant because in any clinical situation the tissue of interest will be surrounded by other tissues which could have higher signal intensity, such as fat. Use of the %ΔSI/°C parameter as opposed to the ΔSI/°C parameter would allow a clinical application of interstitial thermal therapy to compensate for the different relative signal intensity relationships that will be encountered in different patients.

However, the use of the %ΔSI/°C parameter could also be misleading in certain cases. If two tissues have signal intensities of 1000SI and 500SI and each have a 1%ΔSI/°C temperature coefficient, the apparent contrast on the image will be twice as large for the tissue with intensity=1000SI. The %ΔSI/°C parameter is also sensitive to baseline offsets in the image reconstruction. If a tissue would normally have a signal intensity value of 600SI and a 1 %ΔSI/°C , the value would change to 0.75 %ΔSI/°C if a baseline offset of 200SI was added to the image. The inability to determine the value of baseline offsets on typical clinical imagers could inhibit rigorous comparison of different thermally-sensitive imaging techniques, but the values employed are typically small and do not significantly effect the comparison.

An evaluation of the data illustrates the issues discussed above. Comparison of the ΔSI/°C's from sequences FSE2 and FSE4, with echo train lengths =4 and TR's of 300msec and 500msec, respectively, show that for nearly all the gels the ΔSI/°C's can be quite different while the %ΔSI/°C's are much more uniform. The ΔSI/°C's for FSE4 are larger, but so is the magnitude of the signal because of the longer TR used in FSE4. The gels that do not contain any $CuCl_2$ display this property most

strongly. The gel sample with 1% agar and zero $CuCl_2$ has ΔSI/°C's of -3.53 and -6.05 for FSE2 and FSE4 respectively, while their corresponding %ΔSI/°C's are -1.56% and -1.54%. A similar relationship exists for sequences FSE3 and FSE5, which also have TR's of 300msec and 500 msec, respectively. The parameters for the same gel sample are: FSE3 ΔSI/°C=-2.54, FSE5 ΔSI/°C=-5.00, FSE3 %ΔSI/°C=-1.65%, FSE5 %ΔSI/°C=-1.57%.

However, this behavior is dependent on the T1 of the material that is being imaged. The gels that contain the highest concentration of $CuCl_2$ (4mmol) have the shortest T1's and the TR of the pulse sequence will significantly affect the value of the %ΔSI/°C parameter in this material. The %ΔSI/°C values of FSE2 and FSE3, which have TR=300msec, are typically 20% smaller than those of FSE4 and FSE5, which have TR=500msec. Thus, use of the %ΔSI/°C parameter indicates that the temperature sensitivity of sequences with a shorter TR, which are faster, is better than or equivalent to the temperature sensitivity of the longer TR sequences. This has obvious benefits for the monitoring of thermal therapy procedures because of the improved temporal resolution available with the faster pulse sequences.

A comparison of pulse sequences with the same TR but different echo train lengths reveals a similar relationship between the ΔSI/°C parameter and the %ΔSI/°C parameter. The ΔSI/°C parameter for sequence FSE2 is always greater than that for FSE3 (TR=300 msec, ETL= 4 and 8, respectively) and likewise for sequence FSE4 and FSE5 (TR=500 msec, ETL= 4 and 8, respectively). The magnitude of the ΔSI/°C

parameter can differ by as much as 40% relative to the magnitude of the shorter TR sequence value, with the average difference in their relative magnitudes being 21.7%, but the corresponding %ΔSI/°C values have magnitudes whose average difference is only 1.6% of their value, with the longer TR sequence having the better sensitivity. For example, the ΔSI/°C 's from a gel with a 2mmol $CuCl_2$ concentration and a 2% agar concentration have ΔSI/°C 's equal to -11.7 and -8.98 for FSE2 and FSE3, respectively, while their corresponding %ΔSI/°C 's are -1.35% and -1.42%. The gel samples without $CuCl_2$ seem to have larger-than-usual differences in the %ΔSI/°C parameter (-1.56/-1.65, -1.59/-1.75, -1.51/-1.07, -1.34/-1.22, -1.33/-1.51) but they follow no pattern so it is difficult to determine the source of the irregularity. Thus, the results of the echo train length comparison indicate that temporal resolution can be gained by increasing the echo train length and reducing the scan time, with minimal or no loss in temperature sensitivity. This is obviously beneficial to thermal therapy control applications.

3.5.1.2 Optical Phantom Sensitivity

The previous discussion yields insights into the appropriate selection of pulse sequence parameters to maximize thermal sensitivity in MR images and demonstrates the capabilities of the gel phantoms. The gel phantoms are also of value because of their capabilities as optical phantoms, with the optical absorption and scattering coefficients controllable by adding appropriate dopants. However, an interaction between the MR properties and the optical properties of the gel could

complicate their implementation as tissue-simulating materials. The interaction between the optical and MR properties of the gels can be analyzed by examining the data in Table 3.5. The data for the samples without optical dopants is displayed on the line above the corresponding data for the optically-doped sample. The results are rather intriguing.

The results demonstrate that in 58% of the cases the %ΔSI/°C parameter measured at 33 °C of the optically-doped samples are more sensitive than gels without optical dopants, but on average the non-doped samples have a better temperature accuracy, but only by 0.2 °C. Not enough samples were tested to statistically determine if there is a correlation between the concentrations of ink or polystyrene microspheres added to the gel and the relative sensitivity of the doped and dopant-free gels. There is also no apparent signal loss due to the presence of the polystyrene microspheres. The spheres displace water protons so it would be expected that the signal intensity would decrease by the volume fraction of the spheres. The volume fractions are very small in this experiment (<=1.5%) so it is likely that any differences arising from this source are lost in the image noise.

This result has significant implications in the use of gel phantoms in thermal therapy simulation experiments. The ability to maintain or improve the MR thermal sensitivity of the gel with optical dopants strongly recommends the use of this technology for thermal and optical coefficient experiments. The independence of the MR parameters from the optical dopant concentrations suggests that experimental protocols can be developed that would independently vary the optical parameters and allow determination of the optical and

thermal distributions mentioned in Sections 1.4.2. 1&2. This increases the potential for successful development of computer models that can accurately characterize the complex, interacting physical processes involved in a thermal therapy procedure.

3.5.1.3 Accuracy

The %ΔSI/°C and ΔSI/°C parameters reflect the sensitivity of an imaging technique but a parameter that would reflect the accuracy of a technique is also required for comprehensive comparison. The accuracy of an imaging technique's thermometric capabilities is limited by the noise in the images. The standard deviation of the signal intensity taken from a region of interest in a homogeneous area is frequently used to measure noise in an image [2]. Dividing the standard deviation of the signal intensity by the ΔSI/°C parameter produces an effective standard deviation of temperature which can be used to evaluate the accuracy of the technique.

This data is presented in column 5 of Table 3.2 for each gel sample and for each pulse sequence and is summarized in Table 3.3 to allow comparison of pulse sequences and dopant concentrations. The data from pulse sequence FSE1 is discounted from the remainder of the discussion because of the artifacts in the images. Eighty four percent of the temperature accuracy values are less than 4°C and 59% are less than 3°C, while the best value of 1.8°C was attained with pulse sequence FSE5 in a gel containing 1% agar and 3 mmol $CuCl_2$. The most accurate pulse sequence varied for each sample, so there is no single optimal

pulse sequence that can be employed for maximum temperature accuracy in all tissues. FSE4 and FSE5 have better accuracy than the other pulse sequences in all but 5 cases. FSE2 is the best in 2 cases and FSE3 is the best in the remaining 3. A conservative approach to maximum temperature accuracy for any tissue type would use FSE4 in all cases because in the worst case, FSE5 outperforms FSE4 by 0.5°C, while, again in the worst case, FSE4 has an accuracy that is 1.6°C better than FSE5.

The pulse sequences tend to have greater accuracy for the gel samples with lower agar concentrations, but there is little correlation between agar concentration and temperature accuracy (average R^2 for all samples and pulse sequences = 0.32). There is a similar tendency that the temperature accuracy is better for gels with higher $CuCl_2$ concentrations, but again the statistics indicate a weak correlation (average R^2 for all samples and pulse sequences = 0.53).

3.5.1.4 Temperature Dependence of T1 and T2

The temperature dependence of the T1 and T2 parameters shows the relative significance of the agar and $CuCl_2$ dopants as well as their effects. The change in T2 with temperature is much more strongly correlated to the agar concentration than to the $CuCl_2$ concentration (average R^2 =0.76 for agar vs 0.13 for $CuCl_2$) as is the percentage change in T2 with temperature (average R^2 =0.76 for agar vs 0.32 for $CuCl_2$). The change in T1 with temperature is correlated more strongly to $CuCl_2$ concentration than it is to agar concentration (average R^2 =0.39 for agar

vs 0.65 for $CuCl_2$) but the correlations for the percentage change in T1 are similar (average R^2 =0.55 for agar vs 0.51 for $CuCl_2$). The error codes in the temperature sensitivity of the T1 and percentage T1 of the samples with no $CuCl_2$ and less than 2% agar reflect the inability to accurately estimate the T1 of those samples. The long T1 of the samples compared to the TR of the pulse sequence used renders the curve fitting results indeterminate.

3.5.2 Thermal Contour Experiment

The results of the thermal contour experiment in which a bare tip fiber irradiated a gel that contained absorbers without scatterers demonstrates MR's potential to measure temperature distributions in homogeneous media. The agreement between the image-derived and measured temperatures for this fiber/gel combination reflects the accurate characterization of the gel's temperature behavior by the pulse sequence experiment. The irradiation of the gel with scatterers and absorbers by a bare tip fiber, as well as the cases of irradiation of gels with and without scatterers by a diffusing tip fiber, in which the image-derived temperatures did not match the measured values, highlight the difficulties associated with accurate characterization of the gels over the temperature range of interest and the other possible sources of error in the experiment.

The characterization of the gel material was incomplete because the pulse sequence experiment only characterized the behavior during the cooling phase of a thermal experiment. This produced %ΔSI/°C

values that did not match the values characteristic of the gel behavior during a temperature increase. Thus, the shapes of the image-derived and measured temperature curves were very similar but the magnitude of the temperature error was significant. This was most likely due to the melting of the agar gel inside the polyacrylamide matrix in the pulse sequence experiment, which would create a different material than the completely solid gel that existed at the start of the thermal contour experiment.

This type of behavior could also explain the plots of signal intensity versus temperature for the thermal contour experiments. The hysteresis in the curves would support the hypothesis that there was a change in the material over the course of the experiment. This effect could explain the data in the bare tip fiber/absorber only gel experiment. The hysteresis in the proximal thermocouple seen in Figure 3.2 is reflected in the change in the magnitude of the error seen in the heating portion of the curve in Figure 3.1. The slope in the cooling portion of the curve matches the slope determined in the pulse sequence experiment within 0.03%/°C while the slope displayed in the heating portion of the curve is off by 0.06%/°C. This could reflect the creation of a gel state similar to that found in the pulse sequence experiment because of the high temperatures induced in the gel at that location. Thus, the characterization of the gel becomes more accurate and the magnitude of the error decreases during the cooling phase.

The quality of the match between the measured and image-derived temperatures for the distal thermocouple in the same experiment demonstrates that accurate temperature changes can be

predicted with moderate temperature increases also. This thermocouple did not experience a temperature increase that would normally cause the agar component of the gel to melt, and the image-derived temperatures match the measured temperatures very closely for the entire duration of the experiment. The shift from under-estimation to over-estimation of the temperature seen at the end of the laser exposure can even be accounted for by the slight hysteresis in the curve seen in Figure 3.2.

If the temperature sensitive change in the gel could be controlled it could be exploited to mimic tissue changes that occur in response to thermal changes. The temperature-sensitive changes that occur in all the physiologic parameters discussed in Chapter 1 Section 1.4.3 present a moving target for any attempt to correlate signal intensity with temperature. Jolesz et al have shown that there is significant hysteresis in the signal intensity-temperature relation for a variety of biological materials[1]. Gel combinations of agar and polyacrylamide could potentially be developed that would duplicate some of the changes that occur in tissue. This could facilitate the development and testing of imaging strategies that would more accurately characterize the thermally-induced changes in tissue and lead to greater understanding of the nature of those changes.

Another possible source of error is the placement of the ROI's used to measure the signal intensity changes. The slight artifacts associated with the thermocouples facilitates their identification but prohibits signal intensity sampling at their exact locations. The homogeneity of the target material and the symmetry of the irradiation

profile indicate that symmetric positions should experience the same temperature increase so the ROI's were located at positions symmetric to the apparent thermocouple location. However, the thermal gradients in the experiment could be significant, as demonstrated by the different temperatures measured by thermocouples 5mm apart, so a slight error in ROI placement could have noticable effects on the accuracy of the match between the image-derived and measured temperatures.

The presence of the thermocouple array in the irradiated medium is another potential source of error. The thermocouple array has a different thermal conductivity than the gel so its presence will disturb the thermal distribution and weaken the symmetry argument proposed previously. There is also the potential for increased thermal conductivity down the thermocouple wires because of the larger thermal conductivity of the metal. The conduction of heat by the wires would effectively remove a small amount of heat from the distal location, a larger amount from the medial location and the most heat from the proximal location. This would yield successively larger errors for the medial and proximal locations, which is found to be the case in both gels irradiated with a diffusing tip fiber. This was not found in the gels irradiated with the bare tip fiber because the heating was not equal along the length of the array and the largest temperature increases occurred at the medial and proximal locations.

On the other hand, the induction of currents in the thermocouple wires by the RF waves used in the imaging could induce temperature increases in the area of the thermocouples. This effect would also be more significant in areas near the proximal thermocouple where there

was the largest volume of metal. The smallest commercially available thermocouples were used in this experiment to minimize both these effects.

A final potential source of error is the presence of convective flow in the gel during the laser irradiation in response to the thermal gradient. This flow would be perpendicular to the horizontally-oriented imaging plane and would decrease the signal intensity in the regions where it occurred. The pulse sequence experiments derived a signal intensity-temperature relationship for samples at a thermal steady state, which would not have the flow because there was no thermal gradient. The flow-induced signal decrease would mimic a temperature increase and yield an over-estimation of temperature, which was characteristic of all the thermal contour experiments.

3.6 CONCLUSION

This study graphically demonstrates the ability of MRI to detect thermal changes in homogeneous media and reveals some of the sources of error in temperature-signal intensity correlations. The pulse sequence experiment demonstrates that knowledge of the target tissue's MR properties facilitates selection of the optimal MR pulse sequence parameters but that a variety of pulse sequences will produce similar results for a range of T1s and T2s. The temperature range covered in the pulse sequence experiment is representative of the range of temperatures that could be induced in laser thermal therapy treatments. The thermal contour experiment covers a lower temperature range but it illuminates the significance of accurate material characterization thoughout the entire temperature range.

The agar/polyacrylamide gel combination did not appear to maintain consistent structure across the temperature range studied here, but this property was revealed as a potential asset in the study of dynamic tissue responses to thermal treatments. The modification of the gel's optical properties with India ink and polystyrene microspheres was determined to have a minimal or beneficial effect on the gel's MR behavior. This suggests that this material could have significant advantages as a phantom material for quantitive studies of the optical and thermal processes involved in thermal therapy procedures. The ability to independently modify the optical and MR properties of the phantom would be advantageous to experimental verification of optical/thermal/MR computer models.

Experimental verification of more complicated computer models

that more accurately reflect physiologic conditions is possible because of the convenient mechanical parameters of the gels. The catalyst-activated polymerization of the gel that consists of polyacrylamide without agar suggests that a "target" gel with different optical or MR properties could be embedded in a "bulk" gel to simulate a tumor in situ without melting the pre-cast gel at the boundaries, which would occur with agar gels. In addition, gels could be cast around thin-walled tubing that would contain flowing fluid during an experiment to simulate the heat sink behavior of major vessels.

A significant amount of work remains to be done to evaluate MRI's ability to monitor dynamic systems, particularly with regard to temperature sensitive optical and thermal parameters, but this study presents a methodology that can be used to deal with this very complex problem. This study also presents a system that could be used to study new materials currently under investigation such as temperature sensitive MRI contrast agents, which could more clearly delineate thermal contours. Experiments of this type would obviously benefit from the use of faster imaging techniques but these experiments have shown that the FSE imaging sequences employed here were capable of demonstrating the thermal changes induced by the laser protocol with either bare tip fibers or diffusing tip fibers with a temporal resolution of 1 image every 10 seconds.

REFERENCES

1. Jolesz FA, Bleier AR, Jakab P, Ruenzel PW, Huttl K, Jako GJ. "MR Imaging of Laser-Tissue Interactions," Radiology 1988; 168:249-253.

2. Matsumoto R, Oshio K, Jolesz FA. Monitoring of laser and freezing-induced ablation in the liver with T1-weighted MR imaging. *Journal of Magnetic Resonance Imaging*, 2(5):555-562, 1992.

3. Hushek SG, Date V, Morrison PR, Fried MP, Jolesz FA. Phantoms for MRI of laser interactions. (abstract) *Journal of Magnetic Resonance Imaging*, 3P:220, 1993.

4. Lilge L, Flotte T, Kochevar IE, Jacques SL, Hillenkamp F. Photoactivable fluorophores for the measurement of fluence in turbid media. (in press).

5. Madsen AJ, Patterson MS and Wilson BC. The use of India ink as an optical absorber in tissue-simulating phantoms. *Physics in Medicine and Biology*, 37(4):985-993, 1992.

6. Gore JC, Brown MS, Zhong J, FritzMueller K and Good W. NMR relaxation of water in hydrogel polymers: A model for tissue. *Magnetic Resonance in Medicine*, 9:325-332, 1989.

7. Murase N and Watanabe R. Nuclear magnetic relaxation studies of the compartmentalized water in crosslinked polymer gels. *Magnetic Resonance in Medicine*, 9:1-7, 1989.

8. Matsumoto R, Mulkern RV, Hushek SG, Jolesz FA. Tissue temperature monitoring for thermal intervention: A comparison of T1-weighted MR pulse sequences. *Journal of Magnetic Resonace Imaging*, V7(6):47-53, 1994.

9. Bini MG, Ignesti A, Millanta L, Olmi R, Rubino N, Vanni R. The polyacrylamide as a phantom material for electromagnetic hyperthermia studies. *IEEE* 31:317-322, 1984.

10. De Luca F, Maraviglia B, Mercurio A. Biological tissue simulation and standard testing material for MRI. *Magnetic Resonance in Medicine*. 4:189-192, 1987.

11. Madsen EL, Zagzebski JA, Banjavie RA, Jutila RE. Tissue mimicking materials for ultrasound phantoms. *Medical Physics*. 5:391-394, 1978.

12. Cline HC, Schenck JF, Hynynen K, Watkins RD, Souza SP, Jolesz

FA. MR-guided focused ultrasound surgery. *Journal of Computer Assisted Tomography*. 16:956-965,1992.

Chapter 4. Animal Experiments: Material and Methods

4.1 Introduction

The animal experiments were designed to test the hypothesis that the signal intensity changes in MR images acquired during a laser thermal therapy treatment could be related to the effect of the treatment. The experimental system was designed to collect as much of the data generated by the experiment as possible with the minimum amount of operator involvement. A tumor model was chosen because the response of normal tissue to thermal therapy treatments is very different from tumor tissue and the intent was to simulate as many aspects of a clinical thermal therapy treatment as possible.

The 9L-50 gliosarcoma[4] was chosen as the in vivo tumor model because it could be grown reliably on a rat to a size that would allow a range of treatment levels within a single tumor. The surviving fraction was used to gauge the severity of the treatment because it was felt that histological evaluation would not reveal the changes in the tumor that could impact the survival probability of the tumor tissue due to the short delay between treatment and tumor excision. The surviving fraction was also a more quantifiable measurement than histological evaluation.

The laser treatment protocol was designed to produce a slowly expanding volume of treatment severity that would eventually yield a very severe zone of treatment at the center of the tumor with the periphery receiving only a mild treatment. The Nd:YAG wavelength of 1064nm was chosen for its depth of penetration. The exposure duration was selected to

be long enough that the tumor reponse that occurred during the treatment could be detected with the temporal resolution available with a standard MR imaging system. The laser power was selected to prevent intra-tumor temperatures in excess of 60 °C and to avoid the very high temperatures that could damage the diffusing tip optical fibers.

The sequence of computational steps in the image processing procedure was designed to mathematically duplicate the sequence of steps in the physical processing of the tumor tissue.

4.2 Treatment Protocol

4.2.1 Tumor Model

Female Fischer 344 rats (Taconic Farms Inc., Germantown, N.Y.) weighing 100-125 g were implanted with 0.2cc containing alpha-MEM (Grand Island Biological Co., Grand Island, NY) and $2X10^6$ 9L-50 gliosarcoma cells. The 9L cells were implanted subcutaneously on both flanks and the tumors were allowed to grow to at least 2 cm in diameter.

4.2.2 Animal Preparation

The tumor-bearing animal was weighed and then was anesthetized by placing them in a large glass jar filled with methoxyflurane vapor (Pitman-Moore Inc., Mundelein IL). The animal was observed until mildly sedated, then injected intra-peritoneally with a combination anesthetic of 35 mg/kg ketamine and 25 mg/kg xylazine. The skin over the tumors was shaved and the animal was placed in a special MR-compatible animal

holder designed and built for these experiments. The animal holder was made of a half cylinder of 3.5 inch outer diameter plexiglass tubing with a 1/4 inch wall thickness, approximately 18 inches long. No fixation was used.

Fiducials designed to facilitate alignment of locations on the images with physical locations on the animal were created by marking the skin over the tumors with a mascara pencil (Noxell Corp., Hunt Valley MD). The mascara contains iron oxide, which creates easily recognizable artifacts on the images. The spatial extent of the artifacts created by these markings was limited so they did not interfere with the quality of the images.

The animal was palpated to determine the size and position of the tumor. A needle entrypoint that would yield a needle position at the center of the tumor was identified. A small incision was made in the skin over both tumors at these entrypoints to facilitate the insertion of the 16 gauge catheter (Johnson & Johnson, Tampa FL) that guides the optical fiber into the approximate center of the tumor. A custom made needleholder is used to position the tips of the catheters at the incisions. The needleholder consists of a 3cc syringe barrel (Becton-Dickinson, Franklin Lakes, NJ) with the twist-n-lock connector that mates with the connector on the catheter, running through a plexiglass arm attached to the back of the animal holder. The arm can pivot and slide along a slot to position the syringe barrel at any location in the cross-section of the animal holder. A locking screw is used to hold the arm and syringe barrel in place during

the experiment. See Figure 4.1.

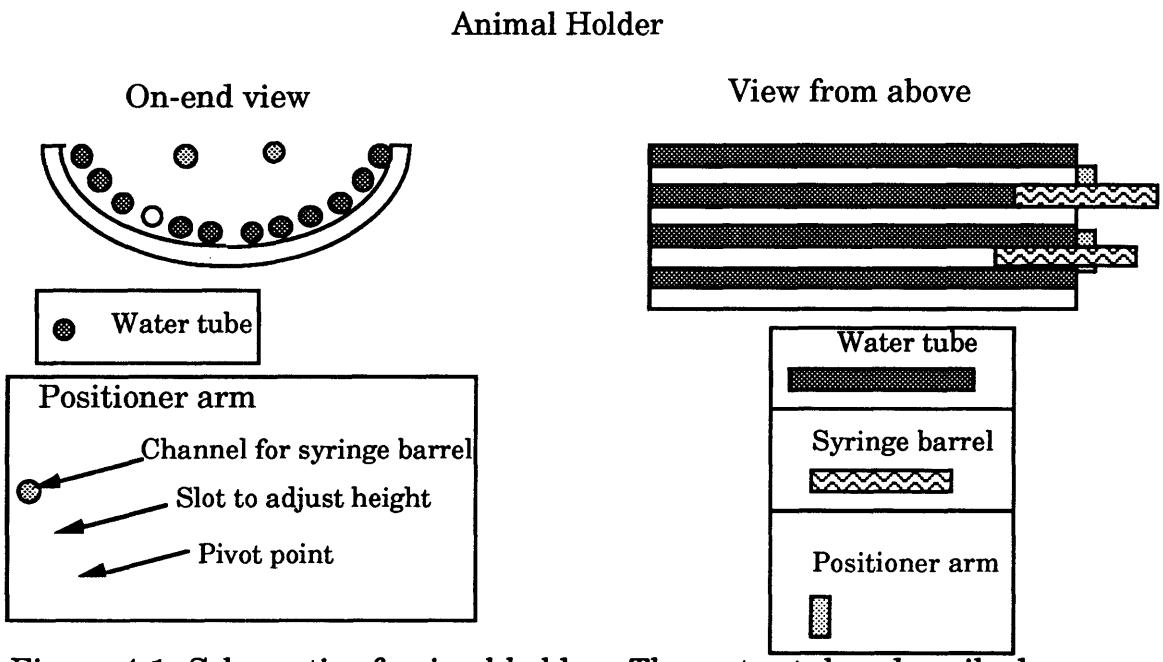

Figure 4.1 Schematic of animal holder. The water tubes described on Page 162 run the length of the device. The positioner arms can pivot and slide along a slot to position the syringe barrel at nearly any insertion point.

The 16 gauge catheter was the minimum size required to accommodate the 1mm diameter optical fiber. The distal 7mm of the catheter were cut off so that when the catheter+trocar assembly was inserted into the tissue the trocars would protrude 7 mm beyond the catheter tip to create the space required for the optical fibers, minimizing the mechanical damage that would be done by the blunt tip optical fiber. The trocars were then removed and replaced with the optical fibers. See Page 168, Figure 4.5 for descriptions of the optical fiber.

4.2.3 Temperature Measurement

4.2.3.1 Core Temperature Regulation

The temperatures are measured simultaneously at 5 locations during the experiment to determine the temperatures that are created in the treated volume and to observe the core temperature of the animal. Teflon-insulated, 36 gauge, copper constantin thermocouples (Omega Inc, Stamford, CT) were used because of their minimal effect on the images. A rectal temperature probe was inserted to observe the core temperature of the animal during the experiment. The MR scanner room is maintained at a relatively low temperature (≈15°C) , therefore an external heat source was used to maintain the animal's core temperature at physiologic levels. The bed of the animal holder was made up of an array of thin-walled, 1/4 inch outer diameter tygon tubes which were connected to a thermally regulated water pump (Endocal, Neslab Instruments Inc., Newington, NH). The temperature of the water was adjusted to maintain an animal's core temperature at 36 °C.

The animal's core temperature can reach dangerously high levels (49°C) during the laser treatment. A bypass loop in the tubing that supplies the water to the bed of the animal holder passes the water through a copper coil submerged in an ice bath. The relative amounts of warm and cold water flowing to the animal holder were adjusted by a pair of valves during the experiment to cool the animal when necessary and maintain a core temperature within 3°C of normal physiologic levels through all phases of the experiment.

4.2.3.2 Tumor Temperature Measurement: Thermal Probe Design

Four thermocouples were located in the tumor to observe the temperatures produced by the laser thermal treatment. The catheter that guides the optical fiber had a thermocouple mounted at its tip. The thermocouple is bound to the catheter by punching a small hole in the catheter 1mm from the tip, threading the bare wire of the thermocouple through the hole and looping it around to the outside surface of the catheter, as shown in Figure 2. The mechanical forces on the thermocouple were sufficient to hold it in place, therefore, no glue or material that would make the circumference of the catheter larger was needed. This also allows the thermocouple wire to ride on the outside of the catheter, permitting use of a 16 gauge catheter.

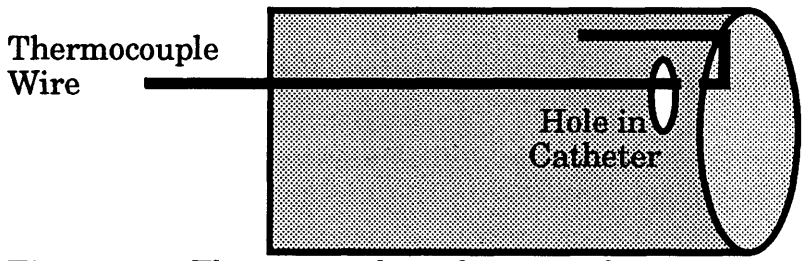

Figure 4.2 Thermocouple-catheter configuration with loop-through fixation. Teflon-coated, 36G copper-constantin thermocouples; 16G catheter. The mechanical forces hold the thermocouple to the catheter so no glue is necessary.

A three thermocouple array shown in Figure 3 was positioned in the tumor near the imaging slice. The thermocouple array was constructed by severing the distal 1cm of a 20G catheter (Baxter Healthcare Corp, Deerfield IL) and connecting three thermocouples, spaced 5mm apart, to the 1cm

section with the same loop-through method used with the optical fiber catheter. When the array was to be inserted into the tumor, the base of the catheter without the 1cm section was placed on the trocar, then the 1cm thermocouple array was added and the entire assembly was inserted perpendicular to the optical fiber through a small incision in the skin. The base of the catheter held the thermocouple array in place while the trocar was removed, then the base of the catheter was also removed.

In this manner, the 1cm length of catheter holding the thermocouples could be positioned in the tumor and no material other than the thermocouple wire protruded from the tissue. Since the thermocouple array was positioned at a right angle to the optical fiber and the fiber was parallel to the coil axis, any protruding catheters would prevent use of the very close fitting imaging coil. Thus, the use of the 1cm implanted array allowed us to combine the excellent image quality obtained with the very close-fitting coil with multi-point invasive thermometry. The animal preparation typically required 30-45 minutes.

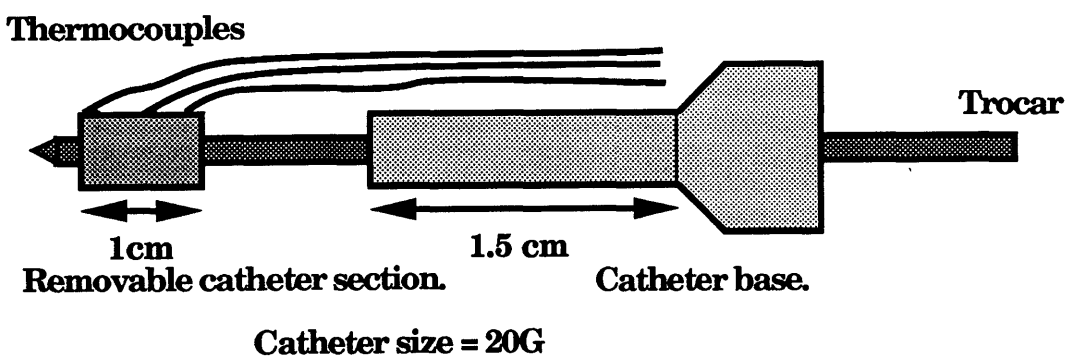

Figure 4.3 Schematic of three thermocouple array. Teflon-coated, 36G, copper-constantin thermocouples mounted on 1cm removable section of 20G catheter. Thermocouples are spaced 5mm apart.

4.2.4 MR Imaging Protocol

When the optical fibers and thermocouples were in place the animal was positioned in the 1.5T, Signa MR imager (GE Medical Systems, Waukesha, WI). The animal holder fits in the quadrature, 10cm diameter, transmit/receive, birdcage imaging coil designed and built by Brigham and Women's Hospital research staff. The coil efficiency was very high because of its small size and the minimum flip angle with the standard system exceeded 90°, so an extra 20 dB of attenuation was added to the RF transmitter to reduce the transmitted power. Localizer scans were acquired to determine the location of the fibers and the optimum imaging planes. If the localizer scans revealed that the fibers were not positioned in the center of the tumor an attempt was made to reposition the fibers when possible. The localizer scans were used to position the intra-operative imaging plane for each tumor at the front edge of the irradiating surface of the optical fiber in that tumor (see Fig. 4). Acquisition and review of the localizer scans typically required 15 minutes, with an additional 20-25 minutes required if fiber repositioning was deemed necessary.

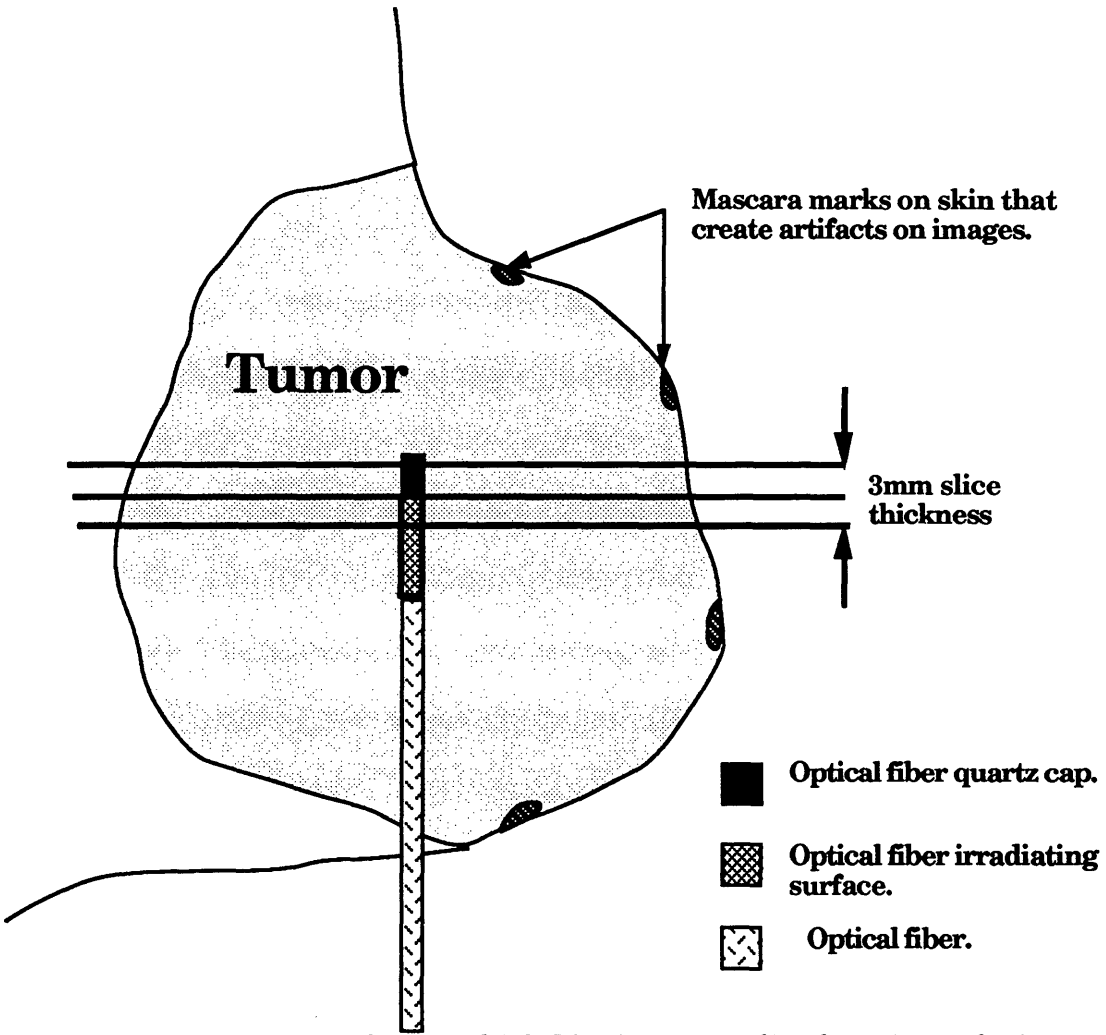

Figure 4.4 Schematic of 3mm thick MR imaging slice location relative to optical fiber tip location. Dimensions of optical fiber tip components are: quartz cap = 2mm, irradiating surface = 10mm length, fiber diameter = 1mm. Mascara-mark fiducials used to align the imaging slice with the excised tumor slice are also shown.

A tissue characterization study, which consists of a Carr-Purcell-Meiboom-Gill (CPMG) imaging series to determine T2 and a variable TR series to determine T1, was performed on the single designated slice location in each tumor. The CPMG series has 48 echoes, an echo spacing of

18 msec, a TR=4000 msec and a total acquisition time of 9 minutes. The first 4 echoes of the sequence were discarded because of stimulated echo effects which corrupt the magnitude of the signal. The remaining 44 points were fit to a mono-exponential decay function with a constant component to represent the noise.

The variable TR series employed a fast spin echo sequence with an echo train of 4 and included 13 images with TR's ranging from 200msec to 4000msec which could be acquired in approximately 10 minutes. This series of images does not yield the best estimate of T1 but time constraints imposed by the animal anesthesia precluded the use of an inversion recovery-based method which would acquire a single image in approximately 8 minutes. The signal intensities were fit to a recovering exponential.

4.2.5 Thermal Treatment

4.2.5.1 Imaging Parameters

Once the tissue characterization studies were complete the tumors were exposed to laser thermal therapy. A fast spin echo, dynamic imaging sequence was employed. The pulse sequence was a standard fast spin echo sequence modified to allow an arbitrary number of images per location to be selected with a programmable delay between the images. A typical dynamic sequence consisted of 70 images: 3 baseline images acquired before the laser therapy was initiated, approximately 40 images during the laser exposure and roughly 27 images during the cool down period for a total

imaging time of approximately 17 minutes. The images used a TE=18msec, TR=1000msec and echo train length = 8. The images were acquired with a 3mm slice thickness, 256X128 matrix, an 8cm field of view (FOV) in the frequency direction and a 6cm FOV in the phase direction, which yielded an image time of 15 seconds. The second tumor was treated immediately after the first tumor with the same imaging strategy. Then the tissue characterization series was repeated to look at the acute effects of the treatment. The total experiment duration was approximately three hours.

4.2.5.2 Laser Parameters

The main laser housing with the control board was located at the MR imager's operator console for simultaneous control of the laser and the imager. The laser used was an Nd:YAG Laserscope Model KTP/YAG 800 (Laserscope, San Jose, CA) with a wavelength of 1064nm, that had been furnished with a custom fiber system. The fiber system consists of a 100 foot long, 600 micron core, base fiber which transmits the laser energy from the laser into the scan room to a fiber-fiber coupler box at the side of the magnet. Another 600 micron core fiber conducts the light from the coupler box to a prototype ring-mode adapter designed for use with the diffusing tip fibers (Dornier Medical Systems, Kennesaw GA). The diffusing tip fiber and its output pattern are drawn in Figure 4.5. The output of the diffusing tip fiber is a cone covering approximately ±45° from a 5mm long irradiating surface. The diffusing tip has a total length of 12mm and a diameter of 1.0mm. The prototype ring mode adapter creates a laser mode in the fiber

that distributes the majority of the light through the cylindrical surface instead of out the tip of the fiber. The quartz blocking cap also blocks some of the light that would otherwise be emitted from the tip of the fiber. The laser power used for the treatment was 1.5W constant power with a duration of 10 minutes.

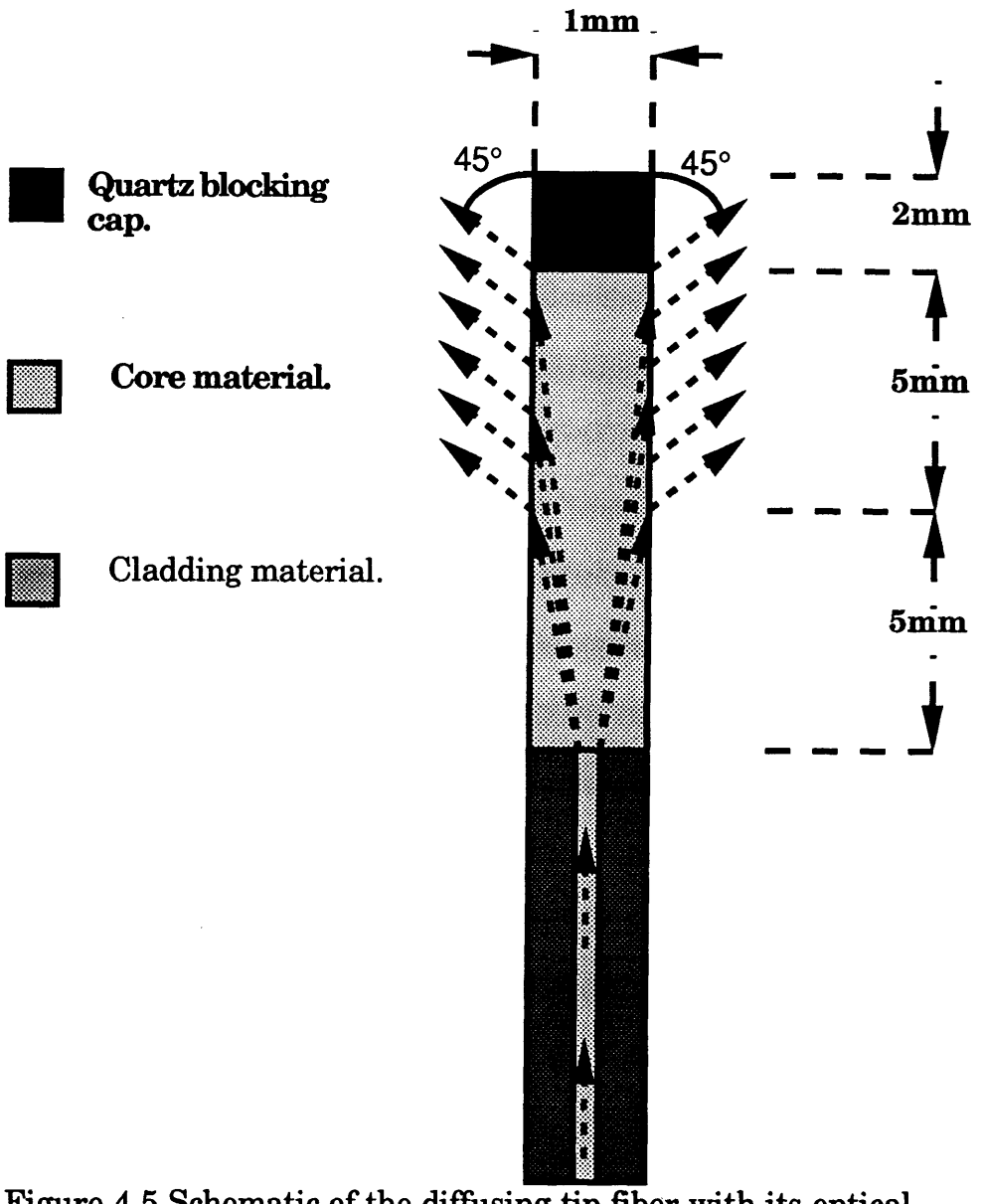

Figure 4.5 Schematic of the diffusing tip fiber with its optical output pattern. The section of core material is 1cm long but the light does not exit from the fiber until the final 5mm of the core material section.

Data Acquisition

Personal Computer Program

An interfacing program written in BASIC and running on a 286-

micro-processor based personal computer (IBM PC AT) was written to synchronize the temperature recording with the image acquisition during the treatment. The program records the time of data acquisition and the temperature and stores the information in a file for later analysis. The program records data on demand or automatically, labels the data columns with names provided by the operator and allows the operator to add comments to the data file for annotation purposes. The current temperatures are displayed at the top of the screen and the 15 most recently recorded temperatures are also displayed with their time of acquisition so the operator can observe the recent temperature history of the experiment. Reference temperatures are recorded between localizer series and between the tissue characterization series.

4.2.5.3.2 MR Imager-PC Coordination

The automatic recording mode was used during the laser treatment. The custom-designed pulse sequence described on page 167, which runs on the imager and acquires sequential images at the same location, communicates with the PC to synchronize the temperature recording with the imaging. The real-time section of the imaging pulse sequence code was re-written for these experiments to run in a loop in which an image is acquired, a variable length delay is executed, a signal is sent to the PC to initiate the temperature recording and a 300 msec delay is executed. The total number of images acquired and the total delay between images is selected by the operator with the Modify Control Variables function on the

imager.

The minimum delay of 300 msec between the images is required to give the PC sufficient time to communicate with the thermocouple measurement electronics and log a set of 4 temperatures. Temperatures were measured at five locations, but only four of the thermocouple measurement electronics were capable of communicating with the PC. The temperature measured by the thermocouple on the catheter was not recorded by the computer. Also, the radio frequency (RF) waves used to generate the image disturbed the thermocouples so the experiments used a total inter-image delay of 1 second, which allowed the thermocouples to stabilize during the 700 msec delay between the image acquisition and the temperature recording.

Communication between the PC and the imager was accomplished using the serial port on each system, with the communications parameters set for 9600 baud, no parity, 8 data bits and 1 stop bit. The PC reads the serial output of the 68020 communications port on the imager, constantly comparing the output strings to an identification string. A variety of strings are written to this port by the imager computer, so the nature of the strings was studied to determine what characters could be used for a unique identification string. The imager sends the unique identification string to the PC with a formatted print statement in the real-time section of the pulse sequence code, then sends the image number to the PC in the same fashion. When the PC detects the identification string it reads the image number from the imager output and records the temperatures, the

image number and the time of acquisition to a file.

4.2.5.3.3 Temperature Rise-Time Data

An additional set of temperatures were recorded at the initiation and cessation of the laser thermal therapy treatment to determine if the laser light had a direct effect on the thermocouple recordings. When the laser was turned on the imaging pulse sequence was paused and a subroutine was initiated in the PC program that recorded the temperatures at the maximum rate possible (approximately three recordings per second if 4 thermocouples were connected). This rate of measurement was continued until 20 temperatures had been recorded. This allowed examination of the rate of change of the temperature and determination of whether the optical energy impacting the thermocouples artificially raised the measured temperatures or if the thermocouples accurately represented the temperature of the surrounding tissue. The temperature increase rate measured with the rapidly acquired thermocouple readings matched the temperature increase rate measured for the first minute of the laser exposure, indicating that there was no direct effect of the laser light on the thermocouples. The combination of reference temperatures recorded between localizer and tissue characterization series, the temperatures recorded during the treatment and the rapid temperature acquisition at the beginning and end of the laser exposure completely characterize the temperature history of the experiment.

4.2.6 Fiber and Slice Location Alignment

Following the laser thermal therapy and tissue characterization series, the optical fibers were removed and replaced with a thin piece of pasta (Creamette Angel Hair, Borden Inc., Minneapolis MN). The pasta was guided down the catheter to the same depth as the fiber to mark the fiber location. The catheter was removed while the piece of pasta was held in place and then the protruding length of pasta was snapped off. The section of pasta that remained in the tissue absorbed fluid, becoming pliable and capable of moving within the tumor. In addition, the relative positions of the artifacts associated with the mascara marks and the imaging planes were noted and compared to the mascara marks on the animal's skin. Lines were drawn on the animal's skin with marker to designate the approximate location of the imaging plane for each tumor. The animal was sacrificed approximately 2 hours after the treatment and the tumors excised for cell survival analysis.

4.3 Regional Tumor Excision

4.3.1 Region Definition

The tumors were excised under sterile conditions in a laminar flow hood. Two types of tumor excision were performed: the volume regional excision and the single slice regional excision. The volume regional excision was designed to investigate the laser thermal therapy response of various volumes within the tumor, ranging from the core of the tumor near the tip of the optical fiber to the periphery of the tumor. The single slice

regional excision was designed to match the imaged tumor slice and the excised tumor slice and assess the laser thermal therapy response of various tissue volumes within that slice.

The volume regional tumor excision was performed by sacrificing the animals with cervical dislocation under anesthesia, immersing the rats in 95% ethanol and removing the entire tumor. The tumors were then cut into successively smaller volumes, centering the cut volumes on the best estimate of the fiber tip location during the treatment. Each region of tissue was analyzed for tumor cell survival by colony formation.

The single slice regional tumor excision was performed by sacrificing the animals with cervical dislocation under anesthesia, immersing the rats in 95% ethanol and removing the slice of tissue that corresponded as closely as possible to the imaging slice of the tumor. The mascara marks and the marker lines drawn on the animal's skin during the procedure were used to determine the location of the appropriate slice. A tumor slice approximately 3-5 mm thick was removed. The slice of tissue was separated into circular regions using sterile brass tubes with diameters of 5mm, 8mm, 11mm and 14mm as guides. The brass tubes are used as cutting templates to try and produce tissue samples with consistent shapes from consistent positions relative to the optical fiber location.

The brass tube was placed against the tissue with its center approximately at the fiber location, and the tissue outside the tube is cut away be tracing around the tube with a scalpel. In most cases the piece of pasta marking the fiber location can be seen as a light colored element in

the otherwise dark red tumor tissue, allowing the tubes to be placed fairly precisely. Successively smaller tubes are used to separate out the successively smaller annuli. The tumors were irregularly shaped, so there was no guarantee that the outer regions will be complete annuli. Figure 6 contains a schematic of the procedure.

Several factors reduce the ability to match the excised tumor volume with the imaged tumor volume. The consistency of the tumor tissue, particularly after the laserthermia treatment, makes the precise cutting of consistent tumor volumes exceedingly difficult. The skin surrounding the tumor must be removed during the excision, which significantly changes the shape of the tumor. Thus, the orientation of the excised slice may not be the same as the imaged slice and the cross section seen during excision may not exactly match the image.

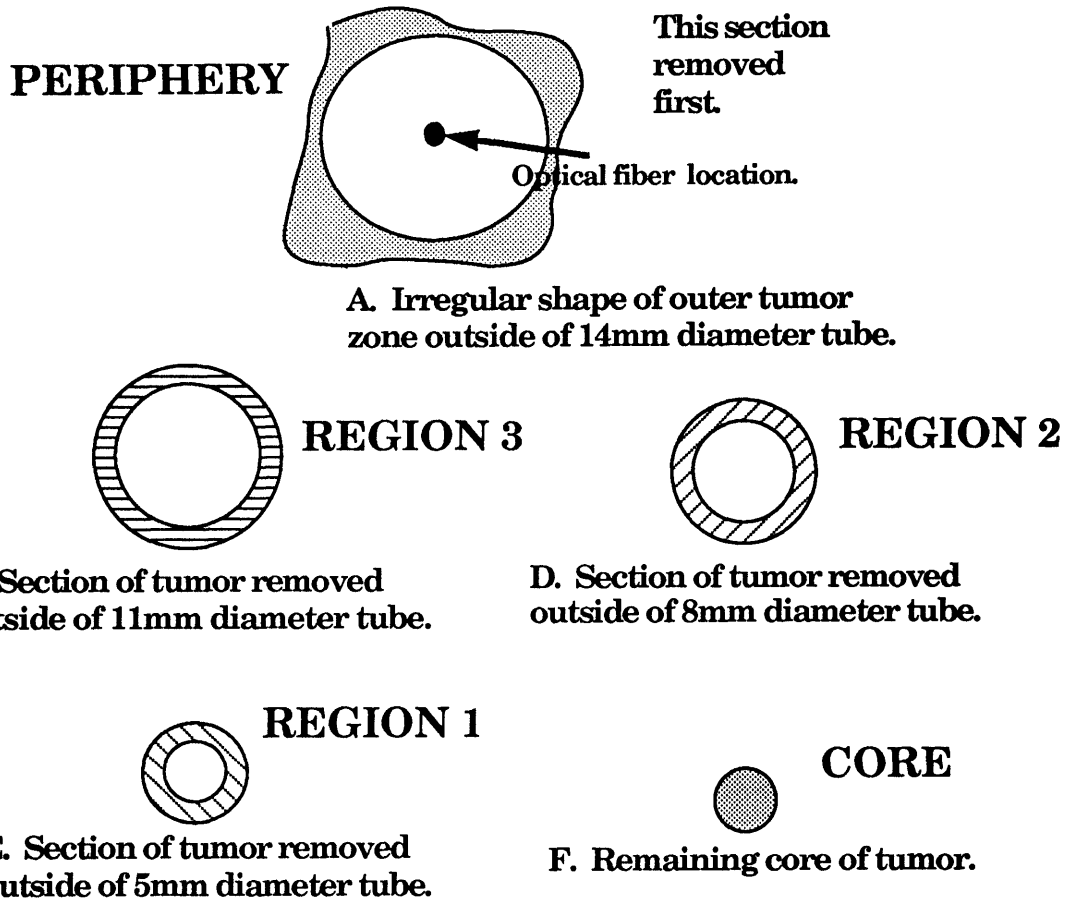

Figure 5.6 Schematic of single slice regional tumor excision procedure. Outermost section of tissue beyond the 14mm outer diameter of the largest cutting template is termed the periphery. Annuli between the successively smaller cutting templates are labelled regions 1, 2 and 3. The remaining section of tissue inside the smallest cutting template is the core.

4.3.2 Preparation of Single Cell Suspensions from the Excised Tumor Regions[5]

All reagants used in the processing were sterilized with 0.22 uM Millipore filters and were added aseptically to the tumor cells. The tissue from a particular region was minced to a fine brei with 2 scalpels. Each sample was washed in 20 ml α-MEM and mixed on a vortex mixer, then the

supernatant was removed and discarded.

The samples were resuspended in α-MEM with the addition of 450 units/ml collagenase (Sigma Chemical Co., St. Louis, MO) and 0.1 mg/ml DNase (Sigma Chemical Co., St. Louis, MO) and incubated for 10 minutes at 37 °C. The samples were then centrifuged at 1000 r.p.m. for one minute and the supernatant was discarded. The samples were again suspended in an identical α-MEM, collagenase and DNase solution and incubated at 37 °C for 15 minutes. One ml of 1 mg/ml DNase was added and incubation was continued for 5 min at 37 °C. The samples were then filtered (Beckton-Dickinson Co., Lincoln Park, NJ). The samples were washed with α-MEM, then resuspended in α-MEM supplemented with 10% fetal bovine serum (Sigma Chemical Co., St. Louis, MO). This process was designed to yield a suspension of single tumor cells representing the cell population of the tumor obtained from each treament region.

The number of cells in each single cell suspension were determined by counting the number of intact tumor cells in 4) $1X10^{-5}$ mL volumes under a microscope with a hemocytometer and computing the average number of cells per mL. This value was used to calculate the suspension volume required to supply a specific number of cells for the different cell densities plated on cell culture dishes. There were six different cell densities plated for each original tumor region. The suspension volume containing the cells is added to a 10mL solution of α-MEM supplemented with 10% Fetal

Bovine Serum in a 100mm^2 cell culture dish and placed in an incubator at 37 °C and 5% CO_2.

The peripheral region of the tumor had the highest surviving fraction of cells, therefore, the number of cells plated for that region ranged from 500 to 10^5 per dish. The number of cells plated for the core region and annular regions 1, 2 and 3, were: 10^4 to $5X10^6$, $5X10^3$ to 10^6, $5X10^3$ to 10^6 and 10^3 to $5X10^5$, respectively. The cells were allowed to grow for one week, then the plates were stained with crystal violet and colonies of 50 cells or more were counted manually. The average plating efficiency of the 6 plates for each region, calculated as the number of colonies divided by the number of cells plated, was normalized to the laboratory standard value for the plating efficiency of untreated, control 9L tumors and the results were expressed as the surviving fraction +/- SE. The resulting data is the average survival probability of a cell in that region.

4.3.3 Assigned Data Values

The tissue sample from the core of the tumor treated in Study #1413-L was lost during the tumor excision procedure. A surviving fraction value was assigned to this region which would eliminate it's significance in any subsequent data analysis but still facilitate data manipulation. The data analysis and fitting programs were allowed to run on this artificial data to evaluate what survival value the program would predict for this region in the abscence of a measured value. Other regions in Studies #1336, #1392, #1413-L and #1413-R had zero colony growth in either the core or the first

annular region. The surviving fraction values in these regions were indeterminate. Similar artificial survival fraction values were assigned to these regions.

4.4 Image Processing

4.4.1 Region of Interest (ROI) Definition

The initial image processing steps were performed with the ANALYZE software package (Mayo Foundation, Rochester MN). Regions of interest (ROIs) were defined whose shape approximately matches the shape of the tumor excision regions. In the first step, the outline of the tumor was traced to determine the outer limits of the ROI. If the thermocouple array could be seen in the image its signal void and any artifacts associated with it were also traced to enclose them and exclude the pixels in that area from any further consideration.

A small circular region was placed over the signal void that represents the fiber location and ROI's of 15, 25, 35 and 45 pixel diameters (physical dimensions of 4.7, 7.8, 10.9 and 14.1 mm) were centered on the optical fiber ROI. The size and location of these regions were designed to represent the size and location of the tumor excision regions. The pixel dimensions used in the annular ROI definitions were the closest match to the physical size of the cutting templates used in the single slice tumor excision procedure.

The match between these ROIs and the excised tumor pieces from

the volume tumor excision experiment was only approximate because of the relatively arbitrary shape and position of the excised tissue pieces. The match between these ROIs and the excised tissue pieces from the single slice tumor excision experiment should be better because of the use of the pasta marker to determine the center of the excision pieces and the consistent size and shape of the cutting pattern.

4.4.2 Tissue Characterization Analysis

The average signal intensity and the standard deviation of the signal intensity from each region was sampled for every image in the pre- and post-treatment tissue characterization studies. The signal intensity values from the CPMG sequence were plotted versus the echo time and fitted to a mono-exponential decay curve described by the equation

$$SI = A \exp\left(\frac{-TE}{T2}\right) + C \qquad 4.1$$

The signal intensity values from the variable TR sequence were plotted versus TR and fitted to an exponential recovery curve described by the equation below. All curve fitting was done with the CPLOT software package.

$$SI = A - B\exp\left(\frac{-TI}{T1}\right) \qquad 4.2$$

4.4.3 Surviving Fraction Analysis

4.4.3.1 Data Preparation

The same ROIs employed in the tissue characterization section were used to analyze the MR images acquired during the laser thermal therapy

treatment, but in these images the signal intensities were sampled on a pixel-by-pixel basis for each of the baseline images and each of the images acquired during the laser treatment. The baseline signal intensity for each pixel was determined by taking the average of it's intensities in the pre-treatment baseline images. The signal intensity changes over time were determined by subtracting the signal intensity of each pixel in each image from its baseline value. The signal intensity changes for each pixel were then converted to percentage signal changes by dividing by the baseline value.

The percentage change values were "DC-filtered" by normalizing to several reference ROIs. The signal intensity changes in the reference ROIs over the course of the treatment were averaged and used to compute a baseline shift factor representing global changes in the signal intensity throughout the entire image over time. Typical values for this factor indicated that the signal intensities in the reference ROIs were typically within 3% of the baseline value, so the system was stable for the duration of the laser thermal therapy treatment. If the system had not been stable the use of the reference ROIs would prevent any slowly varying signal intensity component caused by instabilities in the imaging hardware from creating artificial shifts from baseline. Reference ROI's were chosen in the subcutaneous fat and muscle because their signal intensities should not be affected by the treatment.

4.4.3.2 Calculation of Surviving Fraction from MR Images

The surviving fraction was computed with a multi-step process. The first step involved calculation of the "image dose" for a single pixel for a single image with the image dose equation specified in the image-to-actual-function (IAF) section below. The concept of an "image dose" is introduced to represent the value produced by processing the signal intensity changes over the course of the treatment. The image dose was calculated if the percent signal intensity change ($\%\Delta SI_i$) exceeded the percent signal intensity change threshold (TH_I). TH_I is one of the thresholds used to filter noise out of the computation. If $\%\Delta SI_i$ did not exceed TH_I, the signal intensity change was deemed insignificant and was considered random image noise, and the image dose for that pixel in that image was zero. If the image dose did not reach this threshold level the surviving fraction for that pixel was set to one. If the dose reached the threshold level the dose-response equation was used to compute the surviving fraction.

The image doses of an individual pixel for each image acquired during the treatment were summed. If this sum exceeded the image-dose threshold TH_D, the surviving fraction for that pixel was computed with the dose response equation, the mathematical relationship between the image dose and the image derived surviving fraction. The image dose threshold is the second threshold used to filter noise out of the computation and was used to represent a threshold level of image dose that was required before the tissue would be affected. If the image dose did not exceed the image dose threshold the processed signal intensity changes for that individual

pixel were not significant and the surviving fraction for that pixel was set to one. Both the percent signal intensity change threshold TH_I and the image dose threshold TH_D were subject to change by the fitting algorithm.

This process was repeated for every pixel in an ROI. The average of the surviving fractions of all the individual pixels in an ROI was the surviving fraction for a complete region. Mathematically, this can be represented by

$$SF_{Region} = \frac{1}{\#\text{ of pixels in the region}} \sum_{pixels}^{Region} \left(SF_{pixel} = \text{Dose Response}\left(\sum_{images}^{Treatment} \text{Image Dose}(\%\Delta SI) \right) \right) \quad 4.3$$

A list of the image dose and dose response equations, along with a description of the motiviation for their use, is included in the section on IAFs below.

4.4.3.3 Use of A Priori Knowledge

Several modifiers were used to adjust the cell survival value when the image-derived survival is outside the boundary conditions of the experiment or when it is known that the equations will not account for the changes in the image. If the cell survival value is computed to be >1 the survival value for that pixel is set equal to one. This simply reflects the fact that the surviving fraction value can never be greater than one. It also gives a physical meaning to the sub-threshold section of a dose-response curve. Similarly, the cell survival could not have a negative value.

A second modifier uses information from Lufkin et al[1] that above 60

°C, hemoglobin converts to methemoglobin, which has a significantly shorter T1. This yields a dramatic increase in signal, which is the exact opposite of the signal decrease expected with higher temperatures. However, this change in signal intensity indicates that the voxel of tissue has reached a very high temperature and physiologic changes have occurred which suggest that the surviving fraction there will be effectively zero. This bi-phasic signal intensity change would confuse the image dose algorithm if not handled explicitly.

The algorithms account for this by checking if the signal intensity during the treatment would exceed the baseline average by a certain threshold and setting the surviving fraction of that pixel equal to zero, regardless of the calculated image dose. The threshold must be set high enough that random noise spikes will not cause a pixel's surviving fraction to be set to zero. Analysis of several images that contained this phenomenon determined that 25% was an appropriate value for this threshold. This criteria was also limited in its applicability to the volume immediately adjacent to the fiber and the smallest annular region since changes of this type were not seen beyond the 25 pixel diameter region. The value of this threshold could not be changed by the fitting program.

4.4.3.4 Constrained Coefficients

The boundary conditions in the experiment also led to constraints on the values of coefficients that could be set by the fitting program. All the coefficients in the equations that contributed to the image dose were

constrained to have positive values, signifying that any change in the image represents a negative impact on the surviving fraction. Additionally, coefficients that determine the maximum surviving fraction were not allowed to be less than one, since it was assumed that the tissue was patent at the beginning of the treatment.

4.4.3.5 Fitting Algorithm

The image-derived surviving fraction values for each region in a tumor excision group were compared to the corresponding surviving fraction values measured in the tumor excision experiments. A modified Marquardt-Levenberg, non-linear, least squares curve fitting algorithm[2] was used to determine the equation coefficients that optimize the match between the measured and image-derived values. The algorithm modifications required by these experiments involve the constraints on the possible values of the equation coefficients discussed above and the use of a calculated derivative to determine the multi-dimensional gradient in the coefficient space, discussed below. The Marquardt-Levenberg algorithm optimizes the match between the image-derived and measured surviving fraction values by minimizing the chi squared value, given by

$$\chi^2 = \sum_{\substack{\text{all regions in a given} \\ \text{tumor excision experiment}}} \frac{(SF_M - SF_{ID})^2}{(S.D.)^2} \qquad 4.4$$

where SF_M is the measured surviving fraction from the colony growth

assay, SF_{ID} is the image derived surviving fraction, S.D. is the standard deviation of the surviving fraction in that region and the sum is applied over all the regions in either the volume tumor excision experiment or the single slice tumor excision experiment. The standard deviation reflects the level of confidence in the measured value and thus the priority the algorithm places on fitting the equation to that value.

Preliminary studies showed that the equations employed were not able to account for the multiple logs of cell kill achieved by the treatment. The lowest surviving fraction values were fit most accurately in the initial fitting attempts at the expense of the larger surviving fraction values because of the smaller magnitude standard deviations associated with the lowest surviving fraction values. The smaller magnitude standard deviations are factored into the denominator of the chi-squared computation, effectively multiplying any difference between the measured and image derived values by a large number. It was decided to adjust the standard deviation values to weight the fitting of the highest surviving fraction values most strongly. This was justified by the consideration that in a treatment situation the clinician would be much more interested in knowing the difference between a 50% and 5% surviving fraction than between a 0.01% and 0.001% surviving fraction. The absolute value of the natural log of the surviving fraction was chosen as the S.D. because it was a smoothly varying function, the magnitude did not have the same wide range of values that the true standard deviations did and it weighted the surviving fraction values appropriately with larger numbers for smaller

surviving fractions.

The Marquardt-Levenberg algorithm adjusts the equation coefficients in both the image dose equation and the dose-response equation iteratively by evaluating the surviving fraction with an initial set of coefficients and calculating the partial derivatives of the surviving fraction with respect to each coefficient. The algorithm adjusts each coefficient in the direction that is predicted to reduce the chi squared value, recomputes the function with the new coefficients and evaluates the new chi-squared value. If the new coefficients yield a lower chi-squared value (a better fit), the process begins again. If the new coefficients do not yield a lower chi-squared value the algorithm reduces the magnitude of the coefficient adjustment and tries again.

This approach assumes that the gradient of the chi-squared space near the starting point is accurately reflected by the partial derivatives but that large adjustments in the coefficient values can exceed the range over which the partial derivatives apply. Normally an analytic derivative is computed to provide the algorithm with the appropriate partial derivative, but the use of thresholds in the equations precludes the evaluation of the partial derivatives analytically. The partial derivatives were instead calculated manually by evaluating the functions with 10% positive and negative changes in the coefficients, then dividing the difference in the result by 20% of the coefficient value.

4.4.3.6 Image-to-Actual Functions

Nine different equations were used to attempt to fit the image-derived surviving fraction values to the measured surviving fraction values. Each equation represents a different possible relationship between the signal intensity changes and the surviving fraction. The evolution of the choices of the equations is described below. Several equations were derived from similar equations employed in classical hyperthermia studies, others attempted to mathematically represent the review of the images by a radiologist and others were chosen for their computational simplicity, which could give them a speed advantage in a clinical situation. The symbols for each equation are identical. The percentage signal intensity change in the image *i* is represented by $\%\Delta SI_i$, TH_I is the noise threshold, TH_D is the image dose threshold, a[ ] denotes a fitted parameter, τ_{im} is the duration of an image acquisition, and N is the number of images in the treatment.

4.4.3.6.1 Modified Sapareto-Dewey

In one approach we used a method for determination of an imaging dose that is analogous to the determination of an equivalent thermal dose developed by Sapareto and Dewey[3]. They use the equation

$$t_{equiv} = t * 2^{(T - 43)} \qquad 4.5$$

to compute the equivalent time at 43 °C for a temperature history that covers a range of temperatures. The basic premise is that the effective time at

43°C is the duration of the higher temperature exposure multiplied by a factor of two for every degree Centigrade above 43 °C. Thus, the level of cell kill reached with an hour exposure at 43 °C would be reached in 30 minutes at 44 °C, 15 minutes at 45 °C, etc. This relationship only applies to a limited temperature range. Above 60 °C the mechanisms appropriate to the limited hyperthermia temperature range can be superseded by other mechanisms and the equation could no longer apply.

The equation was modified slightly to allow the coefficients of the equation to be fit by the computer. We added a multiplicative factor in front of the difference between the percentage signal intensity change and the threshold. This effectively acts as a scale factor. For example, a value of 100 would dictate that every 1% change in image intensity has the same impact on cell survival that a 1 °C change does for Sapareto-Dewey. We also allowed the rate factor to be fit by the computer since we could not predict if the signal intensity-survival relationship would use a factor of two, as in the thermal dose calculation of Sapareto-Dewey. This produced the following image dose equation:

$$\tau_{equiv} = \tau_{im} * \sum_{i=1}^{N} a[1]^{a[2]\,(\%\Delta SI - TH_I)} \qquad \text{for } \%\Delta SI > TH_I \tag{4.6}$$

$$\tau_{equiv} = 0 \qquad \text{for } \%\Delta SI < TH_I \tag{4.7}$$

The τ_{equiv} is then used in the following dose-response equation to compute the image-derived cell survival.

$$S.F. = a[3] * \exp\left(\frac{TH_D - \tau_{equiv}}{a[4]}\right) \quad \text{for } \tau_{equiv} > TH_D \tag{4.8}$$

$$S.F. = 1 \quad \text{for } \tau_{equiv} < TH_D \tag{4.9}$$

4.4.3.6.2 Exponential

This approach tries to relate the measured to image-derived surviving fractions with an exponential function as the dose-response function and a polynomial of the percent signal intensity change as the image dose function. The sum of the terms for each image reflects the progressive impact continued changes have on the remaining cells, since a sum of terms in an exponential is equivalent to successive multiplications of an exponential of each term.

$$e^{x1} * e^{x2} * e^{x3} = e^{(x1 + x2 + x3)} \tag{4.10}$$

The equation used is

$$dose = \sum_{i=1}^{N} \left(a[4]*(\%\Delta SI_I - TH_I) + a[5]*(\%\Delta SI_I - TH_I)^2 + a[6]*(\%\Delta SI_I - TH_I)^3\right) * \tau \quad \text{for } \%\Delta SI_I > TH_I \tag{4.11}$$

$$dose = 0 \quad \text{for } \%\Delta SI_I < TH_I \tag{4.12}$$

$$S.F. = a[3] * \exp(TH_D - dose) \quad \text{for dose} > TH_D \tag{4.13}$$

$$S.F. = 1 \quad \text{for dose} < TH_D \tag{4.14}$$

These were the first two equations tested. The ability to fit the measured cell survival values with the image-derived values with these

equations was limited. The highest level of survival could be fit fairly well, as will be shown in Chapter 5, but the multiple logs of cell kill could not be accounted for. This led to the use of other dose equations with terms emphasizing different physical aspects of the experiment.

4.4.3.6.3 Exponential-Rate

This approach also employed an exponential function for the dose-response relationship, but it replaced the $\%\Delta SI_i{}^3$ term in the dose calculation with a term representing the rate of change of the signal intensity, since rates frequently have a significant impact on treatment effectiveness. This function is described by the following equation

$$dose = \sum_{i=1}^{N} \left(a[4]*(\%\Delta SI_I - TH_I) + a[5]*(\%\Delta SI_I - TH_I)^2\right) * \tau + a[6]*\frac{(\%\Delta SI_I - \%\Delta SI_{I-1})}{\tau} \quad \text{for } \%\Delta SI_I > TH_I \tag{4.15}$$

$$dose = 0 \quad \text{for } \%\Delta SI_I < TH_I \tag{4.16}$$

$$S.F. = a[3] * \exp(TH_D - dose) \quad \text{for dose} > TH_D \tag{4.17}$$

$$S.F. = 1 \quad \text{for dose} < TH_D \tag{4.18}$$

4.4.3.6.4 Exponential-Rate-Cubed

This approach also employed an exponential function for the dose-response relationship, but it dropped the magnitude squared term and employed both the $\%\Delta SI_i{}^3$ term and the term representing the rate of change of the signal intensity in the dose calculation. This function is described by the following equation

$$\text{dose} = \sum_{i=1}^{N} \left(a[4]*(\%\Delta SI_I - TH_I) + a[5]*(\%\Delta SI_I - TH_I)^3\right) * \tau + a[6]*\frac{(\%\Delta SI_I - \%\Delta SI_{I-1})}{\tau} \quad \text{for } \%\Delta SI_I > TH_I \tag{4.19}$$

$$\text{dose} = 0 \quad \text{for } \%\Delta SI_I < TH_I \tag{4.20}$$

$$S.F. = a[3] * \exp(TH_D - \text{dose}) \quad \text{for dose} > TH_D \tag{4.21}$$

$$S.F. = 1 \quad \text{for dose} < TH_D \tag{4.22}$$

4.4.3.6.5 Exponential-Rate-Magnitude

A further adaptation of this approach continued to use a polynomial of the percent signal intensity change but exchanged the magnitude squared term with a term employing the rate-of-change multiplied by the magnitude, to represent the greater significance of changes that continue to occur at signal intensity changes of greater magnitude. The function is

$$\text{dose} = \sum_{i=1}^{N} \begin{array}{l} a[4]*(\%\Delta SI_I - TH_I)*\tau \\ + a[5]*(\%\Delta SI_I - TH_I)*\frac{(\%\Delta SI_I - \%\Delta SI_{I-1})}{\tau} \\ + a[6]*\frac{(\%\Delta SI_I - \%\Delta SI_{I-1})}{\tau} \end{array} \quad \text{for } \%\Delta SI_I > TH_I \tag{4.23}$$

$$\text{dose} = 0 \quad \text{for } \%\Delta SI_I < TH_I \tag{4.24}$$

$$S.F. = a[3] * \exp(TH_D - \text{dose}) \quad \text{for dose} > TH_D \tag{4.25}$$

$$S.F. = 1 \quad \text{for dose} < TH_D \tag{4.26}$$

4.4.3.6.6 Polynomial

This approach tried to relate the measured to image-derived surviving fractions with a simple polynomial. This is a mathematically simple approach the could approximate interpretation of dynamic images by a

radiologist or surgeon. This approach could be approximated by the statement that a 25% decrease in signal intensity would represent a 25% cell kill. The actual equation employed is more complex and a three term polynomial with the signal intensity to the first, second and third power is used to account for the possibility of quadratic or cubic dependencies in addition to the basic linear dependency.

$$\text{dose} = \sum_{i=1}^{N} \left(a[4]*(\%\Delta SI_I - TH_I) + a[5]*(\%\Delta SI_I - TH_I)^2 + a[6]*(\%\Delta SI_I - TH_I)^3\right) * \tau \quad \text{for } \%\Delta SI_I > TH_I \tag{4.27}$$

$$\text{dose} = 0 \quad \text{for } \%\Delta SI_I < TH_I \tag{4.28}$$

$$S.F. = 1 - (\text{dose} - TH_D) \quad \text{for dose} < TH_D \tag{4.29}$$

$$S.F. = 1 \quad \text{for dose} < TH_D \tag{4.30}$$

4.4.3.6.7 Maximum-Exponential

This approach postulates that the image dose could be related to the maximum signal intensity change detected over the course of the treatment. This could reflect the possibility that the accumulated signal intensity history of the experiment, which was used in the earlier equations, is less significant than the maximum temperature that was reached or the maximum signal intensity change that was achieved. This approach used an exponential for the dose-response equation.

$$\text{dose} = \left(a[4]*\text{max} + a[5]*\text{max}^2\right) * \tau \tag{4.31}$$

$$S.F. = a[3] * \exp(TH_D - \text{dose}) \quad \text{for dose} > TH_D \tag{4.32}$$

$$S.F. = 1 \quad \text{for dose} < TH_D$$

4.33

4.4.3.6.8 Maximum-Polynomial

This approach uses the same idea that the maximum signal intensity change detected over the course of the treatment is the most significant parameter, but it used a polynomial instead of an exponential for the dose-response equation.

$$\text{dose} = \left(a[4]*\max + a[5]*\max^2\right) * \tau \tag{4.34}$$

$$\text{dose} = 0 \quad \text{for } \%\Delta SI_I < TH_I \tag{4.35}$$

$$\text{S.F.} = 1 - (\text{dose} - TH_D) \quad \text{for dose} < TH_D \tag{4.36}$$

$$\text{S.F.} = 1 \quad \text{for dose} < TH_D \tag{4.37}$$

4.4.3.6.9 Activation Energy

This approach uses a polynomial to compute the image dose but uses an activation energy-type equation as the dose response equation. The equation for the image dose is

$$\text{dose} = \sum_{i=1}^{N} \left(a[4]*\left(\%\Delta SI_I - TH_I\right) + a[5]*\left(\%\Delta SI_I - TH_I\right)^2\right) * \tau \quad \text{for } \%\Delta SI_I > TH_I \tag{4.38}$$

$$\text{dose} = 0 \quad \text{for } \%\Delta SI_I < TH_I \tag{4.39}$$

and the corresponding dose response equation

$$\text{S.F.} = 1 - \exp\left(\frac{a[6]}{TH_D - \text{dose}}\right) \quad \text{for dose} > TH_D \tag{4.40}$$

$$\text{S.F.} = 1 \quad \text{for dose} < TH_D \tag{4.41}$$

REFERENCES

4. Barker M, Hoshino T, Gurcay O, Wilson CB, Nielsen SL, Downie R and Eliason J. Development of an animal brain tumor model and its response to therapy with 1,3-bis(2-chloroethyl)-1-nitrosourea. *Cancer Research.* 33: 976-986, 1973.

5. Teicher BA, Holden SA, Ara G, Sotomayor EA, Menon K, Tarbell NJ, Sallan SE. Etanidazole as a modulator of combined modality therapy in the rat 9L gliosarcoma. *International Journal of Oncology.* 1:625-630, 1992.

1. Lufkin RB, Saxton RE, Kirlew K, Sinha S, Anzai Y, DeSalles AAF, Black KL. MR imaging of thermally coagulated blood: Applications in image-monitored thermal ablations. *Journal of Magnetic Resonance Imaging (Suppl.)* 4P:S41, 1994.

2. Press WH, Vetterling WT, Teukolsky SA, Flannery BP. *Numerical Recipes in C: The Art of Scientific Computing.* Cambridge University Press, NY, NY, 1992.

3. Sapareto SA, Dewey W. Thermal dose determination in cancer therapy. *Int. Journal of Radiation, Oncology, Biology and Physics.* 10:787-800, 1984.

Chapter 5: Results

5.1 System Performance

5.1.1 System Integration

The data acquisition system designed and built for these experiments performed admirably. The integration of the imaging, laser and temperature measurement systems allowed the operator to focus primarily on the intra-operative MR images, as they were reconstructed and displayed, without having to be concerned about proper recording of the ancillary data acquired during the experiment. The interactive control of the imager and the temperature measurement electronics via the combination of the modified pulse sequence and the program running on the PC guaranteed proper timing of the temperature measurements as well as temperature values uncorrupted by the radio frequency waves employed by the imager. The automatic annotation of the temperature file with the image numbers and time of temperature measurement simplified post-processing of the data and facilitated the signal intensity-temperature correlations reported in Chapter 3 and the surviving fraction-temperature data reported later in this chapter.

5.1.2 Imaging Features

The use of a "product" pulse sequence as the basis for the modified pulse sequence allowed use of the full range of features available in a product sequence. This was critical in reducing the time required for a single intra-operative image acquisition because it allowed use of the 3/4

field of view in the phase direction feature , which effectively reduced the image acquisition time by 1/4. This allowed the acquisition of four images per minute instead of three, a significant improvement in temporal resolution.

5.2 Animal Experimental Results

5.2.1 Data Format

Four tumors were treated and processed with the volume tumor excision technique. The data is labelled with the imaging study number and an R or L to denote the right or left tumor for animals that had two treated tumors. The studies that were done for the volume tumor excision group were #984-R, #984-L, #1151-R and #1151-L. Five tumors were treated and processed with the single slice tumor excision technique. The data will be labelled in the same manner as in the volume tumor excision group. The studies that were done for the single slice tumor excision group were #1282, #1336, #1392, #1413-R and #1413-L.

5.2.2 Optical Fiber Placement

Images from the volume tumor excision group indicate that in Studies #984-R and #984-L the optical fibers were placed close to the center of the tumor, as intended, while the images from Studies #1151-R and #1151-L show that the fibers were much closer to the medial muscle tissue and that the treatment was distinctly asymmetric. See Appendix A1. The outer annular ROI's in Study #1151 only contained tumor tissue in

approximately 1/2 - 2/3 of their pixels. In the single slice tumor excision group the optical fiber locations were also mixed, with the fibers in Studies #1282 and #1336 slightly off-center and the fibers in the remaining studies well-placed in the center of the tumor.

5.2.3 Colony Growth Assay Results

5.2.3.1 Volume Tumor Excision

5.2.3.1.1 Surviving Fraction Data

The colony growth assay results from the volume tumor excision experiments are shown in Figure 1. The results indicate that surviving fraction values <1% were achieved in the core of three of the four tumors with the thermal therapy treatment protocol employed in this study. The maximum surviving fractions in the various regions, starting from the core and moving outwards, was 1.4%, 6.7%, 4.0%, 15.4% and 40.5%. The 15.4% surviving fraction in the third annular region was from Study #984-L and was larger than the surviving fraction from the other tumors (6.3%, 7.4% and 7.0%), which was probably due to the abbreviated treatment in that tumor. The animal woke up during the treatment so the laser exposure only lasted approximately 6 minutes instead of the prescribed 10 minutes.

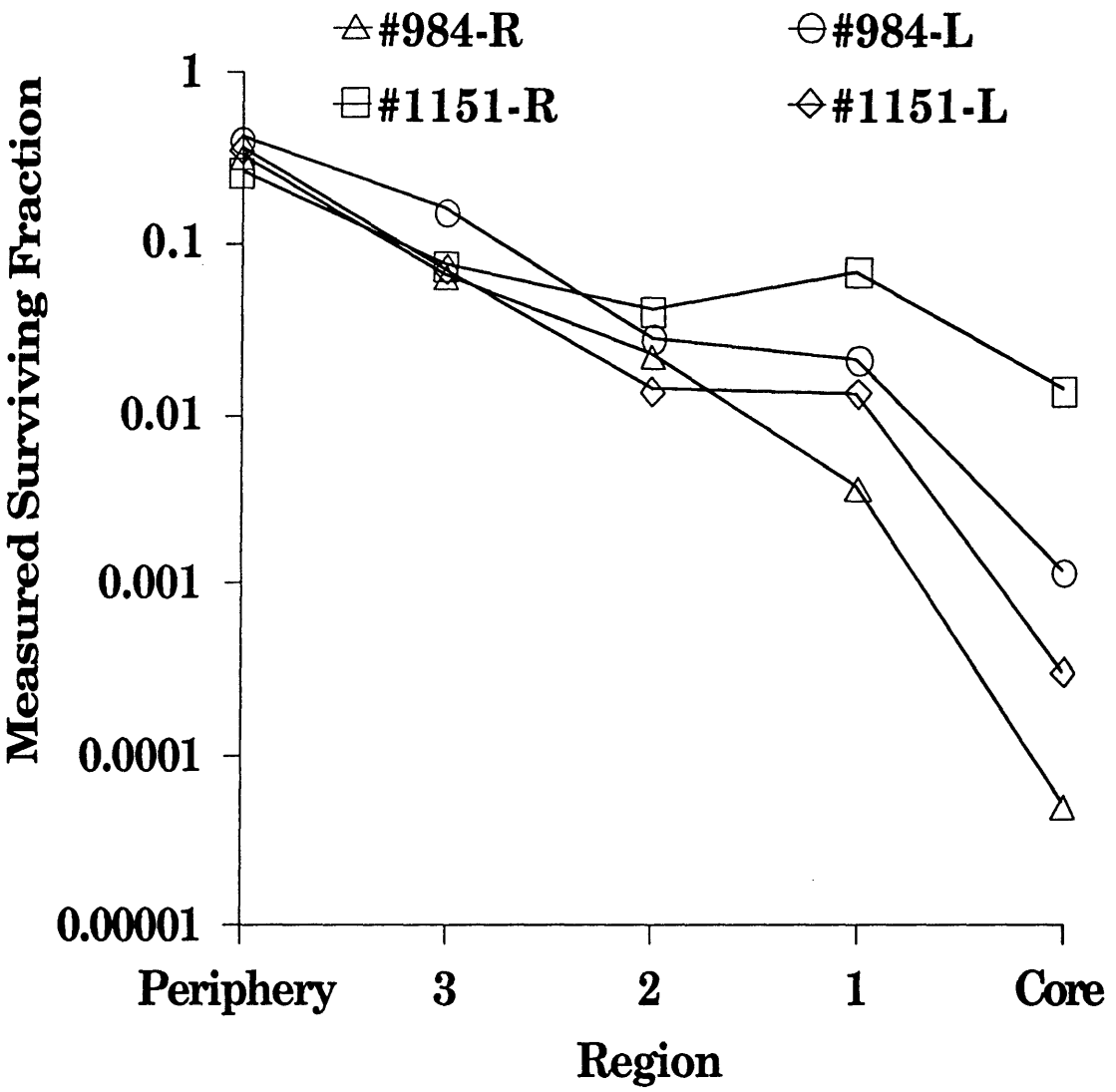

Figure 5.1 Surviving fraction values of four 9L-50 gliosarcoma tumors after laser thermal therapy treatment with Nd:YAG laser (λ=1064 nm) and diffusing tip optical fiber, as measured with the volume tumor excision colony growth assay. Tumor excision ~2 hours after treatment. Treatment for Study #984-L was 1.5W, 6 minutes. Treatment for all other Studies was 1.5W, 10 minutes.

5.2.3.1.2 Intra-Operative Temperature Data

The intra-operative temperature measurements from the tumors in the volume tumor excision group are displayed in Figures 5.2-5.5. All temperatures were measured with teflon-coated, 36G wire, copper-

constantin thermocouples (Omega Inc.) at three locations in the tumor and in the rectum of the animal. Temperatures are °C and are graphed versus time. The location of the thermocouples relative to the optical fiber in the MR images was used to assign each thermocouple to the tumor excision region in which it was most likely located. The artifacts associated with the thermocouples and the gap between localizer slices combine to prevent accurate thermocouple-to-region assignment, but the results represent the best possible estimate with all the information available. The three thermocouple array and the BASIC program for temperature measurement were described in Chapter 4. The higher density of data points at the beginning and end of the laser exposure ($t \approx 50$ seconds and $t \approx 650$ seconds) represent the rapid temperature measurement mode used to study the effect of the laser light on the thermocouples.

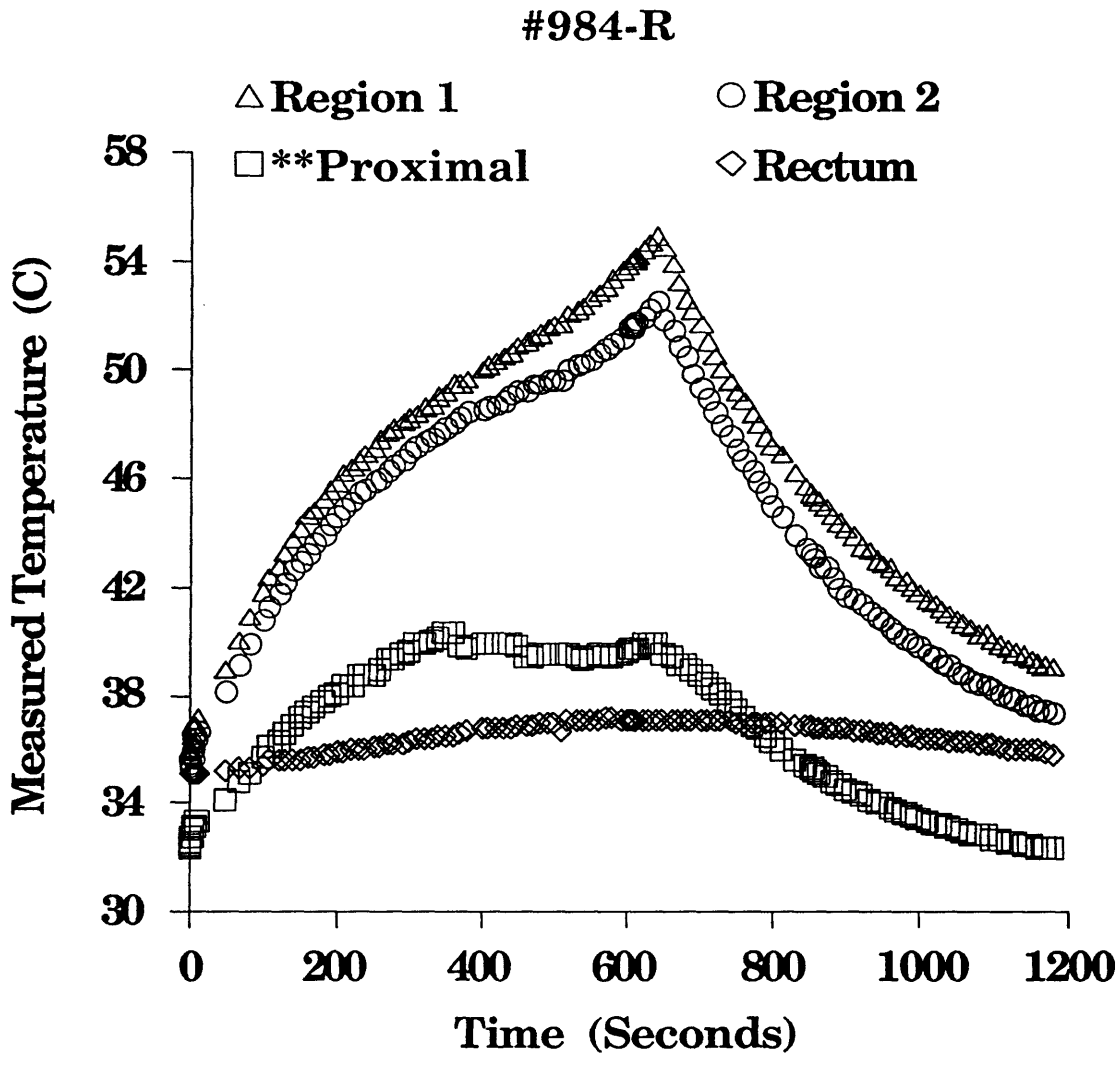

Figure 5.2 Measured tumor and rectal temperatures from Study #984-R. Laser exposure 1.5W, 10 minutes. Tumor excision region correspondence for thermocouple located at proximal position on three thermocouple array could not be determined.

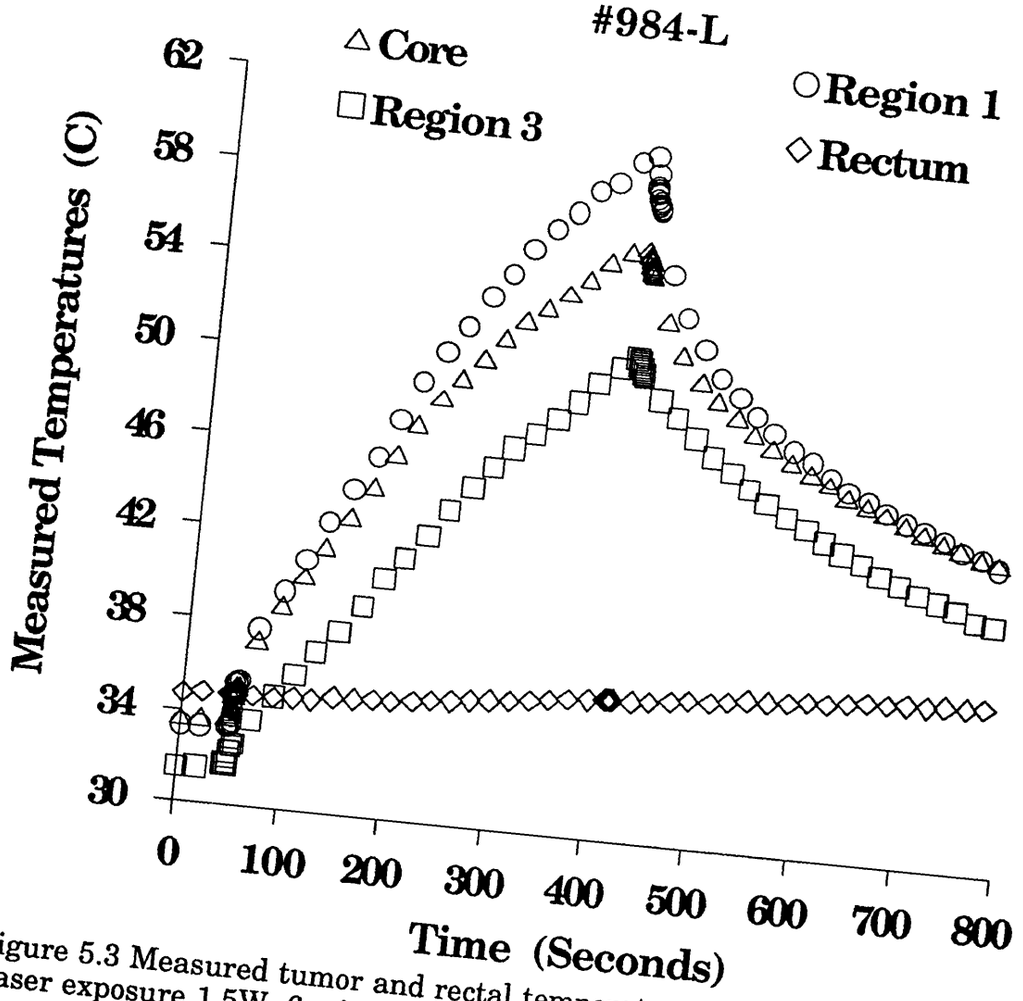

Figure 5.3 Measured tumor and rectal temperatures from Study #984-L. Laser exposure 1.5W, 6 minutes. Animal woke up in the middle of the laser treatment and forced termination of laser exposure prior to prescribed 10 minutes.

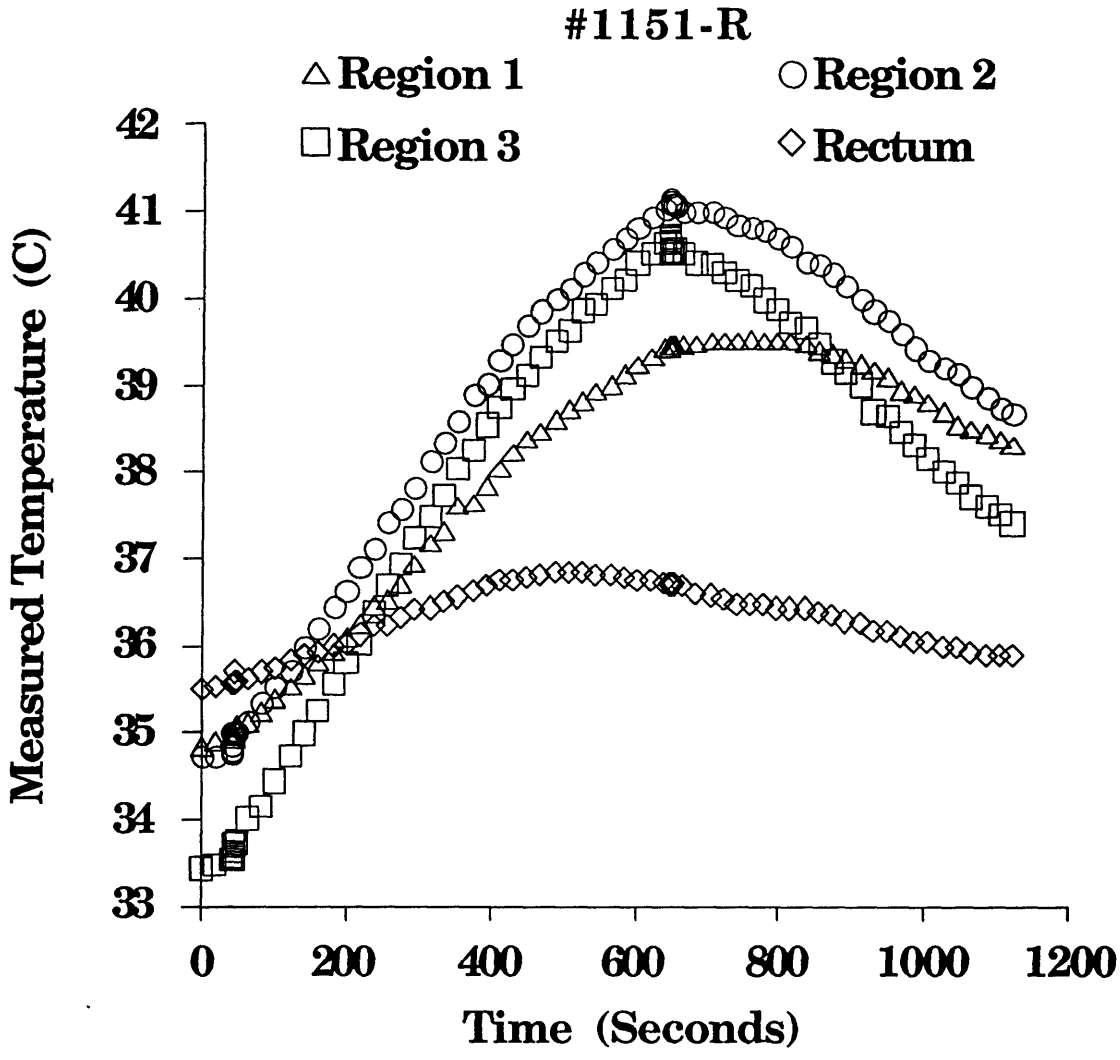

Figure 5.4 Measured tumor and rectal temperatures from Study #1151-R. Laser exposure 1.5W, 10 minutes. Note relatively mild temperature increases.

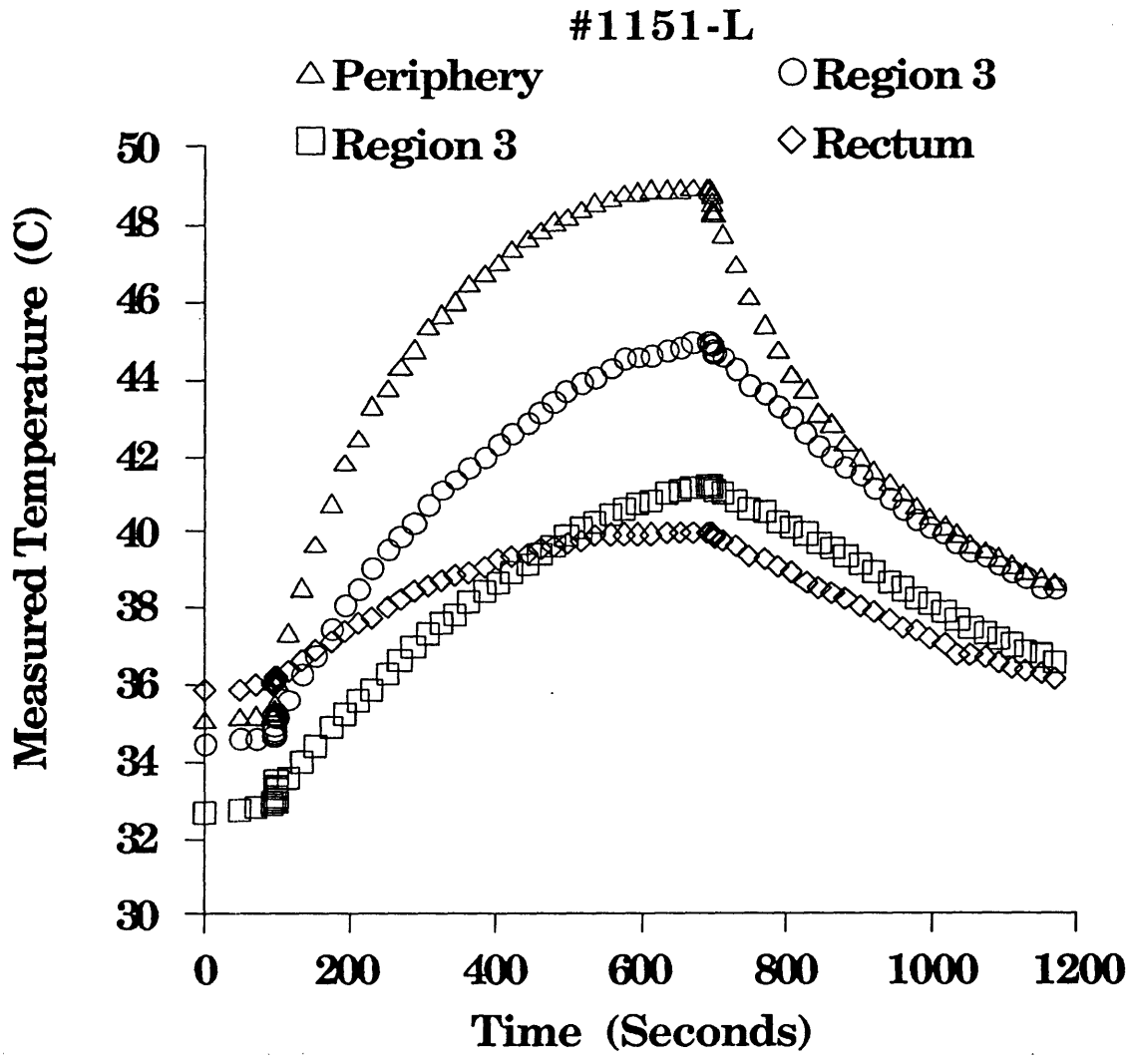

Figure 5.5 Measured tumor and rectal temperatures from Study #1151-L. Laser exposure 1.5W, 10 minutes. Note core temperature approaches 40°C.

5.2.3.1.3 Surviving Fraction vs Peak Measured Temperature

The assignment of thermocouples to tumor excision regions allows examination of the relationship between the measured surviving fraction for a region and the peak temperature measured in the corresponding region. Figure 6 presents this data for the tumors in the volume tumor

excision colony growth assay group. Two thermocouples from Study #1151-L were assigned to Region 3 and the maximum temperature recorded by both was recorded in the graph.

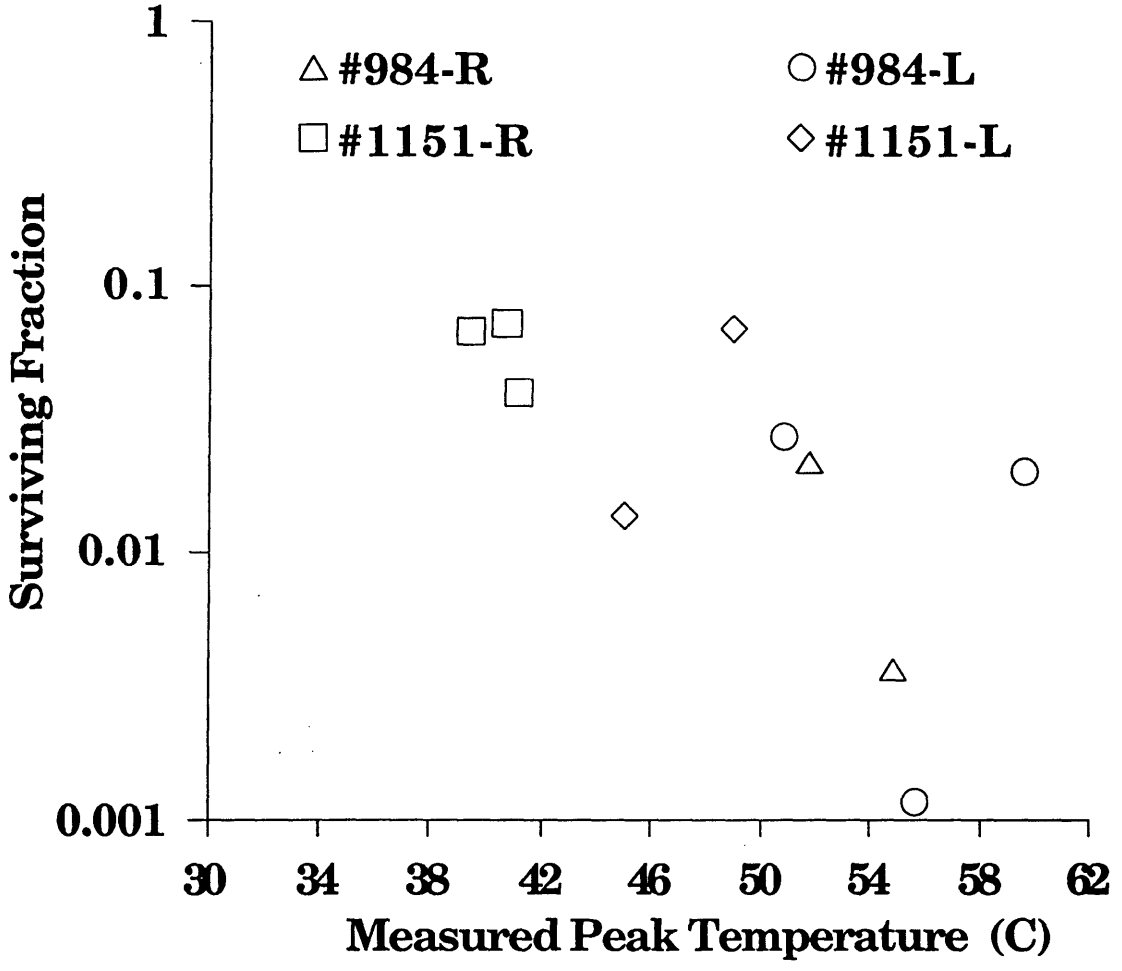

Figure 5.6 Measured surviving fraction vs peak measured temperature for tumors from the volume tumor excision colony growth assay. The thermocouples were assigned to a tumor excision region based on their location relative to the optical fiber as determined from the MR images. The artifacts associated with the thermocouples and the gap between localizer slices prevent accurate assignment but the results represent the best possible estimate with all the information available. The surviving fraction of each region was plotted as a function of the maximum temperature measured with its corresponding thermocouple.

5.2.3.2 Single Slice Tumor Excision

5.2.3.2.1 Surviving Fraction Data

The surviving fraction values from the single slice tumor excision experiment are shown in Figure 7. These surviving fraction values characterize the treatment response in a plane perpendicular to the axis of the fiber and located near the tip of the fiber, which should be the area of maximum effect because of the fiber output pattern. In an ideal situation the treatment Zones discussed in Chapter 1 would be radially symmetric around the fiber in this plane. The maximum surviving fraction in the core region of the single slice excision group was $1X10^{-4}$%, and only four of the thirteen intermediate annular regions had surviving fractions as large as 1-5%. This supports the proposition that the slices excised from these tumors were located in or near the maximum treatment area. These results also indicate that the fiducials and the concentric regional excision centered on the pasta marker combined to improve the alignment of the excision regions with the treatment Zones in the tissue. The outermost region surviving fractions in the single slice tumor excision experiment ranged from 10-38%, which approximately match the peripheral surviving fractions from the volume tumor excision experiment.

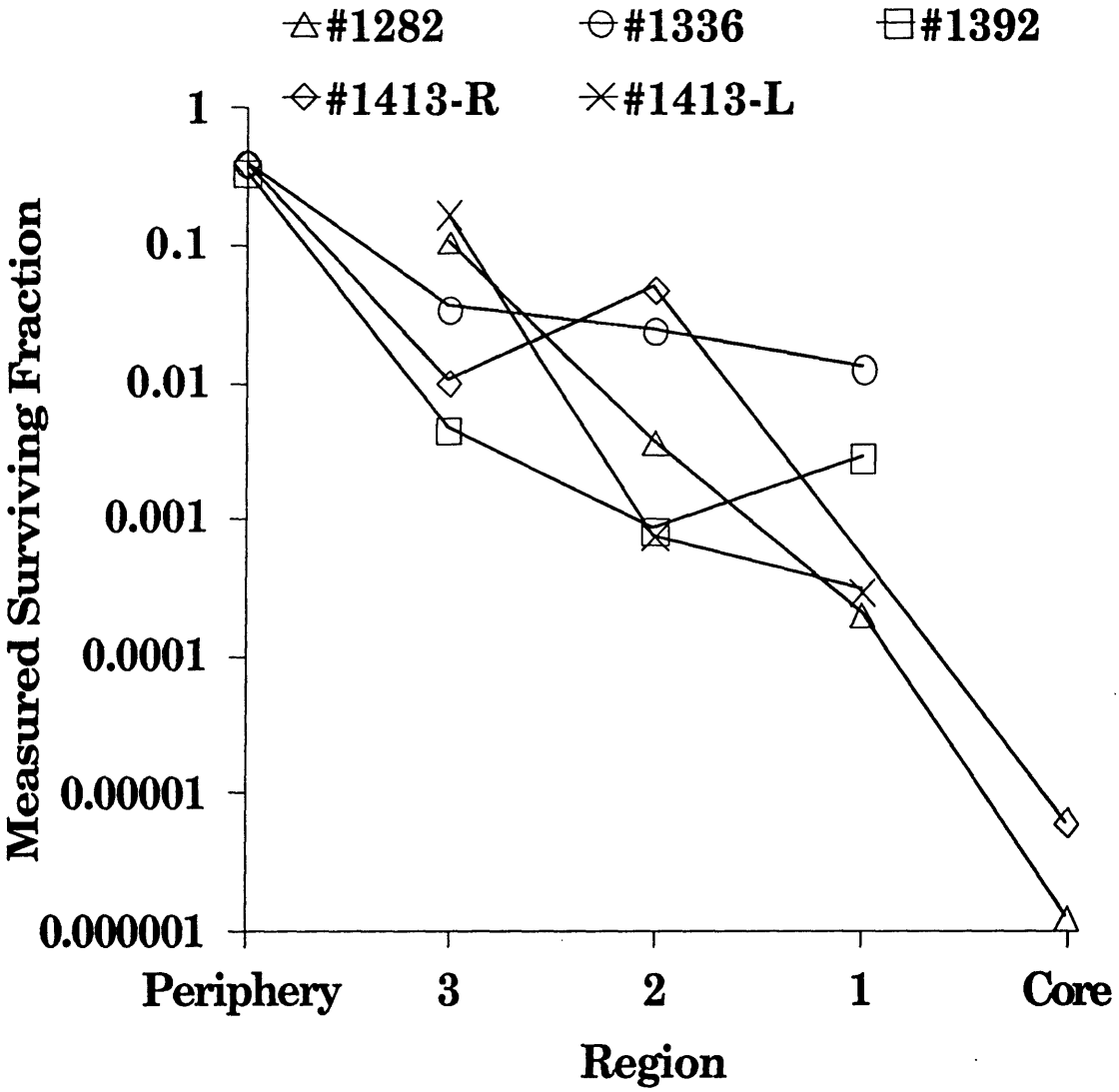

Figure 5.7 Surviving fraction values of five 9L-50 gliosarcoma tumors after laser thermal therapy treatment with Nd:YAG laser (λ=1064 nm) and diffusing tip optical fiber, as measured with the single slice tumor excision colony growth assay. Tumor excision ~2 hours after treatment. Laser treatment for all studies was 1.5W, 10 minutes. Missing data values in core for studies #1336, #1392 and #1413-L and in region 1 for study #1413-R reflect the fact that none of the plated cells formed colonies so the surviving fraction is indeterminate. Missing data values in periphery for studies #1282 and #1413L indicate that the tumor diameter was less than 14mm in the excised slice.

5.2.3.2.2 Intra-Operative Temperature Data

The intra-operative temperature measurements from the tumors in the single slice tumor excision group are displayed in Figures 8-12. All temperatures were measured with teflon-coated, 36G wire, copper-constantin thermocouples (Omega Inc.) at three locations in the tumor and in the rectum of the animal. The location of the thermocouples relative to the optical fiber in the MR images was used to assign each thermocouple to the tumor excision region in which it was most likely located. The artifacts associated with the thermocouples and the gap between localizer slices prevent accurate assignment but the results represent the best possible estimate with all the information available. Temperatures are °C and are graphed vs time. The three thermocouple array and the BASIC program for temperature measurement was described in Chapter 4. The higher density of data points at the beginning and end of the laser exposure ($t \approx 50$ seconds and $t \approx 650$ seconds) represents the rapid temperature measurement mode used to study the effect of the laser light on the thermocouples. Note the lack of a precipitous increase or decrease in temperature that would indicate the laser light has a direct effect on the thermocouples.

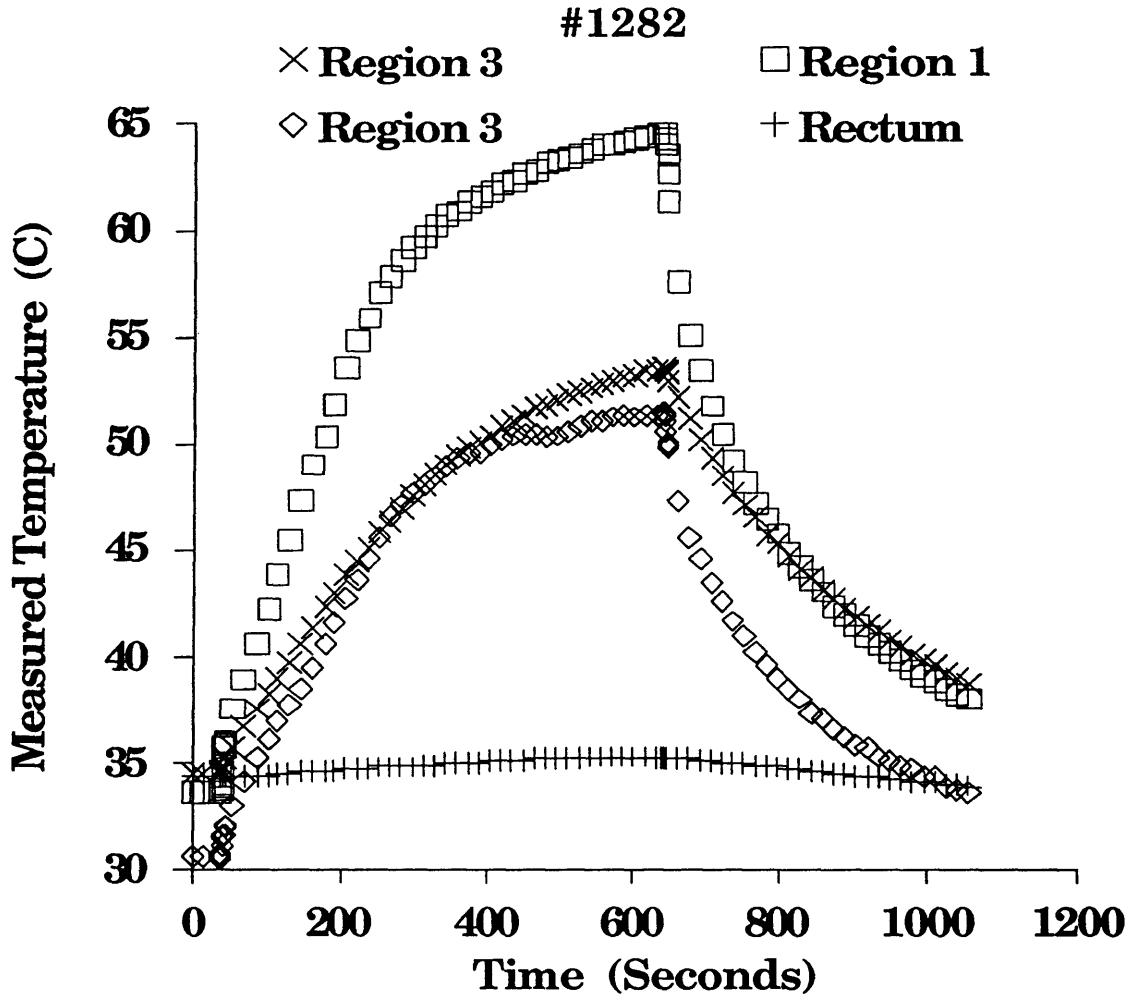

Figure 5.8 Measured tumor and rectal temperatures from Study #1282. Laser exposure 1.5W, 10 minutes.

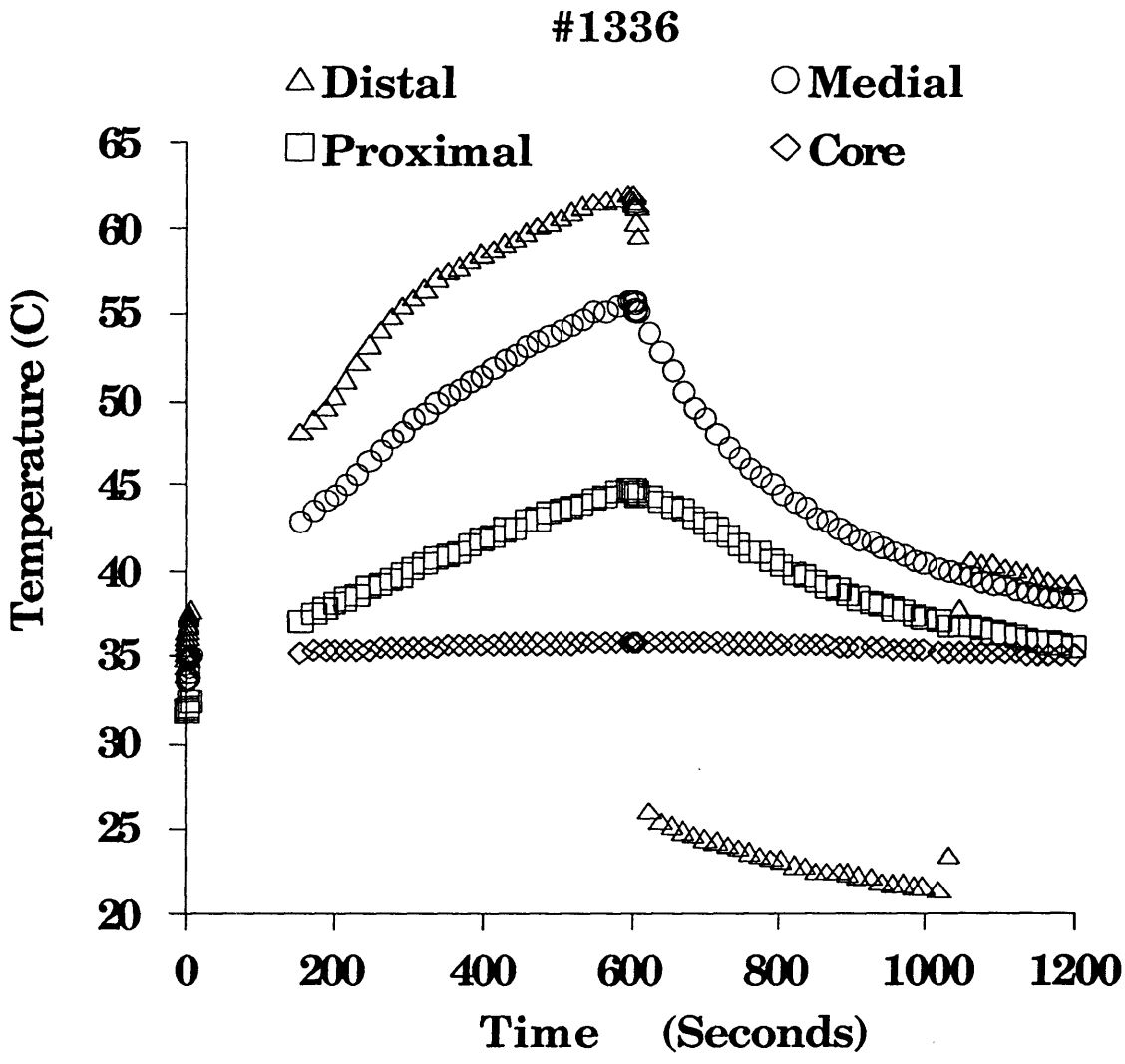

Figure 5.9 Measured tumor and rectal temperatures from Study #1336. Laser exposure 1.5W, 10 minutes. Thermocouple location relative to tumor excision regions could not be determined. Thermocouple locations are sited relative to their position on the three thermocouple array. Thus, the distal thermocouple on the probe is the most medial relative to the animal and the proximal thermocouple is the most lateral relative to the animal. Distal thermocouple electronics failure partway through experiment yielded erroneous values. Communication failure caused delay in automatic temperature recording until ≈140 seconds after start of laser exposure.

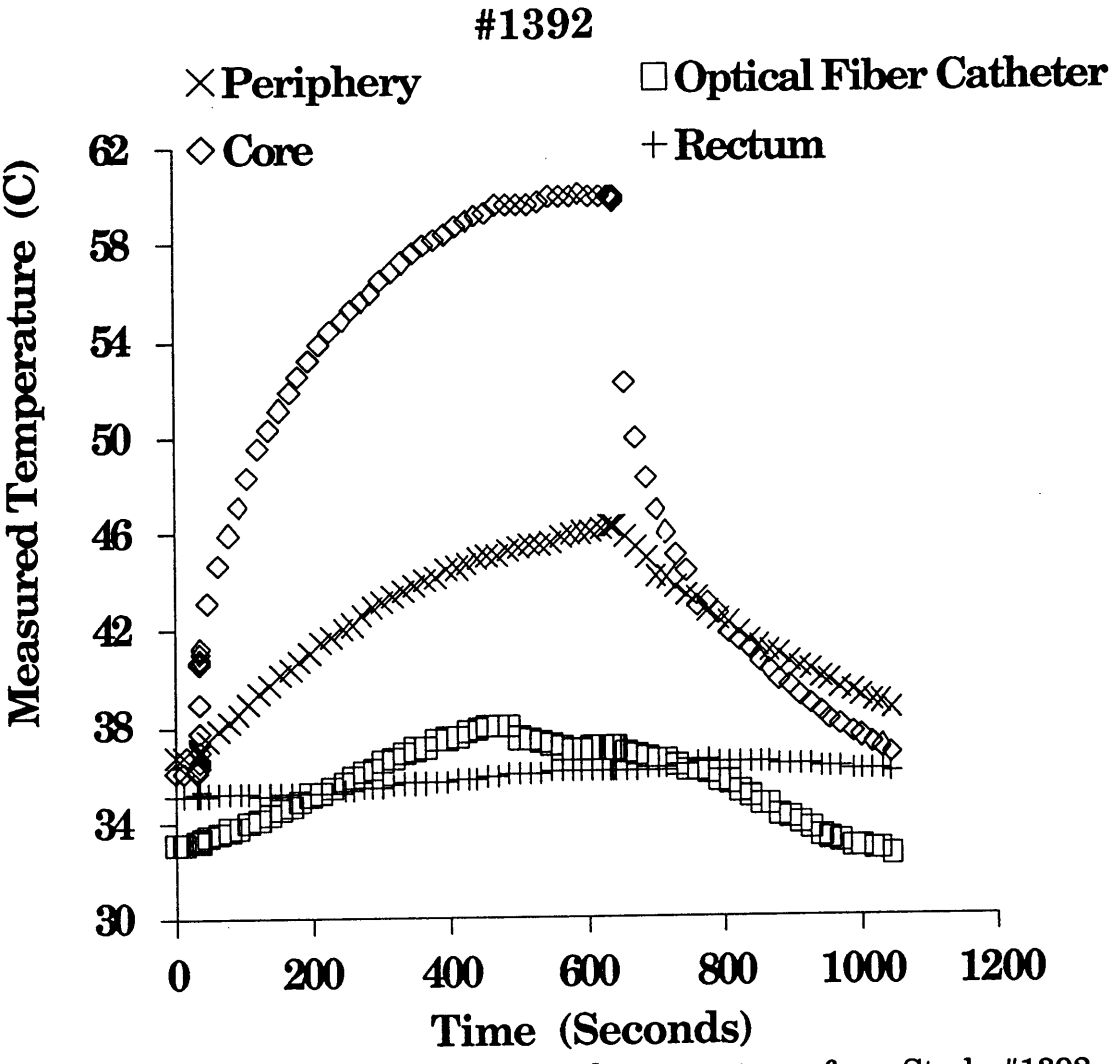

Figure 5.10 Measured tumor and rectal temperatures from Study #1392. Laser exposure 1.5W, 10 minutes. Medial thermocouple on array failed so thermocouple located on optical fiber catheter was used for automatic recording.

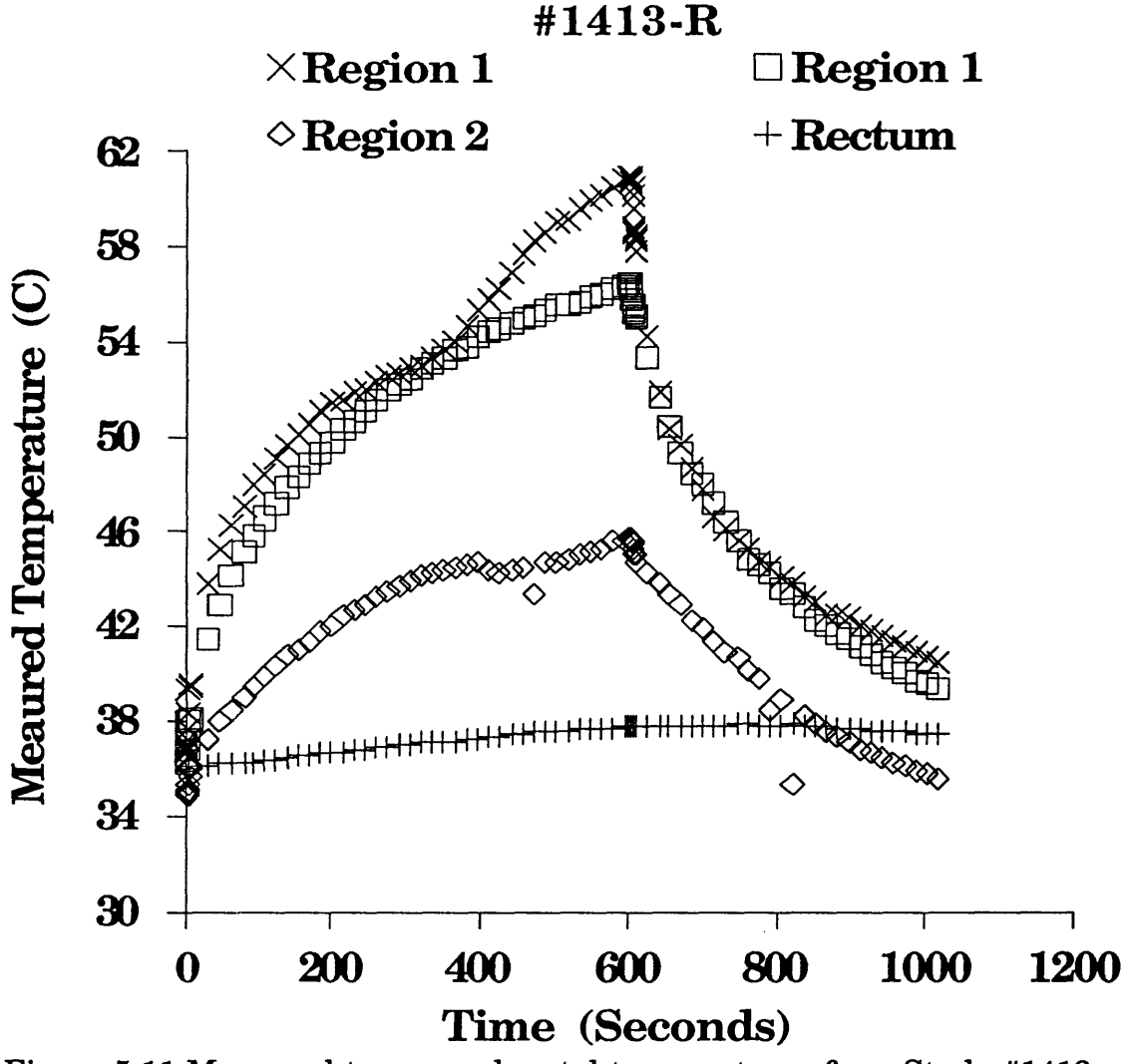

Figure 5.11 Measured tumor and rectal temperatures from Study #1413-R. Laser exposure 1.5W, 10 minutes. Outlier data points in Region 2 curve are attributed to intermittent cable and connection problems.

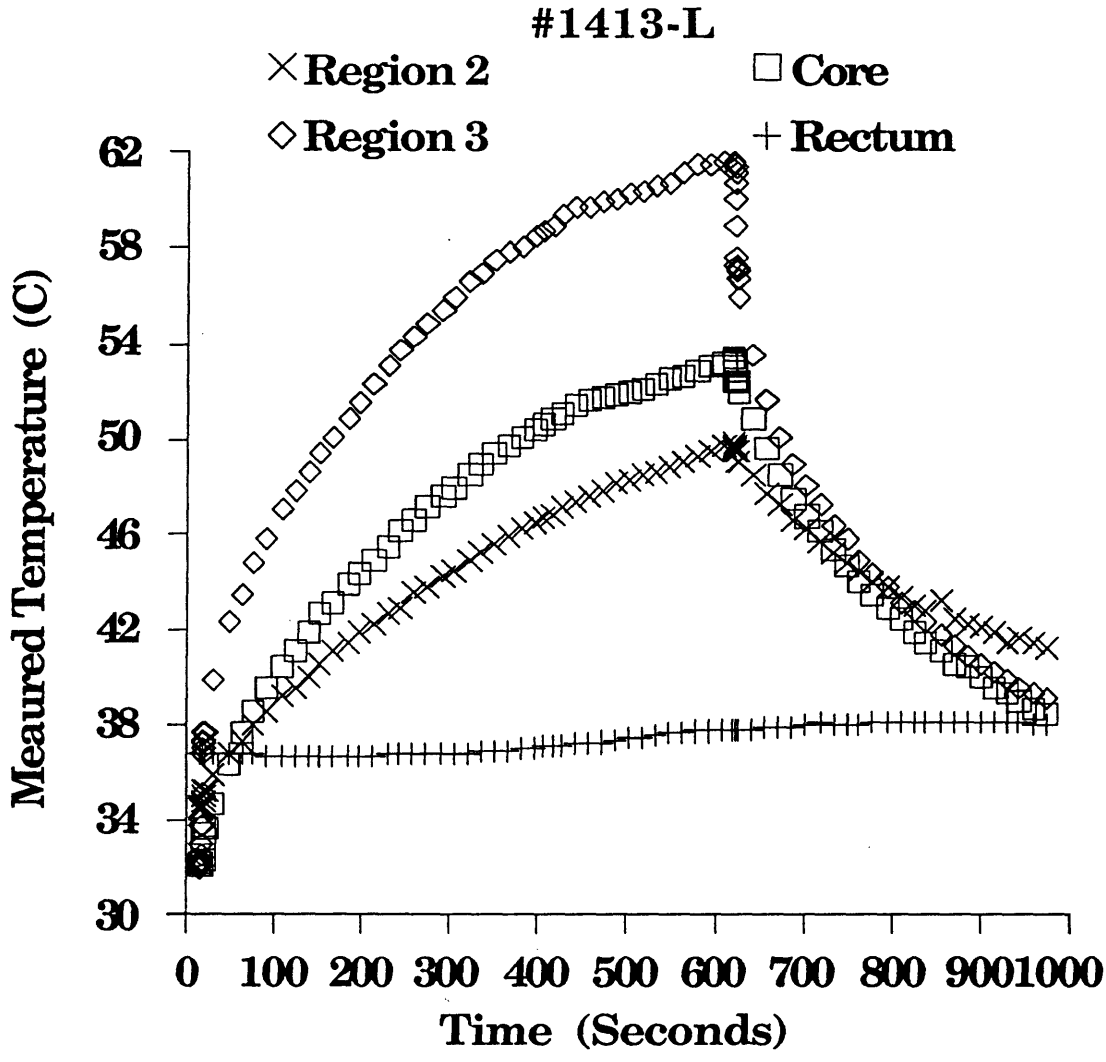

Figure 5.12 Measured tumor and rectal temperatures from Study #1413-L. Laser exposure 1.5W, 10 minutes.

5.2.3.2.3 Surviving Fraction vs Peak Measured Temperature

The relationship between the measured surviving fraction for a region and the peak temperature measured in the corresponding region is displayed for the data from the tumors in the volume tumor excision colony growth assay group in Figure 13. Four regions that were assigned to a thermocouple produced indeterminate surviving fraction results because none of the plated cells developed into colonies. These values are displayed at the bottom of the figure next to the word "Indeterminate".

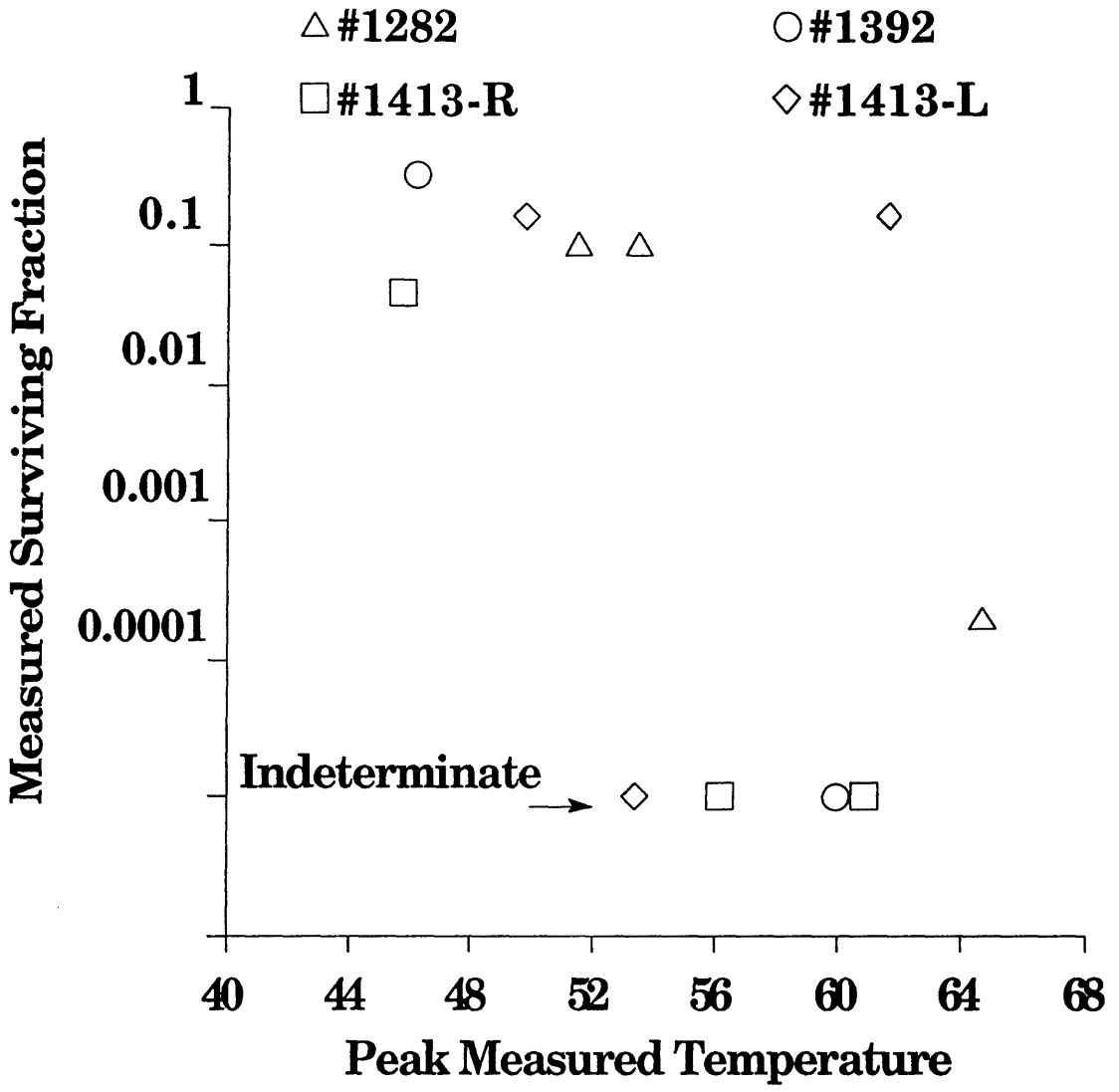

Figure 5.13 Measured surviving fraction vs peak measured temperature for tumors from the single slice tumor excision colony growth assay. The thermocouples were assigned to a tumor excision region based on their location relative to the optical fiber as determined from the MR images. The artifacts associated with the thermocouples and the gap between localizer slices prevent accurate assignment but the results represent the best possible estimate with all the information available. The surviving fraction of each region was plotted as a function of the maximum temperature measured with its corresponding thermocouple. Four surviving fraction values were indeterminate because none of the plated cells developed into colonies. The temperatures for these regions are plotted at the bottom of the graph and labelled *Indeterminate*.

5.2.3.3 Four Region Tumor Results

The tumors treated in Studies #1282 and #1413-L had diameters in the excised slice less than 14mm, which is the outer diameter of Region 3, and thus did not have a peripheral region in the colony growth assay. The image from Study #1282 with the ROI boundaries superimposed on the image demonstrate that the tumor cross section was a similar size on the image so the number of ROIs on the image match the number of tumor excision regions. The images from Study #1413-L with the ROI boundaries superimposed on the image indicate a fairly large tumor with a long axis of 20mm yielding a distinct periphery outside the annular regions.

The mismatch between the number of ROIs and the number of tumor excision regions in Study #1413-L could indicate poor alignment between the imaged slice and the excised slice or considerable tumor shape change upon excision. Poor alignment between the imaged slice and the excised slice would affect all the regions in this slice approximately equally. A change in the shape of the tumor could have a less of an impact on the core and first two annular regions because of their central position in the tumor. The change in the stress and strain of the tumor tissue associated with the excision is greater at the periphery and thus the conformational tissue changes would be greater in those regions. It was decided that all the tissue outside the second annular excision region should be matched to all the pixels outside the second annular ROI, so the pixel data from the third annular ROI was pooled with the data from the peripheral ROI in an attempt to maintain continuity between the image data and the tumor

excision data.

5.2.4 Comparison of Volume Tumor Excision and Single Slice Tumor Excision Data

The surviving fraction values of each region from the four tumors that were processed with the volume tumor excision colony growth assay were averaged. The surviving fraction values of each region from the tumors that were processed with the single slice tumor excision colony growth assay were also averaged. The results are displayed below. The surviving fraction values from the single slice group represent an average of 2 values in the Core region because the Core regions from Studies #1336, 1392 and #1413-L were indeterminate and 4 values in Region 1 because the Region 1 sample in Study #1413-R also produced an indeterminate result. Studies #1282 and #1413-L had excised slices that did not have any tumor tissue outside the 14mm outer diameter of Region 3, so the single slice Periphery avaerage is an average of the 3 data points from the remaining Studies.

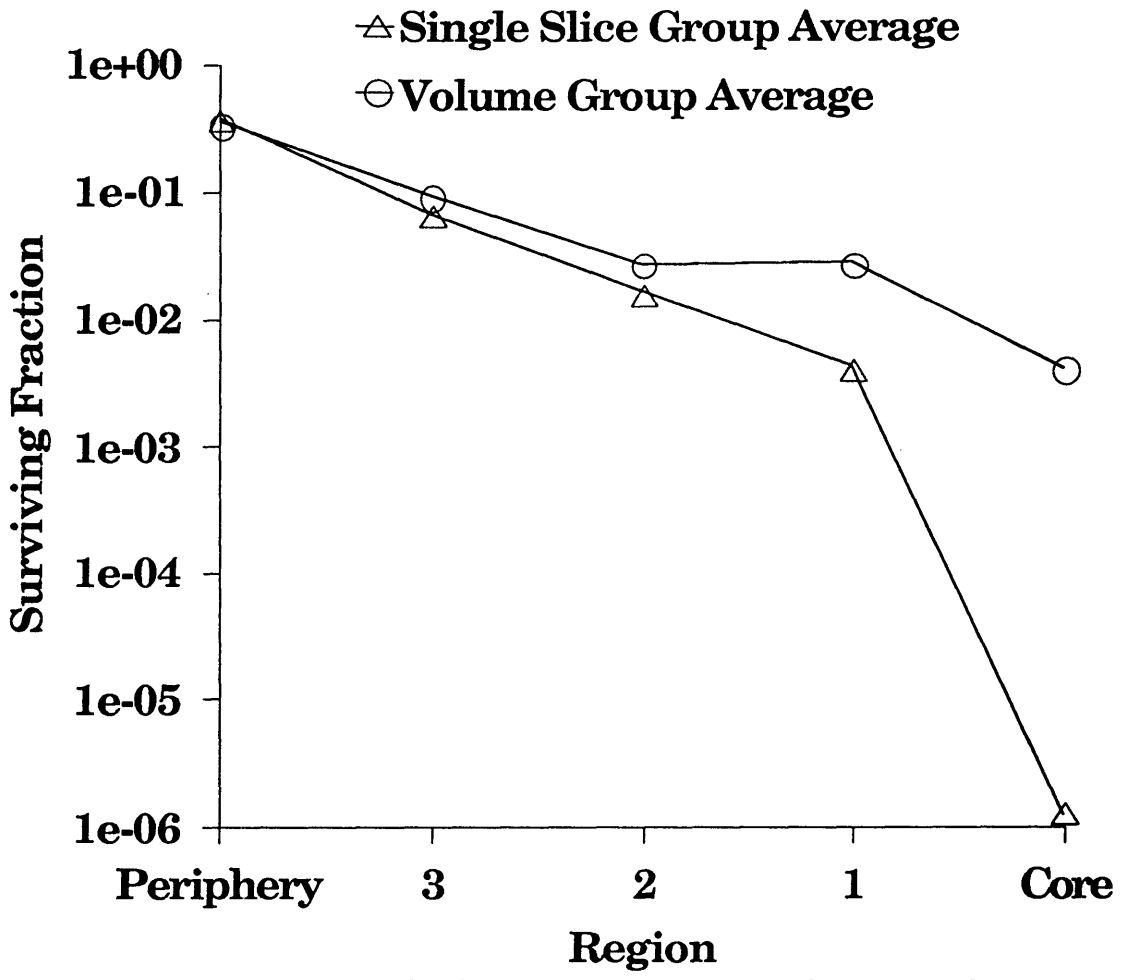

Figure 5.14 Comparison of volume tumor excision colony growth assay results and single slice tumor excision colony growth assay results. Volume tumor excision surviving fraction values are an average of 4 data points. Single slice tumor excision surviving fraction values for each region are an average of: Core- 2 points (3 indeterminate); Region1 - 4 points (1 indeterminate); Region2- 5 points; Region3- 5 points; Periphery- 3 points (2 tumors with no tissue outside Region 3 boundary).

5.3 Measured vs. Image-Derived Surviving Fraction

5.3.1 Volume Tumor Excision Results

The following figures and tables summarize the measured surviving

fraction results and the image-derived surviving fraction results from the volume tumor excision experiment. The image-derived values represent the best fit to the twenty measured surviving fraction values from all four tumors, after processing of the Marquardt-Levenberg fitting operation on each equation.

5.3.1.1 IAFs with Optimum Coefficients

The equations produced by the processing of the Marquardt-Levenberg fitting operation on each equation are included here. The coefficients determined by the iterative fitting process are included in the equations, as well as the percentage signal intensity change and image dose thresholds. The image-derived surviving fraction values that are produced with these equations are then displayed in both graphical and tabular form to facilitate identification of which equations best fit the measured surviving fraction values.

The results labelled SD in all figures and tables were produced with the following image dose equation patterned after the Sapareto-Dewey thermal dose calculation (ref):

$$\tau_{equiv} = \tau_{im} * \sum_{i=1}^{N} 1.706^{53.51\,(\%\Delta SI - 0.0376)} \quad \text{for } \%\Delta SI > 0.0376 \qquad 5.1$$

and the corresponding dose-response equation

$$S.F. = 1.0 * \exp\left(\frac{37.83 - \tau_{equiv}}{2115}\right) \quad \text{for } \tau_{equiv} > 37.83 \qquad 5.2$$

The results labelled EXP in all figures and tables were produced

with the following image dose equation:

$$\text{dose} = \sum_{i=1}^{N} \begin{pmatrix} 366.4*(\%\Delta SI_I - 0.1278) \\ +(7.209E+5)*(\%\Delta SI_I - 0.1278)^2 \\ +(1.5E+9)*(\%\Delta SI_I - 0.1278)^3 \end{pmatrix} * \tau \qquad \text{for } \%\Delta SI_I > 0.1278 \tag{5.3}$$

and the corresponding dose-response equation

$$S.F. = 8.041 * \exp(6.473 - \text{dose}) \qquad \text{for dose} > 6.473 \tag{5.4}$$

The results labelled POLY in all figures and tables were produced with the following image dose equation using a simple polynomial:

$$\text{dose} = \sum_{i=1}^{N} \begin{pmatrix} (8.195e-3)*(\%\Delta SI_I - 0.00664) \\ +0.08927*(\%\Delta SI_I - 0.00664)^2 \\ +0.1391*(\%\Delta SI_I - 0.00664)^3 \end{pmatrix} * \tau \qquad \text{for } \%\Delta SI_I > 0.00664 \tag{5.5}$$

$$S.F. = 1 - (\text{dose} - 0.008359) \qquad \text{for dose} > 0.00835 \tag{5.6}$$

The results labelled EXPR in all figures and tables were produced with the following image dose equation using an exponential containing a term with the rate-of-change of the signal intensity:

$$\text{dose} = \sum_{i=1}^{N} \begin{pmatrix} 0.001*(\%\Delta SI_I - 0.097) \\ +2.672*(\%\Delta SI_I - 0.097)^2 \end{pmatrix} * \tau + 321.2*\frac{(\%\Delta SI_I - \%\Delta SI_{I-1})}{\tau}$$

$$\text{for } \%\Delta SI_I > 0.097 \text{ and } (\%\Delta SI_I - \%\Delta SI_{I-1}) > 0 \tag{5.7}$$

and the corresponding dose-response equation

$$S.F. = 2.761 * \exp(0.11 - \text{dose}) \qquad \text{for dose} > 0.11 \tag{5.8}$$

The results labelled EXPRM in all figures and tables were produced

with the following image dose equation containing terms with the rate-of-change of the signal intensity and the rate-of-change multiplied by the magnitude:

$$\text{dose} = \sum_{i=1}^{N} \begin{array}{c} 0.0*(\%\Delta SI_I - 0.048)*\tau \\ + 8769*(\%\Delta SI_I - 0.048)*\dfrac{(\%\Delta SI_I - \%\Delta SI_{I-1})}{\tau} \\ + 2.623*\dfrac{(\%\Delta SI_I - \%\Delta SI_{I-1})}{\tau} \end{array} \quad \left(\begin{array}{c} \text{for} \\ \%\Delta SI_I > 0.048 \\ \text{and} \\ \%\Delta SI_I - \%\Delta SI_{I-1} > 0 \end{array} \right) \tag{5.9}$$

and the corresponding dose-response equation

$$S.F. = 6.417 * \exp(2.879 - \text{dose}) \quad \text{for dose} > 2.879 \tag{5.10}$$

The results labelled EXPR3 in all figures and tables were produced with the following image dose equation containing terms with the signal intensity change cubed, the rate-of-change of the signal intensity and the rate-of-change multiplied by the magnitude:

$$\text{dose} = \sum_{i=1}^{N} \begin{array}{c} 0.002*(\%\Delta SI_I - 0.045)*\tau \\ + 8.746*(\%\Delta SI_I - 0.045)^3*\tau \\ + 2439*(\%\Delta SI_I - 0.045)*\dfrac{(\%\Delta SI_I - \%\Delta SI_{I-1})}{\tau} \\ + 14.42*\dfrac{(\%\Delta SI_I - \%\Delta SI_{I-1})}{\tau} \end{array} \quad \text{for } \%\Delta SI_I > 0.045 \tag{5.11}$$

and the corresponding dose-response equation

$$S.F. = 2.163 * \exp(0.854 - \text{dose}) \quad \text{for dose} > 0.854 \tag{5.12}$$

The results in the column labelled AE in all figures and tables were produced with the following image dose equation based on an activation energy equation:

$$\text{dose} = \sum_{i=1}^{N} \left(0.083*\left(\%\Delta SI_I - 0.003\right) + 5.217*\left(\%\Delta SI_I - 0.003\right)^2\right) * \tau \qquad \text{for } \%\Delta SI_I > 0.003 \tag{5.13}$$

and the corresponding dose-response equation

$$S.F. = 1 - \exp\left(\frac{(3.695)}{7.129 - \text{dose}}\right) \qquad \text{for dose} > 7.129 \tag{5.14}$$

The results labelled MAXE in all figures and tables were produced with the following image dose equation using the maximum signal intensity change as a term in an exponential:

$$\text{dose} = \left(0.183*\text{max} + 0.008*\text{max}^2\right) * \tau \tag{5.15}$$

and the corresponding dose-response equation

$$S.F. = 1.0 * \exp(0.028 - \text{dose}) \qquad \text{for dose} > 0.028 \tag{5.16}$$

The results labelled MAXP in all figures and tables were produced with the following image dose equation using the maximum signal intensity change as a term in a polynomial:

$$\text{dose} = \left(0.3144*\text{max} + 0.039548*\text{max}^2\right) * \tau \tag{5.17}$$

and the corresponding dose-response equation

$$S.F. = 1.0 - \text{dose} \qquad \text{for dose} > 0.1881 \tag{5.18}$$

5.3.1.2 Graphical Presentation of Results

Figure 15 and 16. Measured and image-derived surviving fraction values for Study #984 - R of the volume tumor excision group. Image-derived values were obtained with equations specified above. Measured surviving fraction values are plotted with a line and a filled symbol.

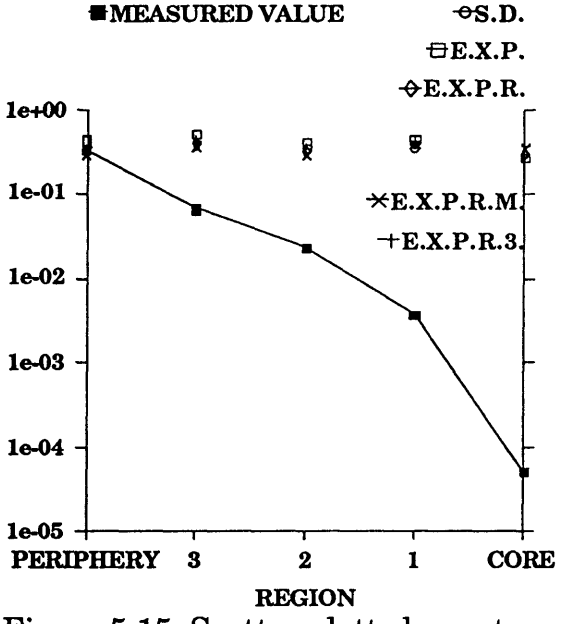

Figure 5.15 Scatter-plotted, empty symbol points are image-derived values obtained with equations SD (Sapareto-Dewey, Eqn.#5.1, 5.2), EXP (Exponential, Eqn.#5.3, 5.4), EXPR (Exponential-Rate, Eqn.#5.7, 5.8), EXPRM (Exponential-Rate-Magnitude, Eqn.#5.9, 5.10), EXPR3 (Exponential-Rate-Magnitude-Cubed, Eqn.#5.11, 5.12).

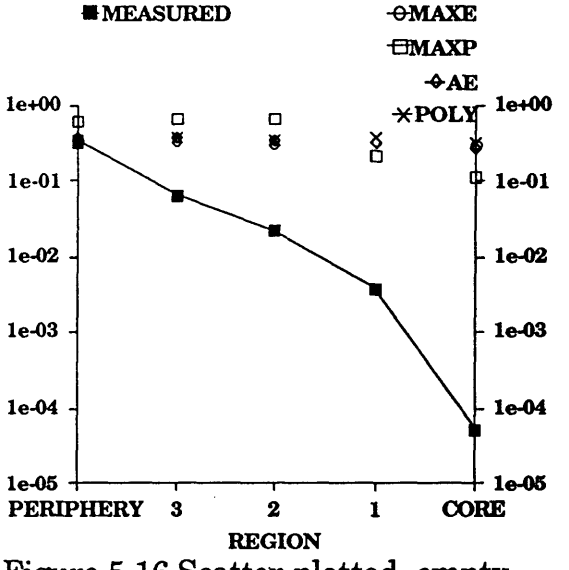

Figure 5.16 Scatter-plotted, empty symbol points are image-derived values obtained with equations POLY (Polynomial, Eqn.#5.5, 5.6), AE (Activation Energy, Eqn.#5.13, 5.14), MAXE (Maximum-Exponential, Eqn.#5.15, 5.16), and MAXP (Maximum-Polynomial, Eqn.#5.17, 5,18).

Figure 17 and 18. Measured and image-derived surviving fraction values for Study #984 - L of the volume tumor excision group. Image-derived values were obtained with equations specified above. Measured values are plotted with a line and a filled symbol.

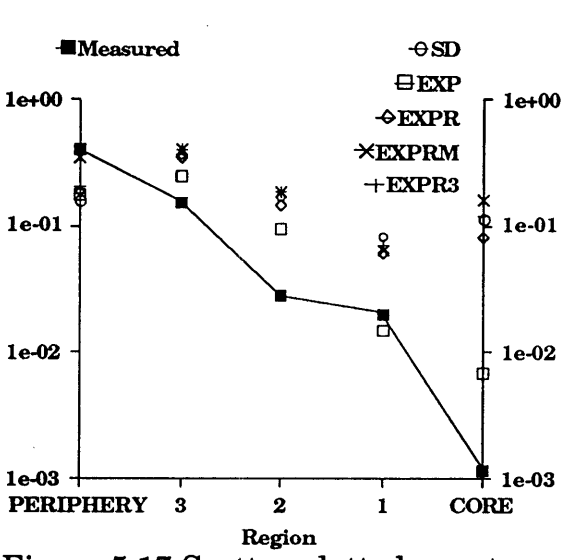

Figure 5.17 Scatter-plotted, empty symbol points are image-derived values obtained with equations SD (Sapareto-Dewey, Eqn.# 5.1, 5.2), EXP (Exponential, Eqn.#5.3, 5.4), EXPR (Exponential-Rate, Eqn.#5.7, 5.8), EXPRM (Exponential-Rate-Magnitude, Eqn.#5.9, 5.10), EXPR3 (Exponential-Rate-Cubed, Eqn.#5.11, 5.12).

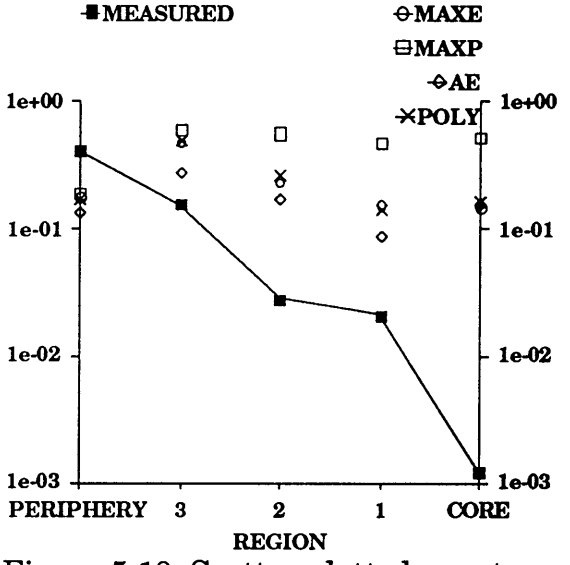

Figure 5.18 Scatter-plotted, empty symbol points are image-derived values obtained with equations POLY (Polynomial, Eqn.#5.5, 5.6), AE (Activation Energy, Eqn.#5.13, 5.14), MAXE (Maximum-Exponential, Eqn.#5.15, 5.16), MAXP (Maximum-Polynomial, Eqn.#5.17, 5.18).

Figure 19 and 20. Measured and image-derived surviving fraction values for Study #1151 - R of the volume tumor excision group. Image-derived values were obtained with equations specified above. Measured values are plotted with a line and a filled symbol.

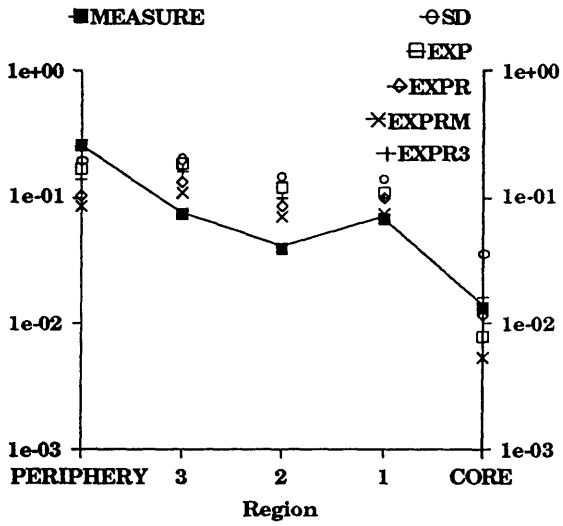

Figure 5.19 Scatter-plotted, empty symbol points are image-derived values obtained with equations SD (Sapareto-Dewey, Eqn.#5.1, 5.2), EXP (Exponential, Eqn.#5.3, 5.4), EXPR (Exponential-Rate, Eqn.#5.7, 5.8), EXPRM (Exponential-Rate-Magnitude, Eqn.#5.9, 5.10), EXPR3 (Exponential-Rate-Cubed, Eqn.#5.11, 5.12).

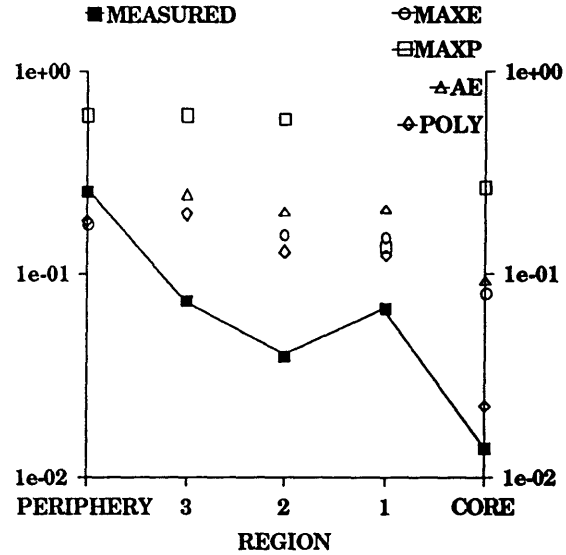

Figure 5.20 Scatter-plotted, empty symbol points are image-derived values obtained with equations POLY (Polynomial, Eqn.#5.5, 5.6), AE (Activation Energy, Eqn.#5.13, 5.14), MAXE (Maximum-Exponential, Eqn.#5.15, 5.16), MAXP (Maximum-Polynomial, Eqn.#5.17, 5.18).

Figure 21 and 22. Measured and image-derived surviving fraction values for Study #1151 - L of the volume tumor excision group. Image-derived values were obtained with equations specified above. Measured values are plotted with a line and a filled symbol.

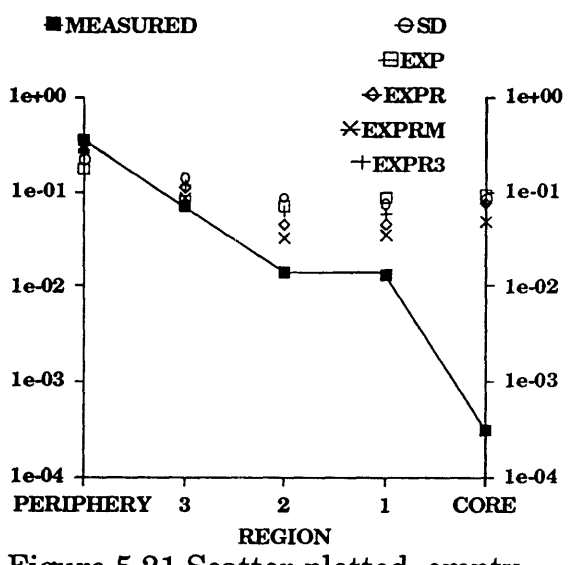

Figure 5.21 Scatter-plotted, empty symbol points are image-derived values obtained with equations SD (Sapareto-Dewey, Eqn.#5.1, 5.2), EXP (Exponential, Eqn.#5.3, 5.4), EXPR (Exponential-Rate, Eqn.#5.7, 5.8), EXPRM (Exponential-Rate-Magnitude,Eqn.#5.9, 5.10), EXPR3 (Exponential-Rate-Cubed, Eqn.#5.11, 5.12).

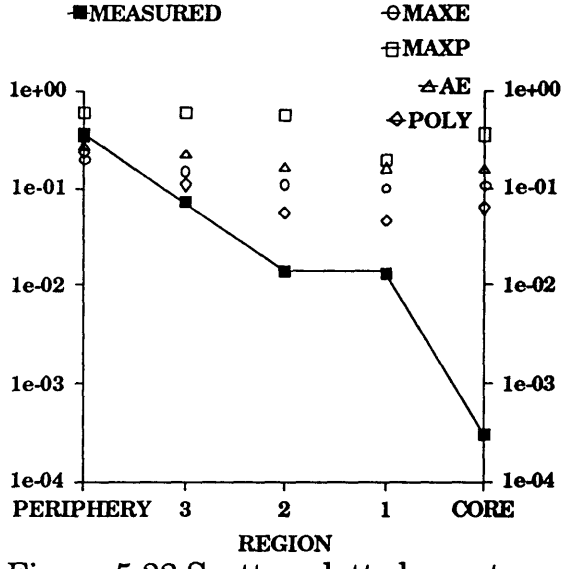

Figure 5.22 Scatter-plotted, empty symbol points are image-derived values obtained with equations POLY (Polynomial, Eqn.#5.5, 5.6)(*to be added)*, AE (Activation Energy, Eqn.#5.13, 5.14), MAXE (Maximum-Exponential, Eqn.#5.15, 5.16), MAXP (Maximum-Polynomial, Eqn.#5.17, 5.18).

5.3.1.3 Tabular Presentation of Results

Table 5.1. Measured surviving fraction and image-derived surviving fraction data from the volume tumor excision group. The measured surviving fraction data are listed in column 2 with the appropriate study number and an R or L to indicate if the tumor was located on the right or left side of the animal. The core region value is listed first, followed by the data from regions 1, 2 and 3 and the periphery, in that order. The image-derived surviving fraction values are listed in columns to the right in the same order. Each column of image-derived values was produced with the equation specified by the label at the top of the column.

Table 5.1A. Measured surviving fraction results and image-derived surviving fraction results from the volume tumor excision experiment. Measured values in column 2. Image-derived values obtained with equations SD (Sapareto-Dewey, Eqn.#5.1, 5.2) in column 3, EXP (Exponential, Eqn.#5.3, 5.4) in column 4 and EXPR (Exponential-Rate, Eqn.#5.7, 5.8) in column 5. The chi-squared value, which reflects the quality of the fit between the measured and image-derived values for that study, is listed under the image-derived values.

984-R	MEASURED	SD	EXP	EXPR
Core	0.000051	0.2934	0.2605	0.3144
Region 1	0.003691	0.3448	0.4391	0.3816
Region 2	0.02212	0.3381	0.3927	0.3178
Region 3	0.06338	0.3833	0.4976	0.405
Periphery	0.3231	0.3555	0.4141	0.3234
χ^2 =		0.025734	0.047454	0.026805
984-L				
Core	0.001166	0.1133	0.006897	0.08227
Region 1	0.02049	0.08257	0.01538	0.06037
Region 2	0.02762	0.172	0.09516	0.1486
Region 3	0.1537	0.3758	0.2553	0.3477
Periphery	0.4053	0.1591	0.1822	0.1908
χ^2 =		0.090529	0.064324	0.068527
1151-R				
Core	0.01379	0.03629	0.00813	0.01179
Region 1	0.06735	0.1419	0.1126	0.09794
Region 2	0.03993	0.1458	0.1206	0.08767
Region 3	0.07354	0.2041	0.1859	0.1325
Periphery	0.2553	0.1976	0.1722	0.1054
χ^2 =		0.00616	0.006468	0.012913
1151-L				
Core	0.000302	0.08292	0.09	0.07579
Region 1	0.0132	0.07406	0.08276	0.04641
Region 2	0.01383	0.08824	0.06988	0.0456
Region 3	0.06957	0.141	0.0786	0.1076
Periphery	0.3527	0.2233	0.1722	0.2664
χ^2 =		0.01674	0.030563	0.007262

Table 5.1B. Measured surviving fraction results and image-derived

surviving fraction results from the volume tumor excision experiment. Measured values in column 2. Image-derived values obtained with equations EXPRM (Exponential-Rate-Magnitude, Eqn.#5.9, 5.10) in column 3, EXPR3 (Exponential-Rate-Cubed, Eqn.#5.11, 5.12) in column 4 and AE (Activation Energy, Eqn.#5.13, 5.14) in column 5. The chi-squared value, which reflects the quality of the fit between the measured and image-derived values for that study, is listed under the image-derived values.

984-R	MEASURED	EXPRM Eqn.# 5.9, 5.10	EXPR3 Eqn.# 5.11, 5.12	AE Eqn.# 5.13, 5.14
Core	0.000051	0.3386	0.3583	0.2976
Region 1	0.003691	0.3785	0.4185	0.3218
Region 2	0.02212	0.2774	0.3442	0.2988
Region 3	0.06338	0.3415	0.4143	0.3352
Periphery	0.3231	0.2856	0.3131	0.3379
χ^2 =		0.021402	0.030199	0.019282
984-L				
Core	0.001166	0.1577	0.1242	0.1452
Region 1	0.02049	0.06456	0.07024	0.1526
Region 2	0.02762	0.1865	0.1839	0.2268
Region 3	0.1537	0.4059	0.4177	0.4758
Periphery	0.4053	0.3574	0.2061	0.1782
χ^2 =		0.023574	0.070913	0.097502
1151-R				
Core	0.01379	0.005338	0.01671	0.08123
Region 1	0.06735	0.07295	0.1002	0.1544
Region 2	0.03993	0.07026	0.1021	0.1581
Region 3	0.07354	0.1073	0.1608	0.1981
Periphery	0.2553	0.08511	0.138	0.1778
χ^2 =		0.015802	0.00902	0.008135
1151-L				
Core	0.000302	0.0489	0.07301	0.1045
Region 1	0.0132	0.03519	0.05659	0.1005
Region 2	0.01383	0.03302	0.06197	0.1075
Region 3	0.06957	0.08757	0.1171	0.148
Periphery	0.3527	0.2953	0.2829	0.1968
χ^2 =		0.003161	0.005111	0.024296

Table 5.1C: Measured surviving fraction results and image-derived

surviving fraction results from the volume tumor excision experiment. Measured values in column 2. Image-derived values obtained with equations MAXE (Maximum-Exponential, Eqn.#5.15, 5.16) in column 3 MAXP (Maximum-Polynomial, Eqn.#5.17, 5.18) in column 4 and POLY (Polynomial, Eqn.#5.5, 5.6) in column 5. The chi-squared value, which reflects the quality of the fit between the measured and image-derived values for that study, is listed under the image-derived values.

984-R	MEASURED	MAXE	MAXP	POLY
Core	0.000051	0.2456	0.2617	0.3144
Region 1	0.003691	0.3224	0.3328	0.3591
Region 2	0.02212	0.3404	0.3527	0.3382
Region 3	0.06338	0.3779	0.3863	0.3922
Periphery	0.3231	0.3625	0.3595	0.3567
χ^2 =		0.025043	0.026417	0.027007
984-L				
Core	0.001166	0.1537	0.1551	0.1617
Region 1	0.02049	0.1149	0.08521	0.1436
Region 2	0.02762	0.1801	0.1674	0.2665
Region 3	0.1537	0.2854	0.2753	0.4874
Periphery	0.4053	0.1372	0.1335	0.1726
χ^2 =		0.095974	0.097103	0.104137
1151-R				
Core	0.01379	0.1093	0.09273	0.02225
Region 1	0.06735	0.2068	0.2106	0.1245
Region 2	0.03993	0.2044	0.2039	0.1305
Region 3	0.07354	0.2396	0.2486	0.1977
Periphery	0.2553	0.2399	0.2583	0.185
χ^2 =		0.009952	0.010255	0.006158
1151-L				
Core	0.000302	0.1731	0.1601	0.06124
Region 1	0.0132	0.1729	0.1609	0.04485
Region 2	0.01383	0.1726	0.1662	0.05565
Region 3	0.06957	0.2132	0.2303	0.1087
Periphery	0.3527	0.2495	0.2702	0.2365
χ^2 =		0.015902	0.012724	0.012854

5.3.2 Single Slice Tumor Excision Results

The following figures and tables summarize the measured surviving fraction results and image-derived surviving fraction results from the single slice tumor excision experiment. The image-derived values represent the best fit between the entire group of measured values and the image-derived values, as a result of the Marquardt-Levenberg fitting operation on each equation.

5.3.2.1 IAFs with Optimum Coefficients

The results labelled SD in all figures and tables were produced with the following image dose equation patterned after the Sapareto-Dewey thermal dose calculation:

$$\tau_{equiv} = \tau_{im} * \sum_{i=1}^{N} 1.325^{30.99\,(\%\Delta SI\ -0.03468)} \qquad \text{for } \%\Delta SI > 0.03468 \tag{5.19}$$

and the corresponding dose-response equation

$$S.F. = 1.0 * \exp\left(\frac{0.07032 - \tau_{equiv}}{900.6}\right) \qquad \text{for } \tau_{equiv} > 0.07032 \tag{5.20}$$

The results labelled EXP in all figures and tables were produced with the following image dose equation:

$$dose = \sum_{i=1}^{N} \begin{pmatrix} 9215*(\%\Delta SI_I - 0.1281) \\ + 598.8*(\%\Delta SI_I - 0.1281)^2 \\ + 1.2E{+}9*(\%\Delta SI_I - 0.1281)^3 \end{pmatrix} * \tau \qquad \text{for } \%\Delta SI_I > 0.1281 \tag{5.21}$$

and the corresponding dose-response equation

$$S.F. = 1922 * \exp(352.6 - dose) \qquad \text{for } dose > 352.6$$

5.22

The results labelled POLY in all figures and tables were produced with the following image dose equation using a simple polynomial:

$$\text{dose} = \sum_{i=1}^{N} \begin{pmatrix} (9.587\text{e-}3)*(\%\Delta SI_I - (2.247\text{e-}6)) \\ +0.0834*(\%\Delta SI_I - (2.247\text{e-}6))^2 \\ +(7.921\text{e-}4)*(\%\Delta SI_I - (2.247\text{e-}6))^3 \end{pmatrix} * \tau \qquad \text{for } \%\Delta SI_I > 2.247\text{e-}6$$

5.23

and the corresponding dose-response equation

$$S.F. = 1 - (\text{dose} - 0.001613) \qquad \text{for dose} > 0.001613$$

5.24

The results labelled EXPR in all figures and tables were produced with the following image dose equation using an exponential containing a term with the rate-of-change of the signal intensity:

$$\text{dose} = \sum_{i=1}^{N} \begin{array}{l} 0.02724*(\%\Delta SI_I - 0.011)*\tau \\ + \ 0.01131*(\%\Delta SI_I - 0.011)^2*\tau \\ + 5.86*\dfrac{(\%\Delta SI_I - \%\Delta SI_{I-1})}{\tau} \end{array} \qquad \text{for } \%\Delta SI_I > 0.011$$

5.25

and the corresponding dose-response equation

$$S.F. = 1.0 * \exp((7.83\text{E-}4) - \text{dose}) \qquad \text{for dose} > 7.83\text{E-}4$$

5.26

The results labelled EXPRM in all figures and tables were produced with the following image dose equation containing terms with the rate-of-change of the signal intensity and the rate-of-change multiplied by the magnitude:

$$\text{dose} = \sum_{i=1}^{N} \begin{cases} 0.02968*(\%\Delta SI_I - 0.001)*\tau \\ + 6.722*(\%\Delta SI_I - 0.001)*\dfrac{(\%\Delta SI_I - \%\Delta SI_{I-1})}{\tau} \\ + 45.42*\dfrac{(\%\Delta SI_I - \%\Delta SI_{I-1})}{\tau} \end{cases} \quad \text{for } \%\Delta SI_I > 0.001 \qquad 5.27$$

and the corresponding dose-response equation

$$S.F. = 1.0 * \exp((6.3E\text{-}5) - \text{dose}) \quad \text{for dose} > 6.3E\text{-}5 \qquad 5.28$$

The results labelled EXPR3 in all figures and tables were produced with the following image dose equation containing terms with the signal intensity change cubed, the rate-of-change of the signal intensity and the rate-of-change multiplied by the magnitude:

$$\text{dose} = \sum_{i=1}^{N} \begin{cases} 0.0126*(\%\Delta SI_I - 0.003)*\tau \\ + 13.38*(\%\Delta SI_I - 0.003)^3*\tau \\ + 5.93*\dfrac{(\%\Delta SI_I - \%\Delta SI_{I-1})}{\tau} \end{cases} \quad \text{for } \%\Delta SI_I > 0.003 \qquad 5.29$$

and the corresponding dose-response equation

$$S.F. = 1.0 * \exp(0.002 - \text{dose}) \quad \text{for dose} > 0.002 \qquad 5.30$$

The results in the column labelled AE in all figures and tables were produced with the following image dose equation based on an activation energy equation:

$$\text{dose} = \sum_{i=1}^{N} \left(0.01501*(\%\Delta SI_I - 0.01704) + 0.2379*(\%\Delta SI_I - 0.01704)^2\right) * \tau \quad \text{for } \%\Delta SI_I > 0.01704 \qquad 5.31$$

and the corresponding dose-response equation

$$S.F. = 1 - \exp\left(\frac{(0.3158)}{(5.958e\text{-}3) - dose}\right) \quad \text{for dose} > (5.958e\text{-}3) \tag{5.32}$$

The results labelled MAXE in all figures and tables were produced with the following image dose equation using the maximum signal intensity change as a term in an exponential:

$$dose = (0.3362*max + 1.728*max^2) * \tau \tag{5.33}$$

and the corresponding dose-response equation

$$S.F. = 1.08 * \exp(0.1214 - dose) \quad \text{for dose} > 0.1214 \tag{5.34}$$

The results labelled MAXP in all figures and tables were produced with the following image dose equation using the maximum signal intensity change as a term in a polynomial:

$$dose = (0.4202*max + 0.05615*max^2) * \tau \tag{5.35}$$

and the corresponding dose-response equation

$$S.F. = 1.0 - (0.3592 - dose) \quad \text{for dose} > 0.3592 \tag{5.36}$$

5.3.2.2 Graphical Presentation of Results

Figure 23 and 24. Measured and image-derived surviving fraction values for Study #1282 of the single slice tumor excision group. Image-derived values were obtained with equations specified above. Measured values are plotted with a line and a filled symbol.

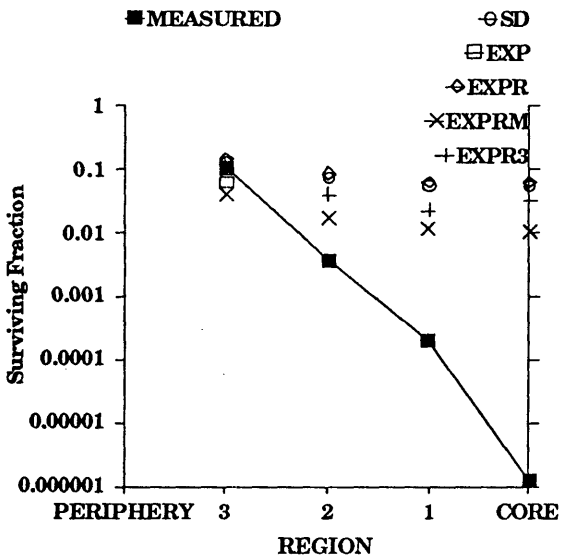

Figure 5.23 Scatter-plotted, empty symbol points are image-derived values obtained with equations SD (Sapareto-Dewey, Eqn.#5.19, 5.20), EXP (Exponential, Eqn.#5.21, 5.22), EXPR (Exponential-Rate, Eqn.#5.25, 5.26), EXPRM (Exponential-Rate-Magnitude, Eqn.#5.27, 5.28), EXPR3 (Exponential-Rate-Cubed, Eqn.#5.29, 5.30).

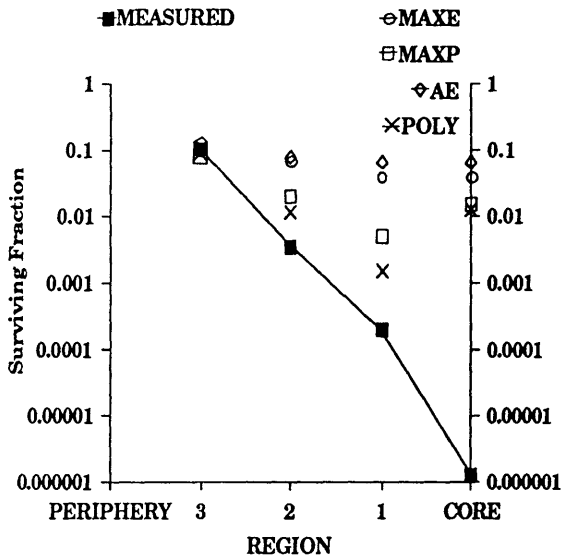

Figure 5.24 Scatter-plotted, empty symbol points are image-derived values obtained with equations POLY (Polynomial, Eqn.#5.23, 5.24), AE (Activation Energy, Eqn.#5.31, 5.32), MAXE (Maximum-Exponential, Eqn.#5.33, 5.34), MAXP (Maximum-Polynomial, Eqn.#5.35, 5.36).

Figure 25 and 26. Measured and image-derived surviving fraction values for Study #1336 of the single slice tumor excision group. Image-derived values were obtained with equations specified above. Measured values are plotted with a line and a filled symbol.

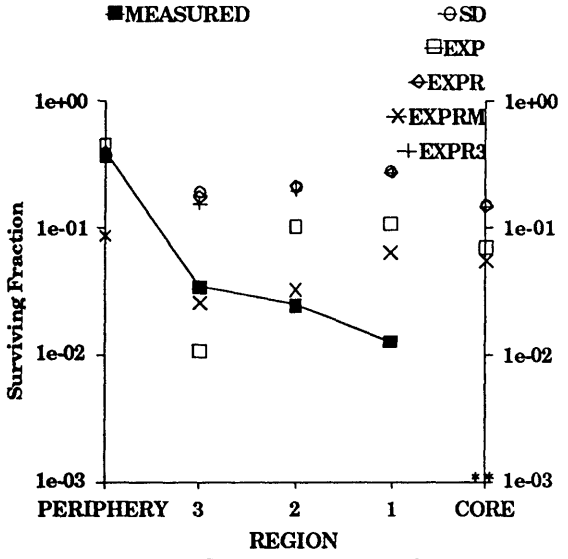

Figure 5.25 Scatter-plotted, empty symbol points are image-derived values obtained with equations SD (Sapareto-Dewey, Eqn.#5.19, 5.20), EXP (Exponential, Eqn.#5.21, 5.22), EXPR (Exponential-Rate, 5.25, 5.26), EXPRM (Exponential-Rate-Magnitude, Eqn.#5.27, 5.28), EXPR3 (Exponential-Rate-Cubed, Eqn.#5.29, 5.30).

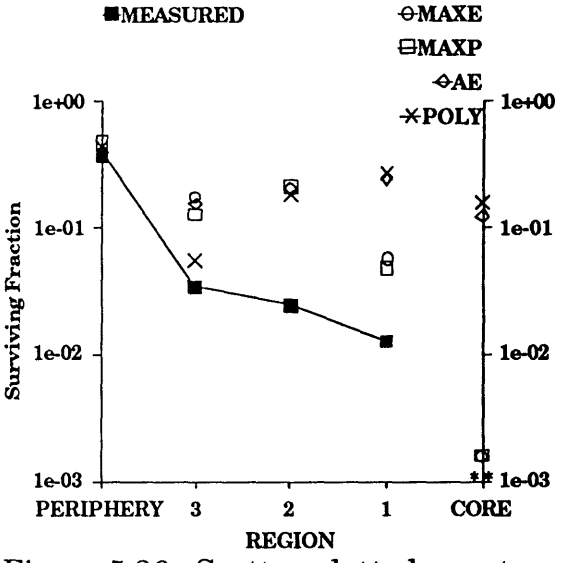

Figure 5.26 Scatter-plotted, empty symbol points are image-derived values obtained with equations POLY (Polynomial, Eqn.#5.23, 5.24), AE (Activation Energy, Eqn.#5.31, 5.32), MAXE (Maximum-Exponential, Eqn.#5.33, 5.34), MAXP (Maximum-Polynomial, Eqn.#5.35, 5.36).

Figure 27 and 28. Measured and image-derived surviving fraction values for Study #1392 of the single slice tumor excision group. Image-derived values were obtained with equations specified above. Measured values are plotted with a line and a filled symbol.

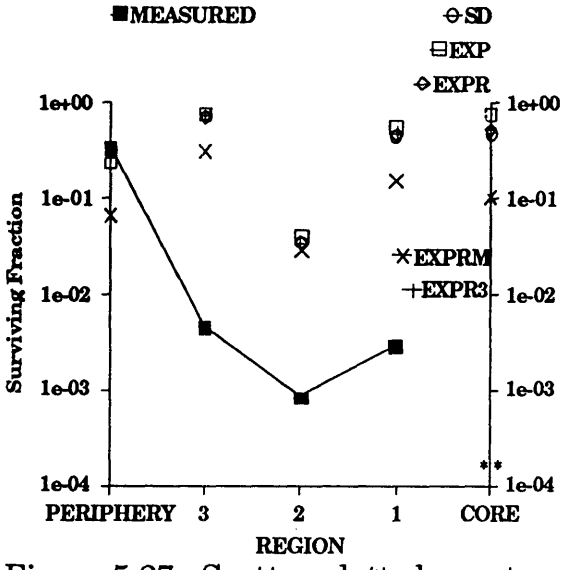

Figure 5.27 Scatter-plotted, empty symbol points are image-derived values obtained with equations SD (Sapareto-Dewey, Eqn.#5.19, 5.2), EXP (Exponential, Eqn.#521, 5.22), EXPR (Exponential-Rate, Eqn.#5.25, 5.26), EXPRM (Exponential-Rate-Magnitude, Eqn.#5.27, 5.28), EXPR3 (Exponential-Rate-Cubed, Eqn.#5.29, 5.30).

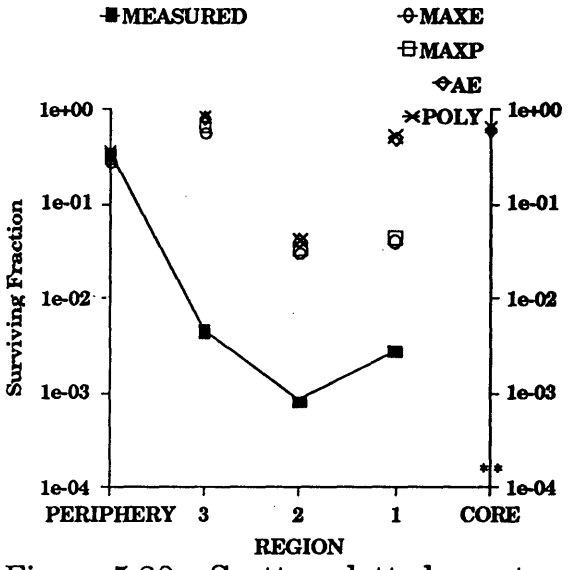

Figure 5.28 Scatter-plotted, empty symbol points are image-derived values obtained with equations POLY (Polynomial, Eqn.#5.25, 5.24)(*to be added)*, AE (Activation Energy, Eqn.#5.31, 5.32), MAXE (Maximum-Exponential, Eqn.# 5.33, 5.34), MAXP (Maximum-Polynomial, Eqn.#5.35, 5.36).

Figure 29 and 30. Measured and image-derived surviving fraction values for Study #1413-R of the single slice tumor excision group. Image-derived values were obtained with equations specified above. Measured values are plotted with a line and a filled symbol.

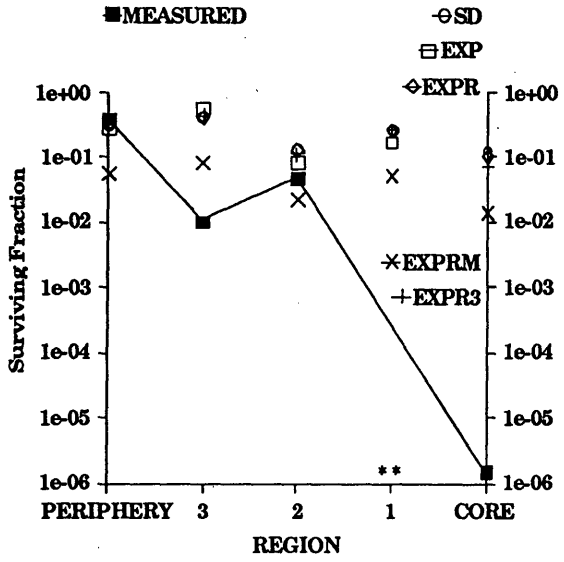

Figure 5.29 Scatter-plotted, empty symbol points are image-derived values obtained with equations SD (Sapareto-Dewey, Eqn.#5.19, 5.20), EXP (Exponential, Eqn.#5.21, 5.22), EXPR (Exponential-Rate, Eqn.#5.25, 5.26), EXPRM (Exponential-Rate-Magnitude, Eqn.#5.27, 5.28), EXPR3 (Exponential-Rate-Cubed, Eqn.#5.29, 5.30).

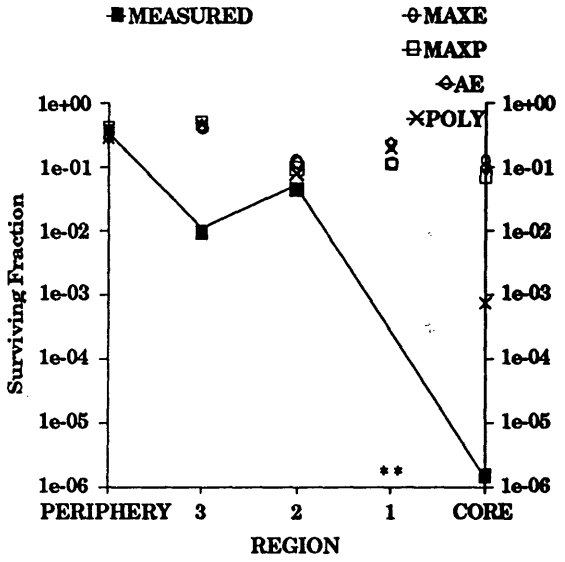

Figure 5.30 Scatter-plotted, empty symbol points are image-derived values obtained with equations POLY (Polynomial, Eqn.#5.23, 5.24), AE (Activation Energy, Eqn.#5.31, 5.32), MAXE (Maximum-Exponential, Eqn.#5.33, 5.34), MAXP (Maximum-Polynomial, Eqn.#5.35, 5.36).

Figure 31 and 32. Measured and image-derived surviving fraction values for Study #1413-L of the single slice tumor excision group. Image-derived values were obtained with equations specified above. Measured values are plotted with a line and a filled symbol.

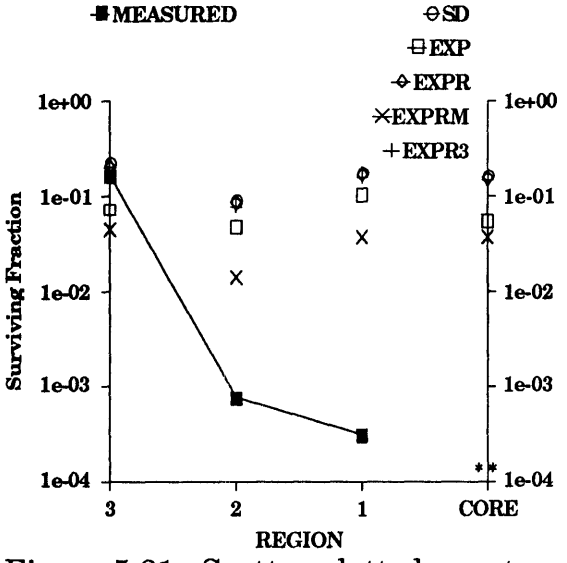

Figure 5.31 Scatter-plotted, empty symbol points are image-derived values obtained with equations SD (Sapareto-Dewey, Eqn.#5.19, 5.20), EXP (Exponential, Eqn.#5.21, 5.22), EXPR (Exponential-Rate, Eqn.#5.25, 5.26), EXPRM (Exponential-Rate-Magnitude, Eqn.#5.27, 5.28), EXPR3 (Exponential-Rate-Cubed, Eqn.#5.29, 5.30).

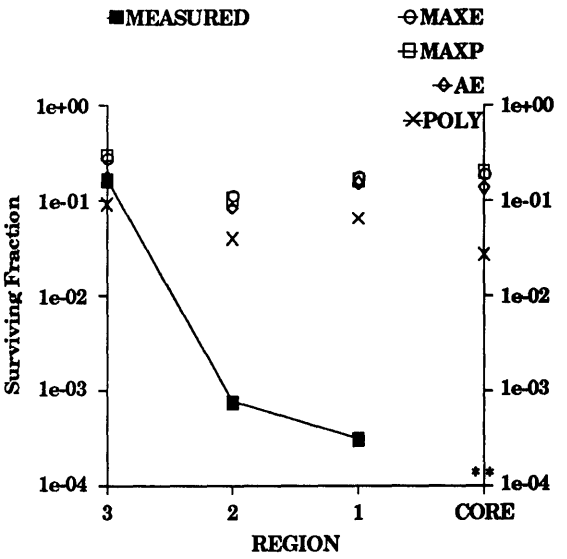

Figure 5.32 Scatter-plotted, empty symbol points are image-derived values obtained with equations POLY (Polynomial, Eqn.#5.23, 5.24), AE (Activation Energy, Eqn.#5.31, 5.32), MAXE (Maximum-Exponential, Eqn.#5.33, 5.34), MAXP (Maximum-Polynomial, 5.35, 5.36).

5.3.2.3 Tabular Presentation of Results

Table 5.2. Measured surviving fraction and image-derived surviving fraction data from the single slice tumor excision group. The measured surviving fraction data are listed in column 2 with the appropriate study number and an R or L to indicate if the tumor was located on the right or left side of the animal. The core region value is listed first, followed by the data from regions 1, 2 and 3 and the periphery, in that order. The image-derived surviving fraction values are listed in columns to the right in the same order. Each column of image-derived values was produced with the equation specified by the label at the top of the column. The chi-squared value, which reflects the quality of the fit between the measured and image-derived values, is listed below image derived values. Entries marked ** represent indeterminate measured surviving fraction values.

Table 5.2A. Measured surviving fraction results and image-derived surviving fraction results from the single slice tumor excision experiment. Measured values in column 2. Image-derived values obtained with equations SD (Sapareto-Dewey, Eqn.#5.19, 5.20) in column 3, EXP

(Exponential, Eqn.#5.21, 5.22) in column 4 and EXPR (Exponential-Rate, Eqn.#5.25, 5.26) in column 5. The chi-squared value, which reflects the quality of the fit between the measured and image-derived values for that study, is listed under the image-derived values.

1282	MEASURED	SD	EXP	EXPR
Core	1.25E-06	0.05442	0	0.0624
Region 1	0.000203	0.05565	0	0.06301
Region 2	0.003634	0.07684	0	0.08491
Region 3	0.1024	0.1274	0.0625	0.15
χ^2 =		3.45E-04	3.07E-04	7.17E-04
1336				
Core	**	0.1546	0.07042	0.15
Region 1	0.01255	0.2843	0.1104	0.2786
Region 2	0.02401	0.2149	0.1013	0.2138
Region 3	0.03418	0.1927	0.01075	0.1775
Periphery	0.388	0.3796	0.4692	0.3979
χ^2 =		0.008812	0.008345	0.008247
1392				
Core	**	0.476	0.75	0.5185
Region 1	0.00278	0.4421	0.5455	0.4643
Region 2	0.000818	0.03558	0.03947	0.03471
Region 3	0.004444	0.705	0.7381	0.7262
Periphery	0.3337	0.3309	0.235	0.3414
χ^2 =		0.02286	0.036279	0.024605
1413-L				
Core	**	0.1675	0.05556	0.1554
Region 1	0.000298	0.1816	0.1043	0.172
Region 2	0.00074	0.09021	0.04878	0.08855
Region 3	0.1659	0.2203	0.0729	0.2084
χ^2 =		0.001635	0.002896	0.001212
1413-R				
Core	6.1E-06	0.1161	0	0.1008
Region 1	**	0.2677	0.1677	0.2601
Region 2	0.0467	0.1297	0.08092	0.1261
Region 3	0.009963	0.4067	0.5591	0.4153
Periphery	0.3806	0.3208	0.2716	0.3163
χ^2 =		0.012218	0.027118	0.013051

Table 5.2B. Measured surviving fraction results and image-derived surviving fraction results from the single slice tumor excision experiment.

Measured values in column 2. Image-derived values obtained with equations EXPRM (Exponential-Rate-Magnitude, Eqn.#5.27, 5.28) in column 3, EXPR3 (Exponential-Rate-Cubed, Eqn.#5.29, 5.30) in column 4 and MAXE (Maximum-Exponential, Eqn.#5.33, 5.34) in column 5.

1282	MEASURED	EXPRM	EXPR3	MAXE
Core	1.25E-06	0.01057	0.03329	0.0403
Region 1	0.000203	0.01144	0.02259	0.03967
Region 2	0.003634	0.01728	0.03943	0.07097
Region 3	0.1024	0.04191	0.1151	0.101
χ^2 =		0.000713	0.000083	0.000172
1336				
Core	**	0.05448	0.1483	0.001589
Region 1	0.01255	0.06302	0.2766	0.05666
Region 2	0.02401	0.03247	0.2012	0.2057
Region 3	0.03418	0.02541	0.1565	0.1775
Periphery	0.388	0.08687	0.4197	0.3975
χ^2 =		0.101318	0.00838	0.004378
1392				
Core	**	0.1032	0.5428	0
Region 1	0.00278	0.1497	0.4902	0.04018
Region 2	0.000818	0.02798	0.03452	0.03067
Region 3	0.004444	0.322	0.7245	0.5536
Periphery	0.3337	0.06609	0.3203	0.2713
χ^2 =		0.063555	0.025391	0.013571
1413-L				
Core	**	0.03736	0.1465	0.1896
Region 1	0.000298	0.03777	0.1633	0.1692
Region 2	0.00074	0.01403	0.07843	0.1146
Region 3	0.1659	0.04471	0.2087	0.2712
χ^2 =		0.004579	0.001137	0.004202
1413-R				
Core	6.1E-06	0.01388	0.06986	0.1332
Region 1	**	0.05101	0.2632	0.1149
Region 2	0.0467	0.02118	0.1109	0.1274
Region 3	0.009963	0.08378	0.4412	0.4233
Periphery	0.3806	0.05783	0.332	0.3355
χ^2 =		0.111975	0.011913	0.011046

Table 5.2C: Measured surviving fraction results and image-derived surviving fraction results from the single slice tumor excision experiment. Measured values in column 2. Image-derived values obtained with equations MAXP (Maximum-Polynomial, Eqn.#5.35, 5.36) in column 3, AE (Activation Energy, Eqn.#5.31, 5.32) in column 4 and POLY (Polynomial, 5.23, 5.24) in column 5.

1282	MEASURED	MAXP	AE	POLY
Core	1.25E-06	0.0158	0.06627	0.01235
Region 1	0.000203	0.005066	0.06555	0.00159
Region 2	0.003634	0.0211	0.07892	0.0121
Region 3	0.1024	0.08486	0.1303	0.08989
χ^2 =		7.03E-05	4.07E-04	3.31E-05
1336				
Core	**	0.001587	0.123	0.1581
Region 1	0.01255	0.04742	0.2452	0.2708
Region 2	0.02401	0.2123	0.2069	0.1807
Region 3	0.03418	0.1287	0.154	0.05554
Periphery	0.388	0.474	0.4062	0.44
χ^2 =		0.011648	0.006893	0.00836
1392				
Core	**	0	0.5992	0.6473
Region 1	0.00278	0.04495	0.4878	0.5265
Region 2	0.000818	0.03497	0.04021	0.04114
Region 3	0.004444	0.6536	0.8262	0.8354
Periphery	0.3337	0.3021	0.3339	0.3477
χ^2 =		0.015269	0.030678	0.032627
1413-R				
Core	6.1E-06	0.07417	0.09966	0.000748
Region 1	**	0.1146	0.2353	0.22
Region 2	0.0467	0.1005	0.1207	0.0817
Region 3	0.009963	0.5152	0.4343	0.467
Periphery	0.3806	0.3969	0.2924	0.3039
χ^2 =		0.012671	0.017581	0.016381
1413-L				
Core	**	0.2018	0.135	0.02762
Region 1	0.000298	0.1648	0.1498	0.06395
Region 2	0.00074	0.103	0.0828	0.03946
Region 3	0.1659	0.2982	0.1786	0.09085
χ^2 =		0.006131	0.000561	0.001838

5.4 Tissue Characterization Results

The results of the tissue characterization experiments are presented in Figures 5.33-5.36. The percent changes in T1 and T2 for the tumors in the volume excision group, as a function of the measured surviving fraction from the colony growth assay, are presented in Figures 5.33 and 5.34. The percent changes in T1 and T2 for the tumors in the single slice excision group, as a function of the measured surviving fraction from the colony growth assay, are presented in Figures 5.35-5.36. T2 data was unavailable for certain studies because the animal woke before data acquisition could be completed or because an error in the imaging software acquired the image information incorrectly.

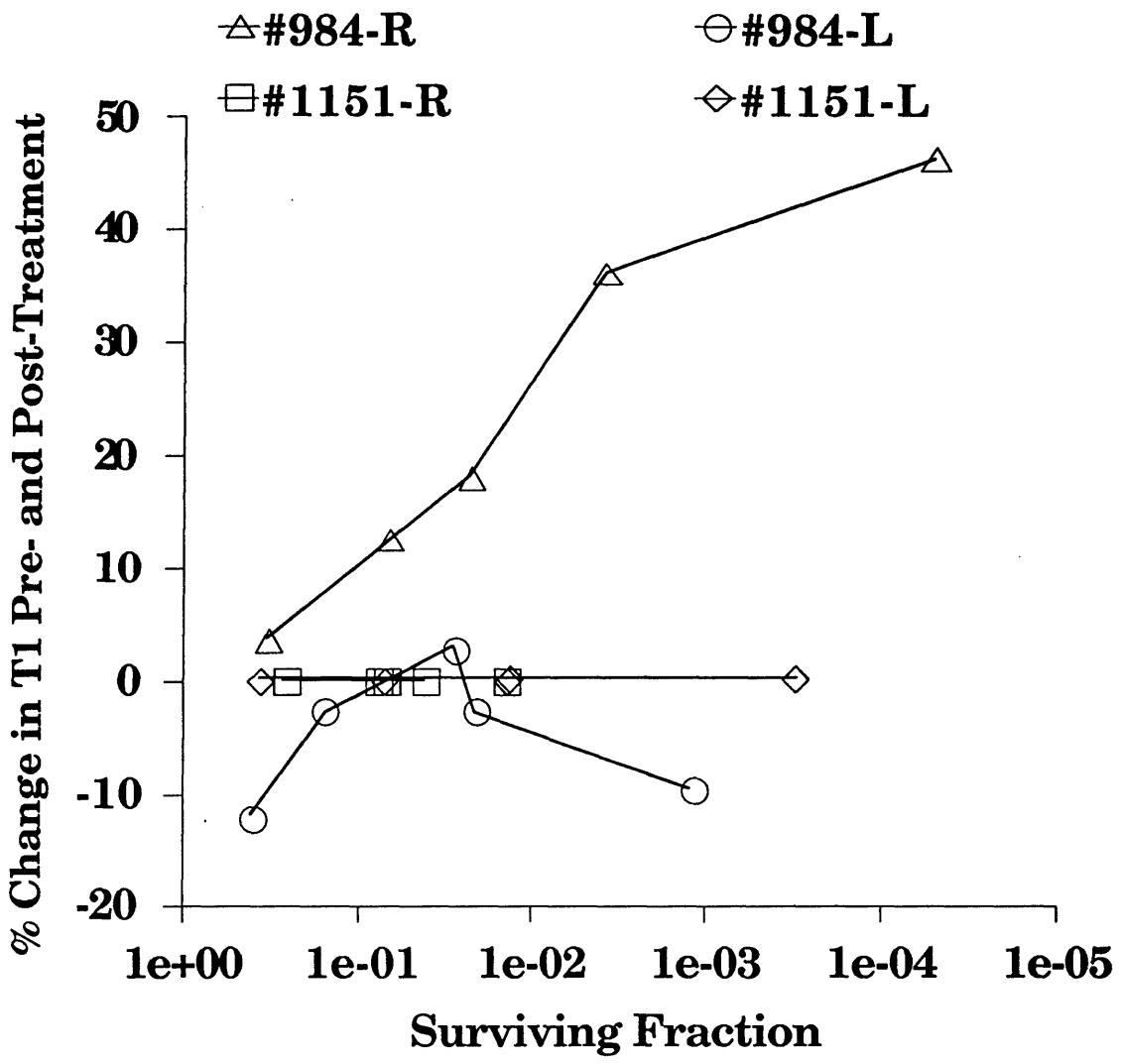

Figure 5.33 Percent changes in T1 pre- and post-treatment for the tumors in the volume excision group, as a function of measured surviving fraction for the corresponding tissue region. T1 was evaluated with a variable TR series using 13 points with TRs ranging from 200msec to 4sec, TE_{eff}=18msec, ETL=4, FOV = 8cmX6cm. Curve fitting was done with the CPLOT software package.

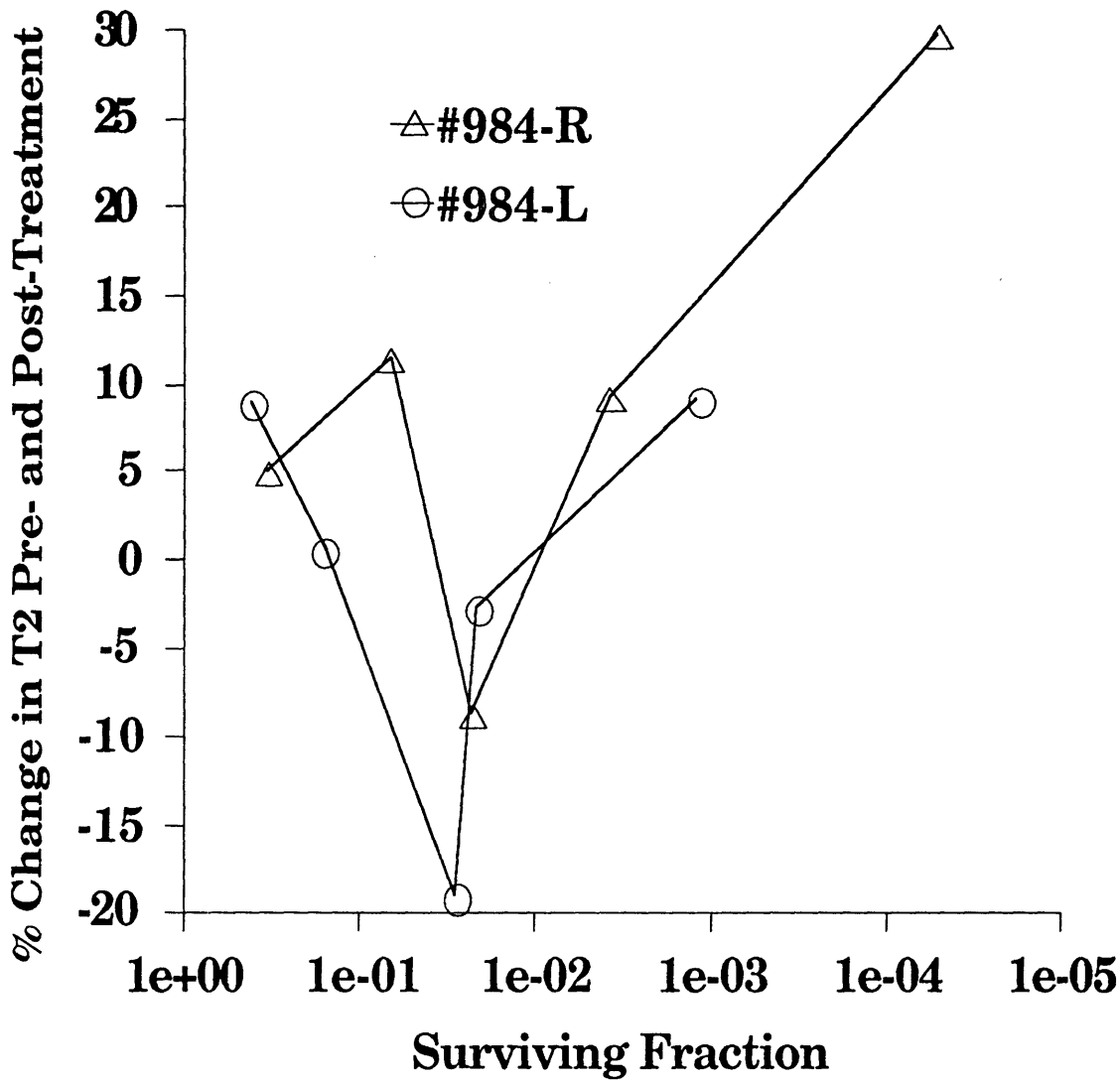

Figure 5.34 Percent changes in T2 pre- and post-treatment for the tumors in the volume excision group, as a function of measured surviving fraction for the corresponding tissue region. T2 was evaluated with a CPMG sequence with 48 echoes, TE_{eff}=18msec, ETL=4, FOV = 8cmX6cm. Curve fitting was done with the CPLOT software package.

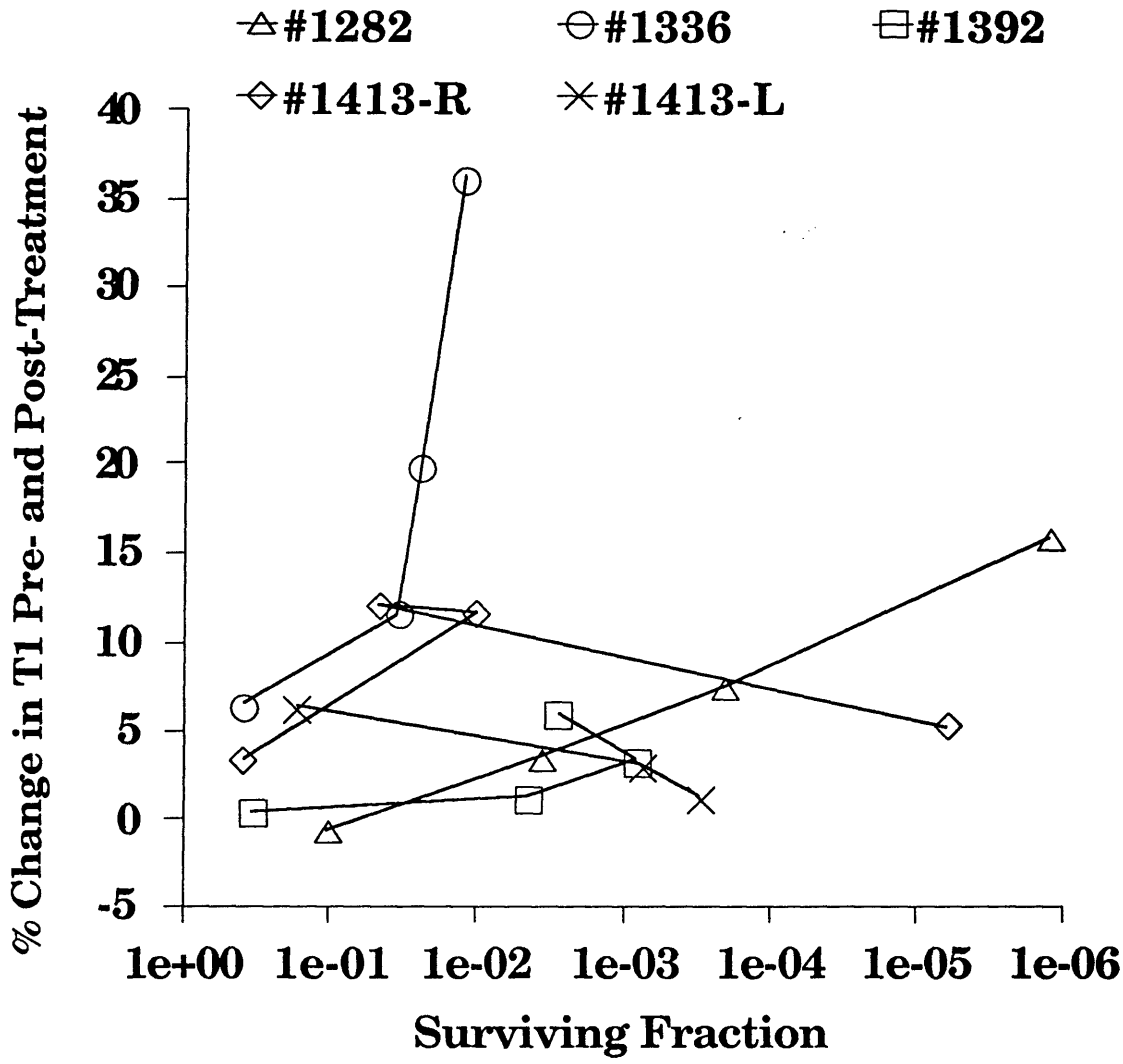

Figure 5.35 Percent changes in T1 pre- and post-treatment for the tumors in the single slice excision group, as a function of measured surviving fraction for the corresponding tissue region. T1 was evaluated with a variable TR series using 13 points with TRs ranging from 200msec to 4sec, TE_{eff}=18msec, ETL=4, FOV = 8cmX6cm. Curve fitting was done with the CPLOT software package.

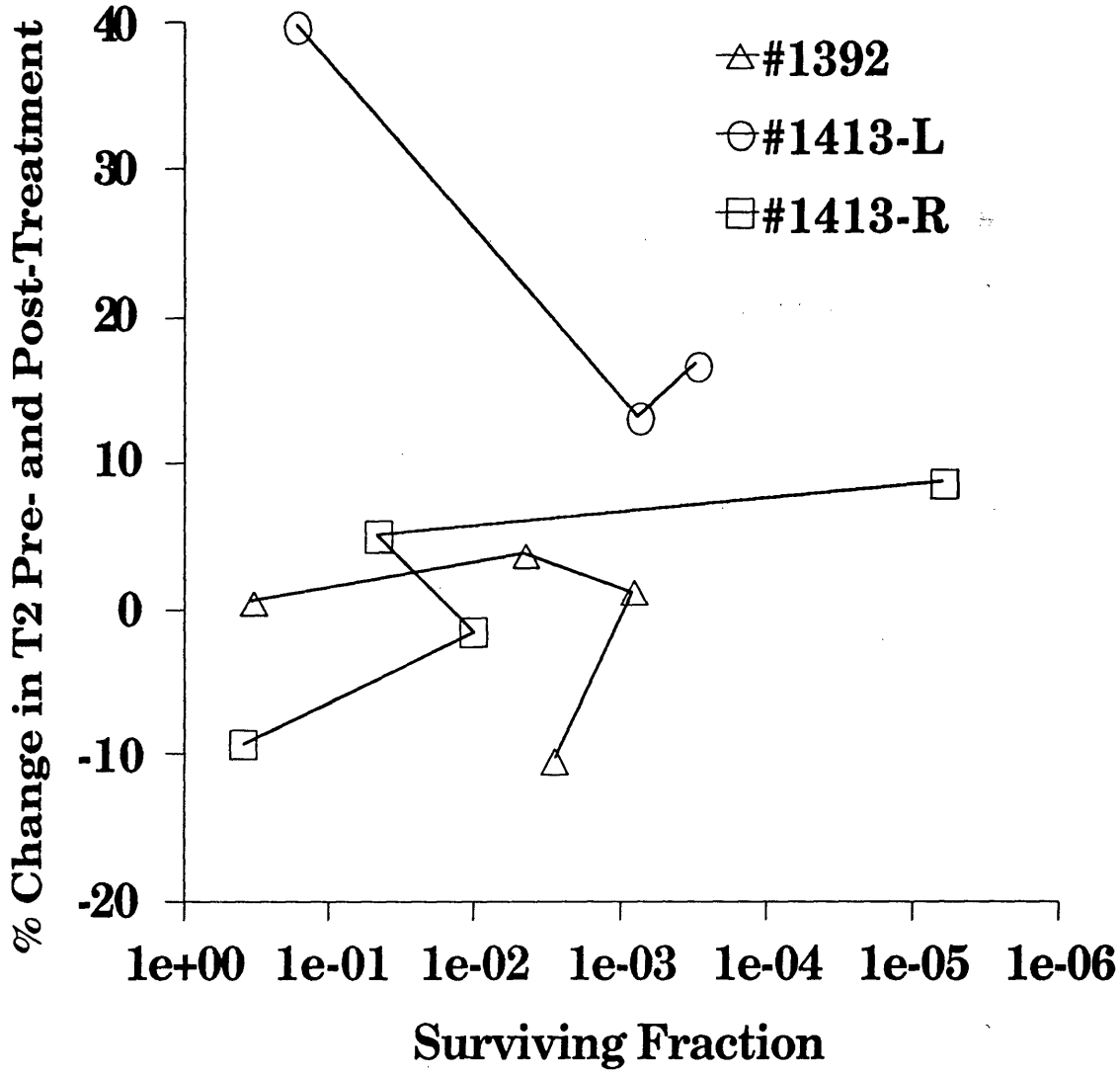

Figure 5.36 Percent changes in T2 pre- and post-treatment for the tumors in thesingle slice excision group, as a function of measured surviving fraction for the corresponding tissue region. T2 was evaluated with a CPMG sequence with 48 echoes, TE_{eff}=18msec, ETL=4, FOV = 8cmX6cm. Curve fitting was done with the CPLOT software package.

5.5 Histological Evaluation

Three tumors from the single slice excision group were also processed for histological evaluation. The superior and inferior halves of the tumor that remained after removal of the central slice were placed in 15% formalin for a period of at least three weeks. A slice close to the cut surface of each tumor section was processed and stained with hematoxylin and eosin and reviewed by a pathologist experienced in the analysis of thermally treated tissue. The pasta marker of the optical fiber tract was identified in five of the six slices and the state of the tissue at positions relative to the marker was reported.

5.5.1 General Findings

The general findings for all six slices indicate a tumor in an advanced stage of development. The periphery showed areas of compressed cells with varying degrees of necrosis and inflammation. The peripheral necrosis was ascribed to the mechanical stress on the tumor cells due to the pressure of tumor expansion against the tightly overlying skin or adjacent muscle. The region immediately adjacent to the fiber tended to have partial, variable necrosis that was ischemic and avascular but not specificly thermally-induced. The intermediate region between the fiber and the periphery had variable, randomly distributed areas of normal cell density and edema correlated with congested vessels. There are also

patches of hemorrhage and necrosis, occasionally containing serum and/or fibrin. The serum and fibrin presence are characteristic of older necrosis, while the random spatial distribution of the necrotic and edematous areas suggests a tumor which is at an advanced stage and is beginning to outgrow its blood supply. In general, the tissue at the periphery of the tumor appeared the least viable, while the tissue in the intermediate region appeared the most viable.

5.5.2 Specific Features

Specific features on particular slides demonstrate other features of the tumor and the treatment. The slide from the superior half of the left tumor treated in Study #1413 had a small piece of muscle tissue in the center of the tumor. There was also some compression of the tumor cells adjacent to the pasta which made that area look relatively normal. In addition, there was a narrow band of chronic ischemic injury in the peripheral region along one edge of the tumor with neutrophil infiltration.

The slide from the inferior half of the right tumor treated in Study #1413 had marked compression in the peripheral region along the boundary with the muscle and there was a small area of muscle tissue attached to the tumor which illustrated the invasion of the muscle tissue by the tumor.

The superior slide from Study #1336 was the only slide in which the pasta marker could not be seen. The slide also did not prepare as well as the other slides. The periphery of the tumor contained some fat and

compressed tissue and appeared viable. There was a typical intermediate region with the characteristically varying degrees of edema with randomly distributed congested vessels. The central portion of this slide appeared compressed with patchy areas of necrotic inflammation. The compression seen in the central portion of the slide, combined with the apparent absence of the optical fiber in this slide and its presence in the inferior slide, suggests that the slice of tissue removed from the tumor was at the very tip of the optical fiber or that the pasta marker was not inserted a sufficient distance.

The inferior slide of the tumor treated in Study #1336 was the only slide with evidence of direct thermal injury. A very small, golden-colored piece of acellular tissue with fused membranes could be seen immediately adjacent to the pasta marker. This slide also had an area of compressed and necrotic tissue surrounding the marker with a fairly distinct edemetous rim, including a focal area of marked interstitial hemorrhage. The symmetry of the edemetous rim is unique to this slide, as opposed to the randomly distributed patched of edema seen on the other slides. The intermediate region outside the edemetous rim and the peripheral region both have the same properties seen on the other slides. There was also a large area of pink necrotic tissue with hemorrhage and inflammation in the peripheral region at the opposite end of the tumor from the pasta marker, but this was not attributed to thermal injury. The volume of necrosis seen on this slide was larger and tended to be more circular instead of ellipsoidal, in contrast to the other slides. The symmetry of the

necrosis and the edemetous rim, combined with the small area of acellular damage, allow the damage in this tumor to be attributed to the thermal treatment with confidence.

Chapter 6 Discussion and Conclusions

6.1 System Performance

6.1.1 System Integration

The data acquisition system designed and built in this thesis performed admirably in all cases, with the exception of the errant temperature values recorded after the laser exposure in Study #1336. The integration of the imaging and temperature measurement systems allowed rapid acquisition of the image and temperature data and permitted the operator to focus primarily on the images as they were reconstructed and displayed. The system insured proper measurement of the temperatures during the experiment, presented the data in a format suitable for quick review during the experiment and recorded the data with full annotation for later review. The interactive control of the imager and the temperature measurement electronics via the modified pulse sequence together with the program running on the PC guaranteed proper timing of the temperature measurements as well as temperature values uncorrupted by the radio frequency waves employed by the imager. The self-annotation of the image numbers in the temperature file simplified post-processing of the data and facilitated the signal intensity-temperature correlations reported in Chapter 3.

The use of the laser as the thermal therapy source allowed the generation of temperatures in excess of 60°C in the tumors with no interference in the images. The extended fiber system allowed control of both the laser and the imager by a single operator at the imager control

console.

6.1.2 Imaging Features

A "product" pulse sequence was used as the basis for the modified pulse sequence to maintain availability of the full range of image quality enhancement options furnished with a clinical imager while still providing the sequential acquisitions of fast spin echo images desired for these experiments. This was critical in reducing the time required for the acquisition of the intra-operative images in the animal experiments. Availability of the full imaging option set allowed acquisition with a 3/4 field of view in the phase direction, which reduced the image acquisition time by 1/4. This allowed the acquisition of four images per minute instead of three, a significant improvement in temporal resolution.

The 3/4 phase direction field of view option was the only option used in the animal experiments because the experimental design eliminated many sources of imaging artifacts, thus, the availability of the full set of imaging options was not exploited. However, the availability of the full set of imaging options may prove to be crucial in application of MR-guided therapy techniques to various areas of anatomy where options such as flow compensation, peripheral gating, cardiac gating, rectangular field of view and others could be critical in providing the image quality required.

Liver or other abdominal treatments could require respiratory compensation to suppress motion aritifacts. Treatments near large blood vessels could require either cardiac or peripheral gating to improve image

quality and would be valuable anywhere in the body, but could be particularly significant in the head and neck. The significance of temporal resolution in MR-guided therapy applications indicates that imaging options which enhance image quality without sacrificing imaging speed will be critical to the development and implementation of these types of therapy.

The final significant feature of the modified pulse sequence is the placement of the loop around the entire image prescription. This would allow sequential acquisition of multiple slices in the same manner as the single slice acquisition in this experiment if the TR and echo train length values were appropriate. This suggests two possible scenarios. In the first, the processes under observation are relatively slow and the imaging parameters chosen to optimize temperature sensitivity or accuracy would allow imaging of multiple slices. The ability to sequentially acquire sets of slices would allow coverage of a larger fraction of the tumor at no cost in temporal resolution. In the second scenario, which would be much more common, both speed and coverage are critical. The pulse sequence developed in this thesis allows a compromise to be made between speed and coverage that could be optimized on a per-patient basis to account for variations in tumor size, thermal source geometry or proximity of critical normal tissue elements.

6.1.3 Potential for Improved System Integration

6.1.3.1 Laser Control

Additional hardware would further automate the system and could potentially produce a one-touch experimental system coordinating all aspects of the laser thermal therapy treatment. The laser control is the primary impediment to the development of such a system because of the patient safety concerns inherent in control of the laser irradiation. The laser manufacturer is extremely hesitant in allowing any type of interfacing to the laser that would eliminate active, constant control of the laser.

However, custom hardware could be designed and added to the laser to allow duplication of the footswitch and "ready" controls by the PC. The custom hardware would duplicate the action of the switches so the laser could not detect the automated aspect of the procedure. The control board of the laser is removed with four screws and the terminals of the "ready-to-lase" switch are accessible on the back panel. Piggyback terminals could be added that would allow closure of the switch by relays on a hardware board added to the PC and a similar piggyback approach could be used to simulate the footswitch with the same PC relay board.

6.1.3.2 Additional Imaging and Annotation Features

Additional features in the imaging pulse sequence could improve the imager/PC synchronization and improve the self-annotation capabilities of the system. The present system employs a uni-directional control approach with the imager sending signals to the PC without any capability to receive signals from the PC. It is possible that a "scanf" statement in the real-time

section of the pulse sequence C language code, which is the receive equivalent of the transmit statement currently employed, could be used to control the imager from the PC.

This feature could enhance the performance of the system, reduce the operator control required and marginally improve the temporal resolution of the system. The operator control could be reduced because the pause in the pulse sequence associated with the initiation and cessation of the laser exposure, and the rapid temperature measurement mode employed at that time, could be automated. The imager would signal the end of the baseline image acquisitions and wait for an instruction to continue. The PC would initiate the sequence of rapid temperature recordings employed to study the effect of the laser light on the thermocouples and initiate the laser exposure. The PC would instruct the imager to continue acquisition once the temperature recording was complete. The imager would acquire the sequential images during the laser exposure and query the PC after every image to determine if the laser was to be turned off and if another pause was required. The PC would either instruct the imager to continue image acquisition or initiate the rapid temperature measurement and turn off the laser. This would eliminate the operator actions required for this process in the current procedure.

The temporal resolution and reliability of the intra-operative temperature measurements would also improve with bi-directional PC/imager communication. The 700 msec delay required for thermocouple

measurement stabilization could be eliminated with bi-directional communication. Instead of using a preset delay duration between images, the imager would inform the PC that image acquisition was complete and wait for a signal that the temperatures had been successfully recorded before beginning the next image acquisition. The PC could monitor the behavior of the thermocouples, determine when their values had stabilized and then record the temperatures. It would then send a signal back to the imager that the next image could be acquired. This could eliminate a portion of the 700 msec delay if the thermocouples could stabilize more quickly and could eliminate a portion of the 300 msec temperature recording delay if there were less than four thermocouples in operation. This time reduction does not seem significant relative to the 15 second image acquisition but the potential use of echo planar techniques, where the image acquisition is less than or on the order of a second, magnifies the significance of the delays employed in this experiment.

The possibilities for enhancement of image annotation with bi-directional communication could also be signficant. The PC could send a signal to the imager as to when the laser was turned on or off and this information could be displayed with the imaging parameters on the screen. This could help prevent both intra-operative and post-operative misinterpretation of the images.

6.1.3.3 Automatic Core Temperature Regulation

The other potential area for improvement in the engineering of the

experimental system lies in the feedback control of the animal's core temperature. The thermocouple measurement electronics have some control features that could be used to control the thermally-regulated water pump that supplies the water to the bed of the animal holder. The use of a high and low temperature alarm mode could be used to either send a signal to the PC or possibly even communicate directly with the water pump. These alarm mode features could also be duplicated by the program running on the PC. The thermocouple electronics or the PC would detect when the core temperature of the animal was too high or too low and instruct the thermally-regulated water pump to start or stop the flow.

Complete automation of the control of the animal's core temperature would depend on the features available on the water pump. The capabilities of the water pump are yet to be explored. The control available could be limited to a simple on/off flow switch or it could extend to remote setting of the temperature of the water in the pump reservoir. A simple on/off switch could be used to maintain the animal's core temperature above a certain level by setting the bath temperature at approximately 40°C and activating the flow whenever the animal's core temperature dropped below some threshold. This system would not be able to cool the animal as required during the laser thermal therapy treatment.

A system that could control the animal's core temperature in both the heating and cooling phases of the experiment would have to be able to adjust the temperature of the pump reservoir. The system could detect core temperature increases of a certain rate or above some threshold and reduce

the reservoir temperature in anticipation of the cooling required. Then the flow switch would be activated when the measured temperature exceeded a pre-determined limit. The opposite adjustments in reservoir temperature could be made if negative temperature changes were measured and the flow switch activated in the same way if the core temperature fell below some threshold. This would eliminate the need for the ice bath bypass loop and manual valve control in the current system and yield a complete experimental system requiring only one operator.

However, consideration of the thermal properties of the water flow system suggests that full automation may not be optimal for core temperature control. The thermal inertia of the water in the pump reservoir, as well as all the tubing between the pump and the animal holder, is significant, and the time required to reduce the temperature of the water flowing in the bed of the animal holder could be prohibitive. These factors could extend the time lag in the feedback loopbetween measurement of a high core temperature and initiation of cooling to the point that the cooling might not begin until the treatment was complete.

A possible compromise allowing effectively complete automation without thermal reservoir temperature control would involve changing the water flow path to be exclusively through the ice bath bypass loop before the laser exposure portion of the experiment. A corresponding change in the flow control temperature setting from a low value to a high value would also be required. This would produce a cool-on-demand system during the laser exposure portion of the experiment and a heat-on-demand system

during the remainder of the experiment that would only require a remote flow control feature on the water pump. The ice bath is positioned inside the MR scan room close to the animal holder so the thermal inertia concerns of the pump reservoir temperature control approach are eliminated.

However, the reactive nature of control systems would not necessarily compensate for the experience gained by human operators over the course of several experiments. Anticipatory cooling was applied during several of the laser thermal therapy treatments because there seemed to be a signficant lag between the initiation of cooling and the response of the core temperature of the animal. This could be attributed to the natural insulation of the animal to its external environment. It is possible that the time lag could be reduced if the animal's abdominal surface was shaved to remove the insulating effect of the fur and improve the thermal conduction between the bed of the animal holder and the animal. The experience of the early experiments allowed the operators to effectively eliminate this time lag by estimating when cooling would be required and initiating it before the increase in the animal's core temperature was measured. A simple control system would not be able to incorporate this complex, anticipatory, human property.

6.2 Tumor Excision Surviving Fraction Results

6.2.1 Surviving Fraction and Temperature Results

The surviving fraction results of the Nd:YAG (λ=1064 nm) laser

thermal therapy treatments of 1.5W for 10 minutes, as measured with the volume tumor excision colony growth assay, yield a range of surviving fraction values from 1.3% or less in the core of the tumor to 25-35% at the periphery. The single treatment in which the laser exposure was 1.5W for 6 minutes produced surviving fractions values ranging from 0.11% in the core to 40.5% at the periphery. The peak temperatures measured in the tumors during the 10 minute exposure treatments ranged from a maximum of 54.9°C in region 1 (Study #984-R) to 39.4°C, also in region 1 (Study #1151-L), while the maximum temperature for all tumors in the volume excision group was 59.6°C and was measured in region 1 of Study #984-L at the end of the 6 minute exposure. No thermocouples were located in the core of the tumors that received the 10 minute treatments. Thus, the highest tumor temperature was measured in the core of a tumor but was produced by a 6 minute exposure. There was some correlation between the peak measured temperatures and the surviving fraction values from these tumors ($R^2 = 0.483$) and a slightly weaker correlation between the temperatures and the natural log of the surviving fraction ($R^2 = 0.405$).

The surviving fraction results of the Nd:YAG (λ=1064 nm) laser thermal therapy treatments of 1.5W for 10 minutes, as measured with the single slice tumor excision colony growth assay, yield a range of surviving fraction values from 0.000125% in the core of the tumor to 38.8% at the periphery. Three of the five core samples in the single slice tumor excision group produced indeterminate results because none of the plated cells

developed into colonies. The peak temperatures measured in these tumors ranged from a low of 46.2°C at the periphery of the tumor in Study #1392 to a maximum of 64.6°C in region 1 of the tumor in Study #1282. There was effectively no correlation between the peak measured temperatures in the single slice tumor excision group and the surviving fractions values (R^2 = 0.18) and a weak correlation between the peak measured temperatures and the natural log of the surviving fraction (R^2 = 0.39). Analysis of all tumors from both groups also showed essentially no relationship between the peak measured temperatures and the surviving fraction (R^2 = 0.0212) and a very weak correlation between the peak measured temperatures and the natural log of the surviving fraction (R^2 = 0.24).

6.2.2 Thermocouple Location Uncertainty

The assignment of thermocouples to tumor excision regions is a difficult process with multiple sources of error. The artifacts associated with the thermocouples do not allow precise determination of their location relative to the optical fiber. Partial voluming effects, in which the thermocouple is on the edge of a MR imaging slice instead of completely contained in the imaging plane, can also make determination of their location difficult. The 3mm slice thickness employed in the animal experiments inserts an automatic ±1.5mm uncertainty factor into determination of the thermocouple position and any errors in the alignment of the imaged slice and the excised slice would also modify the relationship between the temperature and the measured surviving fraction.

All these factors would combine with the 1.5mm region thickness to make thermocouple-to-region assignments very difficult.

The difficulty in identifying the thermocouple location, coupled with the steep thermal gradients in these experiments, could contribute to the statisticly weak correlation between the peak measured temperatures and the surviving fractions. The average thermal gradients, computed by subtracting the peak readings of adjacent thermocouples on the three thermocouple array and dividing by their 5mm separation, were 0.94°C/mm in the volume tumor excision group and 1.61°C/mm in the single slice tumor excision group. This translates to a change of 1.5 - 2.4°C per region if based on a 1.5mm region thickness.

6.2.3 Single Slice vs Volume Tumor Excision Technique

The volume tumor excision experiment was designed to examine the response of the entire tumor volume to the laser thermal therapy treatment. The separation of successive layers of tissue into independent regions was used to investigate the spatial relationships between the optical fiber and the severity of the treatment. Thus, the alignment of the regions relative to the optical fiber is central to interpretation of the results. The alignment in the volume tumor excision experiment is based on the surgical technique employed in the tumor excision.

The pasta marker can be seen at its entrypoint into the tumor, coronal plane MR images were used to estimate the depth of penetration of the optical fiber and axial plane MR images were used to estimate the

optical fiber location in cross section. This information was combined to determine the pattern of cuts used to divide the tumor into 5 regions.

In contrast, the single slice excision technique was designed to optimize the match between the ROIs defined on the image and the region of tumor processed in the colony growth assay. This technique was able to determine the location of the pasta marker, and thus the optical fiber, with greater certainty because the pasta marker could be seen in the excised slice. The relatively consistent size and shape of the excised regions defined by the cutting templates enhances the confidence in the ROI-excision region match. The major source of uncertainty in this technique is then the alignment of the imaging slice with the excised tumor slice. The alignment of the imaged slice with the excised slice appeared successful in four of the five tumors processed with the single slice technique, as evidenced by the match between the number of ROIs and tumor excision regions, but Study #1413-L demonstrates that the technique is imperfect. The lack of a peripheral region in the excised slice of tumor, in contrast to the 20mm long-axis ellipsoidal tumor shown in the image, suggests either significant shape change with excision or misalignment of the slice. The surviving fraction values from the core regions of the single slice excision group (<0.00001 for 2 tumors and indeterminate in the other 3 tumors) indicate that the core regions were well aligned with the optical fiber and received a very high level of treatment.

A comparison of the surviving fraction values in the single slice excision group and the volume excision group demonstrates that there is a

difference in the spatial distribution of the surviving fractions in the two experiments. This suggests that there is a different spatial distribution of the surviving fractions in the excision plane than that characteristic of the entire volume, as reflected by the volume excision results. The average surviving fraction values in the core and first two annular regions are significantly lower in the single slice excision experiment compared to the volume experiment. Seventy percent of the surviving fraction values in the core, region 1 and region 2 of the single slice tumor group are less than 1%, while only 33% of the equivalent regions in the volume excision group have survival values less than 1%.

The single slice excision group also has a transition to an area of intermediate surviving fraction values that is more abrupt than that seen in the volume experiment. The volume excision results produced surviving fraction values for the third (outermost) annular region in the 6-15% range, while the third annular region in the single slice tumor excision group had values ranging from 0.07 - 3%. The percentage change between region 3 and the periphery was an average of 24.5% in the volume excision group but was an average of 35% in the single slice excision group. This demonstrates the more abrupt transition to a higher level of survival.

6.3 Generation of Treatment Zones with the Laser Thermal Protocol

These treatments cannot be considered in the same context as classic hyperthermia treatments because of the high temperatures, rapid rate of temperature change and relatively short treatment duration. However, the

surviving fraction values indicate that the thermal treatment protocol was not wholly successful in its attempts to create regions of effect that match the three treatment Zones described in Section 1.3.1. The maximum surviving fraction of 40% in the periphery of the tumor in study #984-L indicates that the peripheral regions received a significant level of treatment and thus do not qualify for the untreated Zone 3 discussed in Chapter 1. Also, with the exception of a very small piece of tissue from study #1336, the histological evaluation of the treatment did not produce any evidence of the acellular necrosis and coagulation necrosis in the area immediately adjacent to the optical fiber as has been produced by other laser thermal therapy treatments reported in the literature [1, 2 ,3, 4]. Regions did exist in which the surviving fraction was less than $1X10^{-5}$. However, these regions cannot neccessarily be considered characteristic of Zone 1, the most severe treatment Zone, because of the lack of gross morphological change in the tissue detected by histological evaluation with tumor excision two hours after treatment.

This is somewhat unexpected because of the high temperatures measured in the tumor during the treatment. It is possible that the temperatures were not maintained for a sufficient duration to induce the acellular necrosis and coagulation necrosis reported in laserthermia reports[1,2]. Matthewson et al reported charring and cavitation surrounded by a degenerate zone in livers excised 1 hour after treatment[1]. Matsumoto et al were able to distinguish 3 distinct types of damage in livers excised 10 minutes after laser irradiation: a central zone of acellular necrosis, and

intermediate zone of coagulation with enucleated hepatocytes and an outer thin zone with nucleated hepatocytes and some vacuolization[2]. The near complete absence of histological evidence of Zone 1, coupled with maximum measured surviving fraction value of 40%, indicate that the majority of the tumor was covered by Zone 2, the transition Zone between the irreversibly and immediately damaged tissue of Zone 1 and the Zone 3 area of effectively untreated tissue.

The laser power and the length of the exposure were chosen in an attempt to generate a slowly growing combination of treatment Zones whose evolution could be observed over the course of the treatment. The lack of gross morphologic changes in the center of the tumor indicate that the energy deposition rate induced by the laser power setting was too low to create Zone 1. The tumor size of 2cm or larger was selected in an attempt to contain multiple Zones within a single tumor and allow division of the tumor into multiple volumes sufficient for analysis. The spread of significant treatment levels to the periphery indicates that the treatment duration was too long and that Zone 2 extended into the periphery of the tumor. Thus, the intention of expanding the size of Zone 2, the transition Zone, to facilitate study of its properties was successful, but at the expense of the elimination of Zone 1, the untreated Zone.

6.4 Four Region Tumor Results

The slices of the tumors excised from Study #1282 and #1413-L were smaller than the slices from the rest of the tumors, with no tissue outside

the 14mm diameter boundary of the third annular region, and thus with only four excision regions instead of five. The surviving fraction values from the outermost regions in these tumors (10% and 16%) are significantly different from the surviving fraction values in the third annular region of the other three tumors in the single slice excision group (average SF=1.6%, range 0.44%-3.4%), yet they are also significantly different from the surviving fractions values from the periphery of the other tumors (average SF=36.7%, range 33%-39%). The surviving fraction results from Studies #1282 and #1413-L present us with the interesting question of whether the outer region of these tumors should be considered a periphery because of its proximity to the surrounding tissue or a third annular region because of its proximity to the optical fiber. In the context of the thermodynamics of the situation, this is essentially asking if the heat generation of the laser exceeds the ability of the adjacent tissue to re-distribute that heat. This has significant implications in the thermal therapy treatment protocols designed for different size tumors.

If the heat generation of the laser dominates, the severe treatment zone will expand outward until conduction of thermal energy through the surface of the severe treatment volume equals the thermal energy deposition by the laser. This would produce surviving fraction values in the outer regions of these tumors similar to the third region values in the rest of the single slice group. If the thermal energy distribution capabilities of the tissue dominate, the bulk normal tissue adjacent to the treatment area will conduct the thermal energy away as fast as it is generated,

maintaining a relatively cool boundary layer between the severe treatment zone and the normal tissue. This behavior would produce surviving fraction values that are similar to those seen in the periphery of the other tumors in the single slice excision group.

The 10% and 16% surviving fraction values measured for the outer regions in these tumors, combined with consideration of their subcutaneous location, could indicate that both of these effects are signficant. The thermal energy deposition effects could dominate on the skin side of the tumor because any subcutaneous fat would act as an insulator and the temperature in this area could rise significantly. The subcutaneous fat is seen in the image of Study #1413-L as a hyperintense edge of the tumor. The outer region of the tumor seen in the image in Study #1282 appears to be adjacent to muscle on both sides, but there is a thin, hyperintense border between the tumor and the muscle that is partially obscured by the ROI trace. The nature of the hyperintense tissue is unknown so it cannot be determined if it has insulating properties or not so the remainder of the discussion applies only to the tumor in Study #1413-L.

The temperatures for this tumor of Study #1413-L are graphed in Figure 5.12. The highest temperature measured in the tumor was 61.6 °C, detected just under the skin in an area assigned to region 3. One of the other thermocouples in the tumor was assigned to the core region and its peak measured temperature was 53.4 °C, while the third thermocouple was assigned to region 2, but was positioned medial relative to the optical fiber, and its peak measured temperature was 49.8 °C.

The tissue cooling effects may dominate on the muscle side because of the relatively large volume of muscle adjacent to the tumor. The muscle could absorb the heat and re-distribute it to the rest of the body through both conduction and convection, assisted by the vasodilation that is the normal response of muscle tissue to an increase in temperature[5]. This is supported by the increase in core temperature to 49.1°C seen in an animal in a preliminary experiment, which prompted the development of the animal cooling system described in Chapter 4.

The vessels in the skin also respond to a temperature increase with vasodilation[5], but the skin has a much smaller surface area through which it can redistribute the heat to the rest of the body. A simple analogy to compare the re-distribution of heat by the muscle and by the skin would be water pouring into a bowl. When the water reaches the top of the bowl it spills out all around the rim. The skin is the surface of the bowl, the water is the thermal energy and the rim is the area of contact between the skin over the tumor and the rest of the animal. In contrast, the muscle tissue is more like a sieve that has holes throughout its surface because it can transfer the thermal energy to the tissue behind it and prevent a buildup.

Since these effects would occur on opposite sides of the tumor but tissue from all outer areas is mixed in the tumor excision procedure, the effects on both sides might combine to produce an intermediate surviving fraction value. This could be one explanation for the surviving fraction value of 16% for the outermost region in this tumor, which is approximately 1/2 of the value in the peripheral regions of the other tumors in the single

slice excision group. An experiment in which the tissue removed from the medial aspect of the tumor was processed separately from the tissue removed from the lateral aspect of the tumor would help determine if these effects were responsible for the surviving fraction values measured in this case.

6.5 Tissue Characterization Results Discussion

The tissue characterization results do not indicate that there is a strong correlation between the change in the T1 or T2 parameter and the surviving fraction across tumors, however, individual tumors show a strong correlation. The correlation between the percent T1 change and the natural log of the surviving fraction in tumor #1282 is particularly strong (R^2 =0.9995) and the average R^2 value for all the tumors in the single slice group =0.61, but all the tumors combined yield an R^2 =0.0046. A similar behavior is found in the relationship between the percent change in T2 and the natural log of the surviving fraction, with the combined R^2 = 0.003 and the average R^2 for 3 tumors =0.52.

The tumors in the volume excision group also demonstrate similar behavior, with a combined R^2 =0.29 for the correlation between percent change in T1 and natural log of surviving fraction and an average R^2 for the tumors taken independently =0.51. The relationship between the percent change in T2 and the natural log of the surviving fraction has a similar pattern, with a combined R^2 = 0.26 and an average of individual R^2 's = 0.25.

This could be evidence of misalignment between the regions of interest defined in the images and the excised tumor regions. It could also be evidence that the changes in the tissue are not reflected by changes in the MR properties of the tissue on the time scale investigated here. This is additional data to demonstrate the differences between the thermal therapy treatment employed here and laserthermia treatments that employ higher powers and temperatures to produce immediate changes in the tissue.

6.6 Histological Results Discussion

The colony growth assay is able to reveal effects of the laser thermal therapy treatment that cannot be detected by histological evaluation performed on an equivalent time scale. The tumor treated in Study #1336 showed direct evidence of thermal injury while the tumor treated in Study #1413-R had no evidence of direct thermal injury. The cells plated from the core of the tumor in Study #1336 did not develop any colonies while an equal number of cells plated from the core of Study #1413-R developed 1 colony. The surviving fraction values in regions 1, 2 and 3 for Studies #1336/#1413-R are: 0.013/indeterminate, 0.024/0.047, and 0.034/0.010, respectively.

The nearly complete absence of direct evidence of thermal injury with histological evaluation in all three tumors is in contrast to the significant cell kill induced by the treatment as measured by the colony growth assay. This demonstrates the differences in the evaluation techniques and raises questions of the validity of the use of histology for evaluation of laserthermia treatments with prompt tissue excision, which

has been the standard to date. The excision of the tumor immediately after the treatment interrupts the physiologic response mechanisms that would determine the chronic response of the treated tissue. Matthewson et al report that the evolution of laser induced lesions in the liver yields a maximum lesion diameter at day 7 post-treatment, which eventually matures into a fibrous scar[1]. The absence of gross morphologic change in the histology slides indicates that the treatment severity was not sufficient to induce immediate physical changes in the cells that would reflect their change in state. However, the immune response that would occur over the next several days would respond to the biological change and may eventually provide evidence, in the form of basophils, neutrophils, polymorphonuclear cells and other cellular waste processors, that the tissue had indeed changed.

This late biological response would be visible with histology and could be used to grade the severity of the treatment as well as demonstrate the spatial distribution of the treatment severity. However, the use of delayed histology for correlation of intra-operative images to treatment severity can be problematic because of the continued growth of untreated tumor and the associated changes in the geometry of the treated tissue[4]. This would complicate any attempts to directly correlate intra-operative images with treatment effectiveness because it would be very difficult to match pixels on the image with tissue volume elements in the distorted volume.

The late biological response would also effect the results produced with the colony growth assay. The response of the tissue to a thermal

treatment is not immediate, so the prompt excision of the tumor interrupts the recovery and decay processes that would occur over time. The assay could remove cells from an environment in which the vessels had been thrombosed by the treatment, where they would eventually become ischemic and die, and place them in an environment optimized for reproduction, where they could recover and yield a false indication of survival. In contrast, cells that would recover through some process are removed from the environment that could promote their recovery, yielding a false indication of cell kill. Thus, while the colony growth assay has indicated that the treatments in this study were significant, time-lapse studies with tumor excisions on successive days would be required to evaluate the chronic response of the tumors to the treatment.

6.7 Colony Growth Assay and Histological Evaluation

The magnitude of the differences between the colony growth assay and the histology displayed in this study suggest that the colony growth assay is a more accurate gauge of the treatment response for tumor excision less than three hours after treatment. While some recovery could occur and yield higher surviving fraction values than those produced with prompt excision, it is not likely that the recovery processes could account for the drastic change that would be required for the assay results to match the acute histology results.

The reports of laserthermia in the literature commonly use histological grading as a means of treatment evaluation for both acute and

chronic responses[1,4,2] but this author is not aware of any reports of the use of surviving fraction values measured with a colony growth assay as a means of evaluating laser thermal therapy treatments. The typical damage pattern that appears immediately after treatment or as much as 48 hours later includes acellular necrosis immediately adjacent to the thermal source with a rim of coagulation necrosis and a peripheral rim of edema[2,1,6]. The lesion size is usually correlated with the coagulation necrosis boundary or with the edema boundary. The results from this study clearly indicate that histological evaluation does not accurately measure the acute effects of the treatment if tumor excision occurs within 3 hours post-treatment.

The colony growth assay results in this study also suggest that thermal therapy treatments which induce immediate, gross morphologic changes are not necessary to induce significant levels of cell death. Large fractions of cells were killed without reaching the extreme temperatures 70°C or higher that produce immediate degradation in cellular or macroscopic structures. This has implications for the thermal source protocols designed for laser thermal therapy treatments. The results also indicate that there is a fairly abrupt transition between regions with surviving fraction values of 5% or less and regions with surviving fraction values of 10-40%. This would be very important in treatments which seek to minimize damage to the normal tissue adjacent to the target and presents the possibility that if the thermal distribution could be matched to the shape of the tumor, the survival transition could be aligned with the tumor

boundary. However, treatment protocols which are willing to sacrifice a fraction of the normal tissue surrounding a tumor to guarantee the destruction of the neoplastic cells may want to employ the more drastic temperature levels of 60-70°C and higher. These treatment protocols should then develop thermal source protocols which minimize the extent of the transition region between the acellular/coagulation necrosis regions and the unaffected regions as well as optimize the alignment between the target and the volume of increased temperature. MR-guided, scanned, focussed ultrasound which deposits enough energy to raise tissue temperatures to ≈70°C in less than five seconds in a very limited volume[7] is one modality that appears capable of accomplishing this.

6.8 Evaluation of Image-to-Actual-Functions (IAFs)

The relationship between the MR images of a thermally treated tissue volume and the severity of the treatment, as measured by either a colony growth assay or histological evaluation, is of interest for all thermal therapy modalities. This thesis sought to examine if a relationship exists between T1-weighted, temperature sensitive, fast spin echo (FSE) MR images and the surviving fraction from a regional tumor excision as measured with a colony growth assay, with the tumor excision approximately two hours after treatment. The attempt to fit the measured surviving fraction data with image-derived surviving fractions calculated with several different equations stressed the fitting of the largest surviving fraction values most heavily. The process treated all the measured

surviving fractions from the volume tumor excision experiment as one complete data set and all the measured surviving fractions from the single slice tumor excision experiment as another complete data set. The relative success of the fitting procedure will be discussed for each treated tumor. The image noise value cited for each tumor was computed by sampling the signal intensities in an ROI in the tumor and dividing the average signal intensity by the standard deviation[8].

6.8.1 Volume Tumor Excision Experiment Fitting Discussion

The fitting process was not able to account for the decrease in surviving fraction values from the peripheral region to the core for the tumor treated in Study #984-R. The fit between the largest measured surviving fraction value (32%) and the various image-derived values was within 4% for eight of the nine equation tested, thus the iterative fitting process was able to adjust nearly all the equations to fit this value well. However, the image-derived values for the remainder of the regions did not decrease by more than 12% in any of the equations while the measured surviving fractions dropped through 4 orders of magnitude. The equation that was fit most accurately, as measured by the chi-squared value of 0.0193, was the Activation Energy equation (AE Eqn. #5.13 and #5.14). The image noise threshold determined by the fitting process for this equation was 0.003, thus any percentage signal intensity change above 0.3% was considered in the calculation, which is a very low image noise threshold compared to the image noise, which was measured as 7.0%.

The various equations did not produce such uniform results for Study #984-L. The best fit between the measured and image-derived surviving fractions, as measured by chi-squared, was achieved with the Exponential-Rate-Magnitude equation (EXPRM Eqn. #5.9 and #5.10) which sums terms with the magnitude of the signal intensity change, the rate of signal intensity change and the rate multiplied by the magnitude to compute an image dose, then uses an exponential function for the dose-response equation. This equation produced the lowest chi-squared value of 0.0236 because it fit the largest measured surviving fraction value within 5%, while all the other equations underestimated the largest surviving fraction by at least 20%. However, the Exponential (EXP Eqn. #5.3 and #5.4) equation was the most successful describing the decay in surviving fraction and was the only equation to yield a surviving fraction value less than 1%. The EXPRM equation used a noise threshold of 4.8%, which is the approximate value of the measured image noise of 5.1%, while the EXP equation used a noise threshold of 12.8% but applied a very heavy weighting to any changes above that level as shown by the coefficients in Eqn. #5.3.

The fitting process was more successful fitting the image-derived surviving fractions in Study #1151-R to the measured surviving fractions. The Sapareto-Dewey equation[9] (SD Eqn. #5.1 and #5.2) and the Polynomial equation (POLY Eqn #5.5 and #5.6) both fit the measured values equally well (chi-squared =0.00616 and 0.006158, respectively). The image derived values for both equations were within 2% of each other from 20% to 2%. The two equations take a very different approach to computing an image dose

and have very different dose response equations, thus it is unexpected that they should produce such similar image derived surviving fraction values. Both equations used relatively small noise thresholds (SD = 3.76%, POLY=0.664%) compared to the 4.2% measured noise threshold in the image.

Evaluation of Figures 5.21 and 5.22, as well as consideration of the chi-squared values, indicates that the Exponential-Rate-Magnitude equation (EXPRM Eqn. #5.9 and #5.10) provides the best fit between the image derived and measured surviving fraction values in Study #1151-L. It uses a noise threshold of 4.8%, slightly higher than the measured noise value of 3.5% and fits the periphery and annular regions within 6% of the measured value. This fit produced the best match out of all the tumors in the volume tumor excision group with a chi-squared value of 0.003161.

6.8.2 Single Slice Tumor Excision Experiment Fitting Discussion

The fit between the image derived and measured surviving fractions in Study #1282, as measured by the chi squared value, was better than those in the volume tumor excision group by 2 orders of magnitude. This tumor only had 4 tumor excision regions, thus there is one less value to contribute to the chi-squared. Also, the measured surviving fractions in this tumor covered a relatively short range, with the maximum surviving fraction at 10.24%. The equation with lowest chi-squared value = 3.31E-5 was the Polynomial equation (POLY Eqn. #5.23 and #5.24). Examination of Figure 5.24 reveals that this equation not only fit the largest surviving fraction

within 1.3% but also produced surviving fraction values of 1.2% or less for the inner regions. POLY used an image noise threshold of 2.2E-6, effectively allowing all changes in the image to have an impact on the image dose calculation.

The Maximum-Exponential equation (MAXE Eqn. #5.33 and #5.34) produced the best fit for Study #1336 with a chi-squared of 0.00438. Equations SD and EXPR fit the largest surviving fraction value within 1% just as MAXE did, but MAXE also yielded surviving fraction values of 5% and 0.16% for the first annular region and the core where the other equations produced values of 15% and 28%. Thus, MAXE demonstrated a capability to deal with a wider range of surviving fractions for the data in this study. MAXE does not use an image noise threshold because it operates on the maximum signal intensity change experienced by a pixel over the course of the treatment. Thus, comparison of its noise tolerance to other equations is not valid.

The fit for Study #1392 is relatively poor because of the artifacts that corrupted the images during the treatment. The water flow through the bed of the animal holder was the source of the artifacts. The artifacts indicate that the flow was interrupted, probably by an air bubble in the hose system, which produced artifacts that artificially modified the signal intensities throughout the image. The periphery had more pixels than the other regions so its image derived surviving fraction was affected the most. Normally this would produce an artificially low image-derived surviving fraction for the periphery because the signal intensity changes were greater

than normal. However, the priority placed on matching the high surviving fraction in the periphery led instead to artificially high surviving fraction values for the inner regions. The Maximum-Exponential equation (MAXE Eqn. 5.33 and #5.34) produced the best chi-squared value of 0.0136.

The Maximum-Exponential equation (MAXE Eqn. 5.33 and #5.34) also produced the best chi-squared value of 0.011 for Study #1413-R. The Exponential-Rate-Magnitude equation produced lower values for the interior regions and appears to follow the meaured curve better but its chi-squared value is much larger because it estimates a 5.8% surviving fraction for the periphery where the measured value in 38%. Thus, it achieves a better fit at the lower regions but does not have the dynamic range to account for the larger surviving fraction at the periphery.

The Activation Energy equation (AE Eqn. #5.31 and #5.32) provides the best fit for Study #1413-L with a chi-squared of 0.000561. It provides the best match because it matches the 16.6% measured surviving fraction within 1.3% while the other equations best match for the periphery is within 4%. It has a similar dynamic range to the other equations (9.6% vs an average of 10.5% for the other eight equations) and uses a noise floor of 1.7% compared to the measured noise of 3.4% for this study.

6.9 IAF Summary

The results of the fitting between the measured and image-derived surviving fractions indicate that the method is able to match the largest surviving fraction values across studies but is not able to account for the

multiple logs of cell kill achieved with these treatments. No single equation was superior at fitting the measured and image derived values for all the studies or for all the studies in a given group. The Activation Energy equation provided the best fit in 2 studies, Maximum-Exponential in 3 studies, Polynomial in 2 studies, Exponential-Rate-Magnitude in 2 studies, and Exponential and Sapareto-Dewey each in 1 study. The equations were best at matching the measured surviving fraction in the cases where the dynamic range was relatively small, as in Study #1282, Study #984-L and Study #1151-R. The equations also demonstrated a capability to match the measured surviving fractions over a limited range in Study #1151-L.

This suggests that the equations can only be applied to a limited range of temperatures or signal intensity changes. Thus, when high temperatures (>50°C) are reached in the tissue a hysteresis effect similar to that seen by Jolesz[10] and LeBihan[11] could invalidate the applicability of the equations. This suggests that an alternative approach to IAF development examining tissue parameters instead of raw signal intensity could yield better results. This could be difficult to implement because the time required to measure the T1 or T2 of the tissue is on the order of minutes for reliable multi-point measurements[12] and processing time to derive the parameters from the images would further reduce the temporal resolution.

One approach that could be feasible involves examination of the perfusion in the tumor. An intravascular contrast agent could be injected with a drip IV or a bolus injection if its clearance rate was low enough and its distribution in the tumor monitored during the treatment . The use of

albumin-Gd-DTPA as an intravascular contrast agent has been demonstrated[13]. The slow plasma clearance properties of this compound were demonstrated by the constant MR signal intensities in tissue and blood which were maintained from 1 to 11 minutes post-injection. Previous reports documented near constant signal intensities for up to 60 minutes.[14] The toxic limits of contrast agents of this nature would need to be considered simultaneously with the concentration required for good image quality to determine if an IV drip would be feasible.

6.10 Conclusions

This thesis has demonstrated the development and initial use of an integrated MR imaging/laser/temperature measurement system suitable for use in MR-guided thermal therapy treatments. The phantom experiments have shown that polyacrylamide gels doped with agar, CuCl, India ink and polystyrene microspheres have the ability to act as tissue simulating materials, allowing simultaneous control of their optical and MR properties. Also, these gel phantoms could potentially be manipulated to simulate the MR property/temperature hysteresis effects seen in tissue. The phantom experiments have demonstrated the necessity of complete characterization of the material of interest throughout the temperature range that is to be examined for accurate signal intensity to temperature correlations.

The animal experiments have further demonstrated the capabilities of the integrated thermal therapy system design and have provided the first

report of tumor cell surviving fraction from a colony growth assay for an in vivo tumor model treated with laserthermia under MR control. The results have demonstrated the potential weakness of histology when used as a measure of acute treatment severity with tissue excision less than 3 hours post-treatment. The results have also provided an initial examination of the spatial distribution of a quantifiable measure of cell killing for a laser thermal therapy treatment employing an Nd:YAG laser with diffusing tip fibers.

The attempt to fit the measured surviving fraction values to image-derived values demonstrated that a fit can be achieved over a limited range of values and across mutltiple tumors but that the multiple logs of cell kill achieved with the thermal therapy treatment employed in this study cannot be accounted for with the equations tested here. It is possible that other equations could be found that could improve the fit between the measured and image derived surviving fractions, but the various equations tested here represent a cross section of hyperthermia-based, physics-based, intuititve and computationally simple forms that would be the most likely candidates for an automatic therapy monitoring system. This thesis has further demonstrated the capabilities of thermal therapies employing moderate to high temperatures (50-65°C) and has illuminated several possibilities for further work in this area. The possibility of monitoring a thermal therapy treatment with an intravascular MR contrast agent is one particular area that merits investigation.

Appendix A1

Appendix A2

REFERENCES

1 Matthewson K, Coleridge-Smith P, O'Sullivan JP, Northfield TC, Bown SG. Biological effects of intrahepatic neodymium:yttrium-aluminum-garnet laser photocoagulation in rats. *Gastroenterology*, 93:550-557, 1987.

2 Matsumoto R, Selig A, Colucci VM, Jolesz FA. Interstitial Nd:YAG laser ablation in normal rabbit liver: Trial to maximize the size of laser-induced lesions. *Laser in Surgery and Medicine*. 12(6):650-658, 1992.

3 Anzai Y, Lufkin RB, Saxton RE, Fetterman H, Farahani K, Layfield LJ, Jolesz FA, Hanafee WH, Castro DJ. Nd:YAG interstitial laser phototherapy guided by magnetic resonance imaging in an ex vivo model: Dosimetry of laser-MR-tissue interaction. *Laryngoscope* 101:755-760, 1991.

4 El-Ouahabi A, Guttman C, Hushek S, Bleier A, Dashner K, Dikkes P, Black P, Jolesz F. MRI guided interstial laser therapy in a rat malignant glioma model. *Lasers in Surgery and Medicine.* 13:503-510, 1993.

5 Reinhold HS. Physiologic effects of hyperthermia. *Recent Results*

in Cancer Researc; 107:32-43, 1988.

6 Sato H, Sakai T, Fujishima I, Sugiyama K, Sekiguchi Y, Senzaki F, Hiraga T, Daikuzono N. Laserthermia for deep seated brain tumors using a hybrid hyperthermia probe. *Optical Fibers in Medicine SPIE* 120:637-641, 1990.

7 Hynynen K. The threshold for thermally significant cavitation in dog's thigh muscle *in vivo*. *Ultrasound in Medicine and Biology*. 17(2):157-169, 1991.

8 Matsumoto R, Oshio K, Jolesz FA. Monitoring of laser- and freezing-induced ablation in the liver with T1-weighted MR imaging. *Journal of Magnetic Resonance Imaging*, 2(5):555-562, 1992.

9 Sapareto SA, Dewey W. Thermal dose determination in cancer therapy. *International Journal of Radiation, Oncology, Biology and Physics*. 10:787-800, 1984.

10 Jolesz FA, Bleier AR, Jakab P, Ruenzel PW, Huttl K, Jako GJ. MR imaging of laser-tissue interactions. *Radiology* 168:249-253, 1988.

11 Le Bihan D, Delannoy J, Levin RL. Temperature mapping with MR imaging of molecular diffusion: Application to hyperthermia.

Radiology 171:853-857, 1989.

12 Majumdar S, Gore JC. Effects of selective pulses on the measurement of T2 and apparent diffusion in multiecho MRI. *Magnetic Resonance in Medicine* 4:120-128, 1987.

13 Kuwatsuru R, Shames DM, Muhler A, Mintorovitch J, Vexler V, Mann JS, Cohn F, Price D, Huberty J, Brasch RC. Quantification of tissue plasma volume in the rat by contrast-enhanced magnetic resonance imaging. *Magnetic Resonance in Medicine* 30(1):76-81, 1993.

14 Schmeidl U, Organ M, Paajanen H, Marotti M, Crooks LE, Brito AC, Brasch RC. *Radiology* 162(1):205-210, 1987.

Appendix A1

Figure A1.1 MR axial image of tumors treated in Study #984. Regions of interest for image processing are superimposed on the image. Signal void associated with the thermocouple array is seen at the lateral aspect of the tumors. Fiber placement was in the center of the tumor. Imaging parameters are TR=1000msec, TE=18msec, ETL=8, FOV=8X6cm, total imaging time = 15 seconds.

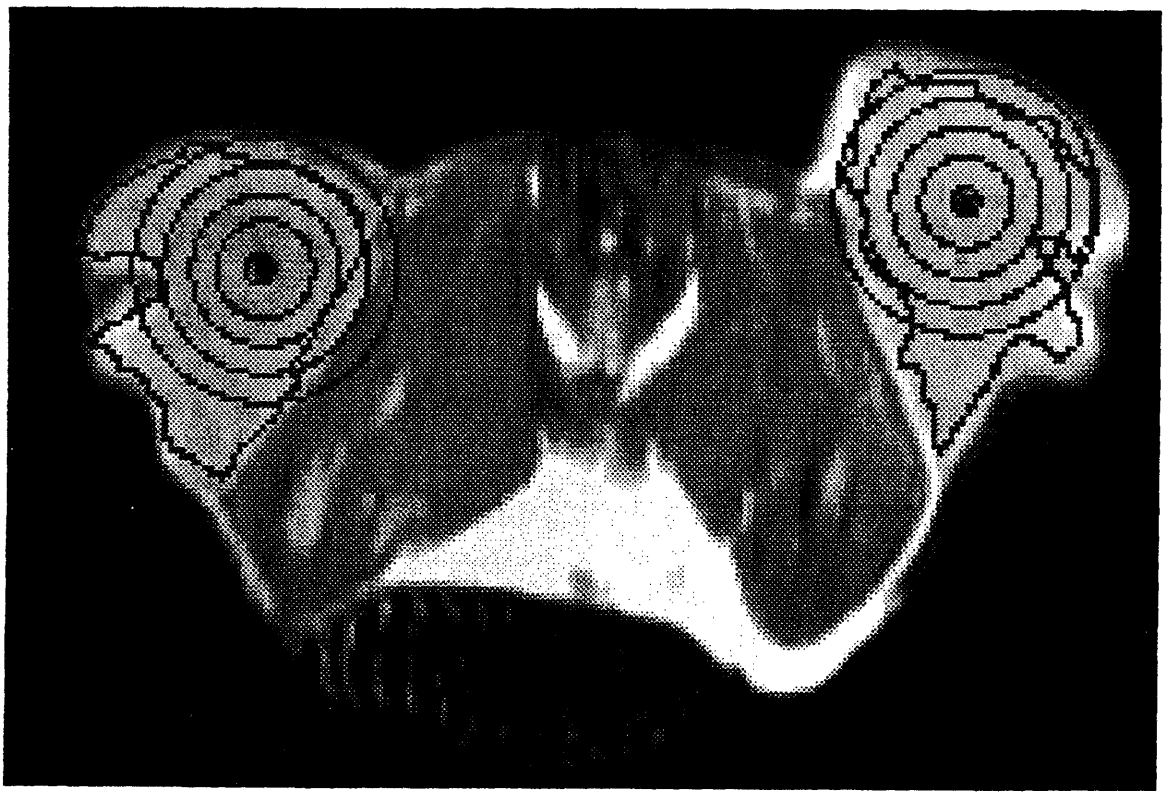

Figure A1.2 MR axial image of the tumor treated in Study #1151-R. Regions of interest for image processing are superimposed on the image. Thermocouple array is not visible. Optical fiber is positioned close to the medial muscle mass. Imaging parameters are TR=1000msec, TE=18msec, ETL=8, FOV=8X6cm, total imaging time = 15 seconds.

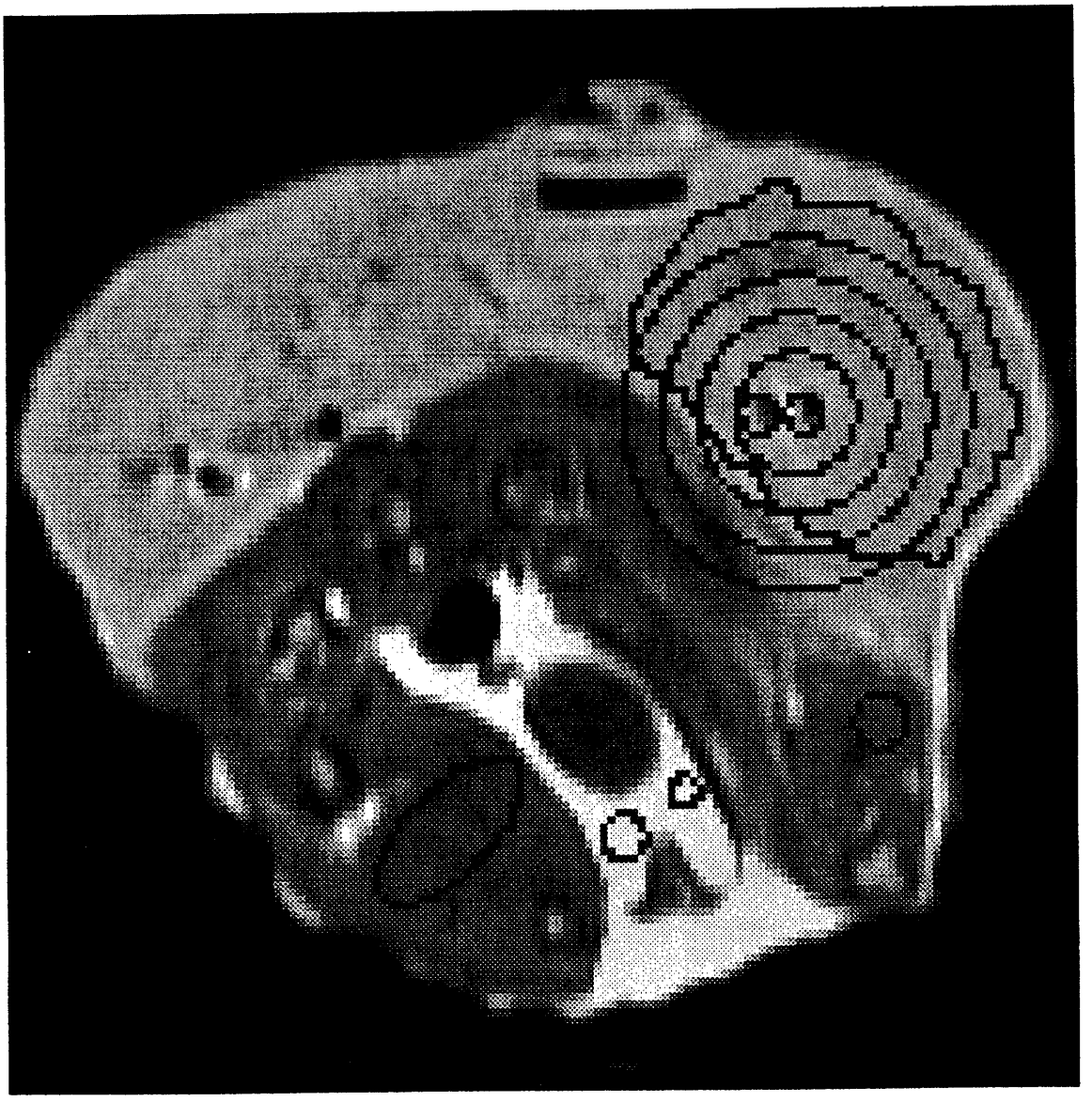

Figure A1.3 MR axial image of the tumor treated in Study #1151-L. Regions of interest for image processing are superimposed on the image. Optical fiber is again positioned close to the medial muscle mass. Imaging parameters are TR=1000msec, TE=18msec, ETL=8, FOV=8X6cm, total imaging time = 15 seconds.

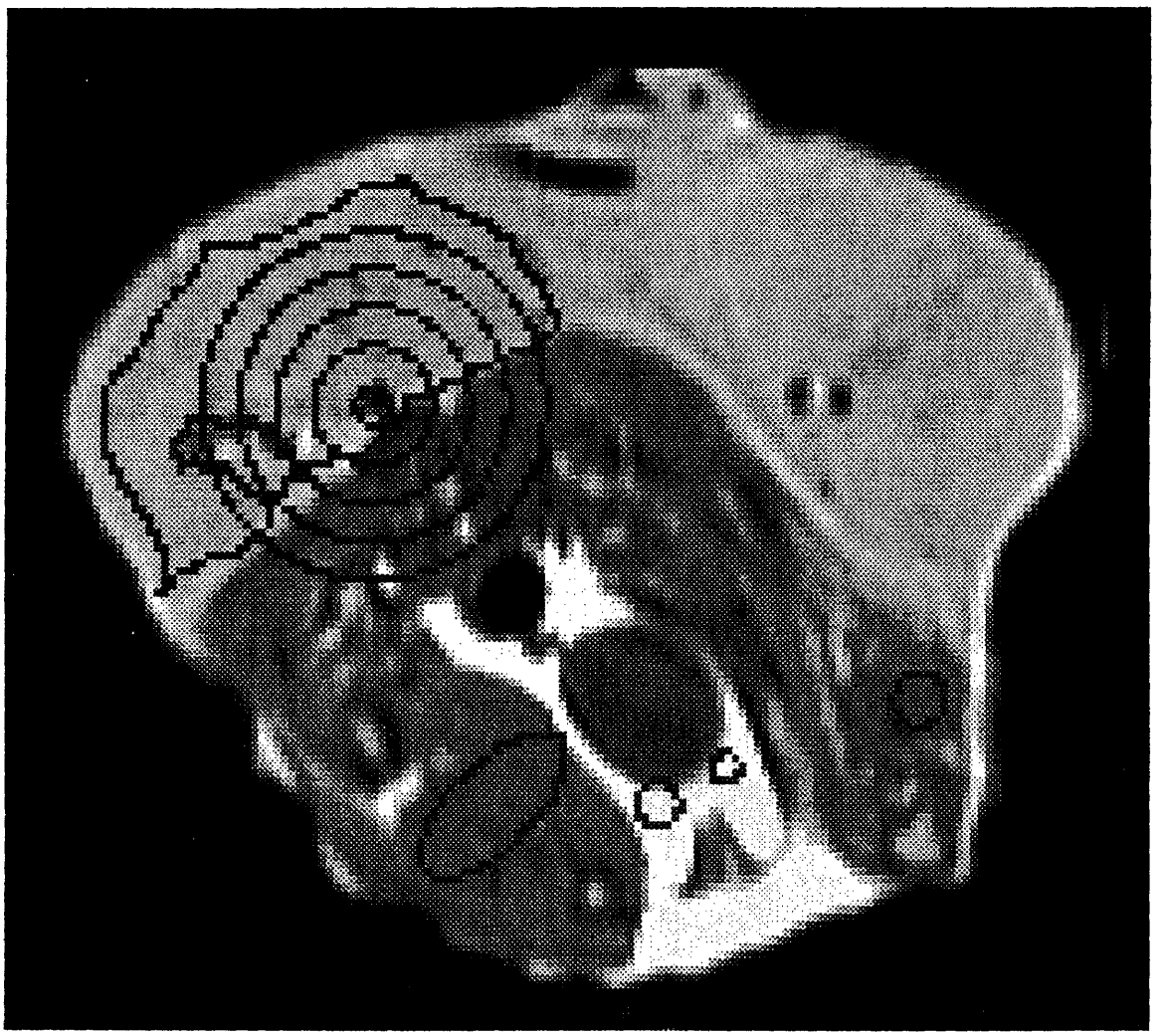

Figure A1.4 MR axial image of the tumor treated in Study #1282. Regions of interest for image processing are superimposed on the image. Only 4 regions of interest are defined for this tumor. Optical fiber is positioned very close to the skin. Imaging parameters are TR=1000msec, TE=18msec, ETL=8, FOV=8X6cm, total imaging time = 15 seconds.

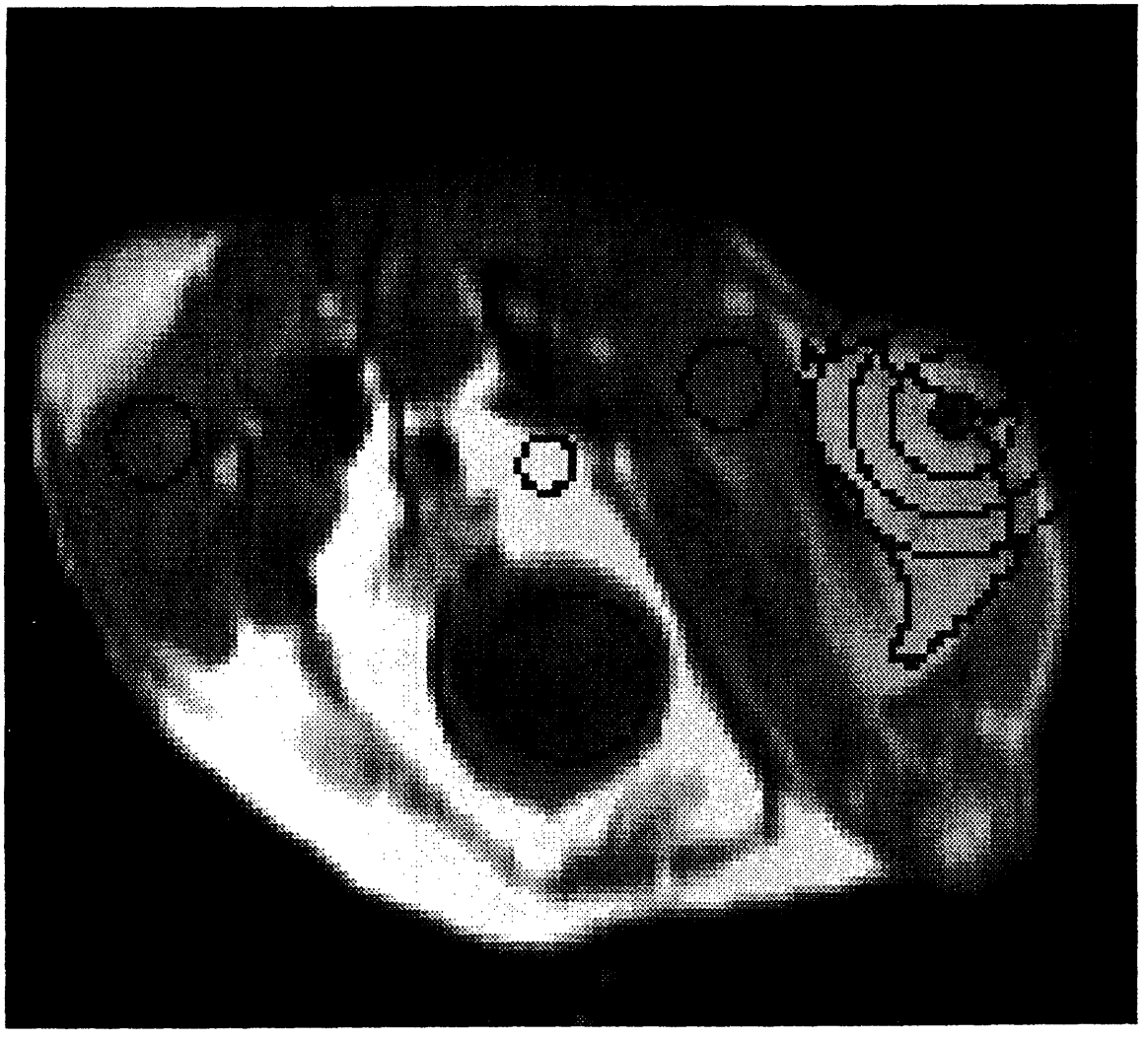

Figure A1.5 MR axial image of the tumor treated in Study #1336. Regions of interest for image processing are superimposed on the image. Regions of interest are limited by the tumor shape to an arc section instead of a complete annulus. Imaging parameters are TR=1000msec, TE=18msec, ETL=8, FOV=8X6cm, total imaging time = 15 seconds.

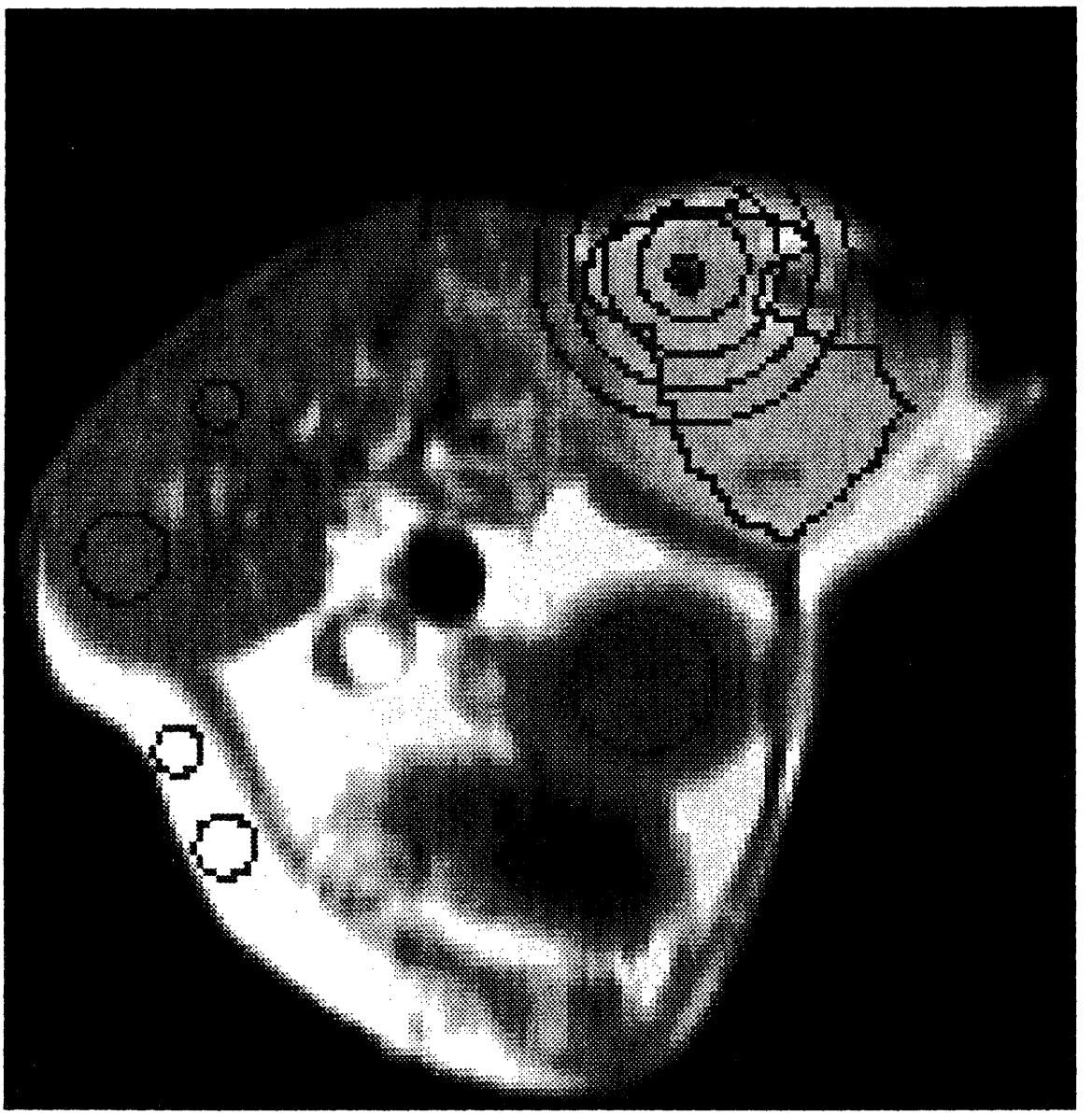

Figure A1.6 MR axial image of the tumor treated in Study #1392. Regions of interest for image processing are superimposed on the image. Vertical rectangular region of interest is used to exclude artifacts associated with a change in the water flow in the bed of the animal holder. Artifacts are not visible on this pre-treatment image. Imaging parameters are TR=1000msec, TE=18msec, ETL=8, FOV=8X6cm, total imaging time = 15 seconds.

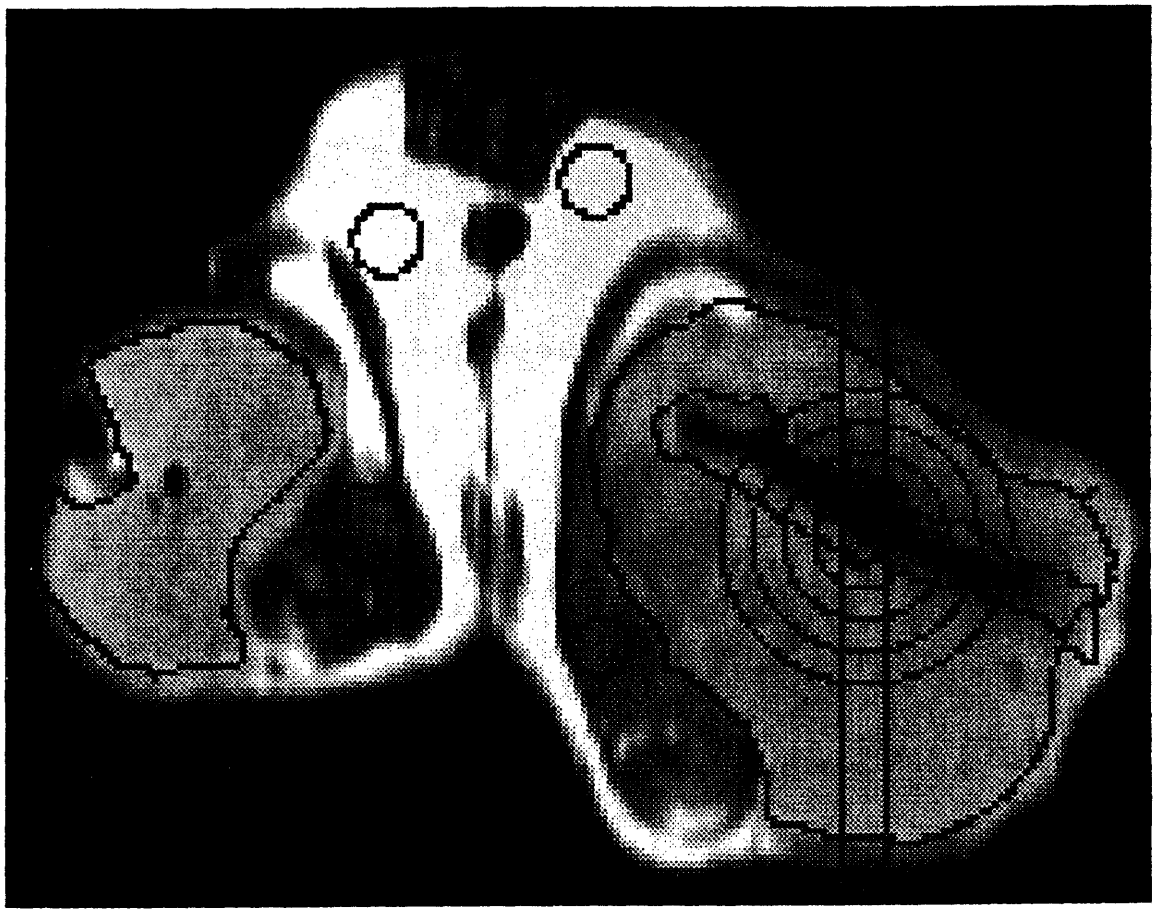

Figure A1.7 MR axial image of the tumor treated in Study #1413-R. Regions of interest for image processing are superimposed on the image. Signal void associated with the thermocouple array is seen cutting through the center of the tumor. Fiber placement was in the center of the tumor. Imaging parameters are TR=1000msec, TE=18msec, ETL=8, FOV=8X6cm, total imaging time = 15 seconds.

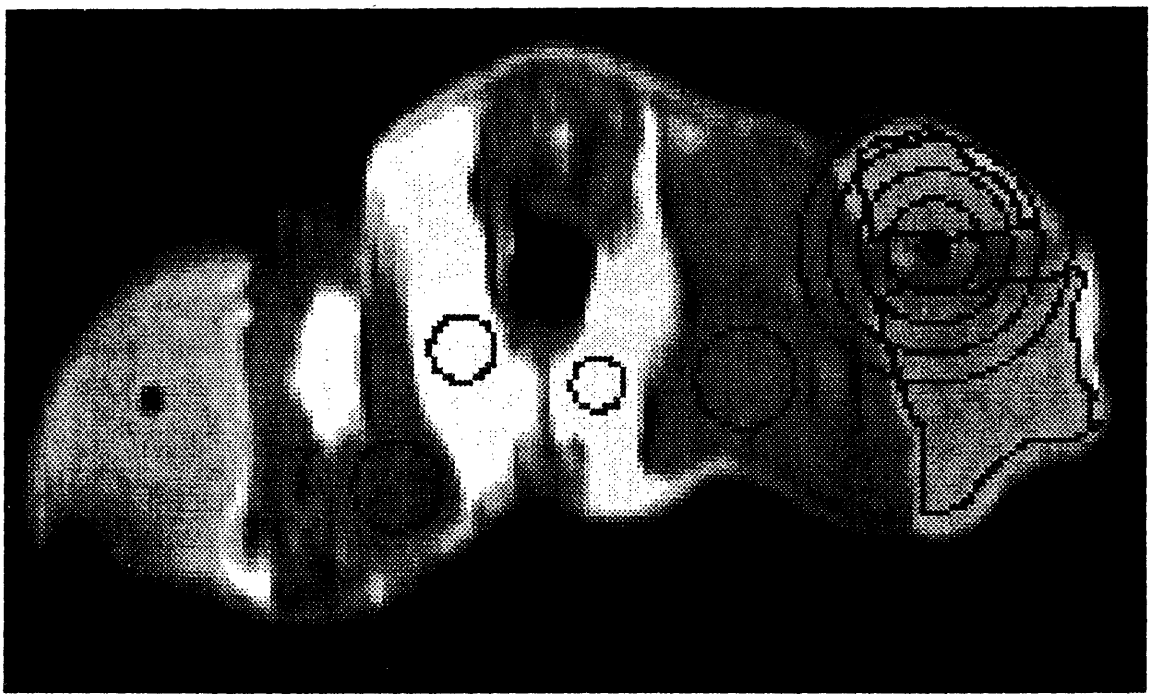

Figure A1.8 MR axial image of the tumor treated in Study #1413-L. Regions of interest for image processing are superimposed on the image. Signal void associated with the thermocouple array is again seen cutting through the center of the tumor. Fiber placement was in the center of the tumor. Heterogeneous signal intensity of tumor can be appreciated in contralateral tumor. Imaging parameters are TR=1000msec, TE=18msec, ETL=8, FOV=8X6cm, total imaging time = 15 seconds.

Appendix A2

This is the C code that was written as the front end of the Marquardt-Levenberg fitting algorithm to fit the measured surviving fraction values to the image derived surviving fraction values. It does all the data preparation including the subtraction and normalizing to get the percent signal intensity changes with the DC filter factors added in. It also has the capability to start the fitting with a variable set of coefficients to see if you get different results with different initial conditions. The following sections of code also include the subroutines that compute the image dose and surviving fraction according to the Sapareto-Dewey algorithm and compute the derivatives of chi squared with respect to the various coefficients in the equation.

```
/*      This program is designed to do the main image processing for my
thesis.
It has full file name handling capabilities but assumes the files come from
my
 Analyze directory.
I have added the data input functions, data sorting and organizing
capabilities
and the basic subtraction and normalization functions.
A complete set of functions, including the Marquardt fitting algorithm
from the Numerical
Recipes in C book have been added.  Program is now fully functional.

*/

#include <stdio.h>
#include <math.h>
#define NRANSI
#include "nr.h"
#include "nrutil.h"
#include <time.h>
#define      MA 7 /******** number of parameters to fit ******/

/*****       global variable section       **********/
int          imgcntdyn[255], rgncnt, *pixcnt, mfit, itst;
float        ***data, tau[255], *sig;
FILE          *foutput;


main(argc, argv)
```

```
int    argc;
char   **argv;
{

char          ch3, ser_name[250], img_prefix[250], in_name[250];
char         anadir1[250], anadir3[250], anadir2[250], datstr[250];
char          cell_prefix[250], out_name[250], cell_filename[255];
char          result_name[255];
float         yinit[90];
int          imgcntavg, img1, img2, cont;
int          zsize1, index, num, combo, rgn1, rgn2;
float        **avg, *x, *y;
int           *ia, NPT;
float         oalamda,  alamda,chisq,ochisq,**covar,**alpha;
int          inputindex, outputindex, i, j, j2, k, m, n;
int          dum1, dum2, dum3, dum4, dum5, pixsum, *pixcnt1;
int          ***pix, pixindex, maxpixcnt;
int          *rgncom, *apixcnt;
int           rgnnrmcnt,  rgnnrm[20];
float         *nrm,  *dynnrmimg,  **dynnrm;
FILE          *finput,*fo, *fcell, *fresult, *maint, *fitparam, *datfile;
float         a[MA+1];
float        chimin, *dyda, ytry;
float         sig2i, dy, ai[MA+1], af[MA+1], incr[50],incr1[MA+1];
int          na, p, ma, min[MA+1], stp[MA+1];
int           NPT1;
int           a1, a2, a3, a4, a5, a6, a1loop, a2loop, loop[50], lnflag;
float         a1incr, a2incr, a3incr, a4incr, a5incr, a6incr, chisqmin,
amin[MA+1],  chisqmin1,  amin1[MA+1];
struct tm     tp;
int           stcnt, stnum, stnum1, stnum2, rgnnum;

      mfit = MA;
      maint = fopen("input/maintotal", "r");
      fscanf(maint, "%d", &stcnt);
    data =  (float ***)malloc(45*sizeof(float *));
      NPT = 45;
    x=vector(1,NPT);
    y=vector(1,NPT);
    dyda=vector(1,NPT);
    sig=vector(1,NPT);
    ia=ivector(1,MA);
     covar=matrix(1,MA,1,MA);
     alpha=matrix(1,MA,1,MA);
    pixcnt = (int *)malloc(255*sizeof(int) );
      rgnnum = NPT = 0;
```

```
      printf("The output filename will have the same name with a .proc
suffix.\n");
       strcpy(out_name, "/laser/steve/ana/results/m1mapmain");
       strcpy(result_name, "/laser/steve/ana/results/resultsvol");

      fresult= fopen(result_name, "a+");
      foutput= fopen(out_name, "a+");



for(stnum=0;stnum<stcnt;stnum++)
{
      strcpy(anadir3,  "/laser/steve/ana/");
      strcpy(ser_name, anadir3);

      printf("Entering the name of the ANALYZE subdirectory the images
are in: \n");
      printf("Program assumes a base path of /laser/steve/ana/.\n");
      fscanf(maint, "%s", anadir1);

     n = strlen(anadir1);
      strncat(ser_name, anadir1,n);
      strncat(ser_name, "/", 1);
      strcpy(img_prefix, ser_name);
     printf("Entering the base name of the ANALYZE file the sampling
results are in: \n");
     printf("Program will add the .stats suffix to the pixel data file.\n");
     printf("Program will add the .cell suffix to the cell survival file.\n");
      fscanf(maint, "%s", anadir2);
     n = strlen(anadir2);
      strncat(img_prefix, anadir2,n);



       strcpy(in_name,  img_prefix);
      strncat(in_name,".stats",6);
      finput = fopen(in_name, "r");


      fscanf(finput, "%d %d", &imgcntavg, &img1);
      printf("The # of averaged images =%d and the starting image #
=%d.\n",imgcntavg,img1);
       fscanf(finput, "%d %d", &imgcntdyn[rgnnum], &img2);
      printf("The # of images for processing =%d and the starting image #
=%d.  \n",imgcntdyn[rgnnum],img2);
     fscanf(finput, "%d", &zsize1);
```

```
        printf("The total # of images that were processed in the series
=%d.\n",zsize1);

        fscanf(finput,  "%f",&tau[rgnnum]);
        printf("The number of seconds each image represents
=%f.\n",tau[rgnnum]);

        fscanf(finput,  "%d",&rgnnrmcnt);
        if(rgnnrmcnt)
                for(i=0;i<rgnnrmcnt;i++)
                        fscanf(finput,  "%d",&rgnnrm[i]);

        printf("The number of regions that will be used for normalization
=%d\n",rgnnrmcnt);
        if(rgnnrmcnt)
        {
                printf("and their region numbers are");
            for(i=0;i<rgnnrmcnt;i++)
                    printf(" %d ",rgnnrm[i]);
        printf("\n");
        }

/*****  read in all the data from the regions file      ************/

       fscanf(finput, "%d ", &rgncnt);
       apixcnt = (int *)malloc(rgncnt*sizeof(int) );

       rgncom = (int *)malloc(rgncnt*sizeof(int) );
        dynnrmimg = (float *)malloc(imgcntdyn[rgnnum]*sizeof(float));
        nrm = (float *)malloc(rgnnrmcnt*sizeof(float));
        dynnrm = (float **)malloc(rgnnrmcnt*sizeof(float *));

       for(i=0; i<rgnnrmcnt; i++)
             dynnrm[i] =  (float *)malloc(imgcntdyn[rgnnum]*sizeof(float));

      for (i=0; i<rgncnt; i++)
      {
        fscanf(finput, "%d", &pixcnt[rgnnum+i]);
       apixcnt[i] = pixcnt[rgnnum+i];
      rgncom[i] = 0;
      }

       fscanf(finput, "%d", &combo);
      for(i=0;i<combo;i++)
     {
       fscanf(finput, "%d %d", &rgn1, &rgn2);
       rgncom[rgn2] = rgn1*-1;
```

```
        if(rgn1 ==0) rgncom[rgn2] = -99;
        apixcnt[rgn1] += pixcnt[rgnnum+rgn2];

      }     /******* close while (combo)  loop     *******/

/*********      allocate the space for all the pixel data      **************/
      pix =  (int ***)malloc(rgncnt*sizeof(int *));

      for(i=0; i<rgncnt; i++)
            pix[i] =  (int **)malloc(zsize1*sizeof(int *));

      for(i=0; i<rgncnt; i++)
      {
      for (j=0; j<zsize1; j++)
            pix[i][j] =  (int *)malloc(apixcnt[i]*sizeof(int));
      }


        printf("Reading in data, please wait.\n");
      for (j=0; j<zsize1; j++)
      {
      for(i=0; i<rgncnt; i++)
      {
            for (k=0; k<pixcnt[rgnnum+i]; k++)
            {
              fscanf(finput,"%d %d %d %d
%d",&dum1,&dum2,&dum3,&dum4,&dum5);

              if (dum1 == (k+1) )  /************* condition 1 good data
***********/
                  pix[i][j][k] = dum5;


              else        /******** condition 4  data mismatch    **************/
              {
                  printf("Error reading in data.  Mismatch between pixel
number and position in pixel array.\n");
                    printf("Array position #%d, image #%d, pixel #%d.\n",i,j,k);
                    printf("Dummy variable values #%d, #%d, #%d, #%d,
#%d.\n",dum1,dum2,dum3,dum4,dum5);
                break;
              }  /* close final else condition   */

            } /* close k loop     */
      } /* close i loop      */
      } /* close j loop      */
```

```
    if(fclose(finput))
          printf("Error closing input file %s . \n", in_name);


/***   find the average of the baseline images in the normalization regions
*****/
     for (m=0; m<rgnnrmcnt; m++)
    {
     k=rgnnrm[m];
    nrm[m] = 0.0;

      for (j=0; j<pixcnt[rgnnum+k]; j++)
         {
        for (i= (img1-1);i<img1+imgcntavg-1; i++)
          nrm[m] += pix[k][i][j];
         }
       nrm[m] = nrm[m]/(pixcnt[rgnnum+k]*imgcntavg);
    } /* close m=0 loop    */
      printf("Normalization factors for the dynamic images.\t\t");
     for (m=0; m<rgnnrmcnt; m++)
            printf("%d:%6.2f\t",rgnnrm[m],nrm[m]);
      printf("\n");

/*****  find the normalization factor for each image in the dynamic series
*****/
     for (j=0; j<imgcntdyn[rgnnum]; j++)
    {
     j2 = img2-1+j;
     dynnrmimg[j] = 0.0;
      for (m=0; m<rgnnrmcnt; m++)
     {
       i=rgnnrm[m];
       dynnrm[m][j] = 0.0;
          for (k=0; k<pixcnt[rgnnum+i]; k++)
                dynnrm[m][j] += pix[i][j2][k]/(nrm[m]*pixcnt[rgnnum+i]);
        dynnrmimg[j] += dynnrm[m][j]/rgnnrmcnt;
     } /* close m=0 loop    */
       printf("img#%d  dynnrmimg=%.4f\t\t",j,dynnrmimg[j]);
    if((fmod(j,3))==0)
         printf("\n");

    } /* close j=0 loop */
     printf("\n");
```

```
      /*     re-assign any pixel values for region that have been added to other
regions.    */
        printf("re-assign any pixel values.\n");
       for (i=0; i<rgncnt; i++)
      {
       if (rgncom[i] < 0)
       {
          rgn1 = -1*rgncom[i];
                if(rgn1==99) rgn1 = 0;
           pixindex = pixcnt[rgnnum+rgn1];
         for (k=0; k<zsize1; k++)
           {
             for (m=0; m<pixcnt[rgnnum+i]; m++)
                  pix[rgn1][k][m + pixindex] = pix[i][k][m];
           } /* close k loop      */
          pixcnt[rgnnum+rgn1] += pixcnt[rgnnum+i];
         pixcnt[rgnnum+i] = 0;
           rgncom[i] = 0;
       } /* close if rgncom[i]      */
      } /* close i=0 loop     */

       printf("Resetting region numbers and order.\n");
       for (i=0; i<rgncnt; i++)
      {
       if (pixcnt[rgnnum+i] ==0)
       {
         for (j=i; j<rgncnt-1; j++)
         {
            *pix[j] = *pix[j+1];
             pixcnt[rgnnum+j] = pixcnt[rgnnum+j+1];
            pixcnt[rgnnum+j+1] = 0;
         } /* close j loop   */
         rgncnt = rgncnt - 1;
           i=i-1; /* prevent sequential zero count regions from screwing up
count.          **/
       } /* close if pixcnt[rgnnum+i]      */
      } /* close i=0 loop     */

/***    remove the normalized regions from the region count
****/
       rgncnt = rgncnt - rgnnrmcnt;

/**********     allocate space for avg, pixel data and biology data and set
dimensions
 for vectors and matrices here, now that final number of
regions and pixel counts is established
```

```
********/

        NPT = rgncnt;
       avg =  (float **)malloc(rgncnt*sizeof(float *));

       for(i=0; i<rgncnt; i++)
      {
        data[rgnnum+i] =  (float **)malloc(imgcntdyn[rgnnum]*sizeof(float
*));
        avg[i] =  (float *)malloc(pixcnt[rgnnum+i]*sizeof(float));
      }

       for(i=0; i<rgncnt; i++)
      {
       for (j=0; j<imgcntdyn[rgnnum]; j++)
            data[rgnnum+i][j] =  (float
*)malloc(pixcnt[rgnnum+i]*sizeof(float));
      }


        strcpy(cell_filename, img_prefix);
       strcat(cell_filename, ".cell", 5);
       fcell = fopen(cell_filename, "r+");

      for (i=1; i<=NPT; i++)
        {
         fscanf(fcell, "%f %f",&y[rgnnum+i], &sig[rgnnum+i]);
        }


      for (i=1; i<=NPT; i++)
        {
        if(y[rgnnum+i]<0)
            /* log of cell survival convert to surviving fraction*/
              y[rgnnum+i] = exp(y[rgnnum+i]);

        yinit[rgnnum+i]=y[rgnnum+i];

      }


      if(fclose(fcell))
            printf("Error closing cell culture results file %s .
\n",cell_filename);


/***   find the average of the baseline images for each pixel
```

```
*****/
      for (k=0; k<rgncnt; k++)
     {
       for (j=0; j<pixcnt[rgnnum+k]; j++)
      {
          avg[k][j] = 0.0;
         for (i= (img1-1);i<img1+imgcntavg-1; i++)
               avg[k][j] += pix[k][i][j]/imgcntavg;
       } /* close j=0 loop     */

     } /* close m=0 loop     */



/*     Now we have the average so do the subtraction
       and normalize.
        adjust the average with the normalization region averages.
*/
       printf("Subtracting and normalizing.\n");

      for (i= 0;i<rgncnt; i++)
     {
       for (j=0; j<imgcntdyn[rgnnum]; j++)
      {
       j2 = img2-1+j;
            for (k=0; k<pixcnt[rgnnum+i]; k++)
           {
           if(avg[i][k]==0.0)
                 data[rgnnum+i][j][k]=-1.0;
           else
                  data[rgnnum+i][j][k]=((dynnrmimg[j]*avg[i][k])-
pix[i][j2][k])/(dynnrmimg[j]*avg[i][k]);
           } /* close k=0 loop */

      } /* close j=0 loop */

     } /* close i=0 loop */

/*     Images have been subtracted from average and normalized, so write
them
      to a file.
*/
       printf("Images have been subtracted from average, normalized and DC
filtered.\n");


/*      a single study's data has been read in
```

```
        set the number of images for all the regions in this study
*/

        for (i=1;i<NPT;i++)
        {
                imgcntdyn[rgnnum+i] = imgcntdyn[rgnnum];
                tau[rgnnum+i] = tau[rgnnum];
        }
       x[rgnnum+1]= 100+rgnnum;
       x[rgnnum+2]= 101+rgnnum;
      for (i=3;i<=NPT;i++)
            x[rgnnum+i]=rgnnum+i-1;

        NPT1 += NPT;
        rgnnum += NPT;



/*      de-allocate all the storage space I allocated
*/
       for(i=0; i<rgncnt; i++)
      {
      for (j=0; j<zsize1; j++)
            free(pix[i][j]);
         free(pix[i]);
      }
        free(pix);
       for(i=0; i<rgncnt; i++)
        free(avg[i]);
      free(avg);
       for(i=0; i<rgnnrmcnt; i++)
            free(dynnrm[i]);
      free(dynnrm);
      free(apixcnt);
      free(rgncom);
        free(dynnrmimg);
        free(nrm);



/*      freed items
      pix =  (int ***)malloc(rgncnt*sizeof(int *));
      for(i=0; i<rgncnt; i++)
           pix[i] =  (int **)malloc(zsize1*sizeof(int *));
      for(i=0; i<rgncnt; i++)
     {
       avg[i] =  (float *)malloc(pixcnt[rgnnum+i]*sizeof(float));
```

```
    }
     avg =  (float **)malloc(rgncnt*sizeof(float *));
     for(i=0; i<rgnnrmcnt; i++)
          dynnrm[i] =  (float *)malloc(imgcntdyn[rgnnum]*sizeof(float));
      dynnrm = (float **)malloc(rgnnrmcnt*sizeof(float *));

     apixcnt = (int *)malloc(rgncnt*sizeof(int) );
     rgncom = (int *)malloc(rgncnt*sizeof(int) );
      dynnrmimg = (float *)malloc(imgcntdyn[rgnnum]*sizeof(float));
      nrm = (float *)malloc(rgnnrmcnt*sizeof(float));

*/



}       /*      close stnum (study number) loop                 ***/
/*      All data has now been entered
*/

     if(fclose(maint))
          printf("Error closing study listing file in program M1.\n");
      rgncnt = NPT = NPT1;

/*    set standard deviations */
/*    write y's and s.d.'s to file    */
     for (i=1; i<=NPT; i++)
     {
        sig[i]= (float)fabs(log(y[i]));
       printf("cell survival region %d = %f S.D.= %f\n",(i), y[i], sig[i]);
       fprintf(foutput, "cell survival region %d = %f.  S.D. =
%f.\n",i,y[i],sig[i]);
     }

       time(&tp);
       strcpy(datstr, ctime(&tp));
     fprintf(foutput, "\n\n\n");
     fprintf(foutput, "This data was generated by m1map.c at
%s.\n",datstr);
     fprintf(fresult, "\n\nThis data was generated by m1map.c for %s at
%s\n",anadir2, datstr);
     fprintf(foutput, "\n");



/*******      initialize first guess at fitting parameter values
```

```
*******/
/***** select which of the parameters to fit          *******/
        maint = fopen("input/mainmapparams", "r");
        printf("Enter the intial values for the fitting parameters and choose
which to fit.\n");
        for (i=1; i<=MA; i++)
        {
        printf("Enter initial value of parameter a[%d] = :",i);
        printf("\n");
        fscanf(maint, "%f",&a[i]);
        ai[i]= a[i];
        printf("Fit parameter a[%d]? (1=yes, 0=no)",i);
        printf("\n");
        fscanf(maint, "%d",&ia[i]);
        printf("Enter the increment and number of steps for the a[%d]
threshold:",i);
        printf("\n");
        fscanf(maint, "%f %d",&incr[i],&loop[i]);
        }



     if(fclose(maint))
            printf("Error closing parameter listing file in program M1.\n");
/****************
The next section includes the actual processing algorithm and the fitting
section
using the recipes downloaded from MIT.
***************/


/***************************************
this is the beginning of a loop I put around the main loop to run the
program
overnight in the background with different threshold settings
***************************************/

     if(fclose(foutput))
          printf("Error closing output file %s . \n", out_name);

       chisqmin1 = 1e6;

       for(a1=0;a1<loop[1];a1++)
       {

       for(a2=0;a2<loop[2];a2++)
```

```
        {

        for(a3=0;a3<loop[3];a3++)
        {

        for(a4=0;a4<loop[4];a4++)
        {

        for(a5=0;a5<loop[5];a5++)
        {

        for(a6=0;a6<loop[6];a6++)
        {

       foutput= fopen(out_name, "a+");
      a[6]=ai[6]+(incr[6]*a6);
      a[5]=ai[5]+(incr[5]*a5);
      a[4]=ai[4]*pow(incr[4],a4);
      a[3]=ai[3]*pow(incr[3],a3);
      a[2]=ai[2]*pow(incr[2],a2);
      a[1]=ai[1]+(incr[1]*a1);
        chisqmin = 1e6;

/*      call mrqmin1 with alamda = -1 to initialize.  mrqmin1 has a
modification to
        prevent any parameter value from being set <0
        ****/
      alamda = -1;
        mrqmin1(x,y,sig,NPT,a,ia,MA,covar,alpha,&chisq,fgauss,&alamda);
        ochisq = chisq;
        k = 1;
        itst =0;

/***** This is the main loop.  Do the fitting until the difference between the
new
         and old chi squared values is <0.1 for 4 consecutive tries.  Then
finish
         by calling mrqmin1 with alamda = 0  so that you can get the
uncertainties
         in the fitted parameters.
*****/
        while (itst < 6)
        {
       printf("\n%s %2d %17s %10.4g %10s %9.2e\n","Iteration #",k,"chi-
squared:",chisq,"alamda:",alamda);
      fprintf(foutput, "\n%s %2d %17s %10.4g %10s %9.2e\n","Iteration
#",k,"chi-squared:",chisq,"alamda:",alamda);
```

```
        for (i=1;i<=MA;i++) printf("%6s%1d%1s      ","a[",i,"]");
        printf("\n");
        for (i=1;i<=MA;i++) printf("%9.4f  ",a[i]);
        printf("\n");
        k++;

        oalamda = alamda;
        ochisq=chisq;
        mrqmin1(x,y,sig,NPT,a,ia,MA,covar,alpha,&chisq,fgauss,&alamda
);
        if(itst<11)
          {
           if (chisq<(0.98*ochisq))
                itst = 0;
           else
                itst++;


           if (chisq<chisqmin)
                {
                 chisqmin=chisq;
                 for(i=1;i<=MA;i++)
                      amin[i]=a[i];
                }

           if (chisq<chisqmin1)
                {
                 chisqmin1=chisq;
                 for(i=1;i<=MA;i++)
                      amin1[i]=a[i];
                }
          }

        }


      for (i=1;i<=MA;i++)
           printf("a[%d] = %9.4f\t",i,a[i]);
        printf("\n");

        alamda=0.0;
        mrqmin1(x,y,sig,NPT,a,ia,MA,covar,alpha,&chisq,fgauss,&alamda
);
        printf("\nUncertainties:\n");
        for (i=1;i<=MA;i++) printf("%6s%1d%1s","a[",i,"]");
      printf("\n");
        for (i=1;i<=MA;i++) printf("%9.2f",sqrt(fabs(covar[i][i])));
```

```
        printf("\n");

        fprintf(foutput, "\nUncertainties:\n");
       for (i=1;i<=MA;i++) fprintf(foutput, "%6s%1d%1s","a[",i,"]");
      fprintf(foutput, "\n");
        for (i=1;i<=MA;i++) fprintf(foutput, "%9.2f",sqrt(fabs(covar[i][i])));
        fprintf(foutput, "\n");

/*      write min chi to the output file  */
     if(itst>15)
            fprintf(foutput, "\nMinimum chi squared value from error-
terminated run.\n");
     else
            fprintf(foutput, "\nMinimum chi squared value from normal
run.\n");

      for(i=1;i<=MA;i++)
           fprintf(foutput, "a[%d]\t\t",i);
      fprintf(foutput, "\n");
      for(i=1;i<=NPT;i++)
           fprintf(foutput, "y[%d]\t\t",i);
       fprintf(foutput, "\n%10.4g.\n",chisqmin);
      for(i=1;i<=MA;i++)
                {
           fprintf(foutput, "%10.4g\t",amin[i]);
               a[i]=amin[i];
               }
      fprintf(foutput, "\n");

     for(i=1;i<=NPT;i++)
       {
           ffgauss(x[i],a,&ytry,dyda,na);
               fprintf(foutput, "%10.4g\t",yinit[i]);
               fprintf(foutput, "%10.4g\n",ytry);
    }
       fprintf(foutput, "\n");


     if(fclose(foutput))
           printf("Error closing output file %s . \n", out_name);


       } /********* end of a2loop loop    *****/

       } /********* end of a1loop loop    *****/

       } /********* end of a2loop loop    *****/
```

```
        } /********* end of a1loop loop    *****/

        } /********* end of a2loop loop    *****/

        } /********* end of a1loop loop    *****/
       foutput= fopen(out_name, "a+");

/*******       do manual fitting with this loop
        for (i=1;i<8;i++)
                a[i]=ai[i];
      m=1;
      while(m)
      {
       printf("Enter the number of the parameter value you would like to
change,");
      printf(" 0 to test new values, #<0 to quit and goto regular fitting
program with parameters as set:");
       scanf("%d",&k);
      while(k>0)
           {
            printf("a[%d] = %f.  New value:",k,a[k]);
            scanf("%f",&a[k]);
            printf("Enter the param number to change ");
           printf("0 to test new values, #<0 to quit:");
            scanf("%d",&k);
           }
      if(!(k))
           {
            for(i=1;i<=NPT;i++)
                  ffgauss(x[i],a,&ytry,dyda,na);
           }
      if(k<0)
           break;
      k=1;
      m=1;
      }

        disable manual fitting if running the loop for thresholds
*******/

/*      write absolute min chi to the output file       */
       fprintf(foutput, "\nMinimum chi squared value for whole session\n");

      for(i=1;i<=MA;i++)
           a[i]=amin1[i];
```

```
for(i=1;i<=NPT;i++)
      fprintf(foutput, "y[%d]\t\t",i);
 fprintf(foutput, "\n");

 for(i=1;i<=MA;i++)
      fprintf(foutput, "a[%d]\t\t",i);
 fprintf(foutput, "\n%10.4g.\n",chisqmin1);

 for(i=1;i<=NPT;i++)
   {
       ffgauss(x[i],a,&ytry,dyda,na);
           fprintf(foutput, "%10.4g\t",yinit[i]);
           fprintf(foutput, "%10.4g\t",ytry);
           fprintf(fresult, "%10.4g\t",yinit[i]);
           fprintf(fresult, "%10.4g\t",ytry);
   fprintf(foutput, "\n");
   fprintf(fresult, "\n");
}

 for(i=1;i<=MA;i++)
          {
       fprintf(foutput, "%10.4g\t",amin1[i]);
       fprintf(fresult, "%10.4g\t",amin1[i]);
          }
 fprintf(foutput, "\n");
 fprintf(fresult, "\n");

  fprintf(fresult, "Minimum chi squared value for whole session\t\t");
  fprintf(fresult, "%10.4g.\n",chisqmin1);
 if(fclose(fresult))
        printf("Error closing results file %s . \n", result_name);



 if(fclose(foutput))
        printf("Error closing output file %s . \n", out_name);


   free_matrix(alpha,1,MA,1,MA);
   free_matrix(covar,1,MA,1,MA);
  free_vector(sig,1,NPT);
 free_vector(y,1,NPT);
 free_vector(x,1,NPT);
  free_ivector(ia,1,MA);

 #undef NRANSI
```

```
} /*    close file     temporarily suspended for debugging*/
```

This is the program fgauss.c which calls the subroutine ffgauss.c to actually compute the surviving fraction values. It also calls ffgauss.c with coefficient values of ±10% and computes the gradient in the surviving fraction with respect to the coefficients in that manner.

```
#include <math.h>
#include "global.h"
extern        void ffgauss(float, float [], float *, float [], int);
void fgauss(float x, float a[], float *y, float dyda[], int na)
{

int     xint, i;
float   ai, yp, yn;

      xint = (int)x;
        for(i=1;i<=mfit;i++)
        dyda[i] = 0.0;

        if (!(xint))
        {
      for(i=1;i<=mfit;i++)
            printf("a[%d]=%8.3f, ",i,a[i]);
       printf("\n");
        }

        for (i=1; i<=mfit; i++)
        {
        ai = a[i];
        a[i] = 0.90*ai;
      ffgauss(x,a,y,dyda,na);
        yn = *y;
        a[i] = 1.1*ai;
      ffgauss(x,a,y,dyda,na);
        yp = *y;
        dyda[i] = ((yp-yn)/(ai*0.2));
        a[i] = ai;
        }

        ffgauss(x,a,y,dyda,9);
}       /* end fgauss        *******/
```

This is the program ffgauss.c that actually computes the image doses and surviving fractions.

```
#include <math.h>
#include "global.h"
void ffgauss(float x, float a[], float *y, float dyda[], int na)

/*********
FFGAUSS.C.SAPDEWEY
This is the version that computes cell survival according to the Sapareto-Dewey
equation.
**********/
{

int     rflag, index, cs0flag, cs1, cs0m, cs0f, i, j, k, m, xint, biphase, bicount,
bimax;
float   r, rsum, psum;
float   arg, cs;

        rflag = 0;
        if(x<99)
                {
                xint = (int)x;
                }
        else
                {
                xint=(int)(x-100);
                rflag = 1;
                }
        rsum = 0.0;
        cs0m = cs0f = cs1 = 0;
        for (j=0;j<pixcnt[xint];j++)
        {
                arg = 0.0;
                psum = 0.0;
                cs0flag = bicount = bimax = biphase = 0;
                for(k=0; k<imgcntdyn[xint]; k++)
                {
                if ((data[xint][k][j] - a[1]) > 0.0)
                        {
                        r=a[6];
                        if (bicount > bimax)        bimax = bicount;
                        bicount = 0;
                        psum += pow(r, (a[5]*(data[xint][k][j] - a[1])) );
```

```
                }
        else if(data[xint][k][j] < a[7])
                {
                cs0flag = 1;
                bicount++;
                }
        }

    if (bicount > bimax)    bimax = bicount;

    if ((psum*tau[xint])>a[2])
    {
    arg = (a[2]-(psum * tau[xint]))/a[4];
    cs = a[3] * exp(arg);
    }
    else
            cs = 2.0;

  if(cs>1.0)
            {
            cs1++;
            cs = 1.0;
            }
  if((cs0flag) && (rflag))
            {
            if(cs == 1.0)  cs1--;
            cs = 0.0;
            cs0f++;
            }

    rsum += cs;

    }       /*******       end for (j=0; *****/


    if(rsum<0.0)
    {
    *y = 0.0;
    if(na == 9)
            printf("Error: cell survival sum <0 in region %d.\n",xint);
    }
    else
    *y = rsum/pixcnt[xint];


}       /* end ffgauss.sapdewey *******/
```